UNIVERSITY OF COPENHAGEN
NIELS BOHR INSTITUTE

Optomechanical Memory for Light

Mads Bjerregaard Kristensen

Ph.d. Thesis

Advisor: Professor Albert Schliesser

Date: 11 August 2023

Institute:	Niels Bohr Institute
Author:	Mads Bjerregaard Kristensen
Title:	Optomechanical Memory for Light
Advisor:	Professor Albert Schliesser
External Referees	Professor Philipp Treutlein
	Associate Professor Witlef Wieczorek
Local Referee	Professor Klaus Mølmer
Submission Date:	11 08 2023

This thesis has been submitted to
the PhD school of Science at the University of Copenhagen.

Abstract

Mechanical resonators constitute an essential element in emerging quantum technologies. Since such resonators can couple to a range of different degrees of freedom, they are particularly promising in interfacing disparate quantum systems. The recent developments in the design of mechanical resonators with ever decreasing dissipation and quantum-coherent optical control of their displacement has cemented them as a principal element in the toolbox of hybrid quantum systems.

In this thesis, we report the demonstration of a long-lived and efficient memory for light based on an optomechanical cavity, operating at a wavelength in the telecom C-band. We study the storage and retrieval of coherent fields at room temperature, and demonstrate long life-times and reasonable efficiencies, $T_1 \approx 23\,\mathrm{ms}$ and $\eta \approx 40\%$ respectively, converting optical information to mechanical excitations by the phenomenon of optomechanically induced transparency.

We extrapolate the demonstrated room-temperature performance to cryogenic conditions, with cautious estimates indicating the feasibility of ground state cooling and the associated quantum-coherent storage of light with less than one added noise quantum. Lastly, we show that modest improvements to our platform can enable observing the effects of injecting single photons, as a step towards quantum repeater applications.

Resumé

Mekaniske resonatorer udgør et essentielt element i nye kvanteteknologier. Eftersom sådanne resonatorer kan koble til et bredt udvalg af andre frihedsgrader, er de særligt lovende til at sammensætte forskelligtartede kvantesystemer. De nylige udviklinger indenfor design af mekaniske resonatorer med støt formindskende dissipation og kvantekohærent optisk kontrol over deres forskydning har cementeret dem som et fremstående element i værktøjskassen af kvantehybridsystemer.

I denne afhandling rapporterer vi demonstrationen af en langlivet og effektiv lyshukommelse baseret på en optomekanisk kavitet, som opererer ved en bølgelængde i telekom C-båndet. Vi studerer opbevaring og genudlæsning af kohærente felter ved stuetemperatur, og demonstrerer lang levetid og fornuftig effektivitet, $T_1 \approx 23\,\mathrm{ms}$ og $\eta \approx 40\%$ respektivt. Oversættelsen mellem optisk information of mekaniske eksitationer er muliggjort af fænomenet optomekanisk induceret gennemsigtighed.

Vi ekstrapolererer de demonstrerede egenskaber fra stuetemperatur til et kryogenisk miljø. Forsigtige estimater indikerer muligheden for grundtilstandskøling og den dertilhørende kvantekohærente opbevarelse af lys med mindre end ét støjkvant tilføjet. Slutteligt viser vi hvordan små forbedringer af vores platform kan muliggøre at observere effekterne af at gemme enkelte fotoner, som et trin på vejen mod kvantenetværk.

Acknowledgements

No thesis is produced in a vacuum.

In fact, I have on the contrary been particularly lucky to conduct my Ph.D. studies in the very special environment of the quantum optics groups at the Niels Bohr Institute, surrounded by innumerable kind and inspiring colleagues that I will attempt to thank in the following paragraphs.

Among these, I first and foremost wish to thank my supervisor, Albert Schliesser. Over these past, by now quite a few, years I have learned more than I could have hoped for from you, and I am grateful for the freedom you have given me throughout the at-times convoluted path that has been the memory project.

The fellow members of the SLAB, past and present also deserve the highest praise. In particular I want to thank Yeghishe - your unquenchable enthusiasm when faced with *yet* another wafer of mysterious Q-factors, your insistence that plots ought to look good, and your eternally patient tutoring has in large part shaped who I am as a physicist, and for this I am grateful. Nenad, as my post-doc companion on the memory project through thick and thin, I think it is fair to say that it wouldn't have gotten to this point without your insistence on understanding *everything*. Many problems that at the time seemed like pointless minutiae to an eager Ph.D. student, would have been way trickier to address when they indeed reared their faces down the line, without our many (at times lengthy) discussions. Keep the change.

As for the past generation of members of the lab; Massi, Dave, JC, Letizia, Yannick, Sampo - these acknowledgments would quickly fill the same length as the rest of the document at hand if I were to do an honest job at recounting what a privilege it has been to learn from and with you.

Regarding my lab current colleagues, you definitely all deserve a shoutout: Felix, you're the most cheerful guy I know - stay that way; Eric L, without your COMSOL wizardry and intuition I would still be aligning the cavity instead of writing this; Teresa, your insistence on bringing people together at and outside of work makes the institute and group a better place to be; Thibault, I admire your relentless indignation with the state of the world and I aspire to embody a fraction of it; Aida, I promise you I will eventually master the dabke steps properly; Eric P, I would do good to learn from your ability to organize and prioritize; Sho, your crunchy-dry and surgically dosed sense of humor is magnificent; Ilia, I admire your resilience and ability to keep on going in the face of adversity; Lucio, your attention to aesthetics, in all matters avian or scientific, is something I hope to approach; Xiang, your commitment to sport and culinary activities makes us all more fit and accordingly deserving of your amazing cooking.

As mentioned, the quantum optics community at NBI is bigger than any one group - all the people of the HyQ and Quantop centers contribute to an atmosphere that is egalitarian and academically stimulating, which encourages collaboration rather than competition, not to mention a socially tightly-knit community. In particular I want to thank past office mates Camille and Aslı, as well as travel buddies Emil and Eva for some great times.

On a more serious note I want to thank Christoffer Østfeldt for helping me identify and deal with my work-related issues with mental balance. I think what already was a poor situation would have been exacerbated without you noticing, not hesitating to reach out, sharing your experiences, and regularly checking in.

Sigrid, I owe you the same thanks and infinitely more as well. You have been more supportive and loving than anyone reasonably could expect from a partner. You have been there to support me when I was down and weak, you have been there to share the good times. More than anyone else, I could not have done this without you.

Lastly I want to thank my parents Ole and Heidi for always encouraging my curiosity and supporting me in whatever I wanted to do.

Publication and Presentations

in review Mads Bjerregaard Kristensen, Nenad Kralj, Eric Langman, and Albert Schliesser
"A Long-lived and Efficient Optomechanical Memory for Light"
- Publication, manuscript in review [1].

July 2023 Mads Bjerregaard Kristensen, Nenad Kralj, Eric Langman, and Albert Schliesser
"Storage and retrieval of light using an ultra-coherent membrane resonator"
- Oral presentation (student paper finalist), Optica Quantum 2.0 Conference, Denver, USA.

April 2023 Mads Bjerregaard Kristensen, Nenad Kralj, Eric Langman, and Albert Schliesser
"Storage and Retrieval of Light Using an Ultracoherent Mechanical Resonator"
- Poster presentation, Les Houches thematic school "Optomechanics & NanophoNonics".

June 2022 Mads B. Kristensen, Nenad Kralj, Sho Tamaki, Beatrice Da Lio, Ravitej Uppu, Eva M. G. Ruiz, Anders S. Sørensen, Peter Lodahl, and Albert Schliesser
"Towards an Optomechanical Quantum Memory for Single Photons from a Quantum Dot Source"
- Poster presentation, Gordon Research Conference "Mechanical Systems in the Quantum Regime".

Table of content

List of Figures

List of Tables

1 Introduction

Pursuing a Ph.D. degree a century after the foundations of quantum mechanics [2, 3, 4, 5] in the same field might at first glance seem like a poor career choice; indeed one might ask: *"what's really left to discover?"*.

Luckily for budding quantum physicists, in my opinion this question can legitimately be answered: *"quite a lot as a matter of fact!"*.

As an example, out of the past ten Nobel prizes awarded in physics, no less than half have been given for research in various areas of quantum physics, and a further two in the related field of laser physics, enabled by quantum theory.

The past century of research in quantum physics is too extensive to faithfully summarize in an introduction such as this. Rather than quantum theory as a whole, we can hone in on the sub-field studied in this thesis: quantum cavity optomechanics [6, 7], describing the current state of the field.

1.1 Context

The subject matter of this research field is the quantum physics of light interacting with a mechanical oscillator. The field originates in the pursuit of detecting gravitational waves, whose existence were originally proposed by Einstein [8]. Throughout the 1960's to 1980's, pioneering research elucidated the promise of optical precision measurements of mechanical displacement for gravitational wave detection [9, 10, 11, 12, 13]. The realization that the quantum fluctuations of light would eventually limit the precision of an optomechanical gravitational wave detector due to optomechanical backaction effects [14, 15, 16] and the contemporary first observation of said effects in the optical domain [17] can then be viewed as the birth of *quantum* cavity optomechanics as its own field of research. Instead of viewing these effects as a detrimental limitation, quantum cavity optomechanics takes the complementary perspective and instead investigates this interaction in its own right.

Throughout the 1990's extensive theoretical research in the new field was carried out. Examples include radiation pressure-enabled quantum non-demolition measurements of an intracavity field [18], mechanically mediated (called *ponderomotive*) squeezing of light [19, 20], as well as schemes for generating a mechanical state like that of Schrödinger's thought experiment involving a (perhaps) ill-fated cat [21, 22].

This theoretical wave was followed by an experimental one, since the turn of the millennium. Progress in the fabrication of micro- and nanomechanical devices, enabled rapid diversification of the range of systems available for cavity optomechanical experiments, with examples such as toroidal cavities [23, 24], microspheres [25], optomechanical crystals [26], mechanically compliant capacitors in a superconducting LC-circuit [27], and membranes [28, 29]

among the many explored approaches.

Utilizing these new experimental platforms, exciting results such as strong [30, 27] and quantum-coherent [31] coupling. Furthermore ground state cooling by dynamical backaction [32] and measurement-based feedback [33, 34] with cryogenic pre-cooling, and recently even from room temperature [35, 36, 37] using levitated systems, with larger oscillators steadily approaching the ground state [38, 39, 40]. Moreover, non-classical states of motion [41], displacement measurements approaching [42] and even surpassing [43] the standard quantum limit [15] were demonstrated.

Of particular interest from a quantum network perspective, mechanically mediated entanglement of two optical fields [44] and optically mediated entanglement of two mechanical resonators [45] as well as violation of a Bell-type inequality in an optomechanical system [46, 47] have all been demonstrated.

In the wake of the myriad impressive experimental results, an emerging trend in the field is the development of optomechanical quantum technologies [48, 49]. Cavity optomechanics are not alone in this regard - a host of other quantum systems that can be interconnected are currently being explored as *hybrid quantum systems* [50]. Quantum-coherent coupling of quanta such as phonons and photons with atomic or spin systems holds great technological promise for quantum sensing [51, 52], computation [53, 54, 55], transduction [56], communication [57], and cryptography [58]. Due to the multitude of coupling mechanisms between mechanical and other quantum systems, these constitute an ubiquitous element in emerging quantum technologies.

A unifying vision based on these prospects is the *quantum internet* [59, 60]. In a nutshell, the idea is to interconnect remote quantum computers in a quantum-coherent manner. Apart from requiring quantum computers to interconnect in the first place, transduction from the quantum computer signal to an optical carrier is necessary for long-range communication. A further requirement for long-range quantum communication and networks is to overcome the exponential scaling of loss with distance. One approach is the quantum alternative to standard telecommunication amplification stations: the *quantum repeater* [61].

A prerequisite for a functioning quantum repeater is *quantum memory* for light [62]. By quantum memory we mean a quantum system, which can accept the state of another quantum system (writing a memory register), store it faithfully and eventually return the stored state (reading the stored information).

Typically the case of interest is a stationary, long-lived memory system, storing the state encoded on a traveling optical field, such as a coherent state or a single photon.

Such work was pioneered in the atomic physics community, where in particular the phenomenon of *electromagnetically induced transparency* (EIT) was studied for its quantum memory prospects [63, 64, 65, 66, 67, 68, 69]. During the aforementioned tidal wave of progress in experimental cavity optomechanics, an optomechanical analogue of EIT was discovered, namely *optomechanically induced transparency* (OMIT) [70, 71, 72].

The versatility of the optomechanical interaction, and in particular its largely wavelength-independent nature, presents an inherent advantage over atomic EIT systems, that are natively tied to particular transition wavelengths (though this in principle can be ameliorated by non-linear optical frequency conversion [73]). Since mechanical resonators these days also can be fabricated with exquisitely slow energy decay [74, 33, 75, 76, 77, 78], the prospect of long coherence times is indeed promising.

The application of this phenomenon for light storage was studied in a range of experimental platforms such as silica microspheres [79], diamond microdisks [80], with micro-second, and without quantifying the storage efficiency of such mechanical memory platforms, or in phonon waveguides [81], with reported efficiencies, but even shorter storage times.

Storage times in the milli-seconds have only been demonstrated for devices cryogenically cooled to milli-Kelvin temperatures, with prominent examples including a microwave (rather than optical) experiment [82], that thus however is unsuited for long-range networks [83], and a telecom-wavelength experiment employing the DLCZ protocol [66, 84].

In this thesis we report on a telecom wavelength optomechanical memory device, based on a high-Q membrane resonator embedded in a high-finesse optical Fabry-Pérot cavity [74, 85].

To this end, we introduce new mechanical resonator designs, suited to the practical requirements of such an membrane-based optomechanical memory.

We thoroughly experimentally study and theoretically model the achievable efficiency in such a device in a range of storage experiments with coherent input fields. With a view to quantum repeater applications, we discuss the prospects of applying our platform for the storage and retrieval of single-photon input fields.

In addition to the mechanical memory experiments, we report on high-Q and low-mass mechanical resonator designs, intended for force sensing applications.

1.2 Thesis Structure

In section 2, we develop the necessary understanding of optical cavities. We describe the spectral response of a cavity, as well as the geometry of the intracavity field. Lastly we give a quantum description of a single cavity mode.

In section 3 we derive the equation of motion for a thin, tensioned membrane, and map it to an effective 1D resonator. We then cover relevant sources of dissipation in such resonators and again lastly describe such a single mechanical mode quantum mechanically.

The design of our resonators is motivated in section 4, introducing the physics of dissipation dilution and soft clamping. In addition we give a few rules of thumb for the practical design of high-quality mechanical resonators.

We put optics and mechanics together in section 5. Here we describe cavity optomechanics, covering radiation pressure coupling in the canonical end-mirror model and the membrane-in-the-middle scheme we practically employ. We discuss the connection between the two implementations and how to map the coupling constant appropriately.

Section 6 covers the practicalities of characterizing mechanical resonators and conducting cavity optomechanics experiments. Additionally we describe the process of assembling a membrane-in-the-middle cavity.

In section 7 we report on the characterization of a range of different mechanical resonator designs.

The experiments on optomechanical light storage and retrieval is covered in section 8. We first detail our implemented cavity and surrounding experimental setup, before covering the storage experiments, with a focus on the efficiency. We also discuss the prospects of single-photon experiments in this section, and lastly conclude in section 9.

2 Optical Cavities

"When God said, 'Let there be light,' he surely must have meant perfectly coherent light."

Charles Townes

Optical cavities are ubiquitous throughout our experiments, notably constituting the optical element of our opto-mechanical system. We begin our description of these in a classical picture, in order to develop a number of experimentally relevant quantities. Anchored in these concepts, we switch to a complementary, more abstract model of the intra-cavity electric field as a quantum mechanical harmonic oscillator, coupled to an external environment.

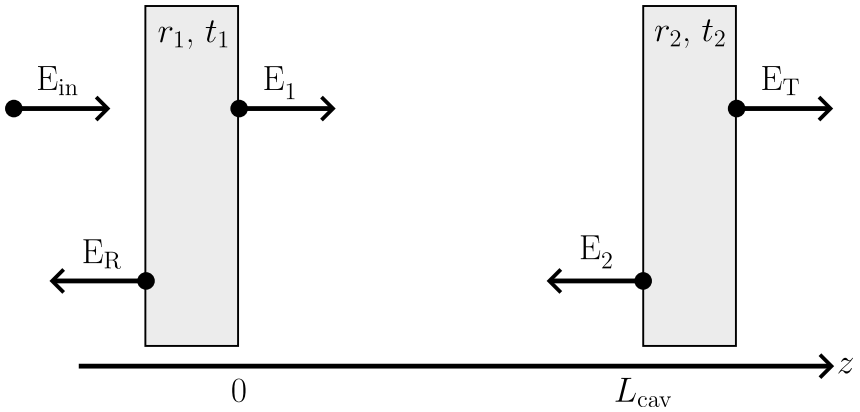

Figure 2.1: Sketch of an optical Fabry-Pérot cavity. An incident optical field E_{in} is either reflected or coupled into the cavity, comprised of two highly-reflective mirrors with reflection and transmission coefficients r_i, t_i, a distance L_{cav} apart.

Two highly reflective mirrors 1 and 2, each with a field reflectivity r and transmissivity t, placed a fixed distance L_{cav} apart, form the archetypal example of an optical cavity, known as the Fabry-Pérot resonator, illustrated in figure 2.1.

If an electric field $E(\mathbf{r}, t)$ at a point in space $\mathbf{r}$ at time t oscillates with a period T that divides into the roundtrip time $\tau_{\text{rt}} \coloneqq 2L_{\text{cav}}/c$ an integer number q, it can be resonantly enhanced by the cavity, and a strong field can build up inside, as we shall see in the following. To give an example of its utility, this strong field can enhance the interaction between light and a system placed inside the cavity.

For simplicity we presently assume the mirrors to be ideal, in the sense that all light which is not reflected must be transmitted,

$$|r_i|^2 + |t_i|^2 = 1, \tag{2.1}$$

where $i \in (1, 2)$ indexes the mirrors. Light inside the cavity will eventually be transmitted by either mirror at a rate κ_i given by the product of the probability of transmission, $|t_i|^2$, and the rate at which the circulating light strikes the mirror in question, namely the inverse roundtrip time:

$$\kappa_i \coloneqq |t_i|^2/\tau_{\mathrm{rt}}. \tag{2.2}$$

The total loss rate of the cavity κ is then given by the sum of the individual loss rates,

$$\kappa = \Sigma_i \kappa_i. \tag{2.3}$$

With identical mirrors, we can now see that the intra-cavity light will leak out of either mirror at equal rates. Oftentimes in quantum optics experiments, where detection efficiency is paramount, it is advisable to make the light exit the cavity preferentially through one mirror, by choosing its transmission coefficient larger than its partner. The degree to which the light decays through the preferred mirror j is quantified by the cavity coupling parameter,

$$\eta_c \coloneqq \kappa_j/\kappa. \tag{2.4}$$

Last but not least, we introduce the finesse $\mathcal{F}$ of a cavity. This handy number describes the average number of roundtrips a resonant photon makes inside the cavity in question and is defined

$$\mathcal{F} \coloneqq \frac{2\pi}{\sum_i \delta_i} = \frac{2\pi}{\kappa \tau_{\mathrm{rt}}}. \tag{2.5}$$

Any excess energy loss in the cavity, for instance due to scattering or absorption of light by dirt particles on a mirror face, will reduce $\mathcal{F}$ and can be accounted for by including a term δ_{exc} in the sum of losses, eq. (2.3).

With the nomenclature in order, let us investigate the intra-cavity field. By tallying up the effect of the two mirrors illustrated in figure 2.1 on an incident beam of laser light E_{in} with wavelength λ and corresponding wavenumber $k \coloneqq 2\pi/\lambda$, one can write a set of equations for the right- and leftward propagating components of the intra-cavity field, E_1 and E_2, as well as the experimentally accessible reflected and transmitted fields E_{R} and E_{T}:

$$E_1 = it_1 E_{\mathrm{in}} + r_1 E_2 \mathrm{e}^{-ikL_{\mathrm{cav}}}, \tag{2.6a}$$

$$E_2 = r_2 E_1 \mathrm{e}^{-ikL_{\mathrm{cav}}}, \tag{2.6b}$$

$$E_{\mathrm{R}} = r_1 E_{\mathrm{in}} + it_1 E_2 \mathrm{e}^{-ikL_{\mathrm{cav}}}, \tag{2.6c}$$

$$E_{\mathrm{T}} = it_2 E_1 \mathrm{e}^{-ikL_{\mathrm{cav}}}. \tag{2.6d}$$

Noting that E_{R} and E_{T} are given in terms of E_1, and that a photodetector

is sensitive to the intensity impinging upon it, we proceed to solve the system of equations (2.6) for the circulating intracavity intensity[1] $|E_1|^2$, normalized to the input intensity $|E_{\text{in}}|^2$,

$$\left|\frac{E_1}{E_{\text{in}}}\right|^2 = \frac{|t_1|^2}{1+|r_1|^2|r_2|^2-2|r_1||r_2|\cos(2kL_{\text{cav}}+\phi)}, \tag{2.7a}$$

$$\phi = \arg(r_1)+\arg(r_2). \tag{2.7b}$$

We make two important and related observations about the intracavity intensity. Firstly it exhibits strong resonant enhancement when λ is an integer q multiple of the roundtrip length $2L_{\text{cav}}$ (ignoring the arbitrary phase ϕ), which alternatively can be stated in terms of the frequency $\nu \coloneqq c/\lambda$ as

$$\nu_q = q\frac{c}{2L_{\text{cav}}}, q \in \mathbb{Z}. \tag{2.8}$$

Additionally, the cavity response is periodic in frequency, supporting resonant modes characterized by the number of nodes of the intracavity intensity, labeled by the longitudinal mode number q. These modes have frequencies equally spaced by the free spectral range (FSR) of the cavity ν_{FSR},

$$\nu_{\text{FSR}} \coloneqq \nu_{q+1}-\nu_q = \frac{c}{2L_{\text{cav}}}, \tag{2.9}$$

which we note is precisely the inverse roundtrip time τ_{rt}. The FSR allows us to recast the finesse as

$$\mathcal{F} = 2\pi\frac{\nu_{\text{FSR}}}{\kappa}. \tag{2.10}$$

Restricting our treatment to high-finesse $\mathcal{F} \gg 1$ cavities, and honing in on a particular longitudinal mode j, looking only at small frequency excursions $\Delta \coloneqq \omega-\omega_j$ from (angular) resonance frequency $\omega_j = 2\pi\nu_j$, we can by expanding the cosine of equation 2.7 and dropping terms $\propto (1/\mathcal{F})$ derive a line shape for a cavity mode

$$\left|\frac{E_1}{E_{\text{in}}}\right|^2 = \frac{2\eta_1\mathcal{F}}{\pi}\frac{(\kappa/2)^2}{(\kappa/2)^2+\Delta^2}. \tag{2.11}$$

Equations (2.7) and (2.11) are plotted in figure 2.2, in the vicinity of a single cavity mode.

We see that the Lorentzian approximation holds very well for the relevant high-finesse ($\mathcal{F} \approx 2\times10^4$ here) case we usually work with. In the following we prefer the Lorentzian description, as it has the advantage of being easier to interpret in terms of cavity parameters. For example from inspecting eq. (2.11) we learn that the intra-cavity intensity is amplified proportionally to

[1] We take a normalization convention such that $|E|^2$ denotes the optical energy flux hitting the mirror.

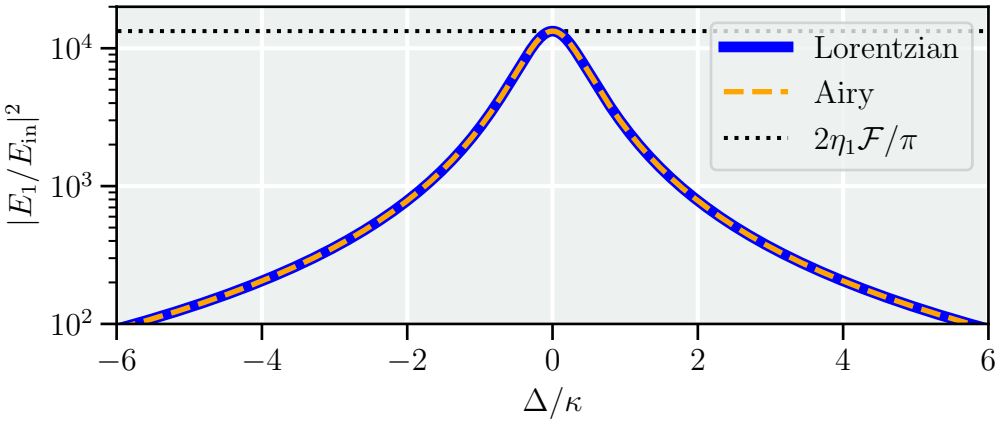

Figure 2.2: Intracavity intensity. In solid blue we plot the Lorentzian approximation (eq. (2.11)) to the Airy function (eq. (2.7)), near a single resonant mode. The dotted black line indicates the resonant enhancement factor $2\eta_1\mathcal{F}/\pi$ from eq. (2.11).

the finesse, and that a given cavity mode exhibits a peaked spectrum with a full-width-half-max κ, lending credence to its identification as the cavity linewidth.

2.1 Shape of the Intracavity Field

So far we have implicitly assumed the field inside the cavity to consist of plane waves, reflecting back and forth between plane mirrors, which it in fact does not. In the following, we remedy the situation, discussing how mirror geometry determines the transverse shape of the intracavity field, and how it varies along, and orthogonal to, the cavity axis. We will review a number of relevant results from a detailed analysis of how the width and angle of divergence of an optical beam is transformed by various optical elements, as given in eg. [86]. In this discussion we assume perfect alignment of the cavity mirrors, i.e. the mirrors are centered on the axis joining them, and not tilted with respect to it.

2.1.1 Cavity Stability

The configuration of plane mirror faces cannot support stable modes in practice - any deviation from absolutely perfect normal incidence will never be corrected, causing the beam to wander off and leave the cavity. On the contrary this is not the case for mirrors with a concave reflective face. Such mirrors can support beams with a spatial profile determined by the geometry of the cavity mirrors, whose stability also is governed by the curvature of the mirror faces and the distance between them. One can derive a stability condition,

which determines whether a given configuration can sustain stable modes [86]

$$0 \leq g_1 g_2 \leq 1, \tag{2.12}$$

where the cavity geometry is encoded in the g-parameters

$$g_i = 1 - \frac{L_{\text{cav}}}{R_i}, \tag{2.13}$$

R_i denoting the radius of curvature of the mirrors. There exists a range of configurations that satisfies eq. 2.12, and in our experiments we make use of two: a plano-concave design comprised of a flat mirror and a concave one for the optomechanical cavity and a concave-concave design with two identical concave mirrors for our filter cavities. In these two cases, stable resonances can be obtained provided $0 < L_{\text{cav}} < R$ and $0 < L_{\text{cav}} < 2R$ respectively.

2.1.2 Gaussian Beams

Determining the intra-cavity field profile boils down to finding a solution to Maxwell's equations, obeying the relevant boundary conditions. In the present case, we consider monochromatic light, which propagates unidirectionally and has a finite cross-section, that obeys the Helmholtz equation. As outlined in [milleber], the simplest electric field obeying these conditions has to the following spatial dependence:

$$E(\mathbf{r}) = \frac{A}{w(z)} \mathrm{e}^{i(kz - \arctan z/z_{\text{R}})} \mathrm{e}^{ik\frac{x^2+y^2}{2R(z)}} \mathrm{e}^{-\frac{x^2+y^2}{w^2(z)}}. \tag{2.14}$$

Equation 2.14 decribes a so-called *gaussian beam*, propagating along the z-direction, named for its transverse (x, y) dependence. A handful of new concepts are introduced here, so their definitions and names are summarized in table 1 and detailed in the following. Such gaussian beams are solutions for the intra-cavity field.

Symbol	Definition	Name
$w(z)$	$w_0\sqrt{1 + (z/z_{\text{R}})^2}$	Beam width
w_0	$\sqrt{\frac{\lambda L}{\pi}} \left(\frac{g_1 g_2 (1-g_1 g_2)}{(g_1+g_2-2g_1 g_2)^2}\right)^{1/4}$	Beam waist
z_{R}	$\pi w_0^2/\lambda$	Rayleigh range
$R(z)$	$z + z_{\text{R}}^2/z$	Radius of curvature

Table 1: Geometric properties of a Gaussian beam.

The beam width describes the radius of the beam as it propagates, while the beam waist defines its minimal radius. The Rayleigh range z_{R} gives a measure for the length over which the beam remains mostly collimated,i.e.

$w(z_R) = \sqrt{2}w_0$.. Finally the radius of beam curvature $R(z)$ is not to be confused with the mirror radii of curvature R_i, though they are related - for a beam to be supported by a given set of mirrors, $R(z)$ must match the curvature of the mirrors.

These modes have resonance frequencies that also are determined by the cavity geometry and can be found by requiring the phase change upon a roundtrip of the intra-cavity field be an integer multiple of 2π. This gives an equation for the q'th mode:

$$\nu_q = \frac{c}{2L_{\text{cav}}}\left(q + \frac{1}{\pi}\sqrt{g_1 g_2}\right), \tag{2.15}$$

from which we also can recover our previous statement of the cavity FSR, $\nu_{\text{FSR}} = c/2L_{\text{cav}}$, even in the case of non-flat mirrors as required by a stable cavity.

2.1.3 Higher-order modes

The gaussian beams of equation 2.14 correspond to our previous description of equidistant modes with frequencies separated by the FSR. They are however not the only stable solutions.

There exists a range of higher-order transverse modes associated with each longitudinal cavity mode. By allowing for a more complex (x, y)-dependence

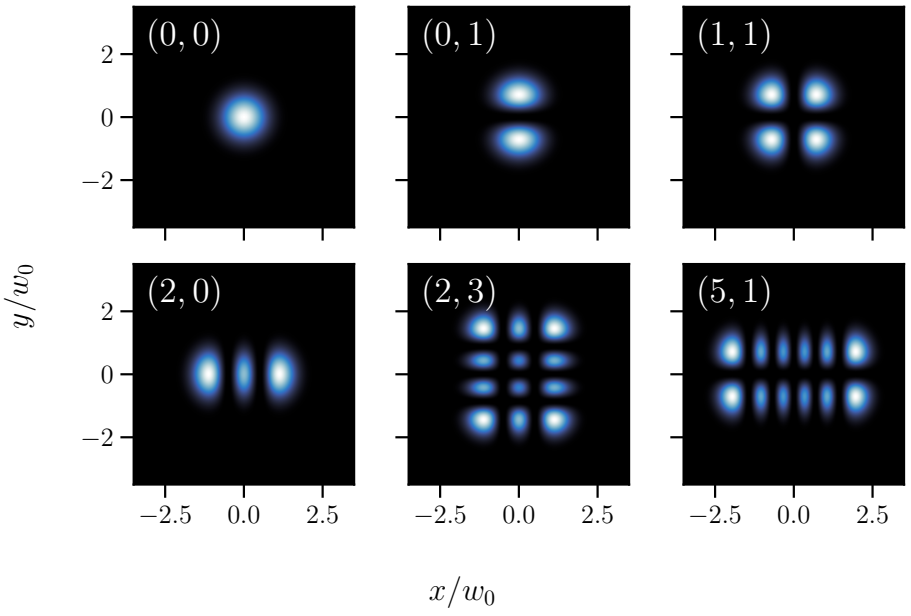

Figure 2.3: Intensity profile of higher order transverse cavity modes. For different (n, m), we plot $|E_{n,m}(x, y)|^2$ for $z = z_0$, according to eq. (2.16).

of the mode shape, one finds so-called *Hermite-Gaussian* modes, with field profiles:

$$E_{n,m}(\mathbf{r}) = E(\mathbf{r}) w_0 H_n\left(\frac{\sqrt{2}x}{w(z)}\right) H_m\left(\frac{\sqrt{2}y}{w(z)}\right) \mathrm{e}^{-i(n+m)\arctan z/z_\mathrm{R}}. \tag{2.16}$$

Here $E(\mathbf{r})$ is the fundamental mode of eq. 2.14 and $(n, m) \in \mathbb{N}$ are transverse mode indices labelling the number of nodal lines. The modes described by eq. 2.16 are referred to as the n, m'th transverse electromagnetic mode, often abbreviated $\mathrm{TEM}_{n,m}$. The frequencies of these resonances can be found in a similar manner to the fundamental case,

$$\nu_{q,n,m} = \nu_\mathrm{FSR}\left(q + \frac{1+n+m}{\pi}\sqrt{g_1 g_2}\right). \tag{2.17}$$

We learn that each longitudinal mode is accompanied by another set of spectrally equidistant, more densely spaced transverse modes, with increasingly spatially broader mode profiles, as seen in figure 2.3.

2.2 Quantized Cavity Modes

In the preceding classical treatment we have seen that a cavity supports a range of distinct longitudinal and transverse modes. In this section we are interested in the quantum properties of such a single mode, and how it is coupled to the environment outside the cavity mirrors. The standing electric and magnetic fields can be written [87]

$$E(z,t) = q(t)\sqrt{\frac{2\Omega_\mathrm{cav}^2}{\epsilon_0 V}}\sin(kz), \tag{2.18a}$$

$$B(z,t) = \frac{\dot{q}(t)}{c^2 k}\sqrt{\frac{2\Omega_\mathrm{cav}^2}{\epsilon_0 V}}\cos(kz). \tag{2.18b}$$

Here $q(t)$ encodes the amplitude of the electric field, Ω_cav is the frequency of the particular cavity mode, ϵ_0 is the permittivity of vacuum, V the mode volume and c is the speed of light.

The Hamiltonian H describing the energy stored in the fields can be found by integrating the electromagnetic energy density over the cavity mode volume

$$H = \frac{1}{2}\int_V \epsilon_0 E^2(z,t) + \frac{1}{\mu_0}B^2(z,t)\mathrm{d}V = \frac{1}{2}\left(\Omega_\mathrm{cav}^2 q^2(t) + \dot{q}^2(t)\right), \tag{2.19}$$

where μ_0 is the vacuum permeability. Equation 2.19 describes a unit-mass harmonic oscillator

$$H = \frac{1}{2}\left(\Omega_{\text{cav}}^2 q(t)^2 + p(t)^2\right) \tag{2.20}$$

with momentum $p(t) \coloneqq \dot{q}(t)$. The Hamiltonian of eq. 2.20 can be quantized in terms of the annihilation operator a and its Hermitian conjugate creation operator $a^\dagger$, which satisfy the commutation relation $\left[a, a^\dagger\right] = 1$ [87]. Position and momentum can be restated using the these

$$q(t) = \sqrt{\frac{\hbar}{2\Omega_{\text{cav}}}}\left(a(t) + a^\dagger(t)\right), \tag{2.21a}$$

$$p(t) = \sqrt{\frac{\hbar\Omega_{\text{cav}}}{2}}\left(a(t) - a^\dagger(t)\right), \tag{2.21b}$$

$$[q(t), p(t)] = i\hbar. \tag{2.21c}$$

Substituting q and p, the quantized cavity Hamiltonian becomes

$$H = \hbar\Omega_{\text{cav}}\left(a^\dagger a + \frac{1}{2}\right). \tag{2.22}$$

Phrasing the physics in terms of the ladder operators gives us the intra-cavity field as

$$E(z,t) = \sqrt{\frac{\hbar\Omega_{\text{cav}}}{\epsilon_0 V}}\sin(kz)(a(t) + a^\dagger(t)), \tag{2.23}$$

revealing that the temporal evolution is determined solely by the evolution of a and its conjugate.

In the Heisenberg picture, time evolution of an operator $\mathcal{O}$ of the system described the Hamiltonian H is given by the Heisenberg equation of motion

$$\dot{\mathcal{O}} = \frac{i}{\hbar}\left[H, \mathcal{O}\right]. \tag{2.24}$$

In our case, eq. 2.24 gives us $\dot{a} = -i\Omega_{\text{cav}}a$, that is, in a Hamiltonian description, devoid of coupling between the single cavity mode and its surroundings, the intra-cavity electric field simply oscillates at the cavity frequency.

To incorporate the physics of shining light into the cavity and measuring its reflection and transmission, the theoretically stringent approach would be to introduce the formalism of open quantum systems [6]. Rather than going into detail on this subject we review the results and relevant assumptions.

The core idea is to make a mental distinction between what we care about, called *the system*, and everything else, which we call *the reservoir*. The isolated evolution of the system is described by equation 2.24, whereas the reservoir can be modeled as a large number of independent harmonic oscillators $a_{\text{R},j}$,

with a bi-linear coupling between the system and reservoir $\propto a^\dagger_{\mathrm{R},j} a + a_{\mathrm{R},j} a^\dagger$ ("a photon is created in a reservoir mode when one is destroyed in the system mode and vice versa"). One furthermore assumes that the reservoir is large enough that it can be considered "memory-less". Formally this is called the *Markov* approximation and means that the bath oscillators at different times are uncorrelated,

$$\left\langle a^\dagger_{\mathrm{R},j}(t_1) a_{\mathrm{R},j}(t_2) \right\rangle = \bar{n}\delta(t_1 - t_2) \tag{2.25a}$$

$$\left\langle a_{\mathrm{R},j}(t_1) a^\dagger_{\mathrm{R},j}(t_2) \right\rangle = (\bar{n}+1)\delta(t_1 - t_2). \tag{2.25b}$$

Here $\bar{n}_j$ denotes the average number excitations, related to the temperature of the bath T via Bose-Einstein statistics

$$\bar{n}_j = \frac{1}{\mathrm{e}^{\hbar\Omega_j / k_\mathrm{B} T} - 1}, \tag{2.26}$$

where k_B is the Boltzmann constant. For lasers with typical frequencies around 10^{14} Hz, the mean occupation of such modes are all essentially zero, even at room temperature. By finally changing frame of reference to one rotating at the laser frequency, and neglecting fast-oscillating terms (invoking the rotating wave approximation), only looking at small detunings from resonance $\Delta = \Omega_\mathrm{L} - \Omega_\mathrm{cav}$, one finds the time-evolution from the *quantum Langevin equation* (QLE) for the cavity mode a

$$\dot{a} = \left(i\Delta - \frac{\kappa}{2} \right) a + \sqrt{\kappa} s_\mathrm{in}. \tag{2.27}$$

Here s_in describes the input photon flux[2], containing a vacuum contribution from the reservoir as well as any laser light we send to the cavity. When the cavity is coupled to the environment through multiple distinct channels, such as two mirrors with different reflectivity, we can modify eq. 2.27 accordingly

$$\dot{a} = \left(i\Delta - \frac{\kappa}{2} \right) a + \sqrt{\eta_1 \kappa} s_{\mathrm{in},1} + \sqrt{\eta_2 \kappa} s_{\mathrm{in},2}, \tag{2.28}$$

where $\eta_{1,2}$ are the cavity coupling parameters previously introduced and $s_{\mathrm{in},1/2}$ is the flux impinging on either mirror. Considering for simplicity eq. 2.27, a solution for a is easily found in the Fourier domain in terms of the cavity susceptibility $\chi_\mathrm{cav}(\Omega)$ defined such that

[2]Often in the literature this quantity is given the symbol a_in. Since (the norm square of) a and s_in describe an energy and a flux respectively, the chosen notation emphasizes this difference, and avoids seemingly identical quantities a and a_in with different units.

$$a(\Omega) = \chi_{\mathrm{cav}}(\Omega)\sqrt{\eta\kappa}s_{\mathrm{in}}, \tag{2.29a}$$

$$\chi_{\mathrm{cav}}(\Omega) = \frac{1}{\kappa/2 - i(\Delta + \Omega)}. \tag{2.29b}$$

The experimentally accessible quantities for probing the cavity field are the output fluxes $s_{\mathrm{out},j}$ emanating from either mirror. These are given by the input-output relation for the j'th channel,

$$s_{\mathrm{out},j} = s_{\mathrm{in},j} - \sqrt{\eta_j\kappa}a. \tag{2.30}$$

For example a photodetector, giving an output proportional to $|s_{\mathrm{out}}|^2$, will depend on a, as described in more detail in section 6.1.2.

3 Mechanical Oscillators

"I love it when things bend out of shape."

Kevin Shields

Here we introduce the dynamics of our mechanical resonators. Starting from the core concepts of linear elasticity theory, namely strain and stress, and their relation, we derive the equation of motion for the out-of-plane displacement of a membrane. For illustrative purposes we first study modeshapes for plain, square membranes. Then we apply Galerkin's model to reach a 1D description with any geometric dependence lumped into an effective mass and spring constant. Lastly we discuss mechanical dissipation, first modelling its origin with Zener's model and then the practicalities of different dissipation channels and their means of mitigation. The description will at times closely follow [88, 89, 90, 91]

3.1 Linear Elasticity: Mechanical Equation of Motion

Elasticity is the theory of mechanics of extended solid objects, large enough to be considered continuous bodies, with any granularity absorbed into macroscopic material constants such as density or stiffness [92, 93]. Such a solid body, subject to some external force, will undergo deformation. We can describe this in terms of the *displacement vector* $\mathbf{u}$, defined through its entries as

$$u_i = r_i' - r_i, \tag{3.1}$$

where $i \in (x, y, z)$ denotes the coordinates of a point $\mathbf{r}'$ in the deformed body relative to the equilibrium position $\mathbf{r}$, as illustrated in figure 3.1 (left). We can recast the deformation in terms of the *strain tensor* $\underline{\underline{\varepsilon}} \coloneqq \{\varepsilon_{ij}\}$,

$$\varepsilon_{ij} = \frac{1}{2}\left(\partial_j u_i + \partial_i u_j + \partial_i u_k \partial_j u_k\right) \tag{3.2}$$

where summation over indices repeated in a term is implied, a convention we keep in the following, and ∂_i is the partial derivative with respect to the i^{th} spatial coordinate.

As the body undergoes deformation, new internal forces arise, tending to restore the body to equilibrium. We call these *internal stresses* and describe them by considering a volume element of the body. Letting $\mathbf{F}$ denote the external force per unit volume, we introduce the *Cauchy stress tensor* $\underline{\underline{\sigma}} \coloneqq \{\sigma_{ij}\}$ by means of the Cauchy stress hypothesis:

$$\sigma_{ij} = \frac{\mathrm{d}F_i}{\mathrm{d}S_j} \tag{3.3}$$

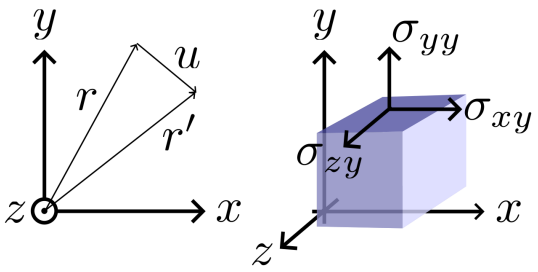

Figure 3.1: Sketch of displacement and stress. Left: the coordinate vector before and after, r and r', are connected by the displacement vector u. Right: The components of the stress tensor is drawn on the y face of a solid body.

In this manner, σ_{ij} denotes i^{th} component of force per unit area, acting on the face of the volume element normal to the j^{th} axis (see figure 3.1, right).

When considering small elastic deformations the relationship between stress and strain is linear and given by *Hooke's law*

$$\sigma_{ij} = C_{ijkl}\varepsilon_{kl} = \frac{E}{1+\nu}\left(\varepsilon_{ij} + \frac{\nu}{1-2\nu}\delta_{ij}\varepsilon_{kk}\right), \tag{3.4}$$

where C_{ijkl} is the elastic modulus tensor, E denotes Young's modulus and ν the Poisson ratio of the particular material, while δ_{ij} is the Kroenecker delta.

We can simplify the problem considerably by making a series of approximations in accordance with the geometry of the membranes in question, and the type of displacement they undergo. We assume:

1. The in-plane components of the displacement are small compared to the out-of-plane component $u_x,\ u_y \ll u_z$.

2. The thickness of the membrane h remains constant during deformation.

3. The out-of-plane displacement component is small relative to the thickness of the membrane, $u_z \ll h$.

4. The thickness is small compared to the lateral size of the membrane, $h \ll L$.

By the first assumption we disregard in-plane motion of the membrane, and instead only consider the out-of-plane component, which we shall re-label $w \coloneqq u_z$. The second assumption implies that w cannot have a z dependence, i.e. $w = w(x, y)$. Additionally the thinness of the membrane means that it is more susceptible to bending due to forces applied on the surface, than to extension and compression, meaning

$$\sigma_{ij} n_j = 0, \tag{3.5}$$

where n_j denotes the j'th component of the membrane normal vector $\mathbf{n}$. Using the third assumption we can approximate the normal vector of the membrane surface $\mathbf{n}$ as remaining oriented along the z direction, $\mathbf{n}||\widehat{\mathbf{z}}$. Together with eq.3.5, this parallelity implies $\sigma_{iz} = 0$ on the upper and lower faces on the membrane, which we extend to the entire body of the membrane, again by virtue of its thinness.

The upshot of the preceding reasoning is that we can restrict the treatment to in-plane strain and stress tensors obtained from equations 3.2 and 3.4 respectively (here we emphasize the switch to a 2D treatment using Greek, rather than Roman indices),

$$\varepsilon_{\alpha\beta} = \varepsilon_0\delta_{\alpha\beta} - z\partial_{\alpha\beta}w + \frac{1}{2}\partial_\alpha w\partial_\beta w, \tag{3.6a}$$

$$\sigma_{\alpha\beta} = \frac{E}{1-\nu^2}\left((1-\nu)\,\varepsilon_{\alpha\beta} + \nu\delta_{\alpha\beta}\varepsilon_{\gamma\gamma}\right). \tag{3.6b}$$

The first term in eq.(3.6)a independent of w, represents a static in-plane strain ε_0 which is known to occur during the fabrication process of the membranes we study. As we shall see when discussing dissipation of mechanical energy, this strain and its associated stress is in fact a salient feature of our devices. Evaluating the stress tensor gives

$$\begin{aligned}\sigma_{\alpha\beta} = \sigma_0\delta_{\alpha\beta} - z\frac{E}{1-\nu^2}\Big((1-\nu)\partial_{\alpha\beta}w + \nu\delta_{\alpha\beta}\partial_{\gamma\gamma}w\Big)\\ +\frac{E}{2(1-\nu^2)}\Big((1-\nu)\partial_\alpha w\partial_\beta w + \nu\delta_{\alpha\beta}\partial_\gamma w\partial_\gamma w\Big),\end{aligned} \tag{3.7}$$

where we identify the static pre-stress $\sigma_0 \coloneqq E\varepsilon_0/(1-\nu)$. The equations of motion comes about from a lengthy calculus of variations of the stored elastic energy density V of the membrane. We will not go into detail here, but they can be found in [92]. It is however instructive to just calculate V at this point, since we need this later in our discussion of dissipation.

Since w is independent of z, we can integrate out any z-dependence and instead consider an in-plane potential energy density $V_{\text{ip}} = \int_{-h/2}^{h/2} V dz$, which means any term linear in z will not contribute. With this in mind, some algebra gives

$$\begin{aligned}V_{\text{ip}} = \frac{1}{2}\sigma_{\alpha\beta}\varepsilon_{\alpha\beta} = h\sigma_0\varepsilon_0 + \frac{1}{2}h\sigma_0\partial_\alpha w\partial_\alpha w + \frac{hE}{1-\nu^2}\partial_\alpha w\partial_\alpha w\partial_\beta w\partial_\beta w\\ +\frac{h^3E}{6(1-\nu^2)}\Big[(1-\nu)\partial_{\alpha\beta}w\partial_{\alpha\beta}w + \nu\partial_{\alpha\alpha}w\partial_{\beta\beta}w\Big].\end{aligned} \tag{3.8}$$

The first constant term represents an arbitrary offset associated with the static strain. The second term contains the energy stored in the pre-stress, while the third describes the non-linear effect of elongation, which is negligible for small oscillations. The last term contains the energy stored in bending of the membrane.

To derive the mechanical equation of motion from $\sigma_{\alpha\beta}$ and $\varepsilon_{\alpha\beta}$, one then needs to do a calculus of variations of eq. (3.8). This is a fairly involved and lengthy procedure, so instead we jump to the outcome, namely the Von Kármán plate equations [94]:

$$\partial_{\alpha\beta} M_{\alpha\beta} + \partial_\alpha \left(N_{\alpha\beta} \partial_\beta w \right) = \rho h \ddot{w} \tag{3.9a}$$

$$\partial_\alpha N_{\alpha\beta} = 0. \tag{3.9b}$$

These have been stated in terms of the shear stresses $N_{\alpha\beta}$ and bending momenta $M_{\alpha\beta}$, known collectively as the *stress resultants*, which can be evaluated using eq. 3.7:

$$N_{\alpha\beta} = \int_{-h/2}^{h/2} \sigma_{\alpha\beta} \mathrm{d}z = h\sigma_0 \delta_{\alpha\beta} + \frac{hE}{2(1-\nu^2)} \left((1-\nu) \partial_\alpha w \partial_\beta w + \nu \delta_{\alpha\beta} \partial_\gamma w \partial_\gamma w \right) \tag{3.10a}$$

$$M_{\alpha\beta} = \int_{-h/2}^{h/2} z \sigma_{\alpha\beta} \mathrm{d}z = -D \left((1-\nu) \partial_{\alpha\beta} w + \nu \delta_{\alpha\beta} \partial_{\gamma\gamma} w \right), \tag{3.10b}$$

where we identify the *flexural rigidity* $D \coloneqq h^3 E / (12(1-\nu^2))$. Since the second term in $N_{\alpha\beta}$ is non-linear in w it can safely be neglected for small vibration amplitudes. Taking eqs. 3.9 and 3.10 together, we find the equation of motion for the out-of-plane displacement as

$$h\sigma_0 \partial_{\alpha\alpha} w - D \partial_{\alpha\alpha\beta\beta} w = \rho h \ddot{w}. \tag{3.11}$$

By identifying $\partial_{\alpha\alpha}$ as the transverse Laplacian ∇^2, eq. 3.11 might look more familiar.

The time dependence of equation 3.11 is all on the right-hand side, and is thus separable from the spatial left-hand side. Therefore we can look for eigenmode solutions like

$$w_{n,m}(x, y, t) = \psi_{n,m}(x, y) q_{n,m}(t), \tag{3.12}$$

where n, m are mode indices, labelling a given eigenmode by its number of antinodes along the x, y directions respectively. Galerkin's method is our tool

of choice for approaching the problem of finding such solutions.

3.2 Galerkin's Method: 1D Effective Resonator

The core idea of the Galerkin method is to reduce the dimensionality of the problem at hand, by deriving an effective mass and spring constant wherein the static effects of the resonator geometry are lumped. When we only are concerned with the time evolution of a single mode, this is a useful simplification.
In practice one assumes an orthogonal set of eigenfunctions $\{\psi_{n,m}(x,y)\}$ of the equation at hand, multiplies the equation by an eigenfunction and integrates the variables to be aggregated into effective parameters over their domain, in this case the membrane surface $\mathcal{S}$. Applying this algorithm to equation 3.11 gets us:

$$\begin{aligned} \rho h \int_{\mathcal{S}} \psi_{n,m} \ddot{w}_{n,m} \mathrm{d}A &= h\sigma_0 \int_{\mathcal{S}} \psi_{n,m} \nabla^2 w_{n,m} \mathrm{d}A - D \int_{\mathcal{S}} \psi_{n,m} \nabla^4 w_{n,m} \mathrm{d}A, \\ \ddot{q}_{n,m} \underbrace{\rho h \int_{\mathcal{S}} \psi_{n,m}^2 \mathrm{d}A}_{m_{\text{eff}}} &= -q_{n,m} \underbrace{\int_{\mathcal{S}} \left[D\psi_{n,m} \nabla^4 \psi_{n,m} - h\sigma_0 \psi_{n,m} \nabla^2 \psi_{n,m} \right] \mathrm{d}A}_{k_{\text{eff}}}. \end{aligned} \tag{3.13}$$

Having managed (in a sensible manner) to reduce the unwieldy three-dimensional deformation problem to simple, harmonic motion we can celebrate an intermediate victory at this point!
The two terms in the effective spring constant distinguish two regimes of deformation: we say the dynamics are either *rigidity*- or *stress*-dominated depending on whether the first or second contribution is the largest. To quantify which regime a certain resonator is in, we first consider the limit of the fundamental mode of a purely stress-dominated square membrane as a benchmark. In this case equation 3.11 reduces to the two-dimensional wave-equation, with eigenmodes and frequencies:

$$\begin{aligned} w_{n,m}^{(0)}(x,y,t) &= A_{n,m} \phi_{n,m}^{(0)}(x,y) \sin \Omega_{n,m}^{(0)} t, \\ \phi_{n,m}^{(0)}(x,y) &= \sin \frac{n\pi x}{L} \sin \frac{m\pi y}{L}, \\ \Omega_{n,m}^{(0)} &= \frac{\pi}{L} \sqrt{\frac{\sigma_0}{\rho} (n^2 + m^2)}, \end{aligned} \tag{3.14}$$

where the superscripts remind us that we neglected the rigidity term. For such a fundamental mode, we can gauge the ratio of the stress and rigidity contributions through the dimensionless stress parameter[3] λ [95]:

[3] For modeshapes similar to those of equation 3.14, the spatial derivatives pick up a factor $1/L$ per order.

$$\lambda \coloneqq \sqrt{\frac{D/L^4}{h\sigma_0/L^2}} = \sqrt{\frac{Eh^2}{12(1-\nu^2)\sigma_0 L^2}}. \tag{3.15}$$

At the edges where the membrane is clamped, it must fulfill the boundary condition $w = \partial_\alpha w = 0$, which the simplified sinusoidal modeshapes of equation 3.14 do not, i.e. the membrane is not supported by a perfect hinge, but rather has to bend over a length scale determined by its rigidity. A refined model, valid for $\lambda n \ll 1$, finds such a correction term near the edges [95]:

$$\begin{aligned} w_{n,m}(x,y,t) &= A_{n,m}\phi_n(x)\phi_m(y)\sin\Omega_{n,m}t, \\ \phi_n(x) &= \begin{cases} \psi_n(x) & \text{if } 0 \le x < L/2 \\ (-1)^{n+1}\psi_n(L-x) & \text{if } L/2 \le x \le L \end{cases}, \\ \psi_n(x) &= \sin\frac{n\pi x}{L} + n\pi\lambda\left(\mathrm{e}^{-x/\lambda L} - \cos\frac{n\pi x}{L}\right), \\ \Omega_{n,m} &= \Omega^{(0)}_{n,m}\sqrt{1+\pi^2\lambda^2\left(n^2+m^2\right)}. \end{aligned} \tag{3.16}$$

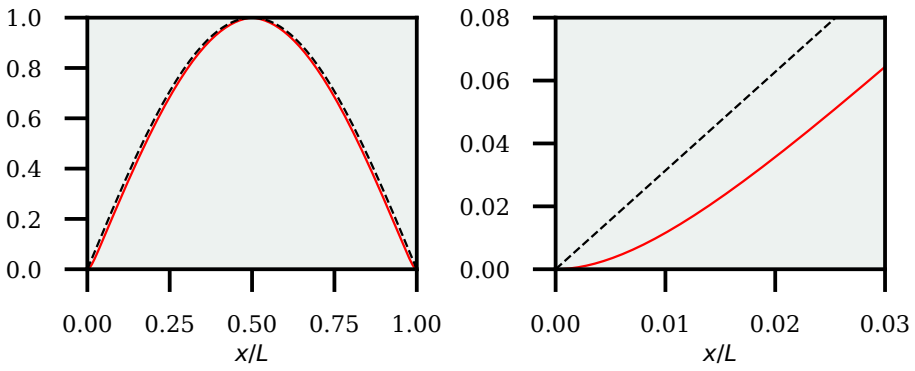

Figure 3.2: Left: comparing modeshapes neglecting (dashed black line) and including (red solid line, $\lambda = 0.01$) rigidity. Right: Zoom in near edge, where the increased rigidity-induced curvature for finite λ is apparent.

A 1D slice of the modeshapes predicted by equations 3.14 and 3.16 is plotted in figure 3.2. Here one indeed sees good agreement between the models at the global scale, but discrepancy near the edges as expected. As we shall see in the coming section, this edge-bending effect implies that clamping conditions have profound impact on the dissipation rate of a resonator.

3.3 Mechanical Dissipation

Our description of mechanical motion has solely considered conservative, non-dissipative processes so far. In this section we expand our model to encompass dissipation. The description of dissipation will stand on two legs, like the preceding sections: firstly introducing a damping term at the abstract level of the effective 1D harmonic oscillator we just derived, and secondly describing and categorising the actual loss mechanisms our samples are subject to, as well as means to alleviate these where possible.

To motivate our chosen approach, let us start by looking at a toy model. Following Schmidt, Villanueva, and Roukes [88], we consider a body undergoing harmonic motion, with a phase lag φ between the strain and stress fields:

$$\varepsilon(t) = \varepsilon_0 \sin(\omega t), \tag{3.17a}$$

$$\sigma(t) = \sigma_0 \sin(\omega t + \varphi). \tag{3.17b}$$

By trigonometric identities, the stress field can be split into two components

$$\sigma(t) = \sigma_0 \big(\underbrace{\cos\varphi \sin\omega t}_{\text{in-phase}} + \underbrace{\sin\varphi \cos\omega t}_{\text{out-of-phase}} \big), \tag{3.18}$$

the former oscillating in phase with the strain field, and the latter out of phase. When assessing energy loss in a resonator, the *quality factor* is a useful quantity. We denote it Q and define it as the ratio of stored energy W to lost energy ΔW during one oscillation cycle:

$$Q \coloneqq 2\pi \frac{W}{\Delta W}. \tag{3.19}$$

Within our toy model we can compute W and ΔW as integrals of the stress-strain product over a quarter and full period respectively, only keeping the in-phase stress term when evaluating the stored energy [88]:

$$W = \int_0^{\pi/2\omega} \sigma\dot{\epsilon} \, \mathrm{d}t = \frac{1}{2}\sigma_0\varepsilon_0 \cos\varphi, \tag{3.20a}$$

$$\Delta W = \int_0^{2\pi/\omega} \sigma\dot{\epsilon} \, \mathrm{d}t = \pi\sigma_0\varepsilon_0 \sin\varphi, \tag{3.20b}$$

which combines to give

$$Q_{\text{int}} = (\tan\varphi)^{-1}. \tag{3.21}$$

From equation 3.21 we see the importance of this phase delay between stress

and strain - its tangent determines in the (inverse) Q factor. For this reason $\tan\varphi$ is also referred to as the *loss tangent* of a resonator (φ being the *loss angle*). Furthermore, we call this quantity the *intrinsic* quality factor in the sense that we only are considering the resonator itself in these considerations.

3.3.1 Anelasticity: Zener's Model

This relation between Q and stress-strain lag was studied by Clarence Zener, within his eponymous model [96]. By including a finite response time for a changing stress under constant strain τ_ε and vice versa τ_σ, Hooke's law can be extended to

$$\sigma + \tau_\varepsilon \dot{\sigma} = E_\mathrm{R}(\varepsilon + \tau_\sigma \dot{\varepsilon}), \tag{3.22}$$

where E_R denotes the Young's modulus under relaxed stress and strain. Solving eq. 3.22 in the Fourier domain reveals an effective, complex-valued Young's modulus E_eff:

$$\sigma = \underbrace{E_\mathrm{R}\frac{1+i\Omega\tau_\sigma}{1+i\Omega\tau_\varepsilon}}_{E_\mathrm{eff}}\varepsilon, \tag{3.23a}$$

$$E_\mathrm{eff} = \frac{1+\Omega^2\tau_\sigma\tau_\varepsilon}{1+\Omega^2\tau_\varepsilon^2} + i\Omega\frac{\tau_\sigma-\tau_\varepsilon}{1+\Omega^2\tau_\varepsilon^2}. \tag{3.23b}$$

The real and imaginary parts of E_eff are analogous to the in- and out-of-phase strain components that we studied in the preceding section. From their ratio we can re-express Q_intr in terms of a relaxation time scale $\bar{\tau}$ and strength Δ_E:

$$Q_\mathrm{intr}^{-1} = \frac{\mathrm{Im}\,(E_\mathrm{eff})}{\mathrm{Re}\,(E_\mathrm{eff})} = \Delta_E\frac{\Omega\bar{\tau}}{1+\Omega^2\bar{\tau}^2}, \tag{3.24a}$$

$$\bar{\tau} = \sqrt{\tau_\sigma\tau_\varepsilon}, \tag{3.24b}$$

$$\Delta_E = (\tau_\sigma - \tau_\varepsilon)/\bar{\tau}. \tag{3.24c}$$

This is a very powerful approach that allows us to treat different physical dissipation mechanisms, provided we can identify the relevant $\bar{\tau}$ and Δ_E.

Considering again the tensorial description, we can now study the consequences of a fast but finite response time $\bar{\tau}$ at a quantitative level. From Hooke's law (eq. 3.4) we have

$$\sigma_{ij}(t) = C_{ijkl}\varepsilon_{kl}(t-\bar{\tau}) \approx \underbrace{C_{ijkl}\varepsilon_{kl}(t)}_{\sigma_{ij}^\mathrm{con}} - \underbrace{C_{ijkl}\bar{\tau}\dot{\varepsilon}_{kl}(t)}_{\sigma_{ij}^\mathrm{dis}}, \tag{3.25}$$

where we also approximated the time derivative in order to separate the stress field into components $\sigma_{ij}^{\mathrm{con}}$ in-phase with and $\sigma_{ij}^{\mathrm{dis}}$ delayed from the strain field. The first term of eq. 3.25 is what we studied so far, culminating in the conservative equation of motion (eqs. 3.11 and 3.13), and for the present discussion, the elastic potential energy of eq. 3.8. The second term gives rise to a damping term, when processed through the stress resultants and only keeping the linear terms. The equation of motion including dissipation becomes

$$h\sigma_0\partial_{\alpha\alpha}w - D\partial_{\alpha\alpha\beta\beta}W + \bar{\tau}D\partial_{\alpha\alpha\beta\beta}\dot{w} = \rho h\ddot{w}. \tag{3.26}$$

As expected from the preceding toy model we indeed find that the magnitude of the dissipative term $\propto \dot{w}$ grows with the stress-strain lag $\bar{\tau}$ and interestingly that it is independent of the tensile pre-stress σ_0.
Applying Galerkin's method to the new term allows us to summarize the preceding considerations in the effective, damped harmonic oscillator equation for a mode of interest, subject to some external force F_{ext}:

$$\ddot{q} + \Omega_{\mathrm{m}}^2 q - \Gamma_{\mathrm{m}}\dot{q} = \frac{1}{m_{\mathrm{eff}}}F_{\mathrm{ext}}, \tag{3.27}$$

with the effective oscillator parameters summarized in table 2.

Symbol	Definition	Name
m_{eff}	$\rho h \int_{\mathcal{S}} \psi_{n,m}^2 \mathrm{d}A$	Mass
k_{eff}	$\int_{\mathcal{S}} D\psi_{n,m}\nabla^4\psi_{n,m} - h\sigma_0\psi_{n,m}\nabla^2\psi_{n,m}\mathrm{d}A$	Spring constant
Γ_{m}	$-m_{\mathrm{eff}}^{-1}\bar{\tau}D\int_{\mathcal{S}}\psi_{n,m}\nabla^4\psi_{n,m}\mathrm{d}A$	Damping rate
Ω_{m}	$\sqrt{k_{\mathrm{eff}}/m_{\mathrm{eff}}}$	Frequency

Table 2: Effective oscillator parameters.

Solving eq. 3.27 is most conveniently done in the Fourier domain, in terms of the mechanical susceptibility for the displacement[4] $q(\Omega) = \chi_{\mathrm{q}}(\Omega)F_{\mathrm{ext}}(\Omega)$, that quantifies the mechanical response to a given force:

$$\chi_{\mathrm{q}}(\Omega) = m_{\mathrm{eff}}^{-1}\frac{1}{-\Omega^2 + \Omega_{\mathrm{m}}^2 + i\Omega\Gamma_{\mathrm{m}}}. \tag{3.28}$$

The mechanical oscillator is always coupled to a thermal bath, which gives rise to a thermal force noise.

Having derived a damped harmonic oscillator model for resonators, we turn the attention to the origins of the damping processes in the following.

[4]Distinct from the mechanical susceptibility χ_{m} used in the quantum-mechanical description in terms of ladder operators b, $b^\dagger$.

3.3.2 Dissipation Mechanisms

Unfortunately, loosing energy is typically easier than keeping it stored. There exists a multitude of means by which a mechanical oscillator can dissipate energy, and to keep track we group them into *extrinsic* and *intrinsic* loss mechanisms. In this way we can express the Q factor as

$$Q^{-1} = Q_{\text{ext}}^{-1} + Q_{\text{int}}^{-1}. \tag{3.29}$$

The extrinsic mechanisms cover the impact of the environment, whereas the intrinsic pertain to the oscillator itself. In terms of extrinsic loss channels, we consider specifically gas damping and coupling to substrate modes, so-called clamping losses.

Extrinsic Mechanisms

Gas Damping covers how anelastic collisions between the resonator and ambient gas molecules can give rise to dissipation. This effect can be described in two regimes; *viscous* gas damping when the atmosphere of the experiment is so dense that it effectively can be considered fluidic, contrasted to *ballistic* gas damping which describes the interaction between a dilute gas, whose effect can be understood as collisions of individual particles and the resonator. The relevant regime for a given experiment is described by the *Knudsen number*, Kn.[5] This is a dimensionless number relating the mean free path Λ_{f} of the gas to the characteristic size L_{car} of the resonator:

$$Kn = \frac{\Lambda_{\text{f}}}{L_{\text{car}}} = \frac{1}{p}\frac{k_{\text{B}}T}{\sqrt{2\pi}d_{\text{k}}^2 L_{\text{car}}}. \tag{3.30}$$

Here p is the pressure of the gas and d_{k} is the typical diameter of gas molecules, called the kinetic diameter [97]. A small Knudsen number $Kn \ll 1$ then is characteristic of the viscous regime, whereas a large Knudsen number $Kn \gg 1$ describes the ballistic regime when collisions are less frequent. From the point of view of an experimentalist that would like to study low-loss mechanical oscillators, the pragmatic approach is simply to operate in a high vacuum, that is at a low pressure. To understand how low pressures are required to not be limited by gas damping, we can describe the ballistic regime in some more detail. The ballistic regime can be described for a resonator far from any surfaces, and for one in close proximity to surfaces where gas molecules can bounce, and thus interact more frequently with the oscillator. These two contributions are called *drag-force* damping and *squeeze-film* damping. Restricting our treatment to the ballistic regime, we can then express the gas-damping limited Q factor as

[5] A rare example in physics where the conventional notation for a quantity is a compound of several letters.

$$Q^{-1} = Q_{\mathrm{df}}^{-1} + Q_{\mathrm{sf}}^{-1}, \tag{3.31}$$

where the drag-force contribution is [98]

$$Q_{\mathrm{df}} = \frac{1}{p}\frac{\rho h \Omega_{\mathrm{m}}}{4}\sqrt{\frac{\pi RT}{2m_{\mathrm{mol}}}} \tag{3.32}$$

and the squeeze-film contribution is [98]

$$Q_{\mathrm{sf}} = \frac{(2\pi)^{3/2}}{p}\rho h \Omega_{\mathrm{m}}\frac{d_0}{L_{\mathrm{car}}}\sqrt{\frac{RT}{m_{\mathrm{mol}}}} = 16\pi\frac{d_0}{L_{\mathrm{car}}}Q_{\mathrm{df}}. \tag{3.33}$$

In equations 3.32 and 3.33 R is the ideal gas constant and m_{mol} is the molar mass of the ambient gas. In equation 3.33 d_0 describes the distance to the nearest surface. Combining equations 3.32 and 3.33 then gives the ballistic gas damping limited Q-factor as

$$Q_{\mathrm{gas}} = \frac{1}{p}\frac{\rho h \Omega_{\mathrm{m}}}{4}\sqrt{\frac{\pi RT}{2m_{\mathrm{mol}}}}\left(1 + \frac{L_{\mathrm{car}}}{16\pi d_0}\right)^{-1}. \tag{3.34}$$

Typically our membranes are sufficiently far from the nearest surfaces such that $L_{\mathrm{car}} \ll 16\pi d_0$ and the squeeze film contribution is negligible.

Clamping Losses can arguably be considered either an intrinsic or an extrinsic damping mechanism, since it pertains to the interface between the resonator and the substrate to which it is clamped. If resonance modes of the substrate and of the resonator overlap in space and in frequency, they can then couple. Since the substrate modes $\mathbf{u}_{\mathrm{S}}(\mathbf{r}, \Omega)$ typically are more lossy than the resonator modes $\mathbf{u}_{\mathrm{R}}(\mathbf{r}, \Omega)$, this coupling can manifest as added damping of the resonator mode. This intuition has been mathematically described by considering the resonator a "phonon cavity" which can leak to substrate modes [99, 100, 101]. When the coupling is weak, an expression for the clamping loss limited Q factor can be found as

$$Q_{\mathrm{clamp}}^{-1} = \frac{\pi}{2\rho_{\mathrm{S}}\rho_{\mathrm{R}}\Omega_{\mathrm{m}}^3}\int_q \left|\int_{\mathcal{A}} \mathrm{d}A(\mathbf{u}_{\mathrm{R}} \cdot \sigma_q - \mathbf{u}_{\mathrm{q}} \cdot \sigma_R) \cdot \hat{n}\right|^2 \delta\left(\Omega_{\mathrm{m}} - \Omega(q)\right). \tag{3.35}$$

In equation 3.35 $\rho_{\mathrm{S/R}}$ are the substrate/resonator mass densities, $\mathcal{A}$ describes the area of the interface between the resonator and the substrate (with normal vector $\hat{n}$) and q is an index labeling substrate modes. Experiments corroborating the hypothesis of hybridization of the resonator of interest with lossy substrate modes have indeed been reported [101, 102, 103].

The mode-overlap integrals are tricky to evaluate analytically, but as a de-

sign guide, we see that one can try to isolate the resonator spatially and/or spectrally from the substrate modes to minimize clamping losses. In our samples we do both, by means of a phononic crystal, which will be detailed in the following phononic engineering section 4. In short such a phononic crystal can be designed to create a bandgap around the mechanical frequency, alleviating the spectral component of equation 3.35. The phononic crystal can either be engineered in the substrate or the resonator itself, and either way reduces the spatial overlap integral of equation 3.35.

Intrinsic Mechanisms

In terms of intrinsic loss mechanisms we discuss thermo-elastic damping, bending losses and surface losses. As the name suggests these all pertain to intrinsic processes of the resonator, necessitating a thorough understand to be mitigated at the design level, since the experimentalist in the lab only has the knobs of pressure and temperature to turn.

Thermo-elastic Damping During an oscillation cycle, the mechanical oscillator is dilated and compressed inhomogenously. To understand this, one can consider two unit volumes, one in the top half along the oscillation direction, and one in the bottom. Since such dilations and compressions are associated with a local change in temperature, described by the Thompson effect, a heat gradient can occur cf. figure 3.3. The thermal reequilibration then invariably leads to energy loss, which we term *thermo-elastic damping* (TED). This effect can be exasperated if the mechanical period is comparable to the characteristic equilibration time.

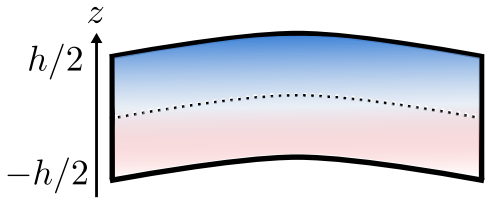

Figure 3.3: Picture of thermo-elastic damping. As an oscillator moves along the z direction, volume elements towards the positive z direction expands, whereas ones towards the negative z direction are compressed. By the Thompson effect (3.36) this leads to a heat gradient across the resonator, indicated by blue and red coloring encoding local cooling and heating respectively.

For oscillations occurring in one well-defined direction, the local heating and cooling is determined by the linear coefficient of thermal expansion α_{L} of the material in question. In our case of out-of-place oscillations this then takes the form:

$$\alpha_{\mathrm{L}} = -\frac{1}{h}\frac{\partial h}{\partial T}. \tag{3.36}$$

Thermoelastic damping has been treated with the Zener model both by Zener himself [96] and later in more detail by Lifshitz and Roukes [104], identifying a relaxation strength and time scale:

$$\Delta_{\mathrm{TED}} = \frac{E\alpha_{\mathrm{L}}^2 T_0}{C_V}, \tag{3.37a}$$

$$\tau_{\mathrm{TED}} = \frac{h^2}{\pi^2 \chi_{\mathrm{th}}}, \tag{3.37b}$$

where $C_V = C_{\mathrm{p}}\rho$ is the heat capacity per unit volume at constant volume (C_p is the specific heat capacity) and $\chi_{\mathrm{th}} = \kappa_{\mathrm{th}}/C_V$ is the thermal diffusivity of the resonator, κ_{th} being the thermal conductivity.

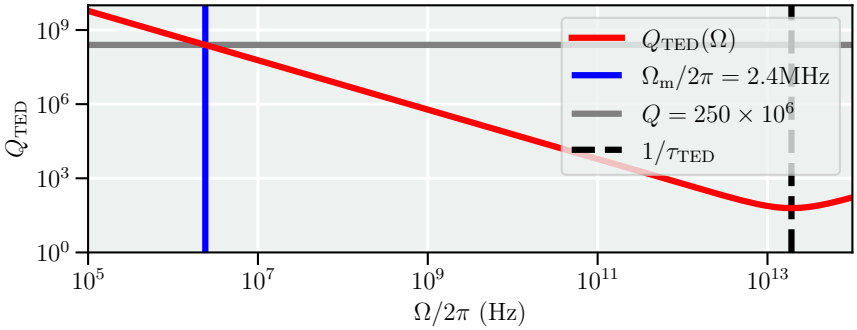

Figure 3.4: TED-limited Q factor. The Zener model prediction eq. (3.24) subject to the TED relaxation strength and time of eq. (3.37) is plotted in red, with the dashed black line indictating the characteristic rate $1/\tau_{\mathrm{TED}}$. At the mechanical frequency $\Omega_{\mathrm{m}}/2\pi = 2.4\,\mathrm{MHz}$ of the mode we later utilize in our mechanical memory experiments (blue), the TED-limited $Q \approx 250 \times 10^6$ (gray).

For the material parameters of our SiN membranes, the thermo-elastic damping-limited Q factor Q_{TED} is plotted according to eqs. (3.24) and (3.37) in figure 3.4, with parameters given in table 3.

E	$270\,\mathrm{GPa}$
α_{L}	$2.8 \times 10^{-6}\,\mathrm{K}^{-1}$
T_0	$294\,\mathrm{K}$
C_{p}	$656\,\mathrm{J\,kg}^{-1}\,\mathrm{K}^{-1}$
ρ	$3200\,\mathrm{kg\,m}^{-3}$
h	$20\,\mathrm{nm}$
κ_{th}	$3.2\,\mathrm{W\,m}^{-1}\,\mathrm{K}^{-1}$

Table 3: Parameters used in evaluating eqs. (3.24) and (3.37) as depicted in fig. 3.4.

From this plot we can see that we are actually not very far off being limited by TED, given that we typically reach $Q \approx 90 \times 10^6$ for the particular mode (more details on the design characterization of these resonators are given in section 7.3). As such we are less than a factor 3 below, despite being far off-resonant $\Omega_m \tau_{TED} \ll 1$. Seeing as we are close to being TED-limited, we conducted an experimental study of varying membrane geometries, which is reported in section 7.1, to assess the limitations of our high-Q oscillators.

Bending Loss Before the advent of soft-clamped membrane resonators (see the following phononic engineering section 4), a major limitation to the achievable Q factors in micromechanical resonators was losses due to the strong bending stemming from the rigid clamping of the resonator to a substrate, as discussed in section 3.2. Here we dig into these *bending losses*.

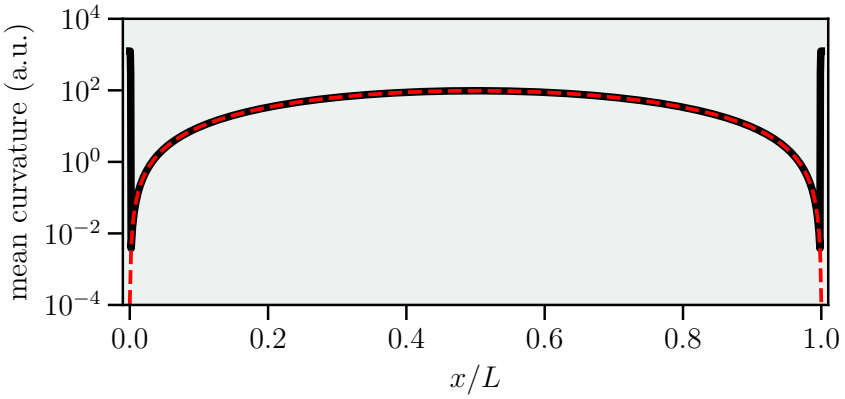

Figure 3.5: Mean curvature from eq. (3.39) of the (1D) modeshape given by eq. (3.16) for $\lambda_{dil} = 10^{-5}$ (black solid), contrasted with a simplistic sinusoidal mode (dashed red).

Returning to the tensorial description of mechanical dissipation, we can calculate the bending losses by considering the instantaneous dissipated in-plane power as

$$p_{ip} = \sigma_{\alpha\beta} \dot{\varepsilon}_{\alpha\beta}. \tag{3.38}$$

This has two contributions, one due to bending p_b and a non-linear part due to elongation p_e. Neglecting non-linear term (again, valid for small oscillation amplitudes), we find

$$p_b = \bar{\tau} D \Big(\underbrace{\partial_{\alpha\alpha}\dot{w}\partial_{\beta\beta}\dot{w}}_{\text{mean curvature}} + (1-\nu) \underbrace{\Big(\partial_{\alpha\beta}\dot{w}\partial_{\alpha\beta}\dot{w} - \partial_{\alpha\alpha}\dot{w}\partial_{\beta\beta}\dot{w} \Big)}_{\text{Gaussian curvature}} \Big). \tag{3.39}$$

The bending losses have here been grouped into mean and Gaussian curvatures. For a flat plane, the Gaussian curvature is identically zero, so we focus on the mean curvature in the following (though we take the Gaussian curvature into account when simulating real devices).

In figure 3.5 we illustrate the importance of bending near the clamped edges. The large spikes near $x \approx 0$ and $x \approx L$ indicates a large amount of bending-induced dissipation. To alleviate this, we localize the mechanical mode *away* from the edges by means of a phononic crystal. This approach is what we call *soft clamping* and is a crucial concept of the phononic engineering section 4.

Surface Loss Since we work with very thin oscillators, with thicknesses in the tens of nanometers, the quality of the material surface becomes important. The bulk material properties are typically more well-behaved than those of the surface, and thus imperfections here can degrade the achievable Q factors. The precise physical and chemical reasons are myriad and difficult to model, hence we lump them together into phenomenological *surface losses*.

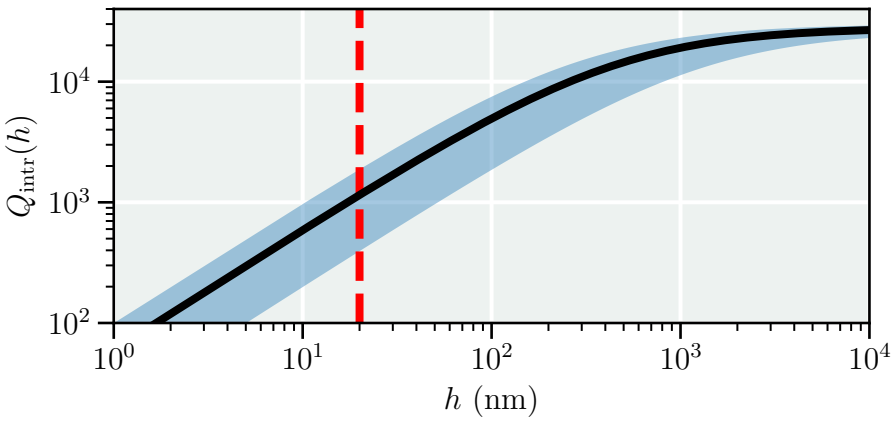

Figure 3.6: Surface-limited intrinsic Q factor. In solid black we plot eq. (3.40) for the mean values of β_{surf} and Q_{vol}, with the shaded area indicating $\pm$ the uncertainty. The red dashed vertical line indicates our typical membrane thickness $h = 20\,\mathrm{nm}$.

We base our description on the meta-study by Villanueva and Schmid [105], where the authors compiled reported intrinsic Q factors for a range of thicknesses - in effect varying the contribution of surface effect relative to the entire body. Based a wide range of designs such as membranes, strings, and cantilevers, the authors found good agreement between reported Q_{intr} and a model of surface losses scaling linearly with thickness, $Q_{\mathrm{surf}}(h) = h\beta_{\mathrm{surf}}$ and a constant volumetric loss:

$$Q_{\mathrm{intr}}^{-1}(h) = Q_{\mathrm{surf}}^{-1}(h) + Q_{\mathrm{vol}}^{-1}, \tag{3.40}$$

with $\beta_{\mathrm{surf}} = 60(40)\,\mathrm{nm}^{-1}$ and $Q_{\mathrm{vol}} = 28(2) \times 10^3$. In figure 3.6 we illustrate eq. (3.40). Indeed for our typical thicknesses in the tens of nanometers, we see that surface losses play a dominant role, giving rise to an intrinsic Q factor approximately linear in thickness.

3.4 Quantized Mechanical Oscillators

Having established the validity of modeling a particular mode of interest as a harmonic oscillator in the preceding text, we can quantize said mode much in the same way as for the cavity modes of section 2.2.

We choose the symbol b to represent a mechanical harmonic oscillator ladder operator, reserving a for optical ones. The operators b and $b^\dagger$ represents the annihilation and creation of a quantum of mechanical energy $\hbar\Omega_{\mathrm{m}}$. We call such quanta *phonons*, in analogy to the optical *photons*. We can write the mechanical position q and momentum p in terms of b and $b^\dagger$ as

$$q = x_{\mathrm{zpf}}(b + b^\dagger), \tag{3.41a}$$

$$p = \frac{\hbar}{2x_{\mathrm{zpf}}}(b - b^\dagger), \tag{3.41b}$$

where $x_{\mathrm{zpf}} = \sqrt{\hbar/(2m_{\mathrm{eff}}\Omega_{\mathrm{m}})}$ denotes the mechanical *zero-point fluctuations*.

We describe the evolution of a quantized mechanical mode with quantum Langevin equations. These can either be written for b and $b^\dagger$ or q and p, with the conversion given by eqs. (3.41). In contrast to the optical case, thermal noise is important for most mechanical oscillators, due to their comparatively smaller frequencies. In terms of q and p, the quantum Langevin equations for the mechanical oscillator are:

$$\dot{q} = p/m_{\mathrm{eff}}, \tag{3.42a}$$

$$\dot{p} = \Gamma_{\mathrm{m}} - m_{\mathrm{eff}}\Omega_{\mathrm{m}}^2 q + F_{\mathrm{th}}, \tag{3.42b}$$

where F_{th} is a stochastic thermal Langevin force, characterized by its first and second moments

$$\langle F_{\mathrm{th}}(t)\rangle = 0, \tag{3.43a}$$

$$\langle F_{\mathrm{th}}(t_1)F_{\mathrm{th}}(t_2) + F_{\mathrm{th}}(t_2)F_{\mathrm{th}}(t_1)\rangle = 4m_{\mathrm{eff}}\Gamma_{\mathrm{m}}k_{\mathrm{B}}T\delta(t_1 - t_2). \tag{3.43b}$$

In the following section, we study mechanical oscillators subject to optical forces, and the interplay between a mechanical and optical degree of freedom.

4 Phononic Engineering

"What happens to the hole when the cheese is gone?"

Bertold Brecht

Grounded in our modelling of mechanical loss mechanisms, this section describes our approaches to mitigate them through the resonator design. These design principles are what we call *phononic engineering*.

4.1 Dissipation Dilution

From the discussion of mode shapes of a square membrane in section 3.2, we learned the relevance of tensile stress, through the dimensionless stress parameter λ (eq. 3.15). Dissipation dilution describes how tensile stress furthermore increases the stored mechanical energy, without substantial increase in the dissipated, thus "diluting" the dissipation. To see this effect, we can compare the energy stored in the in-plane potential energy density V_{ip} calculated in eq. (3.8), neglecting the non-linear term, with the in-plane dissipated energy per cycle $\Delta V_{\mathrm{ip}} = \oint p_{\mathrm{b}} \mathrm{d}t$ (cf. eq. 3.39). By writing out the index-summations and integrating over the area and neglecting the Gaussian curvature, the stored and dissipated V and ΔV energies are then given by:

$$V = \int_{\mathcal{A}} \frac{h\sigma_0}{2} \left[\left(\frac{\partial w}{\partial x} \right)^2 + \left(\frac{\partial w}{\partial y} \right)^2 \right] + \frac{D}{2} \left[\left(\frac{\partial^2 w}{\partial x^2} \right)^2 + \left(\frac{\partial^2 w}{\partial y^2} \right)^2 \right] \mathrm{d}A, \quad (4.1a)$$

$$\Delta V = \int_{\mathcal{A}} \bar{\tau} D \left[\left(\frac{\partial^2 w}{\partial x^2} \right)^2 + \left(\frac{\partial^2 w}{\partial y^2} \right)^2 \right] \mathrm{d}A. \quad (4.1b)$$

We see that increasing the tensile pre-stress σ_0 increases the stored elongation energy without affecting the stored and lost energy due to bending, which is precisely the dilution of loss by more energy, stored in the pre-stress.

Recalling that the dimensionless stress parameter λ quantifies the relative contribution of elongation and bending, we see that $\lambda \ll 1$ is desirable for high-Q oscillators. This is achievable by engineering the membrane stress and its aspect ratio h/L. In figure 4.1 we illustrate the scaling of λ and a typical value we achieve $\lambda \approx 3 \times 10^{-4}$. In fabrication increasing the stress beyond a certain level becomes untenable, leaving one with the aspect ratio. However, this also determines the mechanical frequency, where a large $\Omega_{\mathrm{m}} \propto 1/L$ usually is desirable, eg. for sideband resolution in a cavity optomechanical experiment, or to avoid low-frequency technical noise.

The insight that pre-stress dilutes loss has been taken even further, in what has been termed *strain engineering* [106]. Here the idea is to taper the res-

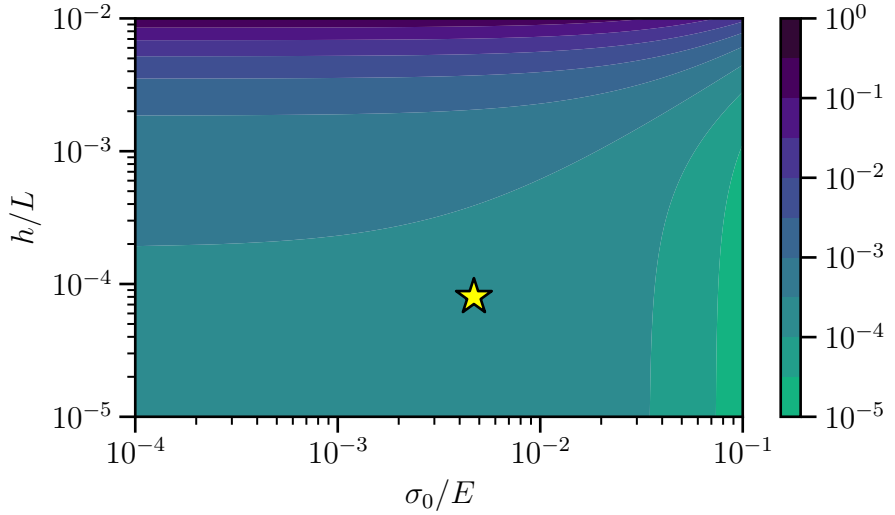

Figure 4.1: Dimensionless stress parameter λ as a function of pre-stress σ_0 normalized to the Young's modulus E and aspect ratio. The lower the λ the more dissipation dilution. The yellow star indicates our typical $\lambda \approx 3 \times 10^{-4}$, for $E = 270\,\mathrm{GPa}$, $\sigma_0 = 1.27\,\mathrm{GPa}$, $\nu = 0.27$, $h = 20\,\mathrm{nm}$, $L = 250\,\mu\mathrm{m}$.

onator so as to co-localize a locally increased strain (and thus stress) with the mechanical mode, leading to further Q-factor increase. A practical downside to this approach is that one ends up with a smaller device, which can prove tricky to couple to an optical cavity without degrading the optical Q-factor. Recently other materials than the conventional Silicon Nitride has been explored. Employing the crystalline material Silicon under tensile stress enabled $Q > 1 \times 10^{10}$ of MHz frequency modes in a cryogenic environment [76]. Silicon Carbide, that has high yield-strength polytypes, has also recently been studied, achieving high Q factors, already for amorphous SiC [107]. Crystalline materials such as III-V semiconductors are also being explored with the motivation of easier fabrication of integrated mechanical devices [108, 109, 110].

4.2 Soft Clamping & Phononic Crystals

Having considered plain, rectangular membranes so far, we turn to the actual type of membrane resonators employed in our experiments. These devices have a more complicated geometry, that the Galerkin method allows us to accommodate. Considering the square membrane as a benchmark, we can evaluate a Q-factor for its fundamental mode, $Q_{\mathrm{sq.}}$. In terms of the dimensionless stress parameter, we find

$$Q_{\mathrm{sq.}}^{-1} = (2\lambda + 2\pi^2\lambda^2)Q_{\mathrm{int}}^{-1}, \tag{4.2}$$

where we suppress the h dependence of Q_{int} for brevity. Since $\lambda \ll 1$ in the dissipation-diluted regime, the first term dominates the losses. The first term,

linear in λ, comes about from the clamping-induced bending, while the second, quadratic in λ, originates in the sinusoidal contribution to the modeshape.

The principle of soft clamping is then to engineer the resonator such that the mode shape has gradually decayed before reaching the clamped boundary. In this manner we can eliminate the linear term of eq. (4.2), and boost the Q-factor by a factor $\lambda^{-1} \gg 1$.

The original method of soft clamping relies on a phononic crystal, engineered in the resonator itself [74], which is also how we design the devices throughout this thesis, with a typical sample shown in 4.2. Interestingly, recent work has demonstrated the similar outcome by different means such as self-similar "fractal" resonators [77] and "perimeter mode" resonators that have periodic boundary conditions [111, 112]. In fact, computer-guided design methods are starting to be applied to the design of high-Q resonators [112, 113].

Figure 4.2: Photograph of a soft-clamped membrane resonator, lying in a sample holder for a cavity optomechanics experiment. The distance between the centers of the square alignment holes in the substrate is 15 mm. Photo courtesy of Julian Robinson-Tait.

Phononic crystals describe a periodic modulation of the sonic velocity of a material. Like the perhaps more established *photonic* crystals (where the speed of light in the material is modified [114]), these are metamaterials whose salient feature is a (acoustic or optical) bandgap - a range of frequencies where waves cannot propagate in the material. Earlier work at NBI first explored phononic crystals in the substrate, rather than the resonator itself. These were realised by etching a periodic cross-shaped pattern into the Silicon substrate. Such designs successfully mitigated the effect of clamping losses, evidenced by

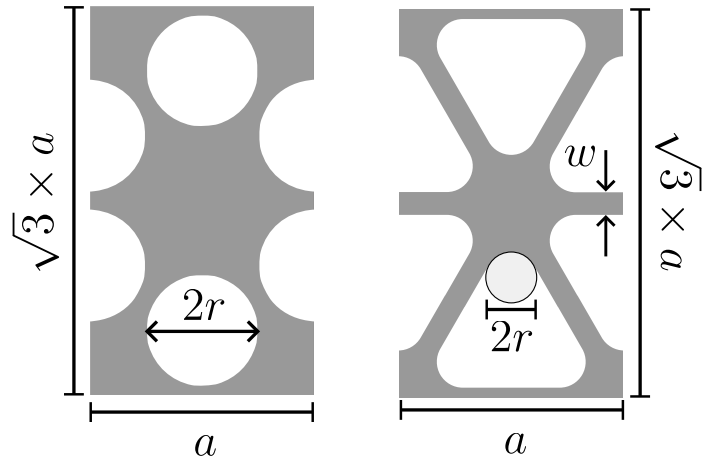

Figure 4.3: Unit cell construction. Left: the original design, constructed purely in terms of holes of radius r. Right: the newer design, with two parameters defining the unit cell, a tether width w and fillet radius r.

Q factors largely independent of clamping conditions [115]. Most prominently they were used in hybrid atom-mechanics experiments, demonstrating back-action evasion by measuring joint quadratures of the coupled system of an atomic spin ensemble and a mechanical resonator, with reduced variance [116].

The insight that embedding the phononic crystal in the resonator itself, rather than the substrate, had the potential to mitigate the edge-bending losses spurred such designs. An exhaustive list of scientific achievements enabled by the dramatically reduced mechanical dissipation of such membranes is beyond the scope of the present text, but include ground state cooling by measurement and feedback [33], sub-SQL displacement measurements [43] and entanglement of atomic spins with mechanical motion [117]. This importance of boundary conditions for the dissipation rate of a resonator has curiously previously been discovered in the context of nanophotonic cavities [118].

In our group we employ a range of phononic crystal designs, that are each optimized for different applications. They are parameterized in one of two ways depending on their construction: either by a lattice constant a defining the unit cell size and a hole radius r, or a lattice constant a, tether width w and fillet-radius r, as seen in figure 4.3. In some sense the main difference between the designs is the trade-off between simplicity and tweakability. With a single parameter defining the phononic crystal, the circle based design is easy to optimize for a desired frequency range, albeit a little limited. On the other hand the tether-based design allows much greater tailoring, at the cost of a now two-dimensional parameter space to explore.

To assess a given phononic crystal design, we simulate it using the finite-element-method software COMSOL Multiphysics. The details of such simulations are decribed meticulously in the thesis of Yeghishe Tsaturyan [119], who pioneered the development of phononic crystals in our group. In short, the idea is to consider the unit cell subject to periodic boundary conditions,

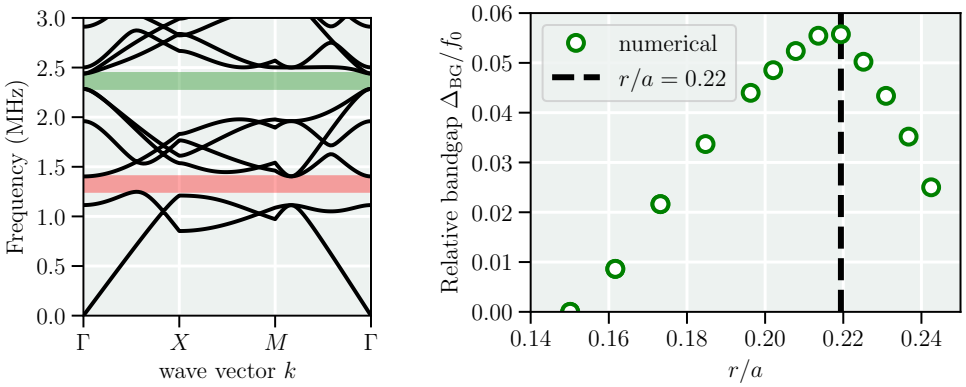

Figure 4.4: Simulated band diagram. Left: In black, the mechanical frequencies versus k vector, as simulated. The colored bands indicate two bandgaps, in red around $\approx 1.4\,\mathrm{MHz}$ and green around $\approx 2.4\,\mathrm{MHz}$. Right: An example of bandgap optimization. In hollow green circles, we plot the width Δ_{BG} of the $\approx 2.4\,\mathrm{MHz}$ relative to the center frequency f_0. The black dashed line indicates the optimum around $r/a = 0.22$.

to imitate a perfect infinite crystal, and then simulating a dispersion relation, as illutrated in figure 4.4. One can then vary the unit cell parameters, for instance to find the widest bandgap around the desired center frequency, also shown in 4.4.

4.3 Defect Design

Having settled on a phononic crystal design, the next step is to break it. A perfectly periodic crystal has little utility as a resonator, precisely since it cannot resonate at the design frequency. Therefore we break the periodicity of the crystal in its center. We refer to this central alteration of the phononic crystal as the *"defect"* of the phononic crystal. By carefully designing the geometry of this defect, one can engineer it to host modes with frequencies that lie in the bandgap of the crystal, thus leveraging soft clamping. At times this procedure is more art than science, yet we review some principles and methods for designing and simulating phononic crystal defects.

Firstly one needs to prioritize which properties of a resonator are the most important. Examples of features one might optimize for include high Q or frequency, low m_{eff}, a large working area (defined as the largest inscribed circle of the defect before hitting a hole), or spectral "cleanliness", i.e. the spacing between the mode of interest and the nearest neighbouring mode (or bandgap edge), with a few different defect designs shown in figure 4.5.

Other noteworthy defect designs than those of fig.4.5 are the "dandelion", a design with low m_{eff}, high Q but at the cost of a small working area. These advantages has been leveraged in a fiber-cavity based cavity room-temperature

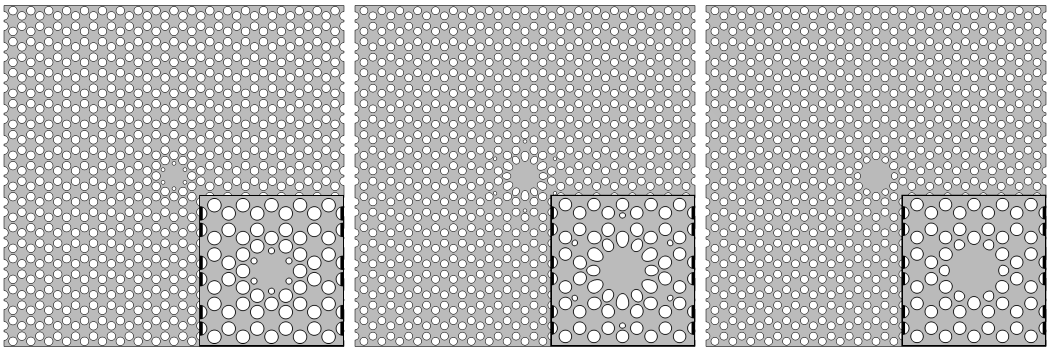

Figure 4.5: Soft-clamped membrane designs. Here we show three types of membrane designs, mainly distinguished by the central defect, which are highlighted as insets. From left to right we have the "generation 3 Dahlia", "generation L", and "generation K".

laser cooling experiment, approaching the quantum ground state, in a room temperature environment [40]. Here the small waist of the short fiber cavity means that the small working area is less problematic. Another design of note is the "lotus", which was used in an electromechanical ground-state cooling experiment [78]. This design has the advantage of being "single mode", in the sense that there only is one mode inside the bandgap, and being more robust to metalization as required in electromechanical experiments.

The dahlia design is split in generations 1, 2, and 3, with generation 3 shown

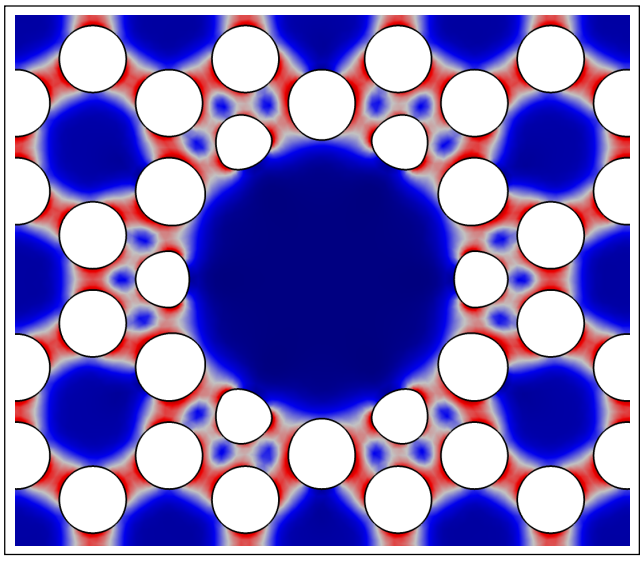

Figure 4.6: Von Mises stress, normalized to the pre-stress, with the colors logarithmically scaled, to highlight the inhomogeneities, zoomed on the defect. Blue regions have reduced stress and red ones increased (up to about 3.3 GPa $<$ σ_{yield}).

in figure 4.5(left). Generation 1 is the design reported in [74], generation 2 is used in [33, 43, 120, 44], and generation 3 is introduced in [119] and studied in 7.1. The differences pertain mainly to the small holes on the defect, with details given in [119]. The other two designs shown in figure 4.5(middle and right) are new designs that are optimized to have a large working area and high frequency, without compromising Q too much.

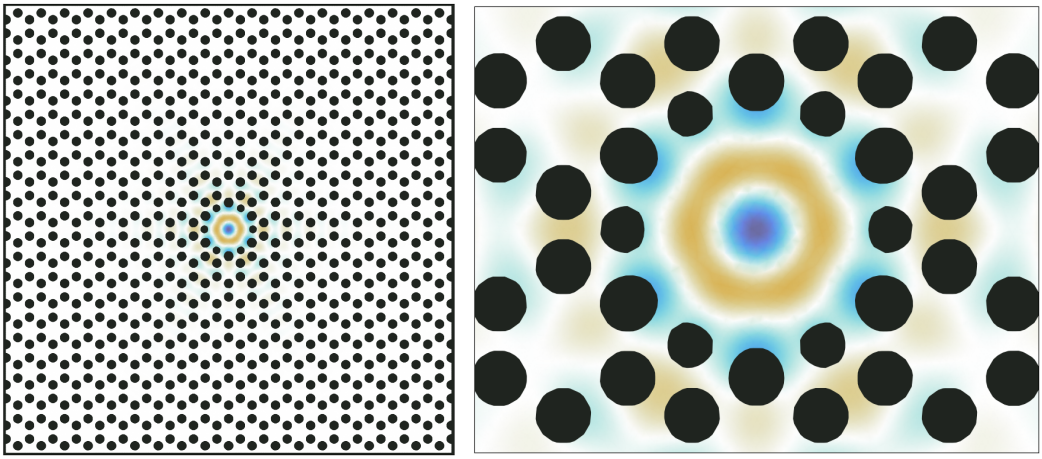

Figure 4.7: Simulated modeshape of the $\Omega_m/2\pi \approx 2.4\,\mathrm{MHz}$ mode of a generation "K" membrane. Left the full membrane is shown, highlighting the localized nature of the mode, with the details near the defect shown to the right.

With an idea for a design, we again do simulations using COMSOL. Having implemented our chosen design, the first simulation calculates how the in-plane stress redistributes, after we perforate the membrane as our design dictates (cf. figure 4.6). We calculate the Von Mises stress, which is used in mechanical engineering to predict yielding. Since the yield stress of Silicon Nitride is around $\sigma_{\mathrm{yield}} \approx 6.4\,\mathrm{GPa}$ [121] and the stress of the deposited film prior to perforation is around $\bar{\sigma} \approx 1.27\,\mathrm{GPa}$ [119], it is not inconceivable to locally exceed the yield stress. Such designs are then not feasible for fabrication.

The next step is then an eigenmode solver, looking for modes around the frequency of interest (typically the center of the bandgap is a good starting point). The output of such a simulation is displacement profiles for the identified modes, with an example shown in figure 4.7.

With these modeshapes, and our understanding of how modeshape curvature impacts mechanical dissipation, we can then assess, to a fair degree of accuracy [74], the expected Q-factor of a given design. This vastly speeds up the whole engineering process, as the iteration time now only depends on your computing power, and not the time it takes to actually fabricate a wafer with the new design, pump it down to a good vacuum, measure each device, which easily totals weeks.

5 Cavity Optomechanics

"Provide ships or sails adapted to the heavenly breezes, and there will be some who will brave even that void."

Johannes Kepler

Having developed a separate understanding for our optical and mechanical systems, we proceed to study their mutual coupling in this section. The chapter structure is as usual: we develop the basics in a simplified model, in this case that of end-mirror coupling, and move to the more complicated reality of a membrane inside a cavity.

5.1 Radiation Pressure Coupling

Light carries momentum. This simple fact implies that it can exert a force on a reflective body, proportional to the transferred momentum. This *radiation pressure* force was first hypothesized by Johannes Kepler to explain his comet tail observations in the 17th century [122] and demonstrated in so-called light-mill experiments at the start of the 20th century [123, 124, 125].

This phenomenon is the underpinning physics in our cavity optomechanical experiments, where a cavity field of sufficient intensity can push the cavity mirrors. In the case of a Fabry-Perot cavity, the radiation pressure F_{rad} force is given as [7]

$$F_{\mathrm{rad}} = \hbar \underbrace{\frac{\Omega_{\mathrm{cav}}}{L_{\mathrm{cav}}}}_{G} a^\dagger a, \tag{5.1}$$

where we have identified the frequency pull parameter G, whose naming will become apparent in the following.

The force pushes the mirrors apart, increasing the cavity length and correspondingly decreasing the cavity resonance frequency. If we consider the Hamiltonian for such a mechanically compliant cavity, we find

$$H = \hbar\Omega_{\mathrm{cav}}(q)a^\dagger a + \hbar\Omega_{\mathrm{m}} b^\dagger b, \tag{5.2}$$

where a and b are annihilation operators for the optical and mechanical modes respectively. For displacements small relative to the cavity length, $\Omega_{\mathrm{cav}}(q)$ is well-described by a first-order Taylor expansion,

$$\Omega_{\mathrm{cav}}(q) = \Omega_{\mathrm{cav}} + q \underbrace{\frac{\partial\Omega_{\mathrm{cav}}}{\partial q}}_{-G} + \mathcal{O}(q^2), \tag{5.3}$$

where the identification of G can be verified by straight-forward computation. The naming now makes sense: G describes the shift in frequency for a given displacement, and the negative sign accounts for the fact that we take a positive displacement to increase the cavity length. Under these conditions the Hamiltonian becomes

$$H = \hbar\Omega_{\mathrm{cav}} a^\dagger a + \hbar\Omega_{\mathrm{m}} b^\dagger b \underbrace{-\hbar G x_{\mathrm{zpf}} a^\dagger a (b + b^\dagger)}_{H_{\mathrm{int}}}. \tag{5.4}$$

We denote the product $g_0 \coloneqq G x_{\mathrm{zpf}}$ as the *vacuum optomechanical coupling rate*, describing the frequency shift induced by one quantum of displacement.

The evolution of a and b and their conjugates is described by quantum Langevin equations, encompassing the Hamiltonian evolution and noises entering the system. For the mechanical oscillator we prefer a description in terms of position q and momentum p:

$$q = x_{\mathrm{zpf}}(b + b^\dagger) \tag{5.5a}$$

$$p = \frac{\hbar}{2x_{\mathrm{zpf}}}(b - b^\dagger) \tag{5.5b}$$

The QLEs for the system described by eq are given as

$$\dot{a} = \left(-\frac{\kappa}{2} + i\Delta + iGq\right) a + \sqrt{\eta_{\mathrm{c}}\kappa}\, s_{\mathrm{in}} + \sqrt{(1-\eta_{\mathrm{c}})\kappa}\, f_{\mathrm{in}} \tag{5.6a}$$

$$\dot{a}^\dagger = \left(-\frac{\kappa}{2} - i\Delta - iGq\right) a^\dagger + \sqrt{\eta_{\mathrm{c}}\kappa}\, s_{\mathrm{in}}^\dagger + \sqrt{(1-\eta_{\mathrm{c}})\kappa}\, f_{\mathrm{in}}^\dagger \tag{5.6b}$$

$$\dot{q} = p/m_{\mathrm{eff}} \tag{5.6c}$$

$$\dot{p} = -\Gamma_{\mathrm{m}} p - m_{\mathrm{eff}}\Omega_{\mathrm{m}}^2 q + \hbar G a^\dagger a + F_{\mathrm{th}} \tag{5.6d}$$

The optical f_{in} and mechanical F_{th} noise terms have zero mean and the following second moments:

$$\left\langle f_{\mathrm{in}}^\dagger(t_1) f_{\mathrm{in}}(t_2) \right\rangle = 0, \tag{5.7a}$$

$$\left\langle f_{\mathrm{in}}(t_1) f_{\mathrm{in}}^\dagger(t_2) \right\rangle = \delta(t_1 - t_2), \tag{5.7b}$$

$$\langle F_{\mathrm{th}}(t_1) F_{\mathrm{th}}(t_2) + F_{\mathrm{th}}(t_2) F_{\mathrm{th}}(t_1) \rangle = 4 m_{\mathrm{eff}} \Gamma_{\mathrm{m}} k_{\mathrm{B}} T \delta(t_1 - t_2). \tag{5.7c}$$

Here we again assume the optical field to be at zero occupancy, which we however cannot justify for the thermo-mechanical noise[6]. The non-linear equa-

[6]It should be noted that the δ-correlated mechanical noise is the limiting case relevant for mechanical coherence times τ_{coh} longer than the characteristic "thermal time" $\tau_T = \hbar/k_{\mathrm{B}}T$. Since $\tau_T(1\mathrm{mK}) \approx 7\mathrm{ns}$, we are always in the regime $\tau_{\mathrm{coh}} \gg \tau_T$ [126].

tions 5.7 are cumbersome to deal with, but reveal important static phenomena. Looking for steady state solutions we find

$$\bar{q} = -\frac{\hbar G}{m_{\mathrm{eff}}\Omega_{\mathrm{m}}^2}\left|\bar{a}\right|^2, \tag{5.8a}$$

$$\left|\bar{a}\right|^2 = \frac{\eta_{\mathrm{c}}\kappa}{(\kappa/2)^2 + (\Delta + G\bar{q})^2}\left|s_{\mathrm{in}}\right|^2. \tag{5.8b}$$

Equation 5.8a alone shows that the mean intra-cavity intensity leads to a static displacement of the membrane. It is possible to eliminate one of the variables and solve the resulting cubic equation, but we choose instead a simpler description. If we assume the radiation-pressure interaction to be purely conservative (that is to say, assume an instantaneous response without lag, valid for $\Omega_{\mathrm{m}} \ll \kappa$), we can approximate the radiation pressure force as the derivative of a potential V_{rad}

$$F_{\mathrm{rad}} \approx -\frac{\partial V_{\mathrm{rad}}(q)}{\partial q}. \tag{5.9}$$

The total potential of the mechanical oscillator now contains its intrinsic harmonic potential and the modification due to the radiation pressure interaction. By combining equations 5.1 and 5.8b to find V_{rad}, we find the total potential

$$V = V_{\mathrm{HO}} + V_{\mathrm{rad}} = \frac{1}{2}m_{\mathrm{eff}}\Omega_{\mathrm{m}}^2 q^2 - \hbar G\eta_{\mathrm{c}}\kappa\bar{n}_{\mathrm{max}}\arctan\left(\frac{Gq+\Delta}{\kappa/2}\right), \tag{5.10}$$

where $\bar{n}_{\mathrm{max}}$ denotes the peak intracavity average photon number. As can be seen in figure 5.1, the radiation pressure interaction modifies the mechanical potential, leading to three regime as the optical power increases: (i) the radiation-pressure potential is weak compared to the intrinsic mechanical potential, so the equilibrium position is only shifted slightly. (ii) The *static bistability regime*, where the two potential contributions are comparable, leading to two stable solutions. (iii) The optical potential dominates the intrinsic, effectively "trapping" the mechanical oscillator optically. In practice the static bistability imposes a bound how much light we can pump our cavity with, before the lower order modes of our membranes enter static bistability, rendering the cavity impossible to lock.

Typically the interaction described by the third term of equation 5.4 is weak, $g_0 \ll \Omega_{\mathrm{cav}}, \Omega_{\mathrm{m}}$. However the factor $a^\dagger a$ allows us to boost the interaction strength by driving the cavity with a strong coherent field α (that is, a laser). In this case we can linearize the non-linear three-wave mixing process

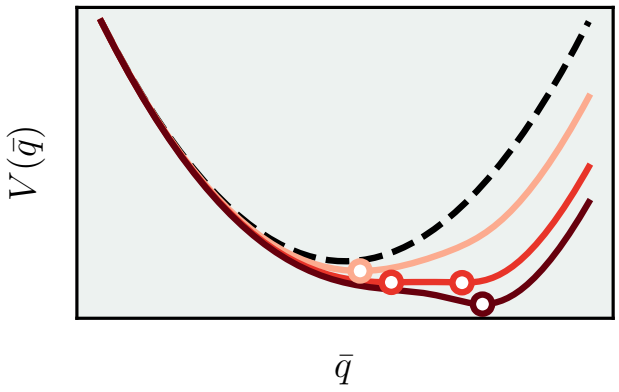

Figure 5.1: Optomechanical static bistability. The optically modified mechanical potential of eq. (5.10) is plotted for (dashed black) the bare case and (from light to dark red) increasing $\bar{n}_{\mathrm{max}}$. Since potentials only are defined up to a constant, the red curves are offset vertically to overlap with the bare potential. Hollow circles indicate the stable positions, determined by potential minima.

by considering field fluctuations around the field average α as,

$$a = \alpha + \delta a$$

From this point, we switch notation such that $a \mapsto \delta a$ denotes the fluctuations.

To proceed further we transform to a reference frame rotating at Ω_{cav} by introducing the detuning $\Delta = \Omega_{\mathrm{L}} - \Omega_{\mathrm{cav}}$ between an incident laser and the cavity. Futhermore we choose the incident field as the phase reference, in effect choosing α purely real. Finally, we only keep terms up to linear order in a and $a^\dagger$ which all together give us the interaction Hamiltonian as

$$H_{\mathrm{int}} = -\hbar \underbrace{g_0 \alpha}_{g} (a + a^\dagger)(b + b^\dagger). \tag{5.11}$$

Equation 5.11 describes a pair of harmonic oscillators, coupled at the *field enhanced* optomechanical coupling rate g. Multiplying out the parentheses yields four terms that in pairs describe two different physical processes, as well as the static displacement:

$$H_{\mathrm{int}} = -\hbar g(ab + a^\dagger b^\dagger + ab^\dagger + a^\dagger b) - \hbar g_0 \alpha^2 (b + b^\dagger). \tag{5.12}$$

The first two terms is the Hamiltonian of a parametric amplifier[7], while

[7] In a quantum optics context, this is also frequently called the *spontaneous parametric downconversion* (SPDC) or *two-mode squeezer* Hamiltonian.

the two last terms is a state-swap Hamiltonian[8]. The static displacement term is conventionally absorbed into the detuning such that $\Delta \mapsto \Delta + G\bar{q}$. Interestingly, these two different processes are resonant at different detunings, which is highlighted by explicitly writing out the time-dependence:

$$H_{\mathrm{int}}(t) = -\hbar g(a_0 b_0 \, \mathrm{e}^{-i(\Omega_{\mathrm{m}}-\Delta)t} + a_0^\dagger b_0 \, \mathrm{e}^{-i(\Omega_{\mathrm{m}}+\Delta)t} + \mathrm{h.c.}), \tag{5.13}$$

where h.c. is shorthand for Hermitian conjugate. Choosing $\Delta = \Omega_{\mathrm{m}}$ then prefentially enhances the parametric amplification and $\Delta = -\Omega_{\mathrm{m}}$ the state-swap interaction. These two processes are analogous to Stokes and anti-Stokes Raman scattering, and produce two sidebands on the strong coherent field α, that respectively are Ω_{m} above and below in frequency. In fact within a rotating-wave approximation (valid in the sideband-resolved regime where $\kappa \ll \Omega_{\mathrm{m}}$, expanded in the following), one can neglect the fast oscillating process, in effect tailoring the interaction for a given experiment.

The QLEs subject to the linearized interaction can be found as

$$\dot{a} = \left(i\Delta - \frac{\kappa}{2}\right) a + ig(b + b^\dagger) + \sqrt{\eta_c \kappa} \; s_{\mathrm{in}} + \sqrt{(1-\eta_c)\kappa} f_{\mathrm{in}}, \tag{5.14a}$$

$$\dot{b} = \left(-i\Omega_{\mathrm{m}} - \frac{\Gamma_{\mathrm{m}}}{2}\right) b + ig(a + a^\dagger) + \sqrt{\Gamma_{\mathrm{m}}}\xi_{\mathrm{in}}. \tag{5.14b}$$

All the optomechanical experiments described in this thesis are conducted within the linearized regime described by eqs. (5.14).

Sometimes it is intructive to consider the Langevin equations in terms of quadrature rather than the ladder operators for the light and mechanics. To this end we define these quadrature operators as:

$$X_{\mathrm{L}} = \frac{a + a^\dagger}{2}, \quad Y_{\mathrm{L}} = \frac{a - a^\dagger}{2}, \tag{5.15a}$$

$$X_{\mathrm{m}} = \frac{b + b^\dagger}{2}, \quad Y_{\mathrm{m}} = \frac{b - b^\dagger}{2}. \tag{5.15b}$$

Additionally we can describe the input terms in a similar manner. Here we distinguish with a superscript indicating the signal whose quadratures we are writing:

[8]Called the *beam splitter* Hamiltonian in quantum optics.

$$X_{\mathrm{L}}^{\mathrm{in}} = \frac{s_{\mathrm{in}} + s_{\mathrm{in}}^{\dagger}}{2}, \quad Y_{\mathrm{L}}^{\mathrm{in}} = \frac{s_{\mathrm{in}} - s_{\mathrm{in}}^{\dagger}}{2}, \tag{5.16a}$$

$$X_{\mathrm{L}}^{\mathrm{ex}} = \frac{f_{\mathrm{in}} + f_{\mathrm{in}}^{\dagger}}{2}, \quad Y_{\mathrm{L}}^{\mathrm{ex}} = \frac{f_{\mathrm{in}} - f_{\mathrm{in}}^{\dagger}}{2}, \tag{5.16b}$$

$$X_{\mathrm{m}}^{\mathrm{ex}} = \frac{\xi_{\mathrm{in}} + \xi_{\mathrm{in}}^{\dagger}}{2}, \quad Y_{\mathrm{m}}^{\mathrm{ex}} = \frac{\xi_{\mathrm{in}} - \xi_{\mathrm{in}}^{\dagger}}{2}, \tag{5.16c}$$

$$\tag{5.16d}$$

such that intentionally applied signals are labeled by "in" and unavoidable noise terms by "ex". Rewriting the Langevin equations in these terms then gives:

$$\dot{X}_{\mathrm{L}} = -\frac{\kappa}{2} X_{\mathrm{L}} + i\Delta Y_{\mathrm{L}} + \sqrt{\eta_{\mathrm{c}}\kappa} X_{\mathrm{L}}^{\mathrm{in}} + \sqrt{(1-\eta_{\mathrm{c}})\kappa} X_{\mathrm{L}}^{\mathrm{ex}}, \tag{5.17a}$$

$$\dot{Y}_{\mathrm{L}} = -\frac{\kappa}{2} Y_{\mathrm{L}} + i\Delta X_{\mathrm{L}} + 2ig X_{\mathrm{m}} + \sqrt{\eta_{\mathrm{c}}\kappa} Y_{\mathrm{L}}^{\mathrm{in}} + \sqrt{(1-\eta_{\mathrm{c}})\kappa} Y_{\mathrm{L}}^{\mathrm{ex}}, \tag{5.17b}$$

$$\dot{X}_{\mathrm{m}} = -\frac{\Gamma_{\mathrm{m}}}{2} X_{\mathrm{m}} - i\Omega_{\mathrm{m}} Y_{\mathrm{m}} + \sqrt{\Gamma_{\mathrm{m}}} X_{\mathrm{m}}^{\mathrm{ex}}, \tag{5.17c}$$

$$\dot{Y}_{\mathrm{m}} = -\frac{\Gamma_{\mathrm{m}}}{2} Y_{\mathrm{m}} - i\Omega_{\mathrm{m}} Y_{\mathrm{m}} + 2ig X_{\mathrm{L}} + \sqrt{\Gamma_{\mathrm{m}}} Y_{\mathrm{m}}^{\mathrm{ex}}. \tag{5.17d}$$

A flicker of intuition about the optomechanical coupling can now be garnered from eqs. (5.17). We can see that the mechanical displacement $X_{\mathrm{m}} \propto q$ only shows up in the equation for the optical Y_{L} quadrature, proportional to the optical phase. In the same way, the optical amplitude quadrature $\propto X_{\mathrm{L}}$ only shows up in the equation for Y_{m}, proportional to the mechanical momentum.

In the quadrature language the cavity output, with operators analogous to eq. (5.16a), can again be found from the input-output relation (2.30)

$$X_{\mathrm{L}}^{\mathrm{out}} = X_{\mathrm{L}}^{\mathrm{in}} - \sqrt{\eta_{\mathrm{c}}\kappa} X_{\mathrm{L}}, \tag{5.18a}$$

$$Y_{\mathrm{L}}^{\mathrm{out}} = Y_{\mathrm{L}}^{\mathrm{in}} - \sqrt{\eta_{\mathrm{c}}\kappa} Y_{\mathrm{L}}. \tag{5.18b}$$

The mechanical signal can then be measured in two ways: either by measuring the phase $\propto Y_{\mathrm{L}}$ of a resonant $\Delta = 0$ field, or the intensity $\propto X_{\mathrm{L}}$ of a detuned $\Delta \neq 0$ field that has interacted with the cavity. Details of such measurements are expanded in section 6.1.2.

5.1.1 Dynamical Backaction

To study the consequences of the equations developed in the preceding beyond static phenomena, we consider the consequences of a delay between the radiation pressure force, and the mechanical oscillations. Such a delay can be induced the cavity susceptibility: when detuned from resonance, the cavity imparts a detuning-dependent phase-shift on the incident field. The physics can also be pictured by noting that a detuned cavity correlates the amplitude and phase of an incident field. Since the position of the mechanical oscillator is encoded in the optical phase, and the amplitude of the intra-cavity field couples to the momentum of the mechanics, the correlations between optical amplitude and phase induced on a detuned field manifests as a backaction on the mechanics. We call this important effect *dynamical backaction*.

Quantitatively the consequences of dynamical backaction can be studied solving equations 5.14 in the Fourier domain. One finds that the mechanical susceptibility $\chi_{\mathrm{q}}^{-1}(\Omega) = m_{\mathrm{eff}}(\Omega_{\mathrm{m}}^2 - \Omega^2 - i\Gamma_{\mathrm{m}}\Omega)$ gets optically modified to an effective mechanical susceptibility χ_{eff}, which contains changes in the apparent resonance frequency and linewidth of the mechanics, $\Delta\Omega_{\mathrm{m}}$ and Γ_{opt}:

$$\chi_{\mathrm{eff}}^{-1}(\Omega) = \chi_{\mathrm{q}}^{-1}(\Omega) + m_{\mathrm{eff}}\Omega\left(2\Delta\Omega_{\mathrm{m}} - i\Gamma_{\mathrm{opt}}\right). \tag{5.19}$$

In this way, the effective oscillator parameters are $\Omega_{\mathrm{eff}} = \Omega_{\mathrm{m}} + \Delta\Omega_{\mathrm{m}}$ and $\Gamma_{\mathrm{eff}} = \Gamma_{\mathrm{opt}} + \Gamma_{\mathrm{m}}$. The modifications to frequency and decay rate are referred to as the optical spring effect and optomechanical dampening respectively, and are given as

$$\Delta\Omega_{\mathrm{m}}(\Omega) = g^2\frac{\Omega_{\mathrm{m}}}{\Omega}\left(\frac{\Delta+\Omega}{(\kappa/2)^2+(\Delta+\Omega)^2} + \frac{\Delta-\Omega}{(\kappa/2)^2+(\Delta-\Omega)^2}\right), \tag{5.20a}$$

$$\Gamma_{\mathrm{opt}}(\Omega) = g^2\frac{\Omega_{\mathrm{m}}}{\Omega}\left(\frac{\kappa}{(\kappa/2)^2+(\Delta+\Omega)^2} - \frac{\kappa}{(\kappa/2)^2+(\Delta-\Omega)^2}\right). \tag{5.20b}$$

Since we work with high Q mechanical oscillators, and the modifications (depending on detuning) are of the same order, the most important effect is the optomechanical dampening. Usually we are in the situation $\Delta\Omega_{\mathrm{m}} \ll \Omega_{\mathrm{m}}$, $\Gamma_{\mathrm{opt}} \gg \Gamma_{\mathrm{m}}$, since $\Omega_{\mathrm{m}}/2\pi > 1\,\mathrm{MHz}$ whereas $\Gamma_{\mathrm{m}}/2\pi \approx 10\,\mathrm{mHz}$. In figure 5.2, we plot eqs. (5.20).

In cavity optomechanics, we typically distinguish two regimes of the nature of the interaction, and thus the modifications of eqs. (5.20). When the cavity linewidth κ is broader than the mechanical frequency Ω_{m} we cannot to a good degree distinguish the two processes of the interaction Hamiltonian (5.13). We hence call the condition $\Omega_{\mathrm{m}} \ll \kappa$ the *unresolved sideband regime*. Conversely, when the cavity is narrowband relative to the mechanical frequency, it's susceptibility allows the distinction between the Stokes and anti-Stokes processes,

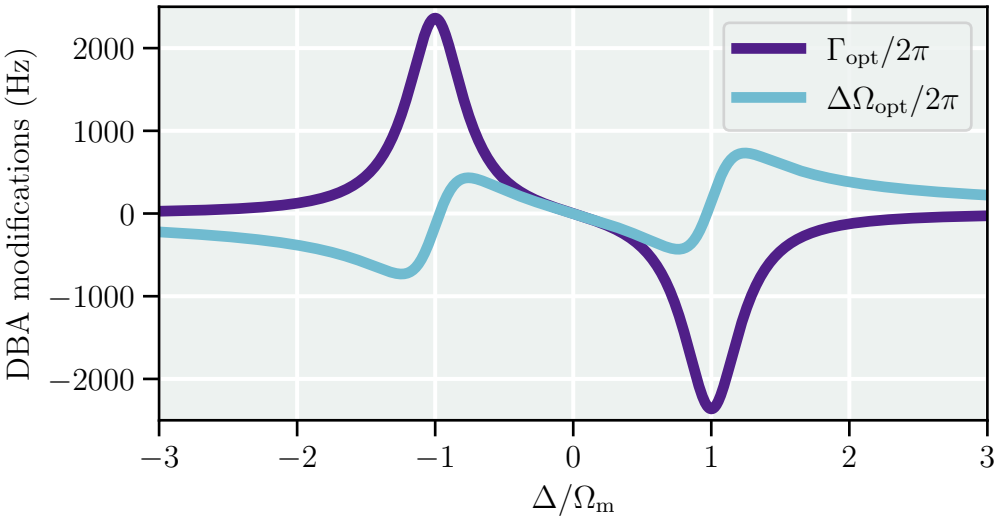

Figure 5.2: Dynamical backaction modifications to the mechanical susceptibility. For $\Omega_\mathrm{m} = 2\kappa$ and $g/2\pi = 30\,\mathrm{kHz}$ we plot the optical spring (teal) and optomechanical damping (purple) as given by eqs. (5.20), evaluated for $\Omega = \Omega_\mathrm{m}$ and varied Δ.

enhancing one and suppressing the other. Accordingly we call the condition $\kappa \ll \Omega_\mathrm{m}$ the *resolved sideband regime*. The optomechanical dampening can in fact be viewed as the competition of Stokes and anti-Stokes scattering: the former is associated with the negative term of equation (5.20b) (compare the frequency dependence to that of eq. (5.13)), and the anti-Stokes process corresponds to the first, positive term.

In the resolved sideband regime, with the strong coherent field detuned below resonance $\Delta = -\Omega_\mathrm{m}$, the optical modifications evaluated at $\Omega = \Omega_\mathrm{m}$ simplify considerably

$$\Delta\Omega_\mathrm{m}(\Omega_\mathrm{m}) \approx 0, \tag{5.21a}$$

$$\Gamma_\mathrm{opt}(\Omega_\mathrm{m}) \approx \frac{4g^2}{\kappa}. \tag{5.21b}$$

.

Equation (5.21b) motivates the introduction of the *classical coorperativity*, $\mathcal{C}$ which compares the rates of coherent interaction and energy decay:

$$\mathcal{C} = \frac{4g^2}{\kappa\Gamma_\mathrm{m}} = \frac{\Gamma_\mathrm{opt}}{\Gamma_\mathrm{m}}. \tag{5.22}$$

Interestingly the resolved sideband regime, in principle, allows ground-state cooling of the mechanical oscillator, in contrast to the unresolved regime. To

see this, we can consider how the optomechanical interaction changes the average number of excitations populating the mechanical oscillator. We have already noted how the two terms of eq. (5.20b) describe the rates $A^{\pm}$ of increasing or decreasing the average phonon number:

$$A^{\pm} = \frac{g^2\kappa}{(\kappa/2)^2 + (\Delta \mp \Omega_{\mathrm{m}})}, \tag{5.23a}$$

$$\Gamma_{\mathrm{opt}} = A^{-} - A^{+}. \tag{5.23b}$$

The up- and downward transition probabilities $\Gamma_{n\to n+1}$ and $\Gamma_{n\to n-1}$ are then given as

$$\Gamma_{n\to n+1} = (n+1)A^{+} \tag{5.24a}$$

$$\Gamma_{n\to n-1} = nA^{-}. \tag{5.24b}$$

.

Together with the definition of the mean phonon number $\bar{n} = \Sigma_n n p_n$ and it's time derivative $\dot{\bar{n}}$, in the steady state $\dot{\bar{n}}$=0, one finds a minimum occupation,

$$\bar{n}_{\mathrm{min}} = \frac{A^{+}}{A^{-} - A^{+}}, \tag{5.25}$$

known as the *back-action limit* for sideband cooling of mechanical motion. Minimizing $\bar{n}_{\mathrm{min}}$ by varying Δ in the resolved and unresolved regimes gives

$$\bar{n}_{\mathrm{min}}^{\mathrm{RSB}} = \left(\frac{\kappa}{4\Omega_{\mathrm{m}}}\right)^2 \ll 1, \tag{5.26a}$$

$$\bar{n}_{\mathrm{min}}^{\mathrm{URSB}} = \frac{\kappa}{4\Omega_{\mathrm{m}}} \gg 1. \tag{5.26b}$$

In the resolved sideband regime, the minimal occupation is found for $\Delta = -\Omega_{\mathrm{m}}$. Apart from back-action heating due to the Stokes process, the equation of motion for mechanical oscillator (5.14b), also contains coupling to a thermal bath, with mean occupation $\bar{n}_{\mathrm{th}}$, at the mechanical decay rate Γ_{m}. The presence of this additional coupling yields a final occupation

$$\bar{n}_{\mathrm{final}} = \frac{\bar{n}_{\mathrm{min}}\Gamma_{\mathrm{opt}} + \bar{n}_{\mathrm{th}}\Gamma_{\mathrm{m}}}{\Gamma_{\mathrm{opt}} + \Gamma_{\mathrm{m}}}. \tag{5.27}$$

In the regime of strong classical coorperativity $\mathcal{C} \gg 1$, the final occupation can be re-expressed in terms of the *quantum* coorperativity $\mathcal{C}_{\mathrm{q}} = \mathcal{C}/\bar{n}_{\mathrm{th}}$:

$$\bar{n}_{\mathrm{final}} = \bar{n}_{\mathrm{th}} + 1/\mathcal{C}_{\mathrm{q}}, \tag{5.28a}$$

$$\mathcal{C}_{\mathrm{q}} = \frac{4g^2}{\kappa\Gamma_{\mathrm{m}}\bar{n}_{\mathrm{th}}} = \frac{\Gamma_{\mathrm{opt}}}{\Gamma_{\mathrm{m}}\bar{n}_{\mathrm{th}}}. \tag{5.28b}$$

The quantum coorperativity describes the rate of coherent interaction relative to the decoherence (rather than energy decay) rate. Evidently $\mathcal{C}_{\mathrm{q}} > 1$ is required for cooling to an average final occupation $\bar{n}_{\mathrm{final}} < 1$, which in the cavity optomechanics community is the criterion for ground-state cooling.

5.1.2 Optomechanically Induced Transparency

The conditions of red-detuning by the mechanical frequency, high coorperativity and sideband resolution also give rise to another interesting phenomenon: *optomechanically induced transparency* (OMIT). This is a close analog of the atomic physics phenomenon of *electromagnetically induced transparency* (EIT). As such, OMIT facilitates the same applications as EIT, such as coherent storage of light in a stationary system, with applications in quantum networks.

The basis of a mathematical description of OMIT is the Langevin equations of eqs. (5.14). If we consider an input flux s_{in} with an optical frequency Ω_{L}, phase-modulated at a small modulation depth $\beta \ll 1$, at a frequency Ω_{mod},

$$s_{\mathrm{in}}(t) = s_0 \mathrm{e}^{i(\Omega_{\mathrm{L}}t + \beta\sin(\Omega_{\mathrm{mod}}t))} = s_0 \mathrm{e}^{i\Omega_{\mathrm{L}}t}\left(1 + i\beta\sin(\Omega_{\mathrm{mod}}t)\right), \tag{5.29}$$

we can investigate its interaction with the optomechanical cavity. The transmitted flux $|s_{\mathrm{out,T}}|^2$ from the cavity, within the linearization of the optomechanical interaction and assuming no excess cavity loss and $\alpha \in \mathbb{R}$, is given as by the input-output relation

$$|s_{\mathrm{out,T}}|^2 = (1-\eta_{\mathrm{c}})\kappa\,|\alpha + a|^2 \approx (1-\eta_{\mathrm{c}})\kappa\left(\alpha\left(a + a^\dagger\right)\right). \tag{5.30}$$

Here we only kept terms $\propto a + a^\dagger$ and disregarded components at DC and $(a + a^\dagger)^2$. Solving the Langevin equations for a, b and their Hermitian conjugates in the Fourier domain and dropping the noise terms then yields

$$a(\Omega) = \chi_{\mathrm{cav}}(\Omega)\left(ig(b + b^\dagger) + \sqrt{\eta_{\mathrm{c}}\kappa}s_{\mathrm{in}}\right), \tag{5.31a}$$

$$a^\dagger(\Omega) = \chi^*_{\mathrm{cav}}(-\Omega)\left(-ig(b + b^\dagger) + \sqrt{\eta_{\mathrm{c}}\kappa}s^\dagger_{\mathrm{in}}\right), \tag{5.31b}$$

$$b(\Omega) = ig\chi_{\mathrm{m}}(\Omega)(a + a^\dagger), \tag{5.31c}$$

$$b^\dagger(\Omega) = -ig\chi_{\mathrm{m}}(-\Omega)(a + a^\dagger). \tag{5.31d}$$

Because the relecant output signal (5.30) is determined by $(a + a^\dagger)$ and

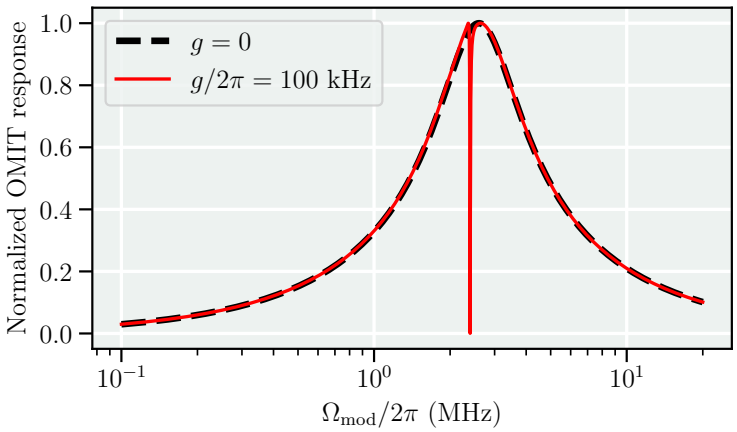

Figure 5.3: Magnitude of OMIT response from equation (5.34). In dashed black the cavity response for $g = 0$ and in red for $g/2\pi = 100\,\mathrm{kHz}$ is plotted. Parameters: $\Omega_\mathrm{m}/2\pi = 2.4\,\mathrm{MHz}$, $\Gamma_\mathrm{m} = 20\,\mathrm{mHz}$, $\eta_\mathrm{c} = 0.9$, $\kappa/2\pi = 2\,\mathrm{MHz}$, $\Delta = -\Omega_\mathrm{m}$.

$(b + b^\dagger)$ we can readily find these from (5.31):

$$a + a^\dagger = ig(b + b^\dagger)\left(\chi_\mathrm{cav}(\Omega) - \chi^*_\mathrm{cav}(-\Omega)\right) + \sqrt{\eta_\mathrm{c}\kappa}\left(\chi_\mathrm{cav}(\Omega)s_\mathrm{in} + \chi^*_\mathrm{cav}(-\Omega)s^*_\mathrm{in}\right), \tag{5.32a}$$

$$b + b^\dagger = ig(a + a^\dagger)\left(\chi_\mathrm{m}(\Omega) - \chi_\mathrm{m}(-\Omega)\right). \tag{5.32b}$$

Since we have taken the carrier α to be real, the modulation sidebands are in general not so. We have to account for the complex cavity transfer function, giving

$$s_\mathrm{in} = i\beta s_0 \frac{|\chi_\mathrm{cav}(0)|}{\chi_\mathrm{cav}(0)}, \tag{5.33a}$$

$$s^\dagger_\mathrm{in} = -i\beta s_0 \frac{|\chi_\mathrm{cav}(0)|}{\chi^*_\mathrm{cav}(0)}. \tag{5.33b}$$

We can now solve (5.32) for $a + a^\dagger$, subject to the input (5.33a), and find:

$$a + a^\dagger = i\sqrt{\eta_\mathrm{c}\kappa}\frac{|\chi_\mathrm{c}(0)|\left(\frac{\chi_\mathrm{cav}(\Omega)}{\chi_\mathrm{cav}(0)} - \frac{\chi^*_\mathrm{cav}(\Omega)}{\chi^*_\mathrm{cav}(0)}\right)}{1 + g^2(\chi_\mathrm{cav}(\Omega) - \chi^*_\mathrm{m}(\Omega))(\chi_\mathrm{m}(\Omega) - \chi^*_\mathrm{cav}(\Omega))}\beta s_0. \tag{5.34}$$

Interestingly, the mechanical response only shows up in the second term of the denominator. This means OMIT is also a useful spectroscopic technique for easily determining cavity parameters such as detuning and linewidth.

In figure 5.3 we show the magnitude of eq. (5.34) for zero and large coupling g. Traces like the black dashed line can acquired from a fast, coarse scan over the cavity lineshape, and robustly fitted the extract Δ and κ. To obtain data like the red line requires a slower, more fine-grained scan, since the time between steps cannot exceed the mechanical response time and also must be able to resolve the sharp mechanical transparency dip.

5.1.3 Transient OMIT

In our mechanical memory experiments, we rely on OMIT to convert an optical input to mechanical excitations for later retrieval. For these storage experiments, the Fourier domain description is insufficient, since we in this case are studying transient effects of OMIT. In particular we are interested in describing how the optomechanical system responds to input fluxes with time-varying amplitudes $s_{\mathrm{in}}(t) = s_0(t)\mathrm{e}^{i\Omega_{\mathrm{L}}t}$. Within the weak coupling regime $g \ll \kappa$ the cavity responds fast such that we can adiabatically eliminate the it and write the output it terms of either b and $b^\dagger$ or the mechanical quadratures.

Adiabatic elimination is a mathematical technique often employed in quantum optics when dealing with a system described by fast and slow variable, that we briefly review following [87]. Considering the pair of coupled dissipative equations of motion for the two variables x_1 and x_2, we write them in a general form

$$\dot{x}_1 = -\gamma_1 x_1 + f_1(x_1, x_2), \tag{5.35a}$$

$$\dot{x}_2 = -\gamma_2 x_2 + f_2(x_1, x_2). \tag{5.35b}$$

Taking x_1 as the fast variable then implies $\gamma_1 \gg \gamma_2$. In this case x_2 is essentially constant over the timescale defined by γ_1^{-1} which then can be utilized to write:

$$x_1 \approx \frac{1}{\gamma_1} f_1(x_1, x_2), \tag{5.36}$$

that can be solved for x_1, to obtain $x_1(x_2)$ in terms of x_2. With an algebraic, rather than differential, equation for the fast variable we can state the differential equation for the slow variable in these terms:

$$\dot{x}_2 \approx -\gamma_2 x_2 + f_2\big(x_1(x_2), x_2\big), \tag{5.37}$$

thus obtaining a only single differential equation for the system dynamics. This can then be written to the form:

$$\dot{x}_2 = \phi(t) x_2 + \psi(t). \tag{5.38}$$

One can then solve eq. (5.38) by formally integrating to get:

$$x_2(t) = \mathrm{e}^{-\int \phi(t')\mathrm{d}t'} \left[\int_{t_0}^{t} \mathrm{e}^{+\int \phi(t'')\mathrm{d}t''} \psi(t')\mathrm{d}t' + C_0 \right], \tag{5.39}$$

with C_0 an initial value determined constant.

In the present case, we can consider the cavity mode a the fast variable and the mechanics b the slow, $\kappa \gg \Gamma_{\mathrm{eff}}$. If we furthermore move to a frame rotating at $-\Omega_{\mathrm{m}}$ and apply a rotating wave approximation, dropping the $b^\dagger$ term, applying the adiabatic elimination result eq. (5.39) to b then yields

$$b(t) = \mathrm{e}^{-\left(\frac{\Gamma_{\mathrm{eff}}}{2}+i\delta\right)t} \left[b(0) + i \int_{t_0}^{t} \mathrm{e}^{+\left(\frac{\Gamma_{\mathrm{eff}}}{2}+i\delta\right)t'} \left(\sqrt{\eta_{\mathrm{c}}\Gamma_{\mathrm{opt}}} s_{\mathrm{in}}(t') + \sqrt{(1-\eta_{\mathrm{c}}\Gamma_{\mathrm{opt}})} f_{\mathrm{in}} \right) \mathrm{d}t' \right], \tag{5.40}$$

where $\delta = \Delta - (-\Omega_{\mathrm{m}})$ defines the two-photon detuning such that $\delta = 0$ when $\Delta = -\Omega_{\mathrm{m}}$. Equation (5.40) is a bit involved at a first glance, so it merits an attempt at unpacking before proceeding.

Firstly we can consider the case of no driving, and two-photon resonance. Then the first term simply predicts mechanical decay at the optically broadened decay rate Γ_{eff}, which is in line with expectations.

If we now consider a coherent input and and disregard the vacuum noise f_{in}, the second term predicts the mechanics ringing up at the same rate. As an example of this, we can consider initially having the mechanics in thermal equilibrium and subject to a strong drive. Then the presence of the optical drive simply tells us that the mechanical amplitude will grow, again in line with expectations.

In a similar manner, the optical output (in reflection) from the cavity s_{out} can be determined

$$s_{\mathrm{out}}(t) = s_{\mathrm{in}}(t) - i\sqrt{\eta_{\mathrm{c}}\Gamma_{\mathrm{opt}}} b(t). \tag{5.41}$$

These equations (5.40,5.41) from the mathematical basis of the mechanical memory experiments, detailed in section 8.

5.2 Membrane in the Middle

The optomechanical system we work with in the lab differs from the canonical optomechanics picture of an optical Fabry Pérot cavity with a mechanically complaint end mirror. Rather, we work with a mechanical resonator placed inside a cavity. This so-called *membrane in the middle* (MIM) design inherits the abstract description of the canonical system, albeit with a frequency pull parameter G that now depends on the properties and alignment of the membrane.

In a cursory sense, the coupling comes about from the fact that the refractive index of the membrane is different from that of vaccum. For certain positions of the membrane relative to the intracavity standing wave, the mechanical vibrations can then modulate the cavity length in a manner reminiscent of the canonical case. As such the mapping from canonical to MIM optomechanics lies in accounting for these effects appropriately, which will be the topic of the following section.

The main advantage of the membrane in the middle approach is that the design of the optical and mechanical resonators now can be separated. For our optical resonator we stay close the canonical picture, relying on a high-finesse Fabry Pérot cavity comprised of highly reflective dielectric mirrors. We buy these from specialized coating companies and focus our attention of the engineering of the mechanical resonator as described in section 3.

5.2.1 Transfer-Matrix Method

We follow the transfer-matrix method of [85] to decribe the effect of a membrane inside a cavity, cf figure 5.4.

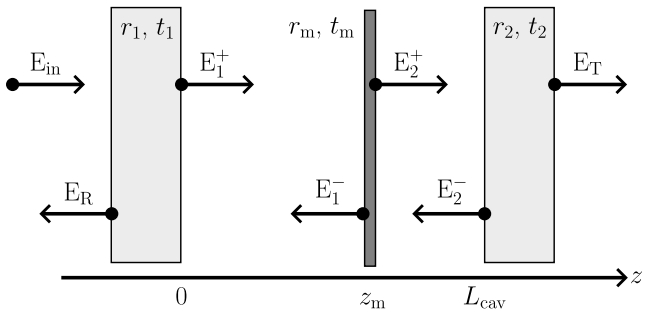

Figure 5.4: Membrane in the middle. We tally up the effects of reflection and transmission through the optical components (the cavity mirrors are drawn thick, in light gray, the membrane thin, in dark gray) by tracking the field components traveling in the positive and negative z direction in either subcavity $E_j^\pm$.

The cavity is comprised of two mirrors, each with a field reflection and transmission coefficient indexed by j, r_j and t_j. The membrane is modelled

as a dielectric slab of thickness h and refractive index n, placed a distance z_m from the incoupling mirror. Such a slab has reflection and transmission coefficients [85]

$$r_\mathrm{m} = \frac{(n^2-1)\sin nkh}{2in\cos nkh + (n^2+1)\sin nkh}, \tag{5.42a}$$

$$t_\mathrm{m} = \frac{2n}{2i\cos nkh + (n^2+1)\sin nkh}, \tag{5.42b}$$

for a monochromatic field with wavenumber $k = 2\pi/\lambda$. The intracavity mode is approximated by plane waves, which is a good approximation as long as the cavity length L_cav is shorter than its Rayliegh range z_R. We follow the phase convention of [...] and write up equations for electric field travelling in the positive and negative z direction in the two sub-cavities $E_j^\pm$ as well as reflected and transmitted fields:

$$E_1^+ = it_1E_\mathrm{in} + r_1E_1^-\mathrm{e}^{ikz_\mathrm{m}}, \tag{5.43a}$$

$$E_1^- = r_\mathrm{m}E_1^+\mathrm{e}^{ikz_\mathrm{m}} + it_\mathrm{m}E_2^-\mathrm{e}^{ik(L_\mathrm{cav}-z_\mathrm{m})}, \tag{5.43b}$$

$$E_2^+ = it_\mathrm{m}E_1^+\mathrm{e}^{ikz_\mathrm{m}} + r_\mathrm{m}E_2^-\mathrm{e}^{ik(L_\mathrm{cav}-z_\mathrm{m})}, \tag{5.43c}$$

$$E_2^- = r_2E_2^+\mathrm{e}^{ik(L_\mathrm{cav}-z_\mathrm{m})}, \tag{5.43d}$$

$$E_\mathrm{R} = r_1E_\mathrm{in} + it_1E_1^-\mathrm{e}^{ikz_\mathrm{m}}, \tag{5.43e}$$

$$E_\mathrm{T} = it_2E_2^+\mathrm{e}^{ik(L_\mathrm{cav}-z_\mathrm{m})}. \tag{5.43f}$$

We write equations (5.43) here to elucidate their origin in the physics pictured in figure 5.4, but in practice solve them in a matrix form:

$$\begin{pmatrix} E_1^+ \\ E_1^- \\ E_2^+ \\ E_2^- \end{pmatrix} = \underbrace{\begin{pmatrix} 0 & r_1\mathrm{e}^{ikz_\mathrm{m}} & 0 & 0 \\ r_\mathrm{m}\mathrm{e}^{ikz_\mathrm{m}} & 0 & 0 & it_\mathrm{m}\mathrm{e}^{ik(L_\mathrm{cav}-z_\mathrm{m})} \\ it_\mathrm{m}\mathrm{e}^{ikz_\mathrm{m}} & 0 & 0 & r_\mathrm{m}\mathrm{e}^{ik(L_\mathrm{cav}-z_\mathrm{m})} \\ 0 & 0 & r_2\mathrm{e}^{ikz_\mathrm{m}} & 0 \end{pmatrix}}_{\mathbb{M}} \underbrace{\begin{pmatrix} E_1^+ \\ E_1^- \\ E_2^+ \\ E_2^- \end{pmatrix}}_{\mathbb{E}}. \tag{5.44}$$

Defining the matrix $\mathbb{T} = \mathbb{I} - \mathbb{M}$, where $\mathbb{I}$ denotes the identity matrix means we can calculate the vector of field components $\mathbb{E}$, driven by an input E_in through the first mirror as

$$\mathbb{E} = \mathbb{T}^{-1}\begin{pmatrix} it_1E_\mathrm{in} & 0 & 0 & 0 \end{pmatrix}^\mathrm{T}. \tag{5.45}$$

Having obtained a solution for the intra-cavity field components, we then

proceed numerically since the analytical expressions quickly get unwieldy. Operationally we first solve the matrix equation (5.45) analytically and then construct $|E_{\mathrm{T}}|^2$ and $|E_{\mathrm{R}}|^2$, using eqs. (5.43e-f) and evaulate them for a large range of wavenumbers. Then we numerically identify and fit resonances in the transmission or reflection, using a peak-finder algorithm. This allows us to extract how the linewidth, transmission peak height and reflection dip depth, as well as resonant frequency all depend on k.

In the MIM model, this k dependence is periodic (deviations can be observed for membranes very close a mirror - the so-called *membrane at the edge* design [127]). As either the membrane is translated along the cavity axis or different longitudinal cavity modes with different resonant k are probed, the membrane position relative to the standing intensity pattern is varied. Therefore we usually discuss the modulation of cavity parameters due to the membrane in terms of the "$2kz_{\mathrm{m}}$" position, since both tuning mechanisms are described by this number. In figure 5.5 we plot the numerically calculated parameter modulations, obtained by the produce outlined above. In the caption we introduce $\Delta\lambda$ which defines the wavelength range we evaluate the model over, and N which is the number of points used in the numerical calculation.

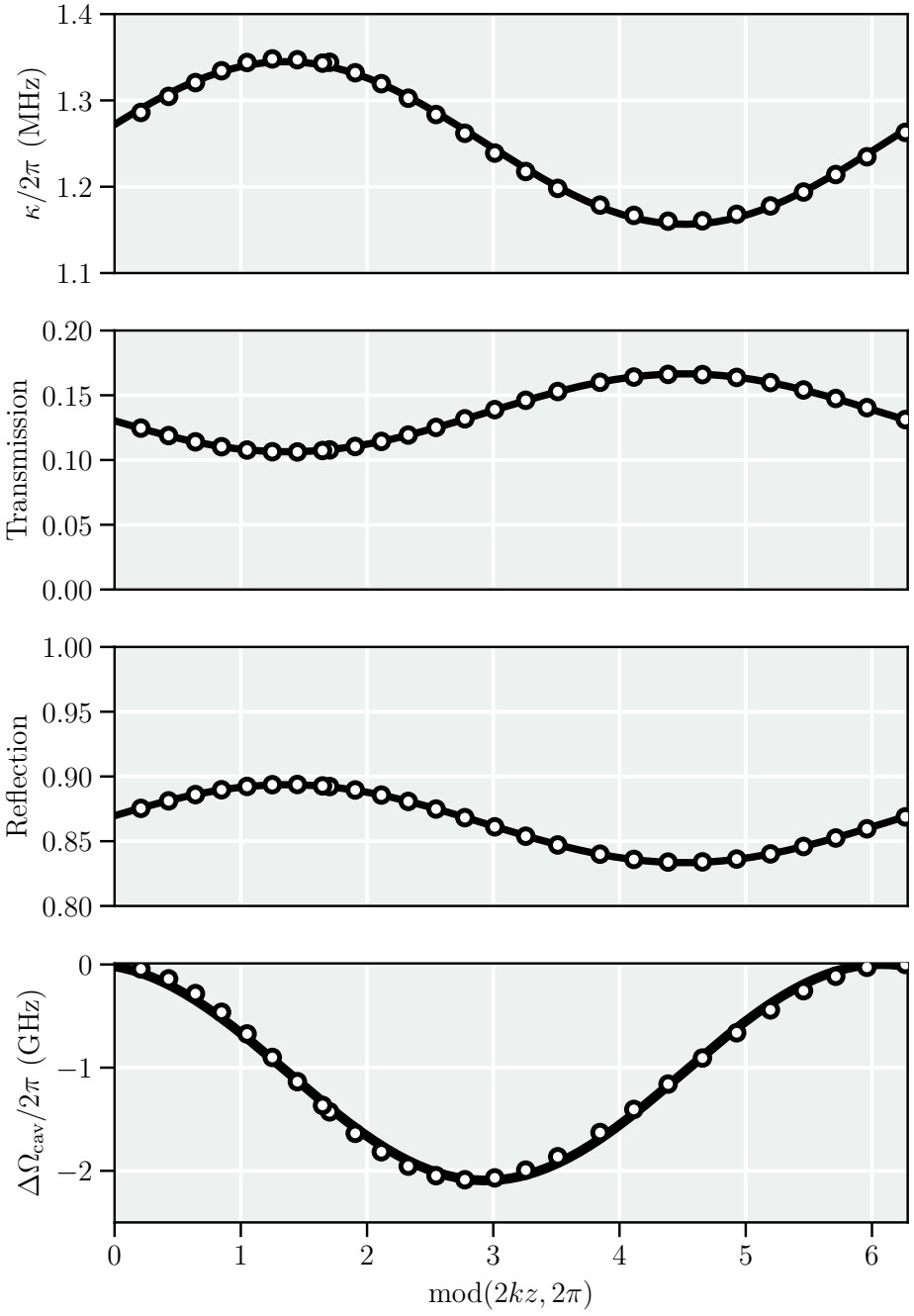

Figure 5.5: $2kz$ modulation cavity parameters. Input parameters: $|t_1|^2 = 280\times 10^{-6}$, $|t_2|^2 = 10 \times 10^{-6}$, $h = 20\,\mathrm{nm}$, $z_{\mathrm{m}} = 1.902\,72\,\mathrm{mm}$, $L_{\mathrm{cav}} = 5.503\,14\,\mathrm{mm}$, $\lambda_0 = 1550.013\,74\,\mathrm{nm}$, $\Delta\lambda = 6\,\mathrm{nm}$, $N = 2 \times 10^7$. The hollow circles indicate values extracted from fits to reflection and transmission peaks, and the solid lines are in turn sinusoidal fits to the extracted values.

For the shown configuration, we learn that we can achieve simultaneous narrowing of the linewidth κ and large $G = -\partial\Delta\Omega_{\mathrm{cav}}/\partial z$, given by the deriva-

tive of the cavity frequency modulation, around $2kz \approx 4.5$. We note that seemingly absurd numerical precision given for eg. z_m and L_cav do not indicate that we know these quantites to such precision. Rather, they are chosen so that they do not divide nicely into one another, since in this case the sinusoidal modulations only are sampled at a few points when taking $\mathrm{mod}\,(2kz, 2\pi)$.

5.2.2 Modified Effective Mass

In section 3.2 we introduced the effective mass for a given mode. Implicit in the given definition is the assumption of an ideal point-like probe of the point of maximum displacement. In real membrane-in-the-middle cavity optomechanics experiment this is never truly the case and the validity of the approximation depends on the relative size of the cavity waist w_0 and the mechanical wavelength Λ. Outside of the regime $w_0 \ll \Lambda$, the cavity field probes significant portions of the membrane, that by definition has smaller out-of-plane displacement than the (typically centered) point of maximal displacement. As such, in a loose sense, the membrane "appears" heavier, with a smaller apparent displacement, despite being driven by the same eg. thermal force noise or radiation pressure force.

We can quantify these ideas by modifying the definition of the effective modal mass to account for the overlap of the optical probing field and mechanical displacement field. For the fundamental longitudinal Gaussian cavity mode (cf. eq. 2.14), the normalized intensity, evaluated at the membrane position, is given by

$$\bar{I}(x,y) = \frac{I(x,y,z_\mathrm{m})}{I_0} = \frac{2}{\pi w(z_\mathrm{m})^2} \mathrm{e}^{-2(x^2+y^2)/w(z_\mathrm{m})^2}. \tag{5.46}$$

Using eq. (5.46) as the shape of the optical mode probing the membrane motion with modeshape w_mech, we can define its peak-normalized version $\psi_w = |w_\mathrm{mech}|/\max|w_\mathrm{mech}|$, and then modify the effective mass as an weighted average of the displacement field over the optical mode

$$m_\mathrm{eff} = \rho h \int_\mathcal{A} (\psi_w)^2 \,\mathrm{d}A, \tag{5.47a}$$

$$\implies m_\mathrm{eff,MO} = \rho h \int_\mathcal{A} \frac{|w_\mathrm{mech}|^2}{(\int_\mathcal{A} |w_\mathrm{mech}| \bar{I}(x',y')\mathrm{d}A')^2} \mathrm{d}A, \tag{5.47b}$$

$$= \underbrace{\left(\int_\mathcal{A} \psi_w \bar{I}(x,y)\mathrm{d}A\right)^{-2}}_{\text{mode overlap penalty } \eta_\mathrm{MO}^{-2}} \underbrace{\rho h \int (\psi_w)^2 \,\mathrm{d}A}_{\text{original } m_\mathrm{eff}}. \tag{5.47c}$$

This new effective mass that accounts for mode overlap, $m_\mathrm{eff,MO}$, in turn

leads to a modified $g_0 = x_{\mathrm{zpf}} G$, since $x_{\mathrm{zpf}} \propto m_{\mathrm{eff}}^{-1}$. The reduction in g_0 due to non-ideal mode overlap is given by η_{MO}, which we evaluate numerically for a simulated displacement profile of the membrane mode used in the memory experiments, see figure 5.6.

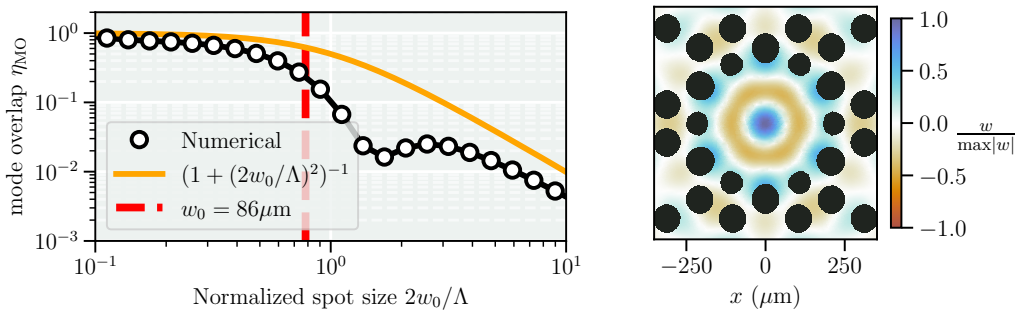

Figure 5.6: Optical-mechanical mode overlap for finite waist size. Left: We numerically evaluate η_{MO} according to eq. (5.47) (hollow black circles) for the normalized mode profile shown to the right, by sweeping w_0 of the cavity mode. In orange we plot a simple guiding line $\eta_{\mathrm{MO}} = (1 + (2w_0/\Lambda)^2)^{-1}$, that follows the overall trend of the numerical points, apart from the dip when the cavity mode also probes negative displacement around $2w_0/\Lambda \approx 2$. The vertical red line is indicative of the cavity used in the memory experiments.

The same numerical machinery can be applied to study the effects of a small enough, but misaligned beam. Instead of varying w_0, we can translate the center of the probing Gaussian beam, such that $(x, y) \mapsto (x + \delta x, y + \delta y)$.

In figure 5.7 we plot numerically evaluated η_{MO} for a fixed waist $w_0 = 89\,\mu\mathrm{m}$, sweeping the center $\delta x, \delta y$ of the gaussian beam along the diagonal, indicated by the red arrow overlaid on the modeshape insets (cf. figure 5.6). Here the relative flatness near $\delta x = 0$ tells us that for the given cavity and membrane modes, we have a roughly $50\,\mu\mathrm{m}$ wide band centered on the middle of the defect, where the mode overlap penalty is small for the radially symmetric (top) mode, and comparatively large for the $(1, 1)$-like mode (bottom). In this way one can attempt to quantify when an optomechanical cavity is aligned "well enough", which otherwise can be tricky to gauge, since *perfect* alignment only exists on paper.

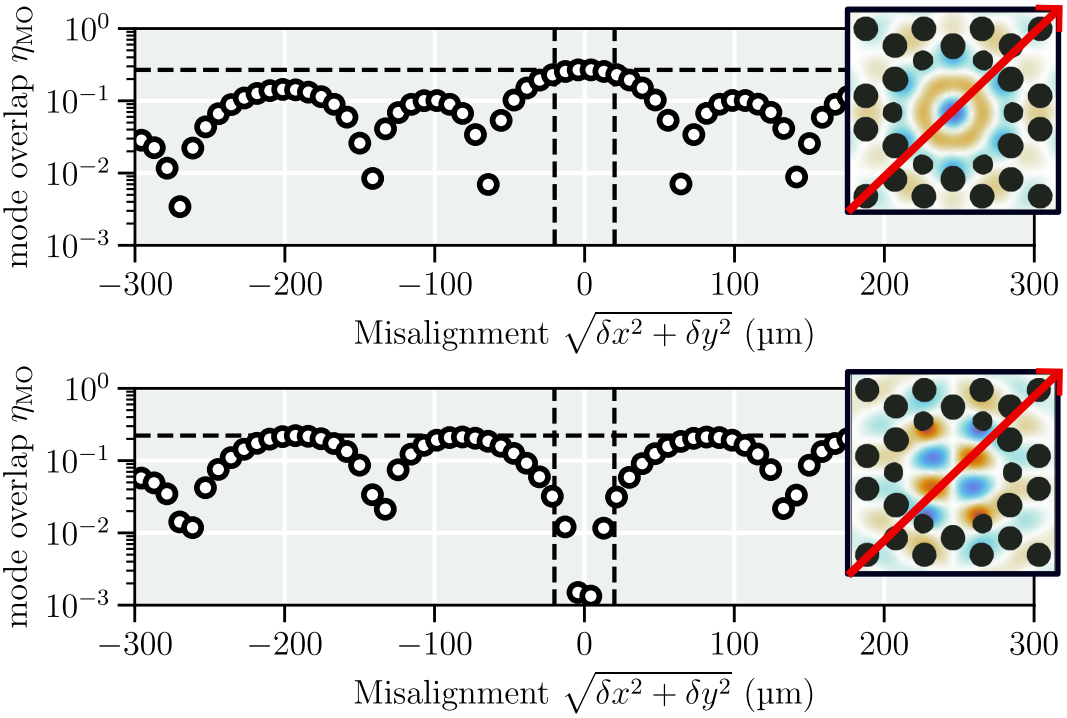

Figure 5.7: g_0 penalty from misalignment, for two defect modes. Hollow black circles are numerical calculations of eq. (5.47), for a probing beam, misaligned by a varying $\sqrt{\delta x^2 + \delta y^2}$ along the diagonal indicated by the red arrow. The vertical black dashed lines indicate a 50 µm wide region, centered on the middle of the defect. The horizontal black dashed line indicates the maximal value of η_{MO}.

6 Experimental Methods

"The struggle itself toward the heights is enough to fill a man's heart. One must imagine Sisyphus happy."

Albert Camus

To connect the theoretical concepts henceforth discussed with the actual experiments conducted, we review some practicalities in this section. We discuss how we actually measure the mechanical oscillators using light, various feedback-stabilization schemes, and our procedure for putting together a membrane-in-the-middle optomechanical cavity.

6.1 Optical Detection of Mechanical Motion

Measurements of interfering optical fields can produce signals that are sensitive to very small fluctuations in the phase difference of the interfering fields. We utilize this fact to measure the small vibrations of our mechanical oscillators, both when characterizing new designs of resonators as well as the "proper" cavity optomechanical experiments. Here we explain the principles of optically measuring mechanical displacement in two cases: with the membrane forming one mirror of a Mach-Zehnder interferometer, and the case of the membrane inside a cavity.

Before carrying on, we must note that this is a vast topic that has been studied meticulously both theoretically and experimentally for more than half a century. The present description does not do this body of work justice in the slightest, but is simply intended as a practical explanation of the techniques we employ in our experiments.

6.1.1 Interferometry

The Mach-Zehnder interferometer is comprised at the most basic level of an input beamsplitter that splits an input field into the two "arms" of the interferometer, that separately each propagate the distances L_1 and L_2, before recombining on a second output beamsplitter, cf. figure 6.1. We call the arm that reflects off the membrane the *probe* arm and the other the *reference* arm.

To calculate the intensity at the two outputs $|E_\pm|^2$, we consider the propagation of $E_{\text{in}} = E_0 \mathrm{e}^{ikx}$ through the optical components. We find for the two fields impinging on the output beamsplitter

$$E_1 = t_1 E_0 \mathrm{e}^{ikL_1}, \quad E_2 = r_1 r_{\text{m}} E_0 \mathrm{e}^{ikL_2}, \tag{6.1}$$

with r_{m} given by eq. (5.42). Taking the output beamsplitter to be equally reflective and transmissive, $r_2 = 1/\sqrt{2}$, $t_2 = i/\sqrt{2}$ (consistent with the conven-

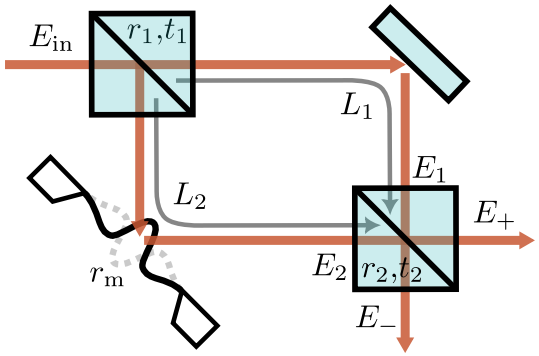

Figure 6.1: Sketch of a Mach-Zehnder interferometer for measuring membrane displacement. An input electric field E_{in} is divided at an input beamsplitter into two beams, one of which reflects on the mechanical resonator whose motion we want to measure. The two beams interfere at a second beamsplitter such that the intensity of the two output modes $|E_\pm|^2$ encode the path length difference, containing a contribution from mechanical oscillations $q(t)$.

tion used in the transfer matrix calculation), we find the output intensities

$$|E_\pm|^2 = \frac{|E_0|^2}{2}\left(|t_1|^2 + |r_{\text{m}}|^2|r_1|^2 \pm 2|r_1||t_1||r_{\text{m}}|\cos\left(2k\Delta L + \phi_{\text{m}}\right)\right), \tag{6.2}$$

where we define the arm length difference $\Delta L = L_2 - L_1$ and an ultimatively irrelevant membrane reflection phase $\phi_{\text{m}} = \arg r_{\text{m}}$.

Since $L_2 \mapsto L_2 + q(t)$ depends contains $q(t)$, the mechanical displacement can be extracted from such an interferometric phase-sensitive measurement. We do so in two different ways, *balanced homodyne* and *balanced heterodyne* detection, each used in different characterization inteferometers. Since mechanical signal is proportional to the geometric mean of the arm powers, it is often advantageous to operate with an unbalanced input beamsplitter $|r_1| \ll |t_1|$, to avoid excessive powers on the membrane, but rather boosting the signal with a stronger reference arm.

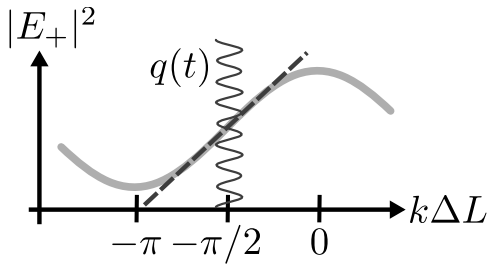

Figure 6.2: Transduction of mechanical displacement to an optical signal. At certain $k\Delta L = -\pi/2 \mod 2\pi$, small amplitude mechanical vibrations $q \ll \lambda$ are linearly transduced to intensity fluctuations which a photodiode can detect.

Balanced detection refers to measuring the difference of two optical signals with equal (balanced) DC level, such as $|E_+|^2$ and $|E_-|^2$. Two nice features of balanced detection is cancellation of common mode noise (eg. classical laser intensity noise), since it is subtracted, as well as the option to operate the photodetector with higher gain without fear of saturation, since the strong DC component is cancelled.

Homo- and heterodyne refers to the optical frequencies of the probe and reference fields.

Homodyne is when these are the same, i.e. what is pictured in figure 6.1. Then the only amendments necessary for balanced homodyne detection is a detector with two photodiodes and a subtraction circuit, as well as active path-length stabilization to keep $k\Delta L = -\pi/2 \mod 2\pi$ cf. figure 6.2.

For heterodyne, the frequencies are different, usually by a RF modulation frequency. We realise this by placing an acousto-optic modulator in the reference arm. This component shifts the optical frequency by an externally applied modulation frequency. Thus the interference fringe is quickly scanned over, dispensing with the need for active path length stabilization, but with the overhead of the modulator in the first place and higher bandwidth electronics that can resolve the modulation frequency.

In our group we have two different characterization interferometers. One is largely free space optics and always homodyne, with details given in [128, 129]. The other setup is fiber-based, where the "plug-and-play" nature of fiber optics eases switching between homo- and heterodyne balanced detection. More details on the fiber-based interferometer can be found in [90, 130].

6.1.2 Cavity-based

Strictly speaking an optical cavity is an interferometer, yet the transduction is more complicated, as described in section 5. Hence we distinguish the two approaches and expand the cavity-based approach in more detail here. For our experiments we almost exclusive measure in reflection[9], so we restrict the present discussion to such measurements.

From the quadrature formulation of the optomechanical Langevin equations (5.17) we already noted two ways of measuring displacements of mechanical resonator in a cavity: phase-sensitive measurements of a resonant probe field and intensity-sensitve measurements of a detuned probe, sketched in figure 6.3.

Resonant probing For simplicity we start by treating the case of resonant s_{in}, where the mechanical information is purely in the optical phase quadrature.

[9]We conduct two types of transmission measurements: fast OMIT scans to determine Δ and κ and measurements of the transmitted DC power, to determine the intra-cavity photon number.

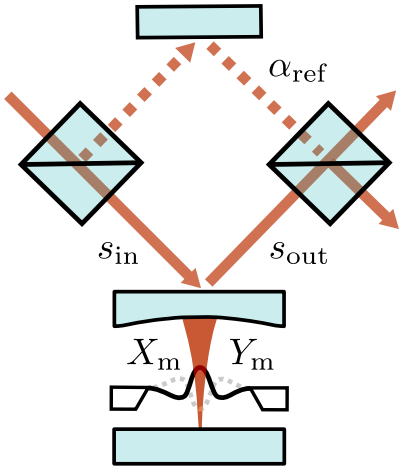

Figure 6.3: Sketch of cavity-based mechanical displacement measurements. An optical input with s_{in} reflects off an optomechanical cavity. For a resonant input $\Delta = 0$, an optional reference beam α_{ref} (dashed red) and output beamsplitter can be added. For a detuned input $\Delta \neq 0$, these are not required. The optomechanical interaction as described by eq. (5.17) imprints the mechanical quadratures X_{m}, Y_{m} on the quadratures $X_{\mathrm{L}}^{\mathrm{out}}$, $Y_{\mathrm{L}}^{\mathrm{out}}$, of the output flux s_{out}.

Then the Langevin equation in the Fourier domain and input-output relation in reflection gives us:

$$Y_{\mathrm{L}}^{\mathrm{out}} = \underbrace{-2ig\frac{\sqrt{\eta_{\mathrm{c}}\kappa}}{\kappa/2 - i\Omega}X_{\mathrm{m}}}_{\text{mechanical signal}} + \underbrace{\left(1 - \frac{\eta_{\mathrm{c}}\kappa}{\kappa/2 - i\Omega}\right)Y_{\mathrm{L}}^{\mathrm{in}} - \frac{\sqrt{\eta_{\mathrm{c}} - \eta_{\mathrm{c}}^2}}{\kappa/2 - i\Omega}Y_{\mathrm{L}}^{\mathrm{ex}}}_{\text{imprecision noise}}. \tag{6.3}$$

This phase-encoded signal is readily measured interferometrically using balanced homodyne detection as described above. For an ideal laser source, with no excess classical noise, the input quadratures are those of a coherent state, i.e. independent of the amplitude of the probing field. Then eq. (6.3) suggests one can achieve arbitrarily precise displacement measurements by increasing the field-enhanced coupling rate g, proportional to the amplitude of the probing field s_{in}, making the mechanical signal dominate the imprecision noise.

What makes this assertion break down is how the mechanics gets perturbed by the light. The mechanical Langevin equations (5.17c-d) tells us that the momentum of the mechanics gets driven by the radiation pressure force $\propto X_{\mathrm{L}}$, which after a quarter period gets rotated to a perturbed displacement, an effect we call *quantum backaction* noise. This tradeoff between imprecision and quantum backaction noise implies an optimal strength of the probing field, and gives rise to the *standard quantum limit* of displacement measurements.

Detuned probing As we already saw eg. in the discussion of OMIT, a detuned cavity correlates the amplitude and phase quadratures of the light. Thus an intensity-sensitive (*direct*) detection of a detuned probe picks up mechanical information since it partially measures the phase quadrature of the intracavity field.

To describe this more rigorously we first consider this amplitude-phase correlation for an empty cavity. Sticking to the convention of a purely real intra-cavity mean field implies $\bar{Y}_{\mathrm{L}} = 0$, which enforces a detuning-dependent phase-space rotation of the input quadratures by an angle ϕ such that

$$\begin{pmatrix} X^{\mathrm{in}}_{\mathrm{L},\phi} \\ Y^{\mathrm{in}}_{\mathrm{L},\phi} \end{pmatrix} = \underbrace{\begin{pmatrix} \cos\phi & \sin\phi \\ -\sin\phi & \cos\phi \end{pmatrix}}_{R(\phi)} \begin{pmatrix} X^{\mathrm{in}}_{\mathrm{L}} \\ Y^{\mathrm{in}}_{\mathrm{L}} \end{pmatrix}, \quad \phi(\Omega) = \arctan\left(\frac{2(\Delta+\Omega)}{\kappa}\right). \tag{6.4}$$

We can then write the Fourier domain Langevin equations for optical quadratures in a matrix form as

$$\underbrace{\begin{pmatrix} \frac{\kappa}{2} - i\Omega & -i\Delta \\ -i\Delta & \frac{\kappa}{2} - i\Omega \end{pmatrix}}_{A} \begin{pmatrix} X_{\mathrm{L}} \\ Y_{\mathrm{L}} \end{pmatrix} = 2ig \begin{pmatrix} 0 \\ X_{\mathrm{m}} \end{pmatrix} + \sqrt{\eta_{\mathrm{c}}\kappa} \begin{pmatrix} X^{\mathrm{in}}_{\mathrm{L},\phi} \\ Y^{\mathrm{in}}_{\mathrm{L},\phi} \end{pmatrix} + \sqrt{(1-\eta_{\mathrm{c}})\kappa} \begin{pmatrix} X^{\mathrm{ex}}_{\mathrm{L}} \\ Y^{\mathrm{ex}}_{\mathrm{L}} \end{pmatrix}. \tag{6.5}$$

From the input-output relation we find the output quadratures:

$$\begin{pmatrix} X^{\mathrm{out}}_{\mathrm{L}} \\ Y^{\mathrm{out}}_{\mathrm{L}} \end{pmatrix} = -2ig\sqrt{\eta_{\mathrm{c}}\kappa}A^{-1} \begin{pmatrix} 0 \\ X_{\mathrm{m}} \end{pmatrix} + (\mathbb{I} - \eta_{\mathrm{c}}\kappa A^{-1}) \begin{pmatrix} X^{\mathrm{in}}_{\mathrm{L},\phi} \\ Y^{\mathrm{in}}_{\mathrm{L},\phi} \end{pmatrix} - \sqrt{\eta_{\mathrm{c}} - \eta_{\mathrm{c}}^2}\kappa A^{-1} \begin{pmatrix} X^{\mathrm{ex}}_{\mathrm{L}} \\ Y^{\mathrm{ex}}_{\mathrm{L}} \end{pmatrix}. \tag{6.6}$$

Like in the resonant case, we find one term with the mechanical information and imprecision noise terms proportional to the inputs. For clarity and brevity's sake, we explicitly write out how the mechanical displacement shows up in the output amplitude quadrature:

$$X^{\mathrm{out}}_{\mathrm{L}} = 2g\frac{\sqrt{\eta_{\mathrm{c}}\kappa}\Delta}{(\kappa/2 - i\Omega)^2 + \Delta^2} X_{\mathrm{m}} + \text{imprecision noise}. \tag{6.7}$$

For our mechanical memory experiments, we rely on direct detection of a detuned probe since we anyway want the dynamical backaction effects associated with $\Delta \approx -\Omega_{\mathrm{m}}$, in particular the optical broadening Γ_{opt}.

6.2 Feedback Techniques

Conducting a systematic physics experiment requires precise knowledge of the relevant system parameters. Apart from appropriate calibrations, controlling the system parameters is paramount. Since ambient conditions, such as temperature or air pressure, can cause drifts and sudden shocks, such as a dropped screwdriver on the optical table (or even the neighbouring one) or the door to the lab being opened, we actively stabilize many critical parameters of our experiment. To do so we rely on feedback techniques, where the general idea is to measure some signal proportional to the disturbances from a desired value (the *error signal*), and after appropriate filtering and amplification, apply the filtered error signal to the system one wishes to stabilize. These principles are illustrated in figure 6.4. Conventionally the mathematical description of feedback takes place in the Laplace domain, which has the advantage over the Fourier domain of handling transient phenomena. The Laplace domain representation of a time domain function $f(t)$ is

$$f(s) = \int_0^\infty f(t)\mathrm{e}^{-st}\mathrm{d}t. \tag{6.8}$$

Another nice feature is the fact that cascaded systems (such as a controller and a system to control) have a transfer function which is simply the product of the individual transfer functions.

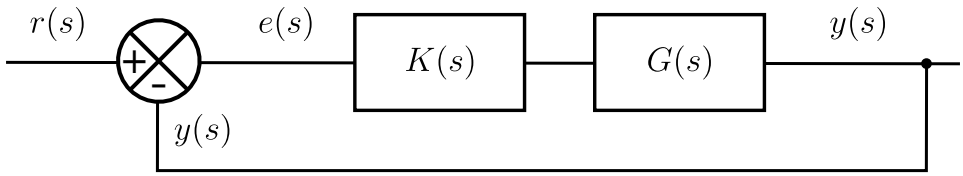

Figure 6.4: Principle of feedback control. The behaviour of a system G can be stabilized with a controller K by feeding the output of the system y back and comparing to a setpoint r, generating an error signal e.

Again referring to figure 6.4, the output $y(s)$ of the system $G(s)$ that we wish to stabilize is subtracted from a setpoint value $r(s)$, thus generating the error signal $e(s)$. The error signal is fed to the controller $K(s)$, whose output is sent to $G(s)$, again producing an output $y(s)$, hopefully closer to the desired value $r(s)$. As a general rule of thumb, a good error signal is anti-symmetric around the desired setpoint.

In the following we outline the basics of the various techniques we employ. The intention is to explain the underlying principles and motivate our experimental setup, rather than provide a comprehensive discussion of feedback and control theory, though more such details can be found in [131]. A more in-depth discussion of our concrete implementations follows in section 8.

6.2.1 Cavity Locking

To stabilize a laser to a specific detuning with respect to a given cavity mode, we rely on three different techniques for deriving an error signal: *slope* locking, *Pound-Drever-Hall* (PDH) locking, and its little brother, *dither* locking, which are discussed in turn. They share the common requirement of generating an optical signal from the cavity response, which is sensitive to excursions around the desired detuning.

Slope Locking Slope locking is the simplest of our cavity-locking techniques. It is applicable to locking away from resonance, but still within the cavity bandwidth $0 < |\Delta| < \kappa$. It simply relies on the fact that the cavity transmission or reflection, for detunings in the appropriate range, has a finite first derivative and thus directly can transduce detuning fluctuations to fluctuations of the reflected or transmitted optical power that readily can be measured.

The advantage of slope locking is its simplicity and low experimental overhead: the error signal comes directly from the photodetector, and only the controller is required (which is always the case for feedback control). On the other hand the simplicity has the drawback that it is not robust against drifts in incident power. In a nutshell, the controller cannot distinguish if the reason for a change in power impinging on the photodetector is due to detuning drift (eg. more or less light being transmitted) or simply to power drift. As such it can be used either as an initial "catching" step in a bigger lock sequence, or for less sensitive applications. Another disadvantage is that slope locking cannot lock on cavity resonance, where the susceptibility is flat.

Pound-Drever-Hall Locking Locking on cavity resonance is quite important for many applications (eg. optomechanical displacement measurements, or maximal transmission through a filter cavity) so we need to go beyond slope locking. Our preferred such method is the Pound-Drever-Hall technique. It requires a means of modulating the frequency (or the phase) of the laser one desires to lock, and relies on the interference between the optical carrier and the modulation sidebands. Typically the modulation is done with an external electro-optic modulator, but directly modulating eg. the laser current also works. We consider an incident flux s_{in}, at an optical frequency Ω_{L}, phase-modulated by small modulation depth $\beta \ll 1$ at a modulation frequency Ω_{mod}:

$$s_{\mathrm{in}} = s_0 \mathrm{e}^{i(\Omega_{\mathrm{L}} t + \beta \sin(\Omega_{\mathrm{mod}} t))} \approx s_0 \left(J_0(\beta) \mathrm{e}^{i\Omega_{\mathrm{L}} t} + J_1(\beta) \left(\mathrm{e}^{i(\Omega_{\mathrm{L}} + \Omega_{\mathrm{mod}})t} - \mathrm{e}^{i(\Omega_{\mathrm{L}} - \Omega_{\mathrm{mod}})t} \right) \right), \tag{6.9}$$

where we applied the Jacobi-Anger expansion and neglected higher harmonics, due to the small modulation depth. Here J_n denotes the n'th Bessel function of the first kind. Directly detecting the reflection of eq. (6.9) off the cavity we wish to lock can be modelled by our Langevin equation and input-output relation toolbox. In this case we neglect the quantum noise and simply write, in the Fourier domain:

$$a(\Omega) = \frac{\sqrt{\eta_c \kappa}}{\kappa/2 - i(\Delta + \Omega)} s_{\text{in}}(\Omega), \tag{6.10a}$$

$$s_{\text{out}}(\Omega) = s_{\text{in}}(\Omega) - \sqrt{\eta_c \kappa} a(\Omega) = (1 - \chi_{\text{cav}}(\Omega)) s_{\text{in}}(\Omega). \tag{6.10b}$$

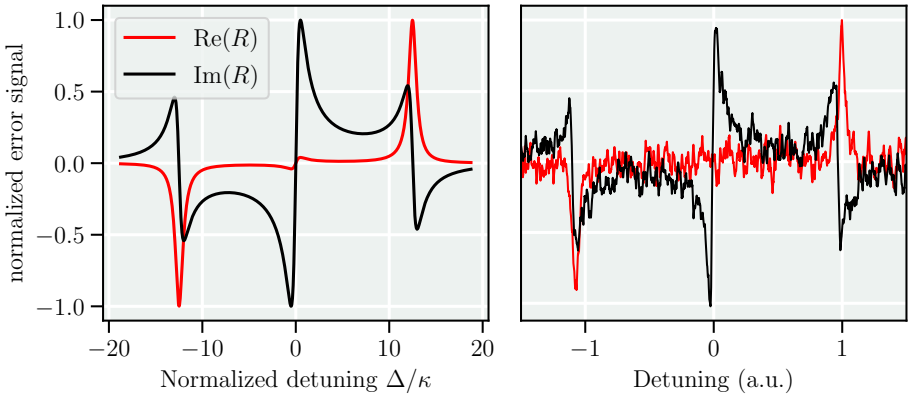

Figure 6.5: Normalized PDH error signal. Left: theory curves according to eq. (6.11) for $\Omega_{\text{mod}} = 12.5\kappa$. Right: Measured error signal for the optomechanical cavity with $\kappa/2\pi \approx 2\,\text{MHz}$ with $\Omega_{\text{mod}}/2\pi = 45\,\text{MHz}$.

Our photodetector is sensitive to $|s_{\text{out}}|^2$. The full calculation of $|s_{\text{out}}|^2$ is fairly verbose, but since we anyway only are interested in frequency components around Ω_{mod}, we only keep these terms. Some algebra then gives

$$|s_{\text{out}}(\Omega)|^2 = 2 s_0 J_0(\beta) J_1(\beta) \Big(\text{Im}\,[R] \sin(\Omega_{\text{mod}} t) + \text{Re}\,[R] \cos(\Omega_{\text{mod}} t) \Big), \tag{6.11}$$

where R is given as

$$R = \big(1 - \chi_{\text{cav}}(\Omega_{\text{mod}})\big)\big(1 - \chi^*_{\text{cav}}(0)\big) - \big(1 - \chi^*_{\text{cav}}(-\Omega_{\text{mod}})\big)\big(1 - \chi_{\text{cav}}(0)\big). \tag{6.12}$$

The real and imaginary parts of the complex reflection coefficient R thus be accessed by demodulating the measured optical signal around the modulation frequency with the appropriate phase, as illustrated in figure 6.5.

Here one sees the imaginary part of R providing a good error signal for resonant cavity locking, essentially probing the derivative of the cavity response. The sensitivity (the slope of the error signal around the setpoint) improves with higher modulation frequency, $\Omega_{\text{mod}} \gg \kappa$, so typically it is desirable to increase this, to a frequency limited by the bandwidth of the rest of the signal processing chain. The error signal is linear roughly in the range $-\kappa/2 < \Delta < \kappa/2$,

which defines the accessible detunings. Apart from the ability to lock resonantly, PDH locking is also less sensitive to drifts in the average laser power, since it is an AC signal. Thus power drifts only change the amplitude of the signal, but not the location of the zero-crossing, which in the end is what we want to stabilize.

Dither locking PDH locking is a powerful technique, but requires a bit of experimental overhead in terms of fast modulation. For less stringent applications, one can alternatively employ *dither* locking, where either the laser or the cavity is modulated at a slow frequency $\Omega_{\text{mod}} \ll \kappa$.

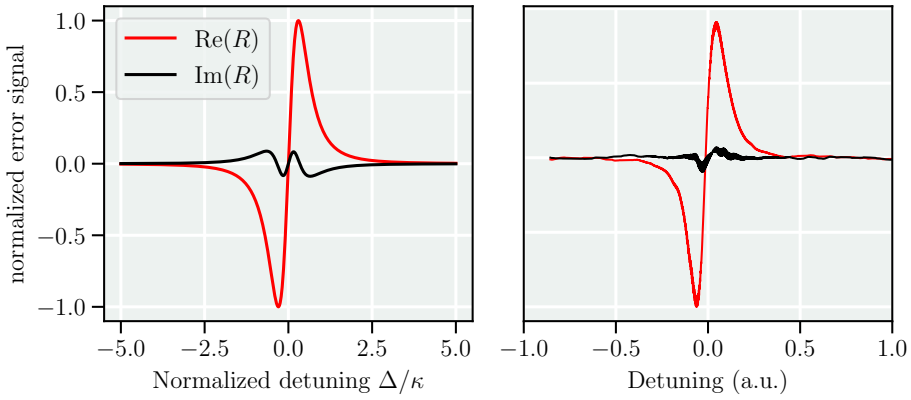

Figure 6.6: Normalized dither locking error signal. Left: theory curves according to eq. (6.11), for $\Omega_{\text{mod}} = 0.125\kappa$. Right: measured data for a cavity with $\kappa/2\pi \approx 1\,\text{MHz}$, $\Omega_{\text{mod}}/2\pi = 30\,\text{kHz}$.

Here the modulation does not manifest as sidebands, but rather a detuning that is periodically scanned back and forth. The slower modulation frequency required practically means piezo actuators in a cavity can do the modulation, thus eliminating a expensive electro-optic modulator. The mathematical framework for PDH locking also applies to dither locking.

In the regime of $\Omega_{\text{mod}} \ll \kappa$ the good error signal is encoded in the opposite quadrature of the PDH case, as seen in figure 6.6. Due to the low modulation frequency, a limitation of dither locking is the correspondingly smaller feedback bandwidth possible.

6.2.2 Frequency-Offset Locking

In the sideband-resolved regime, $\Omega_{\text{m}} \ll \kappa$, stabilizing a laser at the red or blue sideband $\Delta = \pm\Omega_{\text{m}}$ is not possible by any of the above techniques. There are several ways of circumventing this, involving either increasingly complex modulation schemes or using two lasers with a definite frequency difference. We follow the latter approach, locking the cavity on resonance with one laser,

that in turn is locked at a frequency offset from a second laser, whose detuning now can be chosen freely.

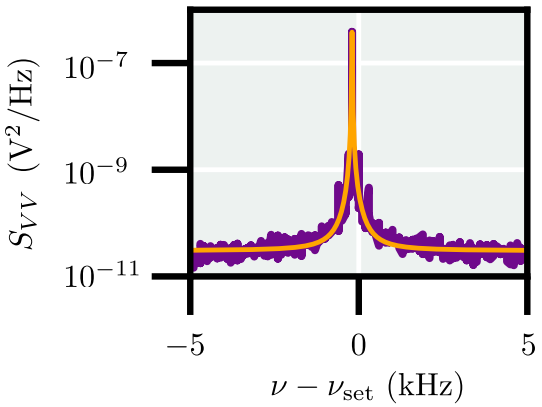

Figure 6.7: Offset-locked beat note. The measured spectrum (purple) is fitted with a Lorentzian (orange) yielding a linewidth $\Gamma_{\mathrm{offset}}/2\pi \approx 2\,\mathrm{Hz}$.

For this lock we derive the error signal from an initial measurement of the beat note of the two lasers. This measurement is done with a high-bandwidth ($\approx 35\,\mathrm{GHz}$) photodiode, and the voltage measured over a $50\,\Omega$ termination is down-mixed to baseband. Sending this downmixed beatnote to a digital phase-frequency detector (PFD) essentially allows us count the difference in fringes between the beatnote and a reference oscillator [132]. Utilizing the phase-response of a delay line can be used to similar effect, where the frequency of the downmixer needs to changed to choose a setpoint [133, 134] The PFD output is now proportional to the frequency difference between our measurement and a setpoint, which is to say an error signal. This error signal is then fed back to the more noisy of the two lasers, effectively stabilizing it at a fixed frequency offset from the quieter one.

An exemplary measurement of the locked beatnote is shown in figure 6.7. We learn that we really can stabilize the lasers well in this way, evidenced by the narrow linewidth of the beatnote $\Gamma_{\mathrm{offset}}/2\pi \approx 2\,\mathrm{Hz}$, limited by the spectrum analyzer resolution.

6.3 Optomechanical Cavity Assembly

Putting anything inside a high-finesse optical cavity is a potentially hazardous endeavour - it is very easy increase optical losses, as a single speck of dust in the wrong place can ruin an otherwise pristine assembly. Since this means cavity assembly can be *very* time consuming to get right, we here report our, dearly bought, assembly procedure.

6.3.1 Handling and Cleanliness Practices

To minimize the risk of dirt contaminating either the membrane, cavity mirrors or the inside of the sample holder, the most important maxim is to do as little handling as possible. In practice this means that the order of operations is important.

The first step is to don the appropriate protection equipment. We wear dust-free nitrile gloves, a hair net and surgical facemask during the assembly process.

Then, collect all the needed tools, such as tweezers and screwdrivers, and clean these. This cleaning is done by a series of sonications, first in acetone and then in isopropanol, for $15 - 20$ minutes each. The cleaned tools can then be stored wrapped in aluminum foil. Clean the sample holder pieces in a similar manner. Instead of aluminum foil, we usually store the cleaned pieces in cleaned plastic boxes until needed.

Next, one should clean the working area thoroughly, which can be done while the tools are sonicated. Tidy the area and remove anything not needed during assembly. Then clean all surfaces by wiping them with isopropanol and lint-free tissues.

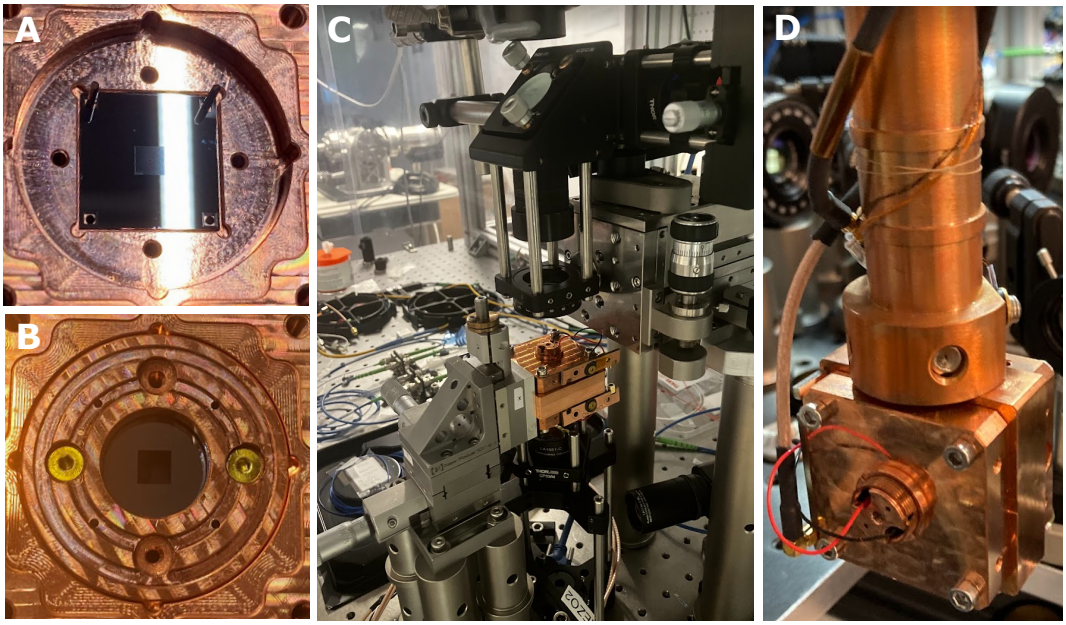

Figure 6.8: Assembly of a membrane-in-the-middle cavity. A: Insertion of alignment rods. In the photograph one sees the membrane placed in the membrane holder piece with two of four alignment rods inserted in the top holes, with the alignment holes visible for the two bottom positions. B: The membrane holder lid is added and partially fixed with two of four screws in place. C: The cavity is transferred to the alignment station, ready for alignment of the cavity mode to the membrane defect. D: A well-aligned cavity is mounted on the cryostat cold finger, ready for experiments.

The first real handling then is to mount the membrane in the membrane holder piece. We pick the membrane up with a Teflon-tipped pair of tweezers and gently place it in the sample holder.

Then we add alignment rods to ensure it stays fixed, cf. figure 6.8a. We found these necessary, since the cryostat we mount the assembled cavity hangs vertically, meaning gravity can pull the membrane down, off the cavity axis, resulting in a different alignment, when transferred from the assembly station to the experiment (compare fig. 6.8C-D). The alignment rods are simply short segments of welding wire, with a gauge that snugly fits the alignment holes in the membrane holder piece.

To hold the membrane in place we first add an o-ring before adding the lid of the membrane holder, which is tightened in place with four screws cf. figure 6.8b. With the membrane in place, it is time to add the first cavity mirror. Since we work with a plano-concave cavity we first add the flat mirror, so that we can test whether the flat mirror and the membrane are parallel.

6.3.2 Parallelity

To gauge the angle between the plane of the membrane and that of the flat mirror surface, we manually scan a focused laser spot in two directions across the membrane defect, and record the reflected DC optical power. A too large angle will firstly and most benignly lead to reduced optomechanical coupling, since the cavity mode now only probes a projection of the mechanics. More problematically, a misaligned membrane can couple different cavity modes by scattering out of a TEM_{00} into a higher order mode with lower longitudinal mode number, rendering locking close to impossible. An example of this mode-coupling phenomenon is shown in figure 6.10. Here we are sweeping a phase-modulated laser across cavity resonance, giving rise to peaks associated with the carrier and two sidebands, as seen in the transmission measurements (see fig. 6.10), that are vertically offset for clarity.

As we increase the voltage applied to one of the cavity piezos, we see two effects. First, the resonance moves, as expected from a different cavity length, but also the peaks are distorted. As we increase the piezo voltage (from orange through purple to blue), the hybridized peak changes from being dominated by the high-frequency partner, to roughly equal in height, over to dominated by the low-frequency peak.

Clearly such a cavity is problematic to work with, so here we describe our process for quantifying the tilt of the membrane. From the period of the interference pattern one can then extract the angle between the two reflective surfaces as

$$\theta = \arctan\left(\lambda/\Delta x\right), \tag{6.13}$$

where Δx is defined in figure 6.9. Ideally the tilt angles should then be as small as possible. We rely on a simulation of how a given tilt angle induces

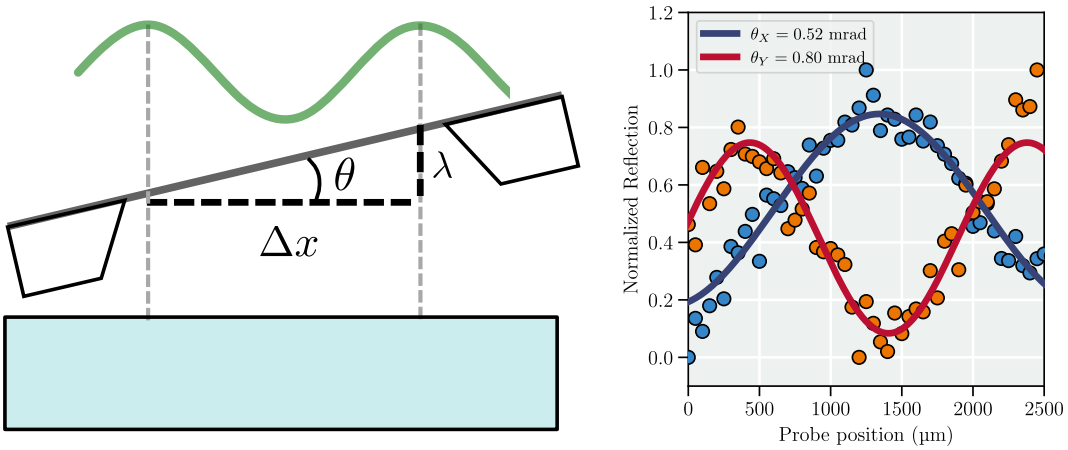

Figure 6.9: Measuring the membrane tilt angle θ. Left: Sketch of the principle. When scanning a focused spot across the open half-cavity comprised of the membrane and flat mirror, one can observe an interference fringe (illustrated in green). The period of this fringe is determined by θ according to eq. (6.13). Right: Measured scans along orthogonal X, Y directions in purple and green, with sinusoidal fits. We extract Δx from the period of such fits.

optical mode-coupling (explained in appendix B), which tells us that angles $\theta < 1\,\text{mrad}$ are adequate. A measurement of a tolerable level of tilt is shown in figure 6.9 (right).

In practice we found the best way of ensuring good parallelity is a thorough cleaning regimen and relying of the flatness of the sample holder pieces, since it is hard to manually adjust at the sub-mrad level.

6.3.3 Transverse Alignment

The final step is then to close the cavity and properly align the cavity axis to the membrane defect by manipulating the position of the curved mirror. Before adding the curved mirror we align the back-reflected light, so that it reflects off the center of the membrane defect and couples back into the optical fiber it is launched from. Then we know that the beam is orthogonal to the flat mirror, and centered where we want it. Since our working wavelength $\lambda \approx 1550\,\text{nm}$ is not visible on a CCD camera and require expensive, specialized cameras, either with a phosphorus-based coating or InGaAs detector, we instead inject a second laser through the same fiber. The wavelength of this laser $\lambda \approx 1310\,\text{nm}$ is chosen low enough such that a focused spot shows up on the CCD camera, and long enough that it is not too different from our actual working wavelength.

With the incoming light well-aligned we fix it and do not touch it for the remainder of the alignment procedure. Rather we translate the piece holding the curved mirror, with the first goal to see any cavity modes. When modes show up when we scan the cavity length, we try to land on the TEM_{00} mode that we want to work with. With the proper mode identified, the task is now

to fine-tune the mirror position, so that the mode lands on the middle of the defect. Our approach for gauging this alignment is from the interference that shows up in reflection, when one scans fast over a cavity resonance. For a fixed slew-rate, the magnitude of the over-shoot above the off-resonant DC level is then a monotonic function of the cavity linewidth.

If we disregard the small $\approx 10\%$ modulation due to the $2kz$ position, a bigger "overshoot" spike tells us we have a more narrow cavity linewidth, cf. figure 6.11 for exemplary measurements.

This interference phenomenon can be understood in terms of the Doppler effect [135, 136]: if the cavity resonance frequency is changed on a time-scale comparable to κ, the intra-cavity field that used to be resonant can now beat with the newly resonant light, giving rise to a chirped interference fringe superimposed on the usual reflection dip.

When we find an overshoot comparable in magnitude to the dip we can start to carefully tighten the screws of the curved mirror holder to the membrane holder, taking care not to misalign by uneven tightening.

Penultimately we can then measure the cavity linewidth using a phase-modulated laser, using the sideband for frequency calibration of the time axis of the scans (see section A.2). In this measurements we reduce the slew rate such that we only measure a clean Lorentzian that can be robustly fitted. If we do not end with an acceptably narrow cavity, we can iterate the procedure

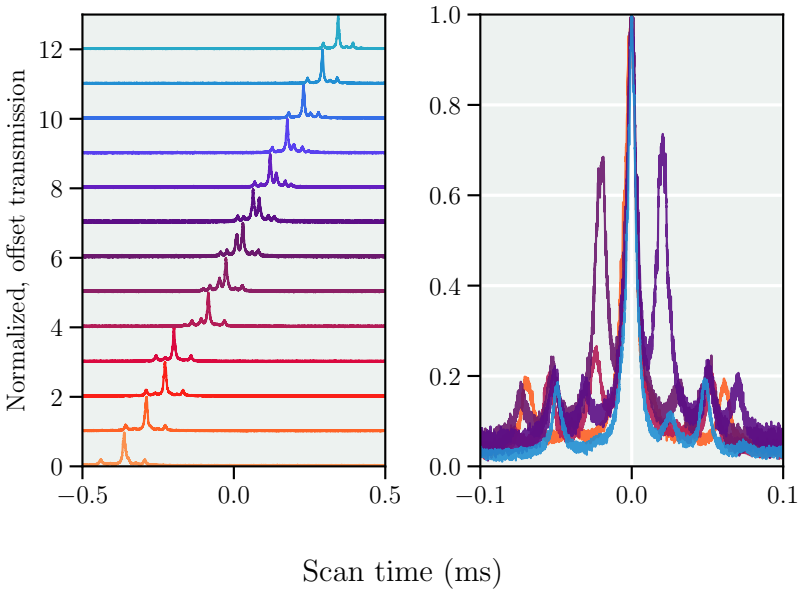

Figure 6.10: Transmission of a misaligned MIM cavity. Left: Cavity transmission scans for a range of piezo bias voltages, different scans vertically offset for clarity. The small sideband (see e.g. first and last traces) are externally applied with a phase modulator, driven at $\Omega_{\mathrm{mod}}/2\pi = 30\,\mathrm{MHz}$. Right: Zoom-in on a few selected scans without offset, highlighting the split resonance.

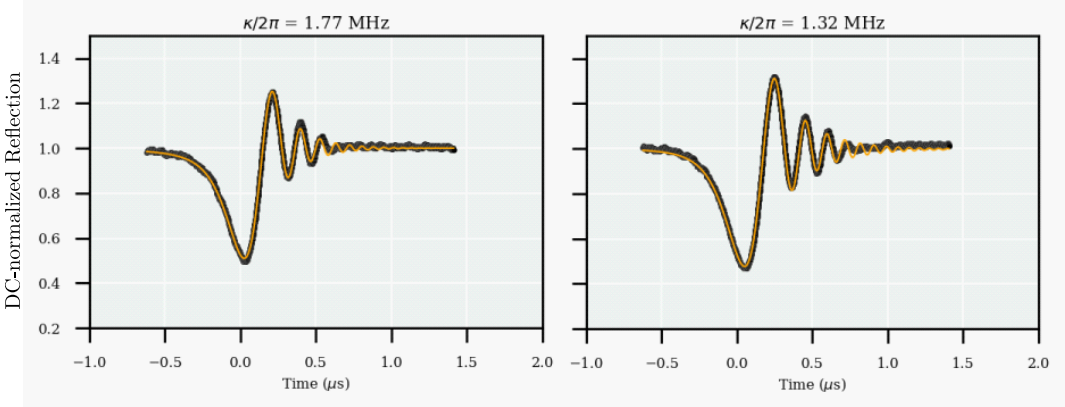

Figure 6.11: Doppler-interference in reflection. We plot two scans over the same cavity resonance, left for a moderately aligned cavity mode and right for a well aligned mode, evidenced by the higher overshoot, ≈ 1.3 compared to ≈ 1.2 relative to the DC level and narrower linewidth.

for the curved mirror until we do.

As a last check, once we find a nice and narrow linewidth, we can turn the 1310 nm alignment laser on again and use it as a proxy for the cavity mode position relative to the membrane. Figure 6.12 illustrates this, showing a white-light image with the 1310 nm spot reasonably centered on the defect.

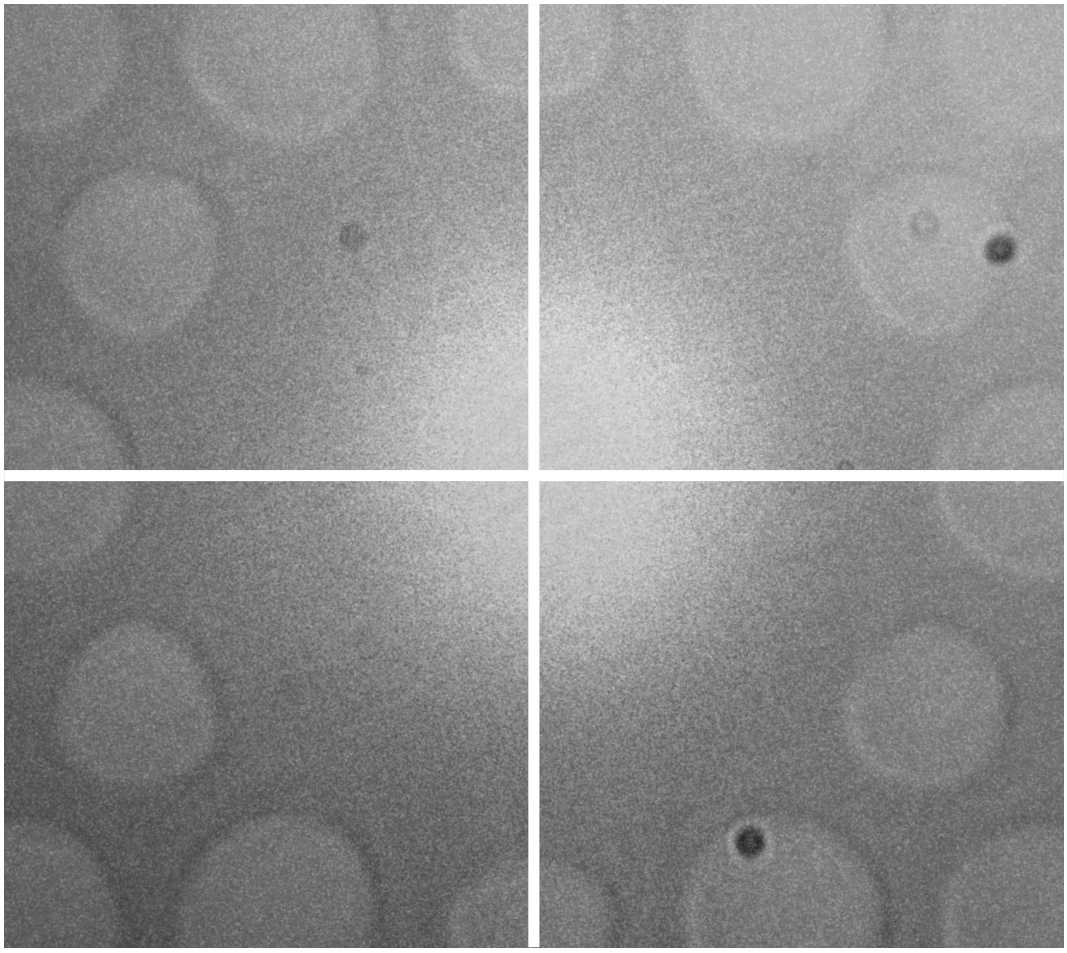

Figure 6.12: White light image of the membrane inside a cavity after the transverse alignment procedure. The central bright spot is the 1310 laser. The black specks are on the imaging optics, not the membrane or cavity mirrors.

7 Mechanical Characterizations

"What's the frequency, Kenneth?"

R.E.M.

In this section we report on different studies of mechanical resonators. These different investigations are all compilations of data for many membranes, characterized interferometrically as described in section 6.1.1. Typically we record frequency and Q factor for a particular mode, occasionally augmented by spectral measurements.

7.1 TED Investigation

As mentioned in section 3.3.2, theoretical considerations suggests that thermoelastic damping is not far off from limiting our Q factors. Therefore we fabricated a range of membranes with the intention of making TED more apparant. To this end, we made thick $h \approx 250\,\mathrm{nm}$ membranes, to move the thermalization rate $1/\tau_{\mathrm{TED}}$ down closer to Ω_{m}. Fabricating membranes with decreasing lateral size, and thus increasing frequency, also should bring the product $\Omega_{\mathrm{m}}\tau_{\mathrm{TED}}$ closer to unity.

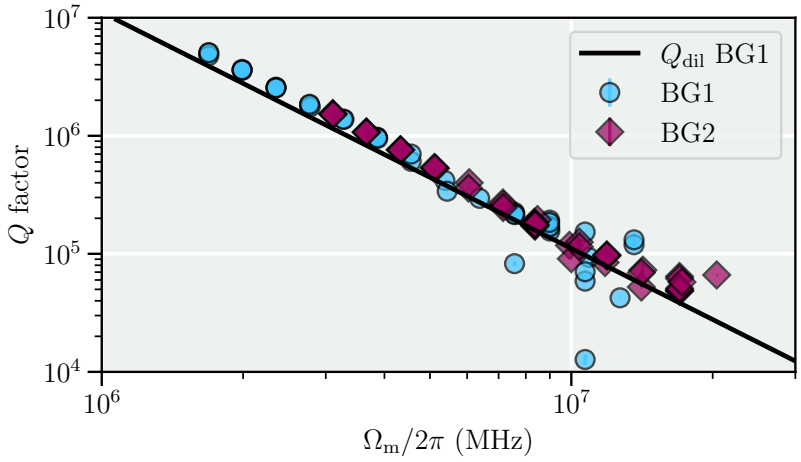

Figure 7.1: Q factor for $h \approx 250\,\mathrm{nm}$ thick membranes. We record Q factors for first bandgap (teal circles) and second bandgap (burgundy diamonds) for 51 membranes, varying the lateral membrane size. The measurements exhibit good agreement with a dissipation-dilution model (solid black).

For this investigation, we used generation 3 dahlia membranes, that have localized modes in two bandgaps. Over 51 samples with varying lateral size, we measured Q factors for the two radially symmetric modes.

The result of the measurements are reported in figure 7.1. The teal circles are the Q factors measured for the first bandgap mode, and the burgundy diamonds are for the second bandgap mode. Remarkably, the measured Q-factors are largely consistent predictions for a simulated dilution factor (indicated in black) across decade in frequency, for both modes.

The model is derived from the expected scalings for soft-clamped membranes, i.e. [74]

$$Q(h, L) = D_Q(h, L)Q_{\text{int}}(h), \tag{7.1a}$$

$$D_Q(h, L) = D_{Q,0}\left(\frac{L}{L_0}\right)^2\left(\frac{h_0}{h}\right)^2, \tag{7.1b}$$

where the dilution factor D_Q is rescaled from an achoring simulation giving $D_{Q,0} = 75 \times 10^3$. We reiterate that the approximately linear increase of $Q_{\text{int}}(h)$ with higher thickness (and thus less prominent surface loss), modifes the overall Q factor scaling to $Q \propto L^2/h$.

Encouragingly, the measurements are well-explained solely by dissipation dilution, and thus seemingly not limited by thermoelastic damping. For the theoretically inclined reader, more details of TED in dissipation-diluted soft-clamped membranes is given in [119].

7.2 Low-mass String Resonators

As already hinted in section 4, the design of phononic crystal membranes is fairly versatile. Here we present an effort towards low-mass devices, with a string, rather than a membrane embedded in a phononic crystal. Such low-mass devices are interesting from a sensing perspective, due to their reduced thermal noise $\propto m_{\text{eff}}$.

Our study of phononic crystal string resonators has been a long and meandering investigation, and as such has been partially reported on in my Master's thesis [130] and the Bachelor's thesis of Simon Krarup Steensen [137]. In the following we collect and summarize all our string-related findings.

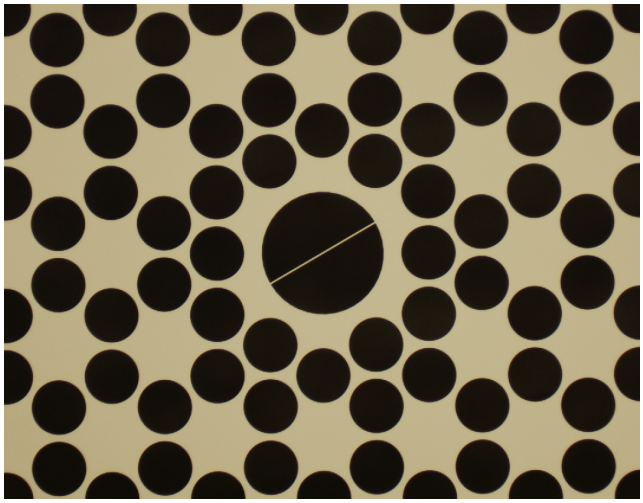

Figure 7.2: Soft-clamped string resonator. An exemplary 1 µm thin ribbon-like string crosses the central big hole where the membrane-like defect usually is. Micrograph courtesy of Yeghishe Tsaturyan.

This idea of embedding a string is shown in practice in figure 7.2, showing a micrograph of a fabricated device, the string being 1 µm wide.

The first characterization step is to model and measure the spectral properties. The band diagram and eigenmodes are simulated in COMSOL (see 4), the band diagram being shown on the left of figure 7.3. We then proceed to measure thermally driven mechanical noise spectra, with a spectrum averaged over many probing positions shown in figure 7.3 right. In the measurements we clearly see the bandgap, evidenced by a greatly suppressed mechanical density of states, and a dense "forest" of modes outside it.

The five peaks inside the bandgap are all well understood: the black peak is an externally injected piezo calibration tone, and the A-D labelled red peaks are the same mechanical modes we find in simulation (cf. fig. 7.4).

Using the raster-scanning modality of one of our characterization interferometers [128], we image the displacement profiles of the modes A-D, as shown in figure 7.4. The excellent agreement between measurements and simulations

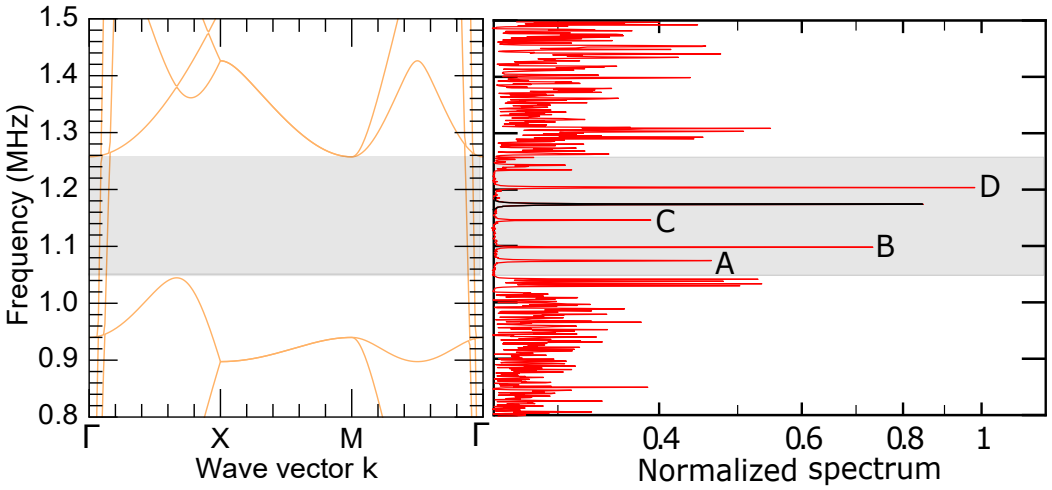

Figure 7.3: Simulated Band diagram and measured normalized thermal spectrum of a string resonator. The gray shaded area indicates the bandgap. Inside the bandgap five peaks are apparent. Four are mechanical modes, labelled A-D, and the last (black) is an injected calibration tone. The shown spectrum is an average of spectra acquired over many probing positions (cf. fig. 7.4).

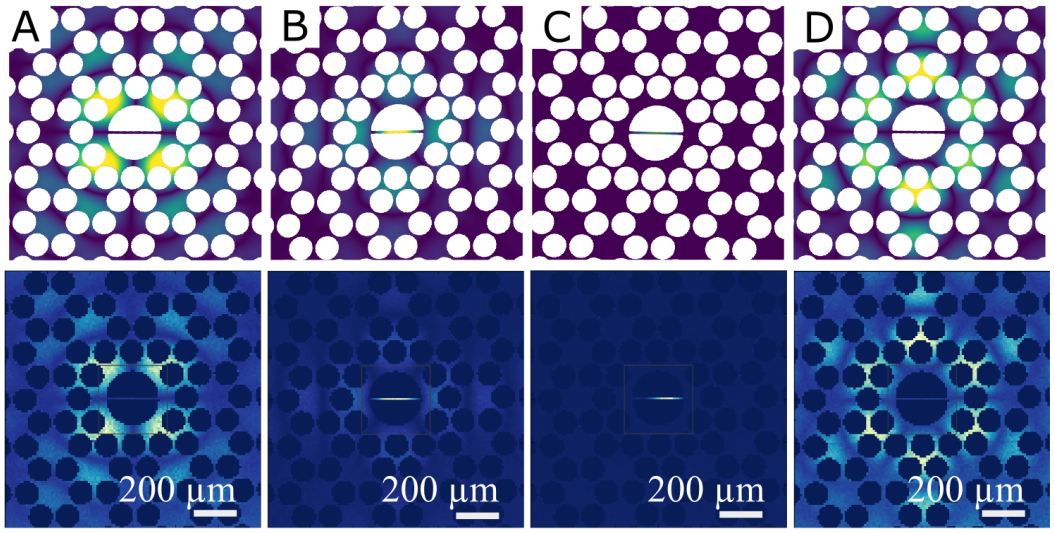

Figure 7.4: String modeshapes. The top row shows simulations, with corresponding measurements below, of the modes inside the bandgap, sorted by frequency.

allows us to hone in on the fundamental string mode, which is the second mode from the lower bandgap edge. The ringdowns and Q factors in the following are always of this string fundamental. Additionally the corroboration lends trust to our simulation techniques in general; if they predict a mode at given frequency, we seemingly can measure them in fabricated devices.

The Q factor and frequency for all the measured devices is shown in figure

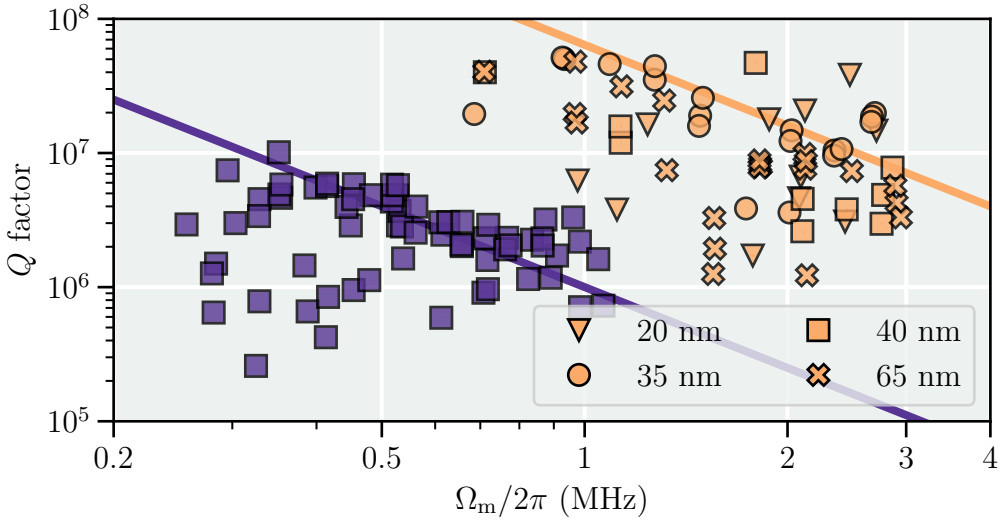

Figure 7.5: Summary of string Q factors. In orange we show samples fabricated from SiN films with our usual high stress $\bar{\sigma} \approx 1.27\,\mathrm{GPa}$, while purple represents low stress samples with $\bar{\sigma} \approx 160\,\mathrm{MPa}$. We measured samples of varying thickness, indicated by the marker type as explained in the legend. The solid lines are $Q \propto 1/\Omega_m^2$ soft-clamping guides to the eye, offset by a factor $\bar{\sigma}_{high}/\bar{\sigma}_{low}$. The measurements of 20 nm and 35 nm thick samples are reported in [137].

7.5. We fabricated samples with high and low pre-stress, $\bar{\sigma} \approx 1.27\,\mathrm{GPa}$ and $\bar{\sigma} \approx 160\,\mathrm{MPa}$, shown in orange and purple respectively. The various sample thicknesses are denoted by different marker types, and explained in the legend of fig. 7.5. The data shows an indication of the expected soft-clamping scaling $Q \propto 1/\Omega_m$, though there is a fair level scatter. This is partially explained by the different thicknesses, since $Q \propto 1/h$ for soft-clamped devices.

We normalize out the thickness dependence by plotting $Q \times h$ as shown in figure 7.6, which does reduce the observed scatter, though not eliminate it entirely. Since we still observe scattered Q factors, we investigated if it could be explained by variations in the deposition stress.

To check this we compare mechanical frequencies against the lattice constant a for the measured devices. Here one expects a $\Omega_m \propto \sqrt{\bar{\sigma}}$ (cf. eq. 3.16). This is displayed in figure 7.7, where we observe a greater degree of consistency than for the Q factors. From this observation we conclude that we can trust the film stress, and that the scatter in the Q must be due to factors.

In figure 7.8 we summarize geometric scalings of our string resonators. The Q factors are scaled by h/a^2 and the frequencies by a, to take out the previously discussed geometric dependence [74], shown in figure 7.8 left. As expected the measurements fall into two well-demarcated clusters, separated by the stress, highlighted by the histograms of geometry-normalized Q factors

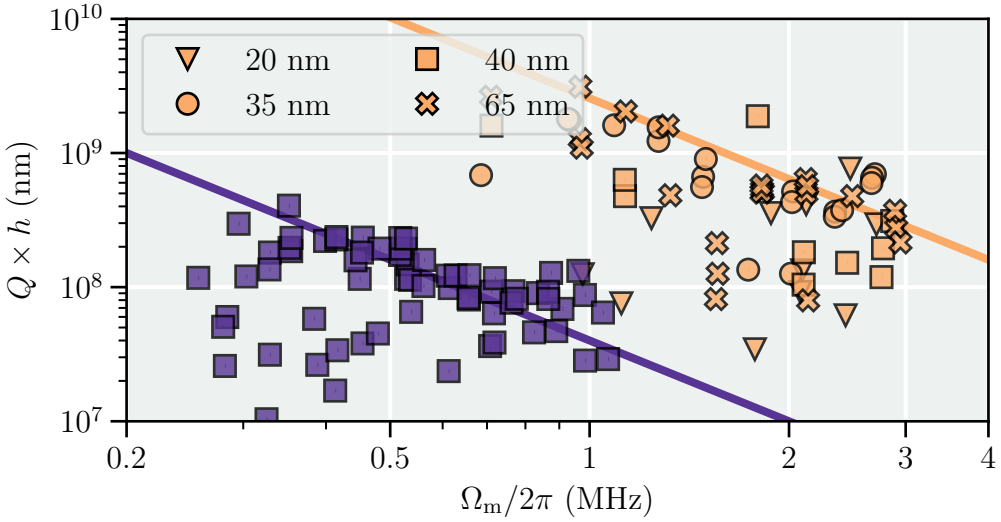

Figure 7.6: $Q \times h$ for string resonators. To better compare devices of different thicknesses, we account for the expected $Q \propto 1/h$ scaling by plotting $Q \times h$, rather than Q. The solid guiding lines are still indicate $\propto \Omega_m^{-2}$ scaling and offset by the same factor $\bar{\sigma}_{high}/\bar{\sigma}_{low}$.

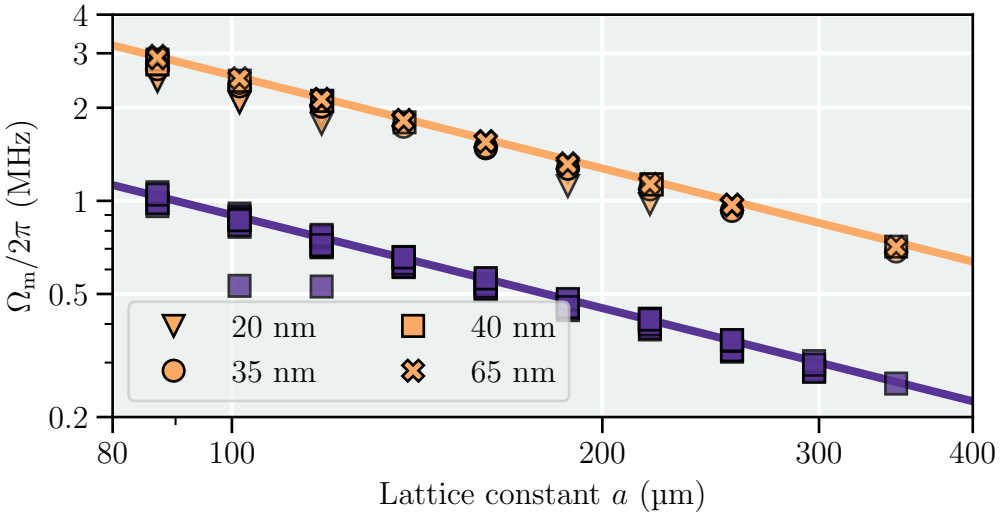

Figure 7.7: $\Omega_m/2\pi$ against a. We plot the mechanical frequencies versus the lattice constant a of each sample, observing very self-consistent frequencies at each a. The guidelines indicate $\Omega_m \propto 1/a$ and are offset by a factor $\sqrt{\bar{\sigma}_{high}/\bar{\sigma}_{low}}$.

in figure 7.8 right. Still the scatter in Q-factors for the high-stress samples is apparent from the large standard deviation, while the low-stress samples however seemingly more well-behaved. The observation that our devices tend

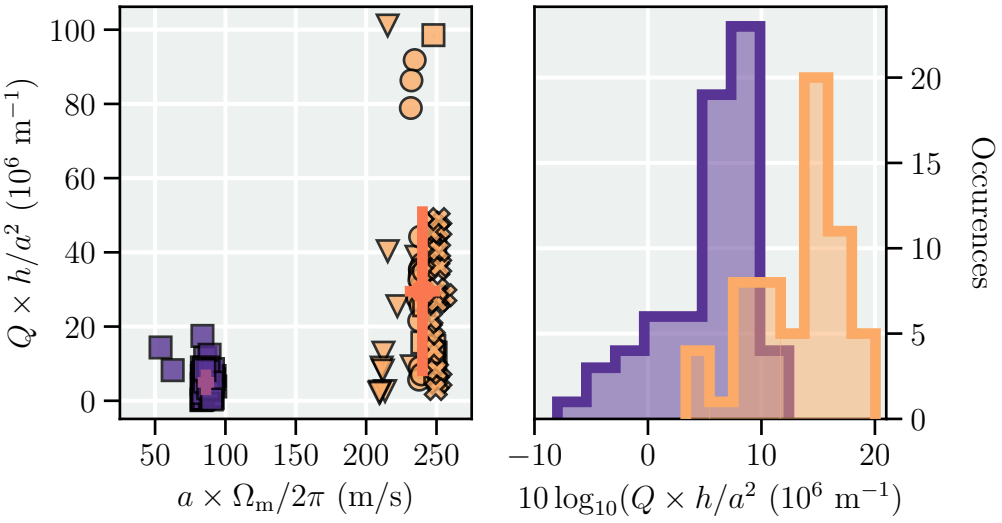

Figure 7.8: Geometric scalings of string resonators. Left: We plot $Q \times h/a^2$ against $a \times \Omega_m/2\pi$, collapsing the measurements into two domains, separated by $\bar{\sigma}$. The overlaid crosses represent the means and standard deviations of the low- and high-stress samples. Right: Histograms of the geometry-normalized Q factors.

to follow the scalings expected for soft-clamped resonators, yet retain a large Q scatter is a little puzzling.

One speculative hypothesis that could explain this observation is that the more "directional" nature of the string mode, compared to a radially symmetric membrane mode, might lead to a longer decay length that in turn implies the risk of insufficient suppression of the mode at the resonator-substrate interface. If this is the case, one would expect to suffer more from clamping losses (see section 3.3) which is a well-known source of scattered Q factors [115].

We attempted to study this in two ways: firstly the defect design was slightly modified such the string mode was less confined to the string, by changing the fillet-radius where string is anchored to the phononic crystal, and secondly to try a larger phononic crystal with more unit cells.

In figure 7.9 we show the results of varying the size of the phononic crystal. For a fixed lattice constant, we vary the number of unit cells. Despite the sparsity of the data, an overall trend of Q increasing with the number of unit cells is observed. From the data we cannot determine an optimal number of unit cells, but certainly we can conclude that the usual 8 unit cells is not sufficient, as there still is large scatter for 10, while 16 unit cells almost gives an order of magnitude increase in Q. Since 8 unit cells is enough to get consistent Q's for membranes [74], we stick with the hypothesis that the string mode shape is not sufficiently suppressed at the substrate interface.

To further investigate our hypothesis, we redesigned the string to make the mode less localized in the string itself, by doubling the width of the string. In figure 7.10 we show ringdown measurements of the less localized design, for $h = 20\,\mathrm{nm}$ thickness. The increase in Q-factor is striking: at a frequency of $\Omega_\mathrm{m}/2\pi = 1.573\,\mathrm{MHz}$ we measure $Q = 132.9(8) \times 10^6$, compared to the $Q \approx 40 \times 10^6$ for the previous design at the same frequency.

Proceeding with this new design in the pursuit of a mechanical resonator with low thermo-mechanical noise, we placed the same sample shown in figure 7.10 in a cryostat (see [129] for details on the setup). The thermo-mechanical noise defines a noise-floor for how weak signals the resonator can sense. To this end, reducing the temperature is beneficial in two ways. Firstly the thermal noise is itself proportional to temperature and secondly the mechanical Q also increases at low temperature.

Such low-temperature ($T \approx 12\,\mathrm{K}$) ringdown measurements are shown in figure 7.11. We observe an increased mechanical quality factor of $Q = 634(20) \times 10^6$, a factor ≈ 5 increase over the room-temperature measurement. To estimate a force sensitivity of our measured device, we need a value for the effective mass, cf. eq. (3.43). We rely on simulations for this, and thus need to take the extracted value with a grain of salt. From simulations of displacement profiles, we can numerically evaulate the effective mass. Since this is not a measured quantity, we assume a 30% errorbar on the mass.

The thermalization of the string with the cryostat is also not well-quantified. We did not conduct thorough mechanical thermometry, so again we assume a conservative precision of measured temperature, taking a 3 K uncertainty. The uncertainty on Γ_rm is calculated by standard error-propagation of the standard

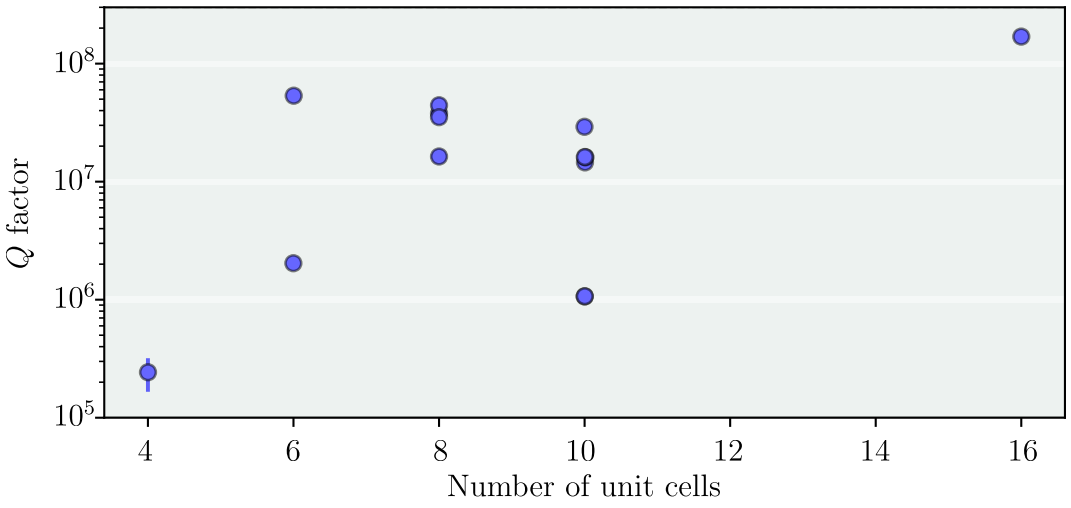

Figure 7.9: Q factor for varying number of unit cells. For a fixed lattice constant, we measure Q factors for an increasing number of phononic crystal unit cells, 8 being the standard value. Reformatted reproduction of figure 7.5 from [130].

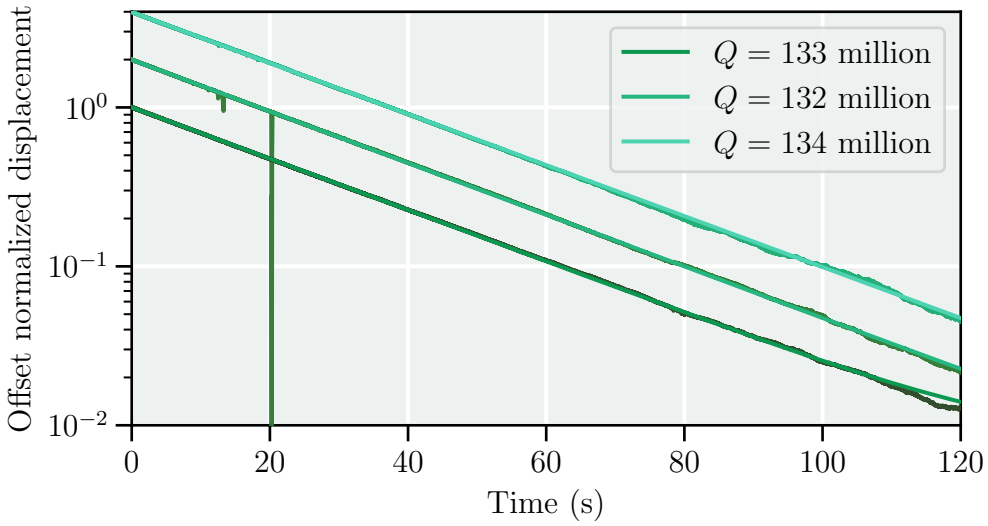

Figure 7.10: Room-temperature ringdown of the less localized string design for a $\Omega_m/2\pi = 1.573\,\mathrm{MHz}$. Normalized ringdowns of the string mode, offset vertically for clarity, with exponential fits to get Q. The noise spike at 20 s is due to the auto-relock of the interferometer.

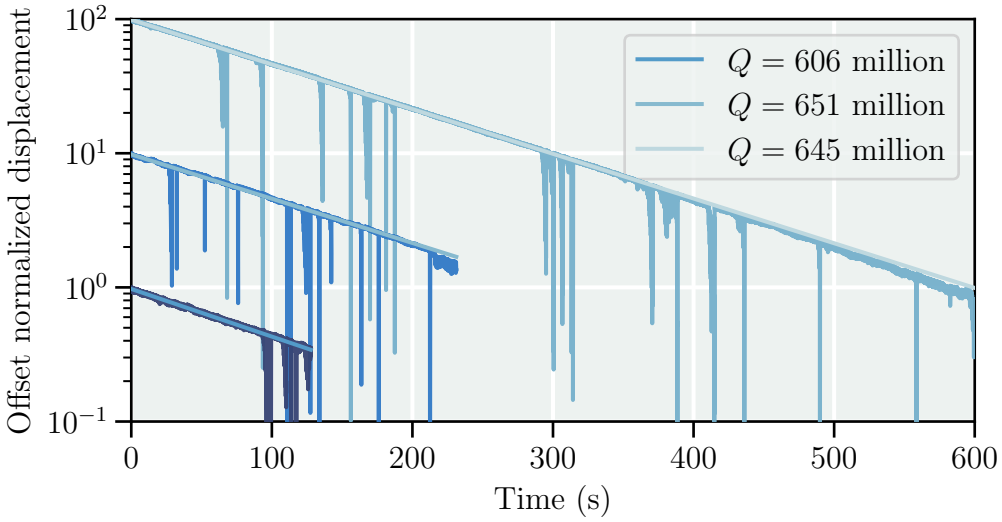

Figure 7.11: Cryogenic string ringdowns. Normalized ringdowns of the string mode in a cryogenic environment, offset vertically for clarity. Each measurement is fitted with an exponential decay from which we extract Q. The noisy interruptions in the measurements stems from the interferometer re-locking.

deviation of the Q measurements. In the end we land on

$$\sqrt{S_{FF}} = \sqrt{4k_B T \Gamma_m m_{\mathrm{eff}}} = 770(290)\,\mathrm{zN}/\sqrt{\mathrm{Hz}}. \tag{7.2}$$

Quantity	Value
m_{eff}	$230(70)\,\mathrm{pg}$
T	$12(3)\,\mathrm{K}$
$\Gamma_{\mathrm{m}}/2\pi$	$2.5(5)\,\mathrm{mHz}$
$\sqrt{S_{FF}}$	$770(290)\,\mathrm{zN}/\sqrt{\mathrm{Hz}}$

Table 4: Estimated force sensitivity of a cryogenic string. See text for explanation of uncertainties.

Based on the calculation detailed in eq. (7.2) and table 4, we cannot conclude that we observed a sub-aN force sensor, partially because this is an inferred value and not a measured force noise and partially due to the large uncertainty, stemming mainly from the temperature and effective mass, contributing roughly equally to the uncertainty on $\sqrt{S_{FF}}$.

7.3 High-frequency, Large Defect Membranes

In the pursuit of a sideband-resolved optomechanical system, we modifed the defect design to on the one hand increase the mechanical frequency and the other to simultaneously increase the physical size of the defect, to mitigate to potential for excess optical losses due to clipping.

These two design goals might seem contradictory at first glance (larger objects tend to have lower frequencies), but we have two knobs to turn. Firstly for a highly stressed and perforated membrane, geometry is not the full story. Due to the perforations, there will be local variations in the stress field, eg. the tethers pulled taut by neighbouring pads, cf. figure 4.6. Secondly, we have learned that we can work with higher order modes in a higher bandgap. Here we are still paying the price of a reduced acoustic wavelength, and thus being more susceptible to mode-matching effects (cf. figure 5.6), but gaining a factor ≈ 2 in frequency for the same defect size.

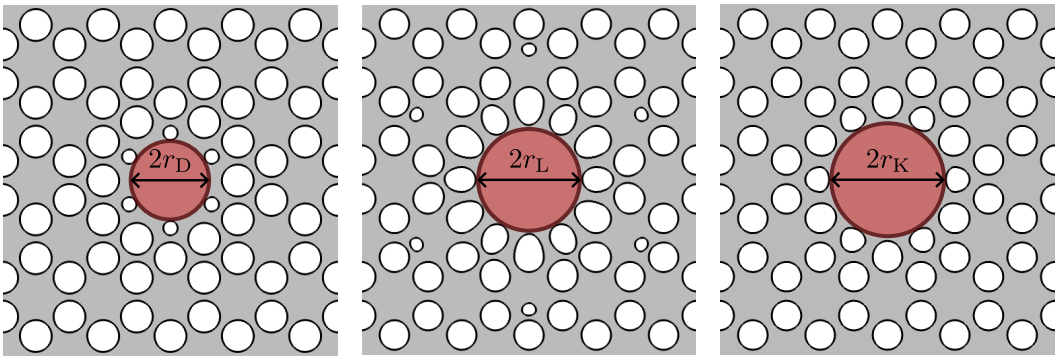

Figure 7.12: Large working area defect designs. From left to right we show the defects of a generation 2 Dahlia, the generation L design, and the generation K. Overlaid on each is the largest circle that can be inscribed on the defect before touching a hole, defining the defect sizes. Relative to the Dahlia design, generation L is larger by a factor $r_{\mathrm{L}}/r_{\mathrm{D}} \approx 1.28$, and for generation K $r_{\mathrm{K}}/r_{\mathrm{D}} \approx 1.42$.

We explored both approaches, and call the new designs generation "L" and generation "K" membranes respectively, with the defects of these designs shown in figure 7.12, with the generation 2 Dahlia design for reference. We learn that for the same lattice constant, the two new designs encouragingly have defects with radii larger by factors $r_{\mathrm{L}}/r_{\mathrm{D}} \approx 1.28$ and $r_{\mathrm{K}}/r_{\mathrm{D}} \approx 1.42$ respectively. With promising new designs, characterize them in terms of Q and Ω_{m}. In figure 7.13 we plot ringdown measurements for the first and second bandgap modes of a generation K membrane, in green and purple respectively, both exhibiting $Q \geq 10 \times 10^8$.

We summarize the performance of the new designs, by showing Q and Ω_{m} for membranes fabricated according to both designs, with a thickness $h = 20\,\mathrm{nm}$ and varying lateral size in figure 7.14 . The green diamond markers are

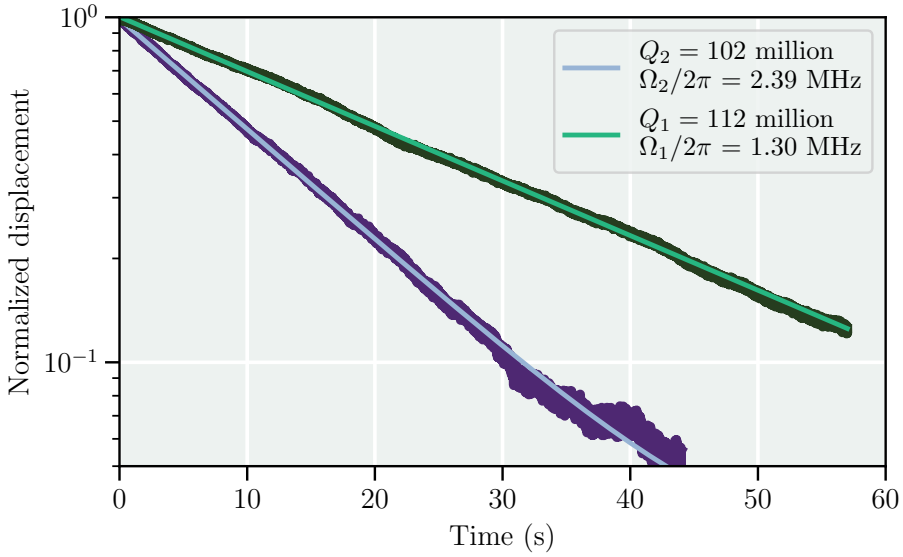

Figure 7.13: Generation K ringdowns. In green and purple respectively, we plot ringdown data with exponential fits (dark and light hues) from which we extract Q factors.

the generation "L" design, showing typical $Q > 100 \times 10^6$ around $\Omega_m/2\pi \approx 1.6\,\mathrm{MHz}$. The circle markers are the generation "K" design, with burgundy points representing the first bandgap mode and blue the second. In terms of Q factor, the first bandgap mode performs the best. Interestingly the second bandgap mode is however not much worse, in terms of Q factor. If one imagines re-scaling a membrane to reach a desired higher mechanical frequency, the second bandgap mode will have a higher Q for the same frequency, since $Q \propto \Omega_m^{-2}$ for soft-clamped resonators.

This is seen more clearly when considering the Qf product, i.e. the product of the Q factor and mechanical frequency $\Omega_m/2\pi$. We present the Qf products for our measured devices in figure 7.15, with the same design encoding as in figure 7.14. Here the advantage of the second bandgap mode of the "K" design is apparent. It consistently achieves simultaneously higher mechanical frequency Ω_m and Qf product.

Honing in on the "K" design, we can also illustrate the advantage provided by the second bandgap mode by plotting the ratios of Q's and frequencies, as in figure 7.16. Here we have removed low Q outlier modes with $Q < 10 \times 10^6$, (these are few but enough to bias averages considerably, cf. figure 7.14). Along with the Q and Ω_m ratios (teal circles), we indicate the mean and twice the standard error on the mean for each, with the black dashed lines and dark blue cross. We observe very consistent frequency ratios $\Omega_2/\Omega_1 = 1.8380(8)$ and reasonably consistent Q ratios $Q_2/Q_1 = 0.70(5)$. At this point it is also instructive to compare our observed scaling quantitatively to the expectations

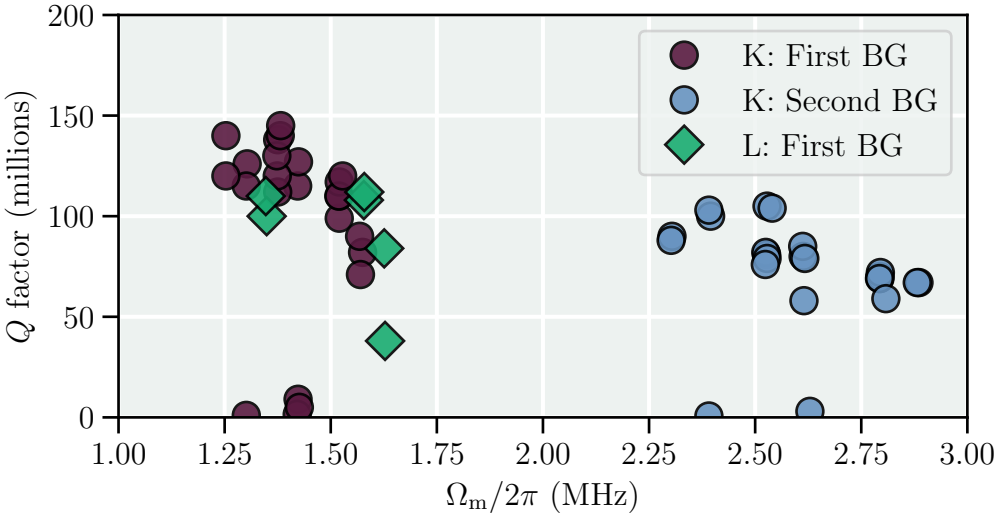

Figure 7.14: Q factors versus mechanical frequency Ω_m for large working area, high-frequency membranes. The circular points are the "K" design, optimized for the second bandgap mode with burgundy indicating the first bandgap mode and blue the second bandgap mode. The "L" design, optimized for the first bandgap is shown as green diamonds.

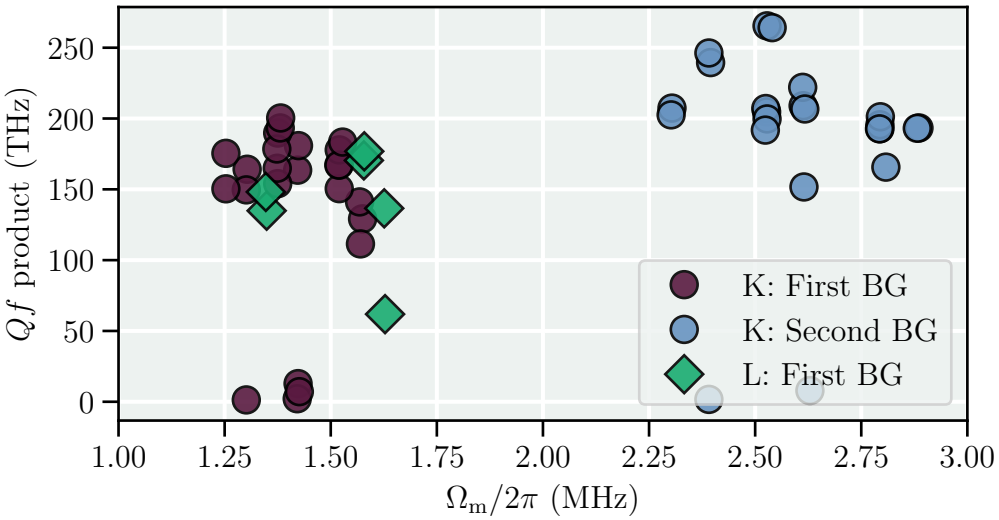

Figure 7.15: Qf products for large working area, high-frequency membranes. The circular points are the "K" design, optimized for the second bandgap mode with burgundy indicating the first bandgap mode and blue the second bandgap mode. The "L" design, optimized for the first bandgap is shown as green diamonds.

from rescaling a soft-clamped membrane. For a soft-clamped mode, $Q^{(\mathrm{s.c.})} \propto \Omega_{\mathrm{m}}^{-2}$, implying

$$Q_2^{(\mathrm{s.c.})} = \left(\frac{\Omega_2}{\Omega_1}\right)^{-2} Q_1^{(\mathrm{s.c.})}, \tag{7.3}$$

For our observed frequency ratio, the soft-clamping scaling only permits $Q_2/Q_1 = (1.838)^{-2} \approx 0.296$, more than a factor two worse than our observations.

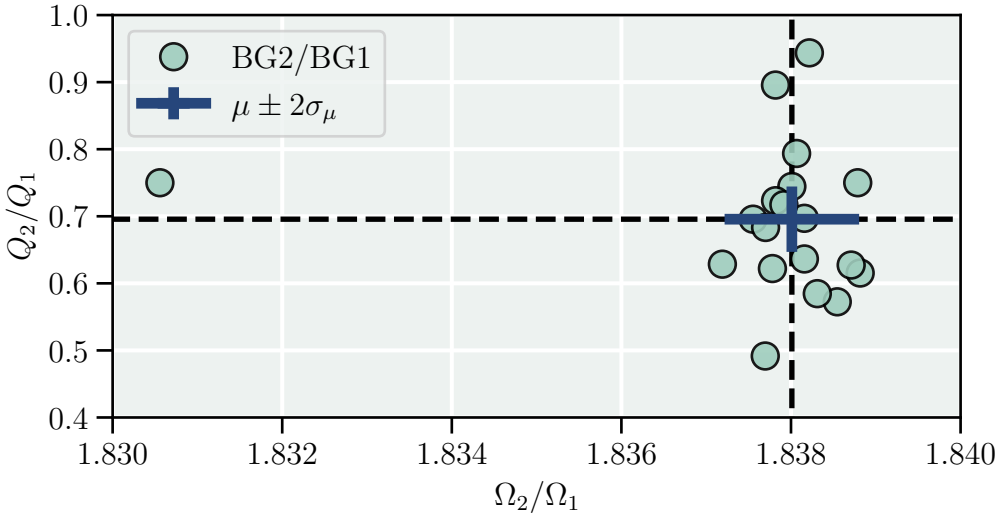

Figure 7.16: Ratios of Q factors and frequencies for the second and first bandgap modes of the "K" design, plotted as teal circles, after removing low-Q $< 10 \times 10^6$ outliers. The dashed lines shows the mean of each ratio, with the dark blue cross indicating twice the standard error on the mean.

Hence we decide to work with the second mode of the "K" design for the cavity optomechanics experiments described in the following section, where simultaneous high Ω_{m} and Q are desirable.

8 Optomechanical Memory for Light

"It was then that I embarked on my investigations. I wasn't short of material: rather, the excess of it drove me to distraction in my darkest hours"

Franz Kafka

In this section we cover our experiments of storage of light in a high-Q mode of a phononic crystal membrane, which is the subject of the manuscript [1]. To this end, we study the efficiency of storing an input coherent optical field and retrieving it again. The physical basis for these experiments is the OMIT phenomenon, which under a dynamical, red-detuned pump field allows interconversion of optical and mechanical excitations.

To begin we describe the details of the experimental platform. This includes the optomechanical cavity, the locking scheme involving two lasers detuned by $\approx \Omega_{\mathrm{FSR}}$ of the cavity and the optical setup interrogating the cavity.

8.1 Optomechanical Cavity

In section 5.2 we learnt the importance of the membrane position relative to the optical standing wave - the $2kz$ position. In our cavity we can tune this by moving the cavity mirrors. These are piezo-actuated, such that an applied differential voltage pushes one mirror and retracts the other. With the membrane rigidly fixed, this translates the standing wave relative to the membrane, tuning $2kz$, while keeping the overall cavity length fixed.

This design is based on developments in one of our sister group at NBI, the optomechanics lab of professor Eugene Polzik's Quantop group. The development of this cavity design is described in great detail in the thesis of Christoffer Østfeldt [138].

As mentioned, our design is greatly influenced by but not identical to theirs, a key difference being the mirror geometry. Quantop works with a bi-concave cavity with the membrane strictly at middle, whereas we work with a plano-concave design with the membrane closer to the flat mirror. A description of our cavity mirrors can be found in appendix C. This choice is in turn influenced by previous optomechanics experiments in SLAB that were carried out using a monolithic, short cavity. In such designs, the $2kz$ position was tuned by tuning the laser frequencies and sampling many longitudinal modes. This is untenable for us, since the telecom fiber laser we work with only has a tuning range of $\approx 0.5\,\mathrm{nm}$ compared to the $\approx 200\,\mathrm{nm}$ of the Titanium:Sapphire laser used in these other experiments.

Instead we tune $2kz$ with piezo-actuated cavity mirrors, as illustrated in figure 8.3. Any voltage applied to the Y input of the sum- and difference amplifier will result in a translation of the standing wave of the cavity, relative to the membrane, thus tuning $2kz$. The mechanical design of the used cavity

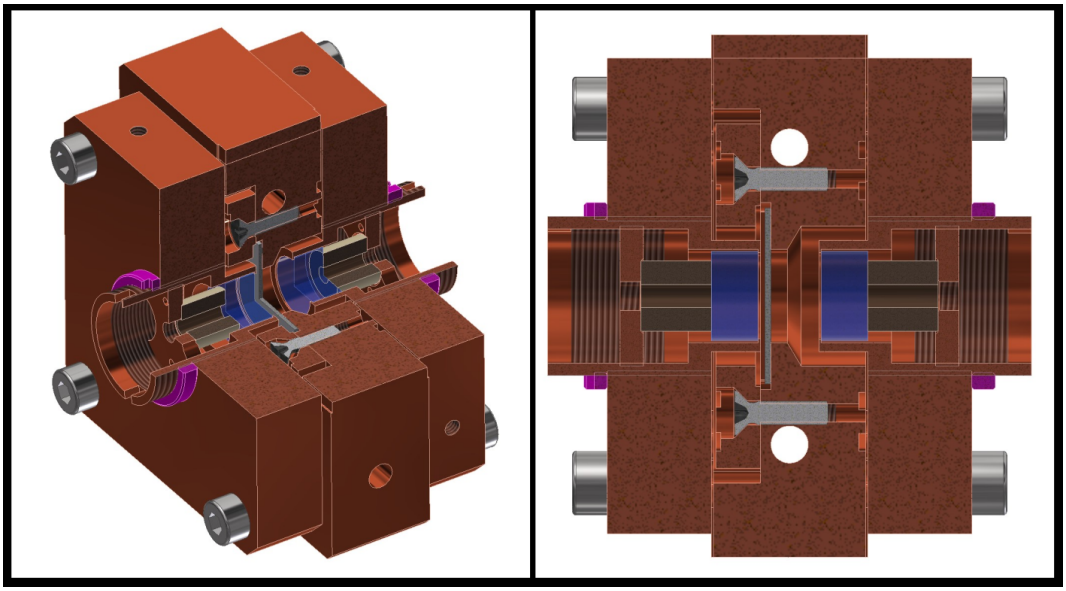

Figure 8.1: Optomechanical cavity assembly (more details in appendix E).The cavity mirrors are held in "barrels" (schematic in fig. E.1) along with a piezo. The barrels are fitted in a SM-05 threaded holder piece which is tightened to the membrane holder piece. The membrane lies in the holder piece (see figure 4.2) and is then clamped with a "coin" piece.

is shown in figure 8.1.

The length of the cavity $L_{\mathrm{cav}} \approx 5.5\,\mathrm{mm}$ is chosen as a compromise between the scalings of a range parameters with the cavity length. The most important system parameters in this consideration are the optomechanical coupling, $G \propto 1/L_{\mathrm{cav}}$, cavity waist $w_0 \propto L_{\mathrm{cav}}^{1/4}$, and cavity linewidth $\kappa \propto 1/L_{\mathrm{cav}}$. For our ideal system we simultaneously would like as large G as possible, while keeping w_0 small compared to the mechanical wavelength and κ compared to the frequency. An additional practical limitation is imposed by our locking scheme (see the following), that relies on two longitudinal cavity modes. Then the cavity free spectral range should also be small enough such that we can detect an optical beat note around $\Omega_{\mathrm{FSR}} \propto 1/L_{\mathrm{cav}}$.

Regarding the mechanical side, for the memory experiments we work with one of the new designs, described in section 7.3, namely the higher-order mode of the generation K design, optimized for the second bandgap.

8.2 Locking Scheme

To use transient OMIT for storage of an optical signal as a mechanical one, the laser facilitating the interconversion should only be switched on when the optical signal impinges on the cavity. If it remains on, then one simply reads out the mechanical state right away, rather than storing it. Since the conversion process is detuning-dependent and the cavity can drift if not actively locked,

we employ a scheme with two lasers. The first we call the *"science"* laser, as it provides the strong, red-detuned pump field that enables OMIT. The second is called the *"lock"* laser, since its purpose is to keep the cavity locked, even when the science laser is off.

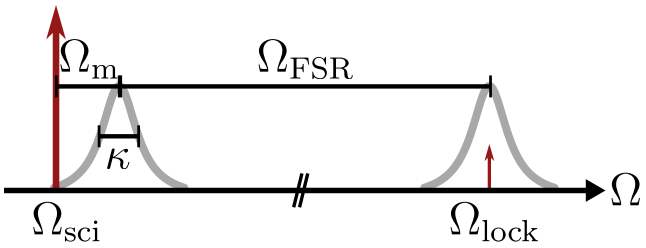

Figure 8.2: Relevant frequencies for the offset lock. The science laser at Ω_{sci} is detuned Ω_{m} below one cavity mode, with linewidth κ. This is achieved by locking the adjacent longitudinal cavity mode on resonance with the lock laser at Ω_{lock}, which in turn is locked at a frequency offset of $\Omega_{\mathrm{m}} + \Omega_{\mathrm{FSR}}$ with respect to the science laser.

This is possible if we stabilize the cavity length to the lock laser, and the lock laser at a frequency offset from the science laser. At a first glance one might think choosing the frequency offset as the mechanical frequency is enough. This is however problematic for a storage experiment, since the two lasers will beat in a manner indistinguishable from how the optical signal and the science laser will beat. In other words, we will essentially always "store" some part of the lock laser, which upon readout will manifest as uncorrelated noise on top of the retrieved signal.

To address this issue, we firstly operate with the two lasers in orthogonal polarizations and secondly have them addressing two different longitudinal cavity modes, see figure 8.2. In this way, the beat note between the two lasers is far off-resonant with any relevant mechanical modes. Our implementation is illustrated in figure 8.3. A small fraction of the two lasers is split off, combined in a fiber beamsplitter, and detected with a high bandwidth photodiode. With the combination of a microwave-frequency synthesizer (ValonRF 5015) and a programmable mixer and amplifier (Analog Devices EVAL-ADAR2004), we mix the beat note down to tens of MHz, that we can measure with a spectrum analyzer and process for the feedback with a Red Pitaya, as described in section 6.2.2 and shown in figure 8.3. The feedback loop is then closed by actuating on the injection current and temperature of the Lock laser. The temperature actuation is to mitigate slow, long-term drifts, enabling high gain on the current feedback.

The cavity lock is a PDH lock, again implemented on a Red Pitaya which modulates the lock laser injection current and processes the reflected lock beam as described in section 6.2.1, where a typical error signal is also shown.

Using an analog PI-controller (Vescent Photonics D2-125), a homebuilt sum and difference pre-amplifier, and a variable gain multichannel high voltage

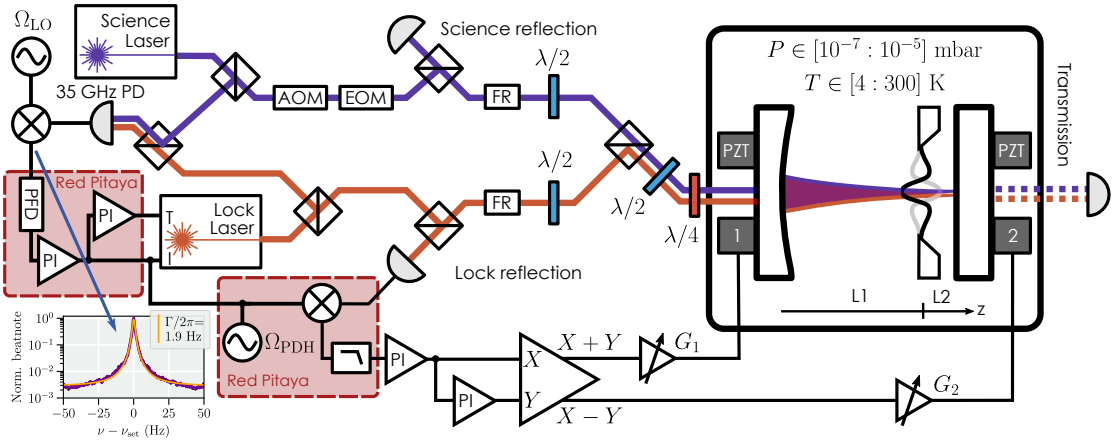

Figure 8.3: Schematic of the mechanical memory experiment. The optomechanical cavity (rightmost) is placed inside an evacuated LHe flow cryostat, with electrical feedthroughs for piezo actuation, and optical viewports for free-space interrogation in both reflection and transmission. We couple two lasers to the cavity, the *"science"* laser, responsible for the optomechanical interaction (beampath drawn in purple) and the *"lock"* laser (beampath in orange), used to stabilize the science laser detuning, even when it is off. A small fraction is split off from each laser and the inference between the two is detected with a fast $\approx 35\,\mathrm{GHz}$ bandwidth photodiode. The measured beatnote is downmixed and processed for the frequency offset lock of the lock to the science laser. The cavity reflection of each laser is independently measured, kept separate using polarization optics, and directly detected. The lock laser reflection is processed for the cavity PDH lock, with the feedback actuating the cavity length. The science laser reflection is analyzed by lock-in detection around the mechanical sideband frequency. An AOM allows us to switch off the science laser, as required for memory experiments, and an EOM lets us perform OMIT spectroscopy and in a memory experiment send an optical input signal with programmable properties. See main text for details.

piezo amplifier (Piezo Mechanik SVR150/3), we actuate on the cavity piezos. We stabilize the cavity length using the X input shown in figure 8.3 and the membrane $2kz$ position with the Y input. In the end this scheme enables us to freely choose the detuning of the science laser, which is necessary for sideband-resolved cavity optomechanics.

8.3 Optical Setup

As mentioned we use two lasers, the science laser that is responsible for the conversion of an optical signal field to mechanical excitations, and the lock laser to keep track of the cavity, when the science laser is off. We switch the science laser off using a fiber-coupled acousto-optic modulator (AOM, AA Opto Electronics MT80-IIR30-Fio-PM0,5-J1-A-lc2), such that we can turn the

conversion process on and off with the AOM drive.

For the storage experiments, we generate signals to store using an electro-optic phase modulator (Thorlabs LN53S-FC). We drive the modulator with gated exponentially rising sinusoids, whose final amplitude, rise-time (and thus bandwidth), and frequency can be programmed.

We directly detect the reflection of each laser independently using a combination of polarizing beamsplitters and Faraday rotators. The two beams are then combined on another polarizing beamsplitter and then co-propagate towards the cavity. The cavity is placed in a liquid Helium flow-cryostat (Janis ST-100). The flow cryostat has the disadvantage compared to closed-cycle systems that the length of a cooldown is limited by the helium content of our dewar, but the advantage of minimal vibrations, since there is no pulse tube, recondenser or pumps for the cryogen. Since we work with high-finesse optical cavities, whose mechaninal noise we try to conduct controlled experiments with, operating these is much easier in the less mechanically shaky environment of the flow cryostat.

We digitize the reflected and transmitted DC photocurrents using an oscilloscope (PicoScope 5442D), and measure the mechanical signal with a Lock-In amplifier (Zürich Instruments HF2-LI). Knowing the mirror transmissivities and detector gain allows us to infer the intra-cavity photon number from the voltage recorded by the transmission detector. The transmission detector is also useful for OMIT spectroscopy of the cavity parameters.

8.4 Dynamical Backaction Characterization

Before conducting storage and retrieval experiments, we always first test how strongly we can couple the light and mechanics. We do so by characterizing the dynamical backaction effects on the mechanics, in particular the optically broadened linewidth Γ_{eff}. We can extract the effective linewidth from spectral measurements. These measurements are done using the Lock-In, demodulating around the mechanical frequency in a wide bandwidth, such that we see the mechanical bandgap.

Of special interest is the vacuum optomechanical coupling rate g_0, that can be extracted from measurements of Γ_{eff}, provided one has simultaneous knowledge of the intra-cavity photon number $\bar{n}_{\text{cav}}$, optical linewidth κ and the laser detuning Δ. Knowing g_0 and the largest Γ_{eff} tells us which experiments we are able to conduct. For instance, ground state cooling using dynamical backaction requires $\Gamma_{\text{eff}} > \Gamma_{\text{m}}\bar{n}_{\text{th}}$.

As such, a complete measurement of a particular configuration entails measuring: a fast OMIT sweep, to get κ and Δ, the transmitted DC power, to infer $\bar{n}_{\text{cav}}$, and a measurement of the mechanical noise, from the sidebands of the reflected science laser. Typically we characterize g_0 by keeping the input power fixed and varying the detuning, by changing the offset-lock setpoint. In figure 8.4 we show the OMIT scans for such a detuning series. Using a coarse

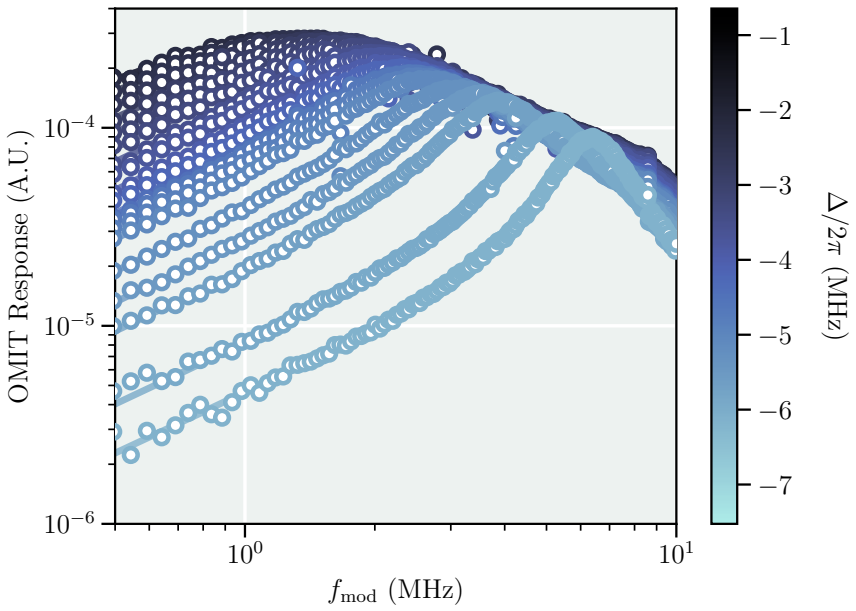

Figure 8.4: Fast OMIT sweeps to extract κ and Δ. Approaching the cavity resonance from below, we measure the cavity linewidth and laser detuning by fitting (solid lines) measured coarse OMIT scans (hollow circles).

frequency step for the sweep $\delta_{\mathrm{sweep}} \approx 49\,\mathrm{kHz} \gg \Gamma_{\mathrm{eff}}$ we are very unlikely to hit any mechanical modes, and can thus easily fit only the cavity lineshape (efffectively setting $g = 0$ in equation 5.34), enabling robust and quick cavity spectroscopy.

After the OMIT sweep, we record a time-trace of the transmitted power. The means of such traces are plotted against the detunings determined via OMIT in figure 8.5, where the color coding indicates the same measurement between OMIT, power and mechanical spectra. The measured transmitted powers (blue circles) are well-fitted by the cavity line shape (gray solid line), with κ determined from the OMIT measurements, and only a single free amplitude parameter, giving the input power. Knowing the input power then allows us to determine the circulating intra-cavity photon number for a given detuning.

We then measure a mechanical noise spectrum on the lock-in amplifier, with an example of such measurements given in figure 8.6. With a wide demodulation bandwidth, the can record the full mechanical bandgap, evidenced by densely packed modes outside and sparse peaks inside it. Inside the bandgap we find three main mechanical peaks around 2.38 MHz, 2.4 MHz and 2.43 MHz, and an externally applied peak stemming from a phase modulation of the laser at 2.36 MHz. For our storage experiments, we choose the work with the 2.4 MHz because of its displacement profile. It is rotationally symmetric and has maximal displacement in the center of the defect, in contrast to the other

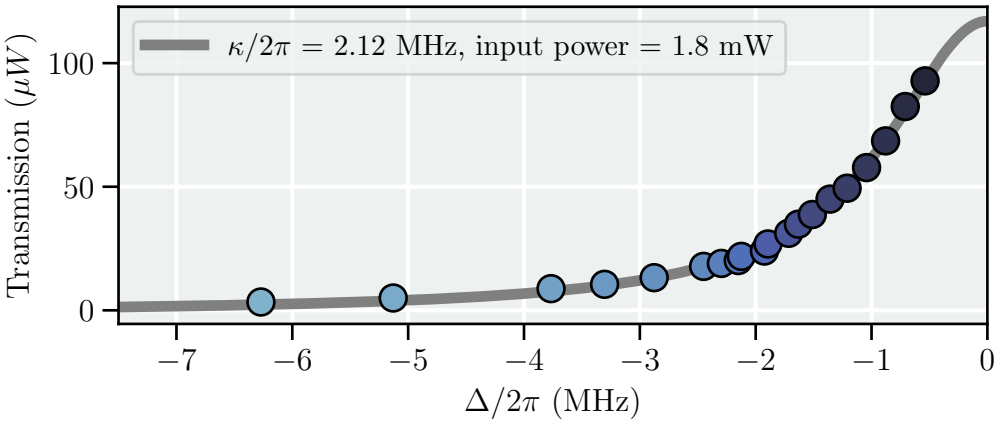

Figure 8.5: Determining the input power. From measurements of the transmitted power for each detuning, we can extract the input power with knowledge of mirror transmissivities and excess loss (determined from the cavity linewidth, see sec. A). Then the input power is found from a 1-parameter fit to a fixed cavity lineshape with a variable amplitude (solid gray).

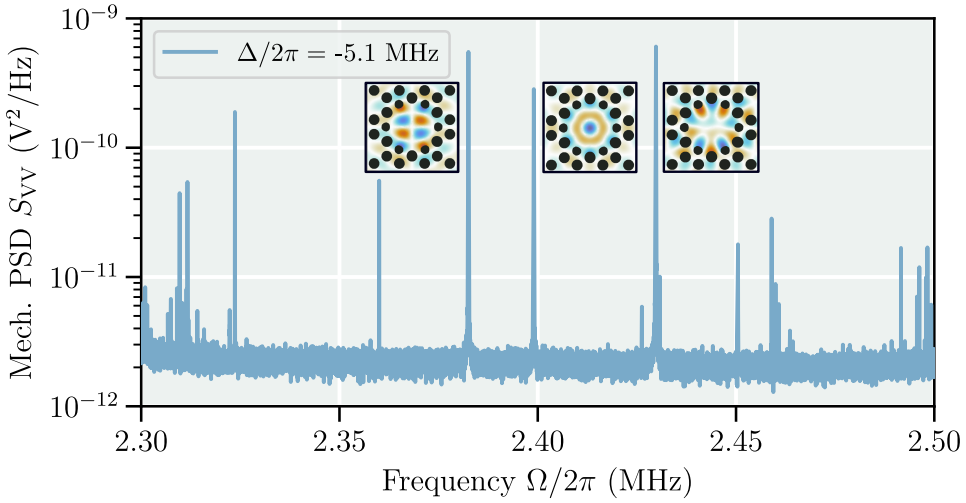

Figure 8.6: Broadband mechanical spectrum with far-detuned science laser, $|\Delta| > \Omega_m, \kappa$. The sparsely populated mechanical bandgap is apparent between $\approx$ 2.32 MHz and $\approx$ 2.48 MHz. Inside the bandgap we find three dominant mechanical modes, annotated by their simulated displacement profiles near the defect. The peak at 2.36 MHz is generated externally with a phase modulator. For our experiments, we work the the radially symmetric $\approx$ 2.4 MHz mode.

two modes. The fact that we even are seeing these other modes in the first place suggests a certain misalignment of the cavity mode on the membrane, which is corroborated by the increased cavity linewidth $\kappa/2\pi \approx 2.1$ MHz, corresponding to excess optical losses $\delta_{ex} \approx 120 \times 10^{-6}$, much larger than what

can be explained purely from $2kz$ modulation (cf. figure 5.5). From the mechanical spectra, we can extract the effective linewidth Γ_{eff} with a Lorentzian fit to the mechanical mode of interest, as shown in figure 8.7. These measurements constitute a complete characterization at one detuning. We can then iterate the procedure; measuring corresponding values of detuning, transmitted power, and effective mechanical bandwidth, eg. for a range of detunings. The result of such a detuning series is also shown in figure 8.7. Here we plot paired values of Δ and Γ_{eff}, and fit them according to

$$\Gamma_{\text{eff}}(\Delta) = \Gamma_{\text{m}} + \bar{n}_{\text{cav}}(\Delta) g_0^2 \kappa \left(\frac{1}{(\kappa/2)^2 + (\Delta + \Omega_{\text{m}})^2} - \frac{1}{(\kappa/2)^2 + (\Delta - \Omega_{\text{m}})^2} \right), \tag{8.1a}$$

$$\bar{n}_{\text{cav}}(\Delta) = \frac{P_{\text{in}}}{\hbar \Omega_{\text{L}}} \frac{\eta_{\text{c}} \kappa}{(\kappa/2)^2 + \Delta^2}, \tag{8.1b}$$

where eq. 8.1a is based on the equation for the optomechanical damping 5.20b, modified with a constant term representing the intrinsic damping Γ_{m} and a detuning-dependent intracavity photon number, given by 8.1b. With all other experimental parameters, namely κ, Ω_{m}, η_{c}, Ω_{L}, P_{in}, independently determined, we can restrict the fit to only two free parameters, Γ_{m} and g_0. From the experiment shown in figure 8.7, we extract a value $g_0/2\pi = 1.0(1)\,\text{Hz}$ using this method.

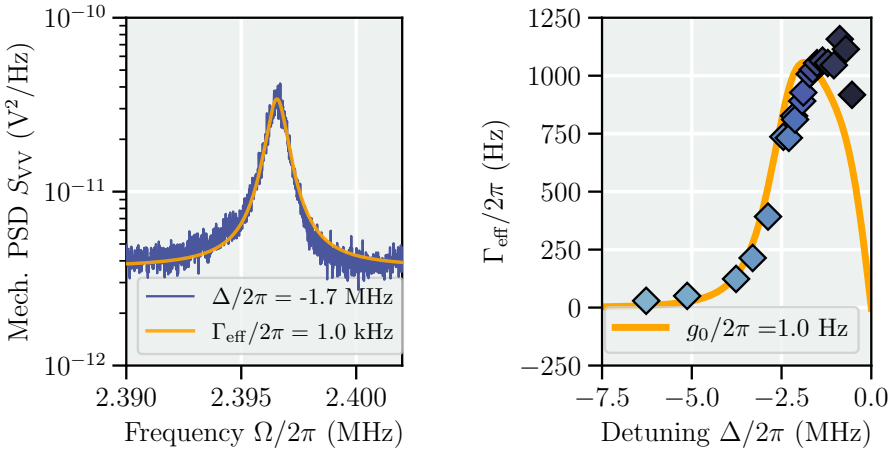

Figure 8.7: Extracting g_0 from dynamical backaction. From a series of different detunings, at fixed power, we fit mechanical noise spectra (left) to extract the optically broadened mechanical linewidth. Right: knowing our experimental parameters then allows determining $g_0/2\pi = 1.0(1)\,\text{Hz}$, from a fit to a dynamical backaction model, eq. (8.1).

8.5 Pulsed Optomechanical Light Storage

The salient feature of a memory device is the ability to leave a stored signal undisturbed for later retrieval. Since the optomechanical beamsplitter interaction is bidirectional (photons are converted to phonons and vice versa), we need the ability to switch the interaction off, once we are satisfied we have captured the input optical signal.

We implement a controllable conversion process by switching the science laser on and off. Since the optomechanical processes happens at a rate $g = g_0\alpha$, turning the laser on and off has the effect of switching the interaction on and off at different points in time, such that $g(t) = g_0\alpha(t)$, where α again is the amplitude of the science laser.

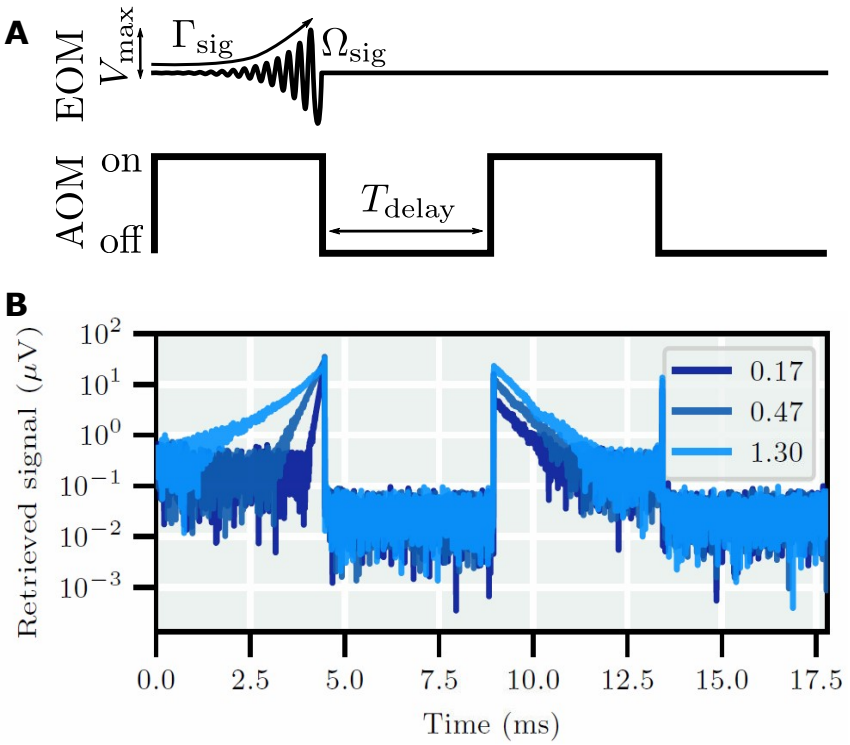

Figure 8.8: Pulsed mechanical storage of an optical field. A: Pulse diagram for the EOM and AOM. We drive the AOM with a TTL square wave, setting the readout delay time T_{delay} with the TTL frequency. Every other period we drive the EOM with programmable exponentially rising sinusoidal waveforms, characterized by their amplitude $V_{\max}$, bandwidth Γ_{sig} and frequency Ω_{sig}. B: Typical measured optical signals for such a pulse sequence. In blue we plot the reflected science laser, demodulated around Ω_{sig}. Initially we see an exponential rise, stemming from the EOM drive, interrupted by the AOM being switched off and followed by a readout of the mechanics, when the AOM is switched back on. From light to dark blue we increase Γ_{sig}, with the legend indicating $\Gamma_{\text{eff}}/\Gamma_{\text{sig}}$.

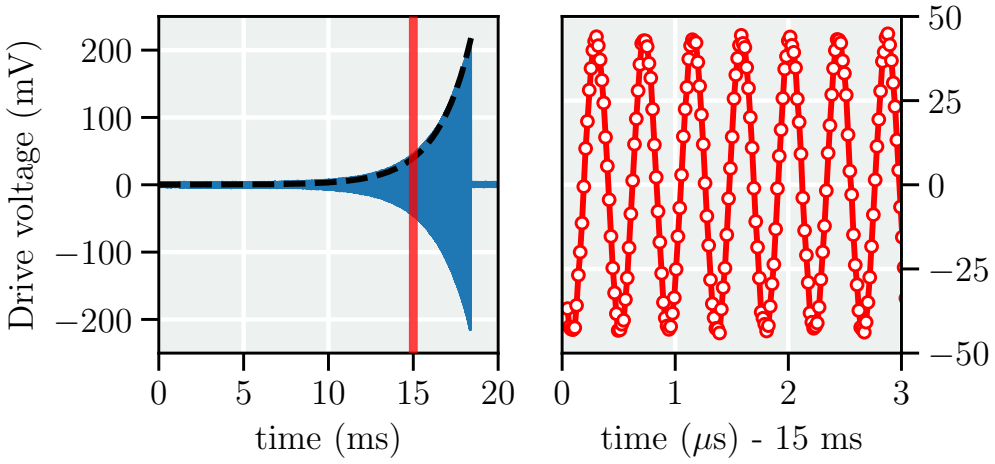

Figure 8.9: Programmable signal field. Left: a measured timetrace of an exemplary exponentially rising sinusoidal drive signal is plotted in blue, with dashed black indicating the exponential envelope. Right: zoom-in of the same data around 15 ms (indicated by red bar) reveals the sinusoidal behaviour.

A measurement demonstrating this pulsing of the science laser is shown in figure 8.8. In the B panel, we show the reflection of the science laser, demodulated by the lock-in amplifier. In addition to the AOM pulsing, we also send an optical signal field $s_{\text{in}}^{\text{sig}}(t)$, that is generated by driving the EOM, with a waveform sketched in figure 8.8a, and measured as shown in figure 8.9.

Measurements such as those shown in figure 8.8 form the basis of our optomechanical memory experiments. By systematically varying the properties of the optical input signal $s_{\text{in}}^{\text{sig}}$ we quantitatively study the efficiency of our optomechanical platform as a memory for light, comparing to theory based on section 5.1.3.

8.6 Efficiency

The total efficiency of the optomechanical memory for light is comprised of multiple factors. These can be broken down into "retrieval" and "detection" contributions $\eta_{\text{total}} = \eta\eta_{\text{det}}$, pertaining to the optomechanical conversion from light to mechanics and back again, and detection efficiency respectively.

The detection efficiency is given by the detector quantum efficiency $\eta_{\text{QE}} = 83\%$ and the collection efficiency, given by optical losses in the beam path $\eta_{\text{loss}} = 60\%$, such that

$$\eta_{\text{ext}} = \eta_{\text{QE}}\eta_{\text{loss}} = 50\%. \tag{8.2}$$

On the other hand, the retrieval efficiency η depends on how well the signal field is matched to the memory and cavity in- and out-coupling η_c^2, such that $\eta \leq \eta_c^2$. The fact that η_c occurs squared accounts for the fact that light has to

traverse the desired coupling port twice - once when injected and once when read out. To study η we store and retrieve input signals of the form

$$s_{\text{in}}^{\text{sig}}(t) = i\beta s_0 \sin(\Omega_{\text{sig}} t) \mathrm{e}^{\Gamma_{\text{sig}} t/2} H(-t), \tag{8.3}$$

where s_0 is the flux of the science laser impinging on the cavity, β is the modulation depth of the applied phase modulation and $H(t)$ is the Heaviside step function. We define the retrieval efficiency η as the ratio of the retrieved energy E_{in} to the input energy E_{out}, $\eta = E_{\text{out}}/E_{\text{in}}$. These are, respectively, proportional to

$$E_{\text{in}} \propto \int_{-T}^{0} |s_{\text{in}}^{\text{sig}}(t)|^2 \mathrm{d}t, \tag{8.4a}$$

$$E_{\text{out}} \propto \int_{0}^{T} |s_{\text{out}}^{\text{sig}}(t)|^2 \mathrm{d}t, \tag{8.4b}$$

where T is the duration of the write pulse (which in turn is equal to the read-write delay T_{delay} for the 50% duty cycle square wave shown in figure 8.8A and used in the following experiments). To compare these two in order to extract η, we can then record traces like shown in figure 8.8B, and analyze them according to eq. (8.4). When estimating the input energy, it is crucial that the signal is not resonant with the mechanics, as it otherwise is (partially) absorbed by the mechanics, much like in steady state OMIT (cf. figure 5.3).

Following the treatment of transient OMIT (section 5.1.3), we can compare measurements with theoretical expectations as we vary the properties of the experiment. We study the effect of varying the readout-delay T_{delay}, the signal bandwidth relative to that of the mechanical memory $\Gamma_{\text{eff}}/\Gamma_{\text{sig}}$, and the two-photon detuning δ between the signal field and the mechanics.

For increasing readout delay, we expect exponential decay of the mechanics. This is essentially what happens when we measure ringdowns: the mechanics is excited to some amplitude, which decays with time. It can also be seen from equation 5.40, where the mechanical amplitude evolves as $\exp(-\Gamma_{\text{m}} t/2)$, in the absence of the science laser, i.e. $\Gamma_{\text{eff}} = \Gamma_{\text{m}}$, during storage.

Indeed, after the delay time, the retrieved amplitude A_{out} divided by that of the input A_{in} should follow

$$\frac{A_{\text{out}}}{A_{\text{in}}} = e^{-\Gamma_{\text{m}} T_{\text{delay}}/2}. \tag{8.5}$$

The result of such an experiment is shown in figure 8.10. Our measurements seem to follow the predicted exponential decay, albeit with a decay rate faster than $\Gamma_{\text{m}}/2\pi \approx 20\,\text{mHz}$. Our hypothesis for this increased mechanical damping is that the lock laser, which remains on during storage, also does some dynamical backaction, despite being weak and close to resonance. For stability

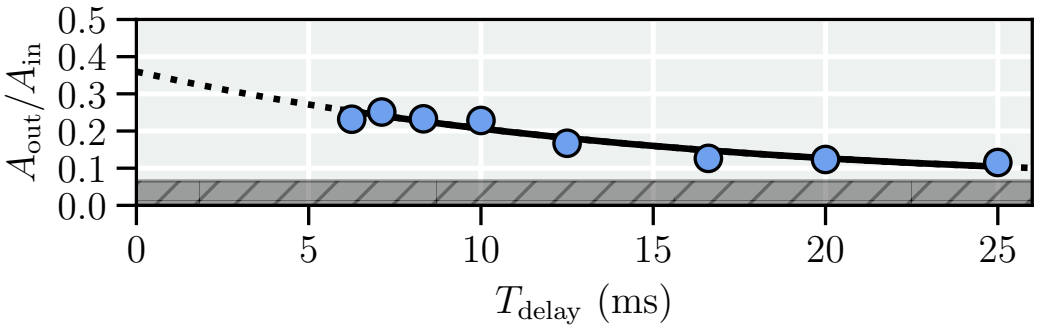

Figure 8.10: Mechanical decay during storage. In blue circles, the initial amplitude of the retrieved mechanical signal A_{out}, normalized to the end-amplitude a detuned drive signal A_{in}, for increasing storage times T_{delay}. The solid black line is an exponential fit, which is extrapolated in dashed black. The gray shaded area indicates the offset of the fit, determined by the thermomechanical background noise.

reasons, we do not lock exactly on resonance, but red-detuned $\approx -0.05\kappa$, to avoid accidentally drifting to the blue side and exciting a mechanical mode. In the reported experiments we operate with a power of the lock laser, immediately before the cryostat of $\approx 2\,\mu\mathrm{W}$. With a far detuned science laser, we saw the linewidth of the mode increase with lock laser power, corroborating the hypothesis. We therefore call this modified damping the "dark" decay rate, Γ_{dark}, in the sense of the science laser being off. From the experiment reported in figure 8.10, we find $\Gamma_{\mathrm{dark}}/2\pi = 6.7\,\mathrm{Hz}$, at our typical operating lock power $P_{\mathrm{lock}} \approx 2\,\mu\mathrm{W}$.

The next focus of our attention is the effect of bandwidth matching. In the limit of large classical coorperativity $\Gamma_{\mathrm{opt}} \gg \Gamma_{\mathrm{m}}$, we can approximate effective mechanical linewidth as being dominated by the optical broadening $\Gamma_{\mathrm{eff}} \approx \Gamma_{\mathrm{opt}}$.

Then, for signal fields like eq. (8.3), on two-photon resonance and for immediate readout $\delta = T_{\mathrm{delay}} = 0$ we can evaluate eqs. (8.4) under these conditions, to isolate the effect of bandwidth matching. We find for the retrieval efficiency

$$\eta = \eta_{\mathrm{c}}^2 \frac{4\Gamma_{\mathrm{eff}}\Gamma_{\mathrm{sig}}}{(\Gamma_{\mathrm{eff}} + \Gamma_{\mathrm{sig}})^2}. \tag{8.6}$$

In figure 8.11 we show the results of such an experiment. We read out without a storage delay, and tune the signal to mechanical resonance, such that $T_{\mathrm{delay}} = \delta = 0$. Varying the signal bandwidth and keeping the mechanical bandwidth fixed, we the plot measurements of the ratio of the retrieved energy to the input energy, $E_{\mathrm{out}}/E_{\mathrm{in}}$. To gauge how efficiently we retrieve the input energy, we fit eq. (8.6) to our data, with η_{c} a single free multiplicative

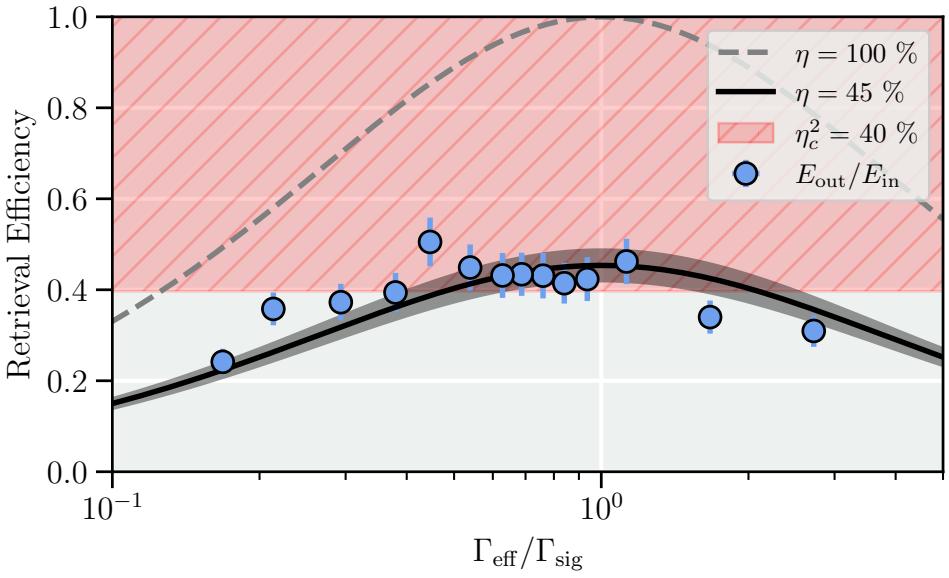

Figure 8.11: Efficiency due to bandwidth matching. Measurements of retrieved energy relative to the input, $E_{\mathrm{out}}/E_{\mathrm{in}}$, are plotted as blue points. The red shaded area indicates the expected limit due to our cavity over-coupling. The dashed gray curve shows the ideal bandwidth scaling, given by eq. (8.6). The black curve is a 1-parameter fit of our data to eq. (8.6), giving a retrieval efficiency of $\eta = 45\%$, in fair agreement with the overcoupling limit. The shaded black error indicates $\pm$ twice the fit error.

constant. The fit is shown as the black curve, with twice the fit uncertainty shown as a black shaded band. The unity-over-coupling case is shown as a dashed gray line for comparison. From the fit we extract a retrieval efficiency $\eta = 45\%$. We compare this to what we ought to be able to get, as dictated by the finite overcoupling of the cavity. This is shown as the red area in figure 8.11. Here we see fair agreement between the fit and the expected limitation, suggesting retrieval efficiencies of 45% and 40% respectively.

Next we studied the effect of two-photon detuning, with a fixed readout delay T_{delay}. In the case of matched bandwidth, the retrieval efficiency as a function of two-photon detuning is

$$\eta = \eta_{\mathrm{c}}^2 \frac{\Gamma_{\mathrm{eff}}^2}{\delta^2 + \Gamma_{\mathrm{eff}}^2} e^{-\Gamma_{\mathrm{dark}} T_{\mathrm{delay}}/2}. \tag{8.7}$$

In figure 8.12 we investigate eq. (8.7). For a matched signal bandwidth, $\Gamma_{\mathrm{sig}} = \Gamma_{\mathrm{eff}}$ and fixed, but non-zero, readout delay $T_{\mathrm{delay}} = 4.48\,\mathrm{ms}$, we measured $E_{\mathrm{out}}/E_{\mathrm{in}}$ for varying signal frequency Ω_{sig} (and accordingly two-photon detuning δ). We fit the Lorentzian response given by eq. (8.7) to our measure-

ments, shown in black, and find good agreement between the model and our data. In particular the quantitative agreement between the observed efficiency and expectations based on cavity overcoupling (as discussed above) and mechanical decay is striking, as highlighted in the inset. The red area indicates the overcoupling limitation, while the gray area shows the mechanical decay at the rate Γ_{dark} for a duration $T_{\mathrm{delay}} = 4.48\,\mathrm{ms}$, limiting the efficiency to 82.8%. The product of the overcoupling and decay effects limits the retrieval efficiency to 33.1%. For comparison we extract 32.4% from the fit to eq. (8.7), exhibiting excellent agreement. Using our established scaling of the mechanical decay, we find the retrieval efficiency at zero delay $\eta \approx 40\%$.

The measurements presented in figures 8.10, 8.11, and 8.12 collectively demonstrate a good understanding of the efficiency of our mechanical memory for light. The highest possible retrieval efficiency, for a matched signal field $\Gamma_{\mathrm{sig}} = \Gamma_{\mathrm{eff}}$, $\delta = 0$, and immediate readout $T_{\mathrm{delay}} = 0$ we find to be $\eta \approx 39\%$. Crucially this number is not limited by the optomechanical conversion, but rather limitations imposed by experimental practicalities, in particular excess intracavity optical losses diminishing the overcoupling. Indeed the transmissiv-

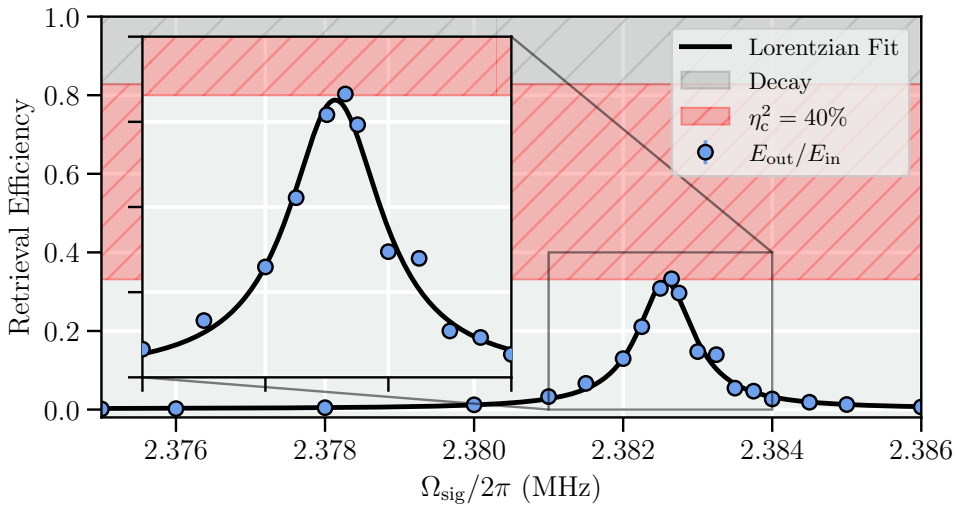

Figure 8.12: Efficiency due to two-photon detuning. Varying the two-photon detuning by changing the signal frequency Ω_{sig}, we show measurements of $E_{\mathrm{out}}/E_{\mathrm{in}}$ as blue circles. This experiment was done with $\Gamma_{\mathrm{sig}} \approx \Gamma_{\mathrm{eff}}$ and $T_{\mathrm{delay}} \approx 4.48\,\mathrm{ms}$. The gray area indicates the mechanical decay during the storage time, limiting the retrieval efficiency to 83%. The red area again indicates the penalty from sub-ideal overcoupling. The data is well-fitted by a Lorentzian (black line). In the inset we highlight the good quantitative agreement between our measured efficiency and expectations based on the aforementioned effects. Errorbars on the measurements are twice the standard error on the mean, but too small to discern.

ities of the mirrors (see appendix C) suggests $\eta_c^2 = 93\%$ is possible in absence of excess loss. We also successfully model how the retrieval efficiency decreases with non-ideal input fields and long storage time, enabling the extrapolation of the efficiency to experiments using input fields that cannot be tailored, e.g. spontaneously emitted single photons, with a frequency and bandwidth fixed by the emitter.

In addition to the efficiency, the phase coherence of a memory is also of interest. At the time of writing, this is an ongoing study. We however note that our membrane resonators previously have been employed in cavity optomechanical experiments without showing dephasing in excess of that associated with heating from a thermal bath [33, 120].

8.7 Prospects for Single-Photon Storage

Having demonstrated storage of coherent fields in section 8, we discuss the prospects for an experiment with single-photon input. Such an experiment would be interesting from the perspective of a quantum repeater [61] as a quantum memory, a key resource in large scale quantum networks [60].

For an actual quantum repeater, storage efficiencies approaching unity are required. This is already is challenging for coherent fields, but as a first step towards the goal, we can consider observing the radiation-pressure-induced heating due to a single photon of a ground-state cooled mechanical oscillator. The signal-to-noise ratio (SNR) for a given all-in efficiency η and number of experimental runs to average over N for such an experiment is calculated in appendix D, and in the limit of large N, one finds

$$\mathrm{SNR} \approx \sqrt{2N}\frac{\eta}{1+2\eta}. \tag{8.8}$$

In figure 8.13 we plot eq. (8.8) for different efficiencies η, with the green area indicating a SNR > 1, indicating a measurable effect of the single photon input on the mechanics. In this way one can estimate the required number of measurements to average N, for a given all-in efficiency η.

For most single-photon sources [139, 140], achieving narrow bandwidths is an ongoing challenge. For instance, ideal spontaneous emission-based nanophotonic sources are limited by the carrier lifetime [141, 142], whereas schemes based on Raman-scattering potentially can suffer from charge and nuclear spin noise [143], although progress in controlling these recently has been made [144]. This poses a difficulty for interfacing them with our narrowband mechanical memory, since the associated penalty in efficiency scales as $\Gamma_{\mathrm{memory}}/\Gamma_{\mathrm{signal}}$, in the regime $\Gamma_{\mathrm{memory}} \ll \Gamma_{\mathrm{signal}}$, as found in section 8.

As an alternative to generating narrowband single photons, one can consider compressing the bandwidth of otherwise high quality single photons. Var-

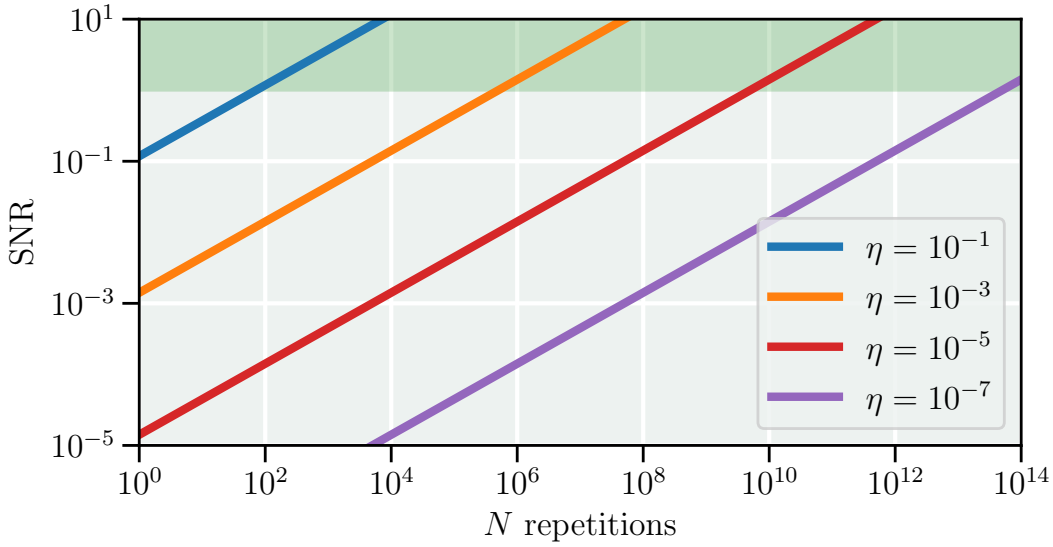

Figure 8.13: Single-photon SNR. We visualize equation (8.8) for varying η (see legend), to gauge how much averaging is necessary to achieve SNR > 1, as indicated by the green area.

ious schemes to this end have been explored [145, 146, 147, 148, 149, 150, 151] with great progress in recent years.

To estimate the running time of such an experiment, given current parameters, we can first estimate an all-in efficiency, as done in table 5. Taking the recent example of a frequency converted quantum dot source as an exemplary telecom wavelength single-photon source [152], we can estimate the total efficiency of such an experiment, giving $\eta = 1.6 \times 10^{-7}$.

η contribution	Description	Value
η_{memory}	All-in memory efficiency	20%
η_{source}	All-in source efficiency	40.8%
η_{BW}	Bandwidth contribution	$\frac{1\,\text{kHz}}{500\,\text{MHz}} = 2 \times 10^{-6}$
η	Total single-photon efficiency	1.6×10^{-7}

Table 5: Single-photon experiment efficiency contributions, for the mechanical memory reported in section 8 and telecom single-photon source of [152].

From these considerations we can consult figure 8.13 and find that $N \approx 10^{14}$ averages are required for SNR > 1 given the estimated efficiency. As the time to conduct a single shot $T_{\text{single}} \approx 10\,\text{ms}$, we estimate the total time $T_{\text{total}} = NT_{\text{single}} > 30 \times 10^3$ years, which is clearly untenable.

Since the dominant contribution is the bandwidth penalty η_{BW}, this ought to be the focus of attention if such an experiment is to be conducted. On the mechanical side we have seen larger $\Gamma_{\text{eff}}/2\pi > 6\,\text{kHz}$ in previous assemblies,

which might optimistically be extended to $\Gamma_{\text{memory}}/2\pi = 10\,\text{kHz}$. Employing a bandwidth compressed source (recently bandwidth compression by a factor ≈ 400 was demonstrated [151]) then reduces the bandwidth ratio to $\approx 8\times10^{-3}$, which (for the efficiencies considered above) in turn implies $N \approx 1 \times 10^6$ repetitions are required.

Since the time required to run a single shot of the experiment also scales with the now increased effective mechanical bandwidth Γ_{eff}, the total time in this case would rather be $T_{\text{total}} = 1 \times 10^6 \times 1\,\text{ms} \approx 16$ minutes, which certainly is possible.

Nevertheless, due to the severity of the $\sqrt{N}$ scaling of eq. (8.8) and the currently low η_{BW} conspiring to give unfeasibly long run times, we are currently exploring various methods for bandwidth compression. One approach described in [153] is to conduct the frequency conversion of [152] inside a cavity which is resonant for the converted wavelength. In such a scheme, the prediction is to compress the bandwidth by a factor limited by the finesse of the employed cavity. Alternatively one can envision an optomechanical photon bandwidth compressor. Here the idea is to design an optomechanical system that can achieve a very large Γ_{opt}, efficiently read the broadband photon in, and then slowly read out the stored excitation over a timescale limited by the mechanical coherence time.

9 Final Remarks

To wrap up the thesis, we summarize the presented findings and discuss them in the context of related research. After understanding where we were and where we have gone, we comment on future pathways where this line of research might venture in the future.

9.1 Summary and Discussion of Results

The main scientific result presented in this thesis is the study of light storage using a cavity optomechanical system, enabled by the new resonator designs developed. For the first time we simultaneously present long $T_1 = 1/\Gamma_{\mathrm{dark}} > 20\,\mathrm{ms}$ energy storage times, respectable efficiency $\eta \approx 40\%$ for a telecom wavelength system - a system of great interest for emerging quantum network applications [60, 154].

Both T_1 and η are presently limited for technical reasons. For η the limiting factor is excess optical losses outside and inside the cavity. For the extra-cavity loss we trust a thorough investigation of the beampath will tell us where we loose the light, and consequently how to amend it. For the intra-cavity loss the culprit is suspected to be imperfect transverse alignment of the cavity to the mechanical mode, which either could be addressed through a more strenuous alignment regimen, or using larger membranes. Regarding the latter point, the hope would be that the reduction in intra-cavity losses scales faster than linearly with the resonator size, since the overlap is an area effect. Following our mode-overlap simulations we expect this to be the case, thus hopefully remaining sideband-resolved as the mechanical frequency also decreases for larger membranes.

Regarding T_1, this is ideally only limited by the intrinsic mechanical decay rate. Reaching this limit would give a $T_1 = 1/\Gamma_{\mathrm{m}} \approx 6.6\,\mathrm{s}$, with futher improvements expected in a cryogenic environment, recalling the factor ≈ 5 seen for the string resonators. If our hypothesis of residual dynamical back-action from the lock laser is correct, a more sensitive photodetector such as an avalanche photodiode or photomultiplier tube would enable running the experiment with lock powers $P_{\mathrm{lock}} < 1\,\mu\mathrm{W}$.

In the context of optomechanical memories for light, recent work demonstrated energy decay time $T_1 \approx 2\,\mathrm{ms}$, and efficiency $\eta \approx 16\%$ (disregarding the low heralding probability) of a GHz frequency mechanical mode, held at 15 mK, in a dilution refridgerator [84]. Our results compare favorably, already at room temperature, with an order of magnitude longer T_1 (with prospects for improvement as discussed) and higher η, that also can be improved with reduced losses. From a more strictly optomechanical perspective, our current system demonstrates a large classical coorperativity $\mathcal{C}_{\mathrm{class}} > 4 \times 10^4$.

9.2 Future Work

The next step for the mechanical memory project is going cryogenic. We have had encouraging preliminary cooldowns, with a optomechanical cavity that remained well-aligned (evidenced by the fact that we could reach comparable Γ_{opt} at room and cryogenic temperatures) using a "L" design membrane.

If we are to cautiously extrapolate our current system performance to a cryogenic environment, we firstly expect a reduced bath temperature, with a conservative estimate for the thermalization temperature being $T = 10\,\mathrm{K}$ in our LHe flow cryostat. Additionally we have seen Q factors increase when cooling down, so again erring on the side of caution we can assume a 3-fold improvement in Q. In such conditions, our demonstrated performance is sufficient to reach a quantum coorperativity $\mathcal{C}_{\mathrm{q}} = \mathcal{C}_{\mathrm{class}}/\bar{n}_{\mathrm{th}} \geq 1$, which is the criterion for quantum-enabled performance. Such performance would enable a sideband-cooling experiment with the ground state within reach. With a ground state cooled membrane, performing storage experiments with less than a single quantum of added noise is a tantalizing prospect.

Another object of study to continue is the phase coherence of our mechanical memory. Indeed previous work has shown our membranes to be devoid of excess dephasing [120, 78], which we need to verify in our concrete implementation. Under the assumption of no excess dephasing, the coherence time of our mechanical memory will rather be limited by the thermal decoherence rate $\Gamma_{\mathrm{dec}} = \Gamma_{\mathrm{m}}\bar{n}_{\mathrm{th}}$. Under the previously explained extrapolations, we expect to contend with $\Gamma_{\mathrm{dec}}/2\pi \approx 750\,\mathrm{Hz}$, or equivalently $T_2^* = 1/\Gamma_{\mathrm{dec}} \approx 200\,\mu\mathrm{s}$. Already this expectation compares favorably with the $\approx 10 - 100\,\mu\mathrm{s}$ reported for a three orders of magnitude lower bath temperature [84].

At this point studying storage of retrieval of single photons becomes a plausible prospect, provided the bandwidth question can be adressed in some of the manners discussed in section 8.7.

Apart from our implemented membrane-in-the-middle memory experiment, a related project in our lab, spearheaded by Ph.D. student Sho Tamaki, studies using the large-bandgap semiconductor Gallium Phosphide for two-dimensional optomechanical crystals, in a collaboration with the group of professor Remi Braive at C2N in Paris. Gallium Phosphide has recently garnered interest in the optomechanics community [155, 156], and two-dimensional optomechanical crystals have been shown to have more favorable laser-heating properties when compared to the conventional one-dimensional designs [157]. By combining the two approaches, the hope is to realize an optomechanical system that can be driven strongly enough to faithfully capture a broadband photon, that then ideally can be read out slowly, without being polluted by excess thermo-mechanical noise.

At this point I wish to sincerely thank any reader that made it to the end.

References

[1] M. B. Kristensen, N. Kralj, E. Langman, and A. Schliesser, "A long-lived and efficient optomechanical memory for light," 2023.

[2] N. Bohr, "I. On the constitution of atoms and molecules," *The London, Edinburgh, and Dublin Philosophical Magazine and Journal of Science*, vol. 26, no. 151, pp. 1–25, 1913. [Online]. Available: https://doi.org/10.1080/14786441308634955

[3] W. Heisenberg, "Uber quantentheoretische Umdeutung kinematischer und mechaniseher Beziehungen," *Zeitschrift für Physik*, vol. 34, pp. 858–888, 1925.

[4] E. Schrödinger, "Quantisierung als Eigenwertproblem," *Annalen der Physik*, vol. 384, no. 4, pp. 361–376, 1926.

[5] M. Born, W. Heisenberg, and P. Jordan, "Zur Quantenmechanik. II." *Zeitschrift für Physik*, vol. 35, no. 8-9, pp. 557–615, 1926.

[6] W. P. Bowen and G. J. Milburn, *Quantum Optomechanics*. CRC Press, 2016.

[7] M. Aspelmeyer, T. J. Kippenberg, and F. Marquardt, "Cavity optomechanics," *Reviews of Modern Physics*, vol. 86, no. 4, pp. 1391–1452, dec 2014. [Online]. Available: https://link.aps.org/doi/10.1103/RevModPhys.86.1391

[8] A. Einstein, "Über gravitationswellen," *Sitzungsberichte der Königlich Preußischen Akademie der Wissenschaften*, 1918.

[9] M. Gertsenshtein, "Wave resonance of light and gravitational waves," *Journal of Experimental and Theoretical Physics, 41, 113-114, English Translation in Soviet Physics JETP0*, 1962.

[10] K. S. Thorne, "Gravitational radiation damping," *Phys. Rev. Lett.*, vol. 21, pp. 320–323, Jul 1968. [Online]. Available: https://link.aps.org/doi/10.1103/PhysRevLett.21.320

[11] V. B. Braginsky and A. B. Manukin, "Ponderomotive effects of electromagnetic radiation," *Soviet Physics JETP*, vol. 25, no. 4, pp. 653–655, 1967.

[12] V. B. Braginsky A. B. Manukin and M. Y. Tikhonov, "Investigation of dissipative pondermotive effects of electromagnetic radiation," *Sov. Phys. JETP*, may 1970.

[13] V. B. Braginsky, Y. I. Vorontsov, and K. S. Thorne, "Quantum nondemolition measurements," *Science*, vol. 209, no. 4456, pp. 547–557, 1980. [Online]. Available: https://www.science.org/doi/abs/10.1126/science.209.4456.547

[14] V. Braginskii, "Classical and Quantum Restrictions on the Detection of Weak Disturbances of a Macroscopic Oscillator," *Soviet Journal of Experimental and Theoretical Physics*, vol. 26, no. 4, p. 831, 1968.

[15] Carlton M. Caves (Caltech), "Quantum Mechanical Radiation-Pressure fluctuations in an interferometer," *Physical Review Letters*, vol. 45, no. 2, pp. 75–79, 1980.

[16] C. M. Caves, "Quantum-mechanical noise in an interferometer," *Physical Review D*, vol. 23, no. 8, pp. 1693–1708, 1981.

[17] A. Dorsel, J. D. McCullen, P. Meystre, E. Vignes, and H. Walther, "Optical Bistability and Mirror Confinement Induced by Radiation Pressure," *Phys. Rev. Lett.*, vol. 51, no. 17, pp. 1550–1553, oct 1983. [Online]. Available: https://link.aps.org/doi/10.1103/PhysRevLett.51.1550

[18] K. Jacobs, P. Tombesi, M. J. Collett, and D. F. Walls, "Quantum-nondemolition measurement of photon number using radiation pressure," *Physical Review A*, vol. 49, no. 3, pp. 1961–1966, 1994.

[19] C. Fabre, M. Pinard, S. Bourzeix, A. Heidmann, E. Giacobino, and S. Reynaud, "Quantum-noise reduction using a cavity with a movable mirror," *Physical Review A*, vol. 49, no. 2, pp. 1337–1343, 1994.

[20] S. Mancini and P. Tombesi, "Quantum noise reduction by radiation pressure," *Physical Review A*, vol. 49, no. 5, pp. 4055–4065, 1994.

[21] E. Schrödinger, "Die gegenwärtige Situation in der Quantenmechanik," *Die Naturwissenschaften*, vol. 23, no. 48, pp. 807–812, nov 1935.

[22] S. Bose, K. Jacobs, and P. L. Knight, "Scheme to probe the decoherence of a macroscopic object," *Phys. Rev. A*, vol. 59, pp. 3204–3210, May 1999. [Online]. Available: https://link.aps.org/doi/10.1103/PhysRevA.59.3204

[23] D. K. Armani, T. J. Kippenberg, S. M. Spillane, and K. J. Vahala, "Ultra-high-Q toroid microcavity on a chip," *Nature*, vol. 421, no. 6926, pp. 925–928, 2003.

[24] T. J. Kippenberg, H. Rokhsari, T. Carmon, A. Scherer, and K. J. Vahala, "Analysis of Radiation-Pressure Induced Mechanical Oscillation of an Optical Microcavity," *Physical Review Letters*,

vol. 95, no. 3, p. 033901, jul 2005. [Online]. Available: https://link.aps.org/doi/10.1103/PhysRevLett.95.033901

[25] Y. S. Park and H. Wang, "Resolved-sideband and cryogenic cooling of an optomechanical resonator," *Nature Physics*, vol. 5, no. 7, pp. 489–493, 2009.

[26] M. Eichenfield, J. Chan, R. M. Camacho, K. J. Vahala, and O. Painter, "Optomechanical crystals," *Nature*, vol. 462, pp. 78 EP –, oct 2009. [Online]. Available: https://doi.org/10.1038/nature08524

[27] J. D. Teufel, D. Li, M. S. Allman, K. Cicak, A. J. Sirois, J. D. Whittaker, and R. W. Simmonds, "Circuit cavity electromechanics in the strong-coupling regime," *Nature*, vol. 471, no. 7337, pp. 204–208, mar 2011. [Online]. Available: http://www.nature.com/articles/nature09898

[28] B. M. Zwickl, W. E. Shanks, A. M. Jayich, C. Yang, A. C. Bleszynski Jayich, J. D. Thompson, and J. G. E. Harris, "High quality mechanical and optical properties of commercial silicon nitride membranes," *Applied Physics Letters*, vol. 92, no. 10, p. 103125, 2008. [Online]. Available: https://doi.org/10.1063/1.2884191

[29] J. D. Thompson, B. M. Zwickl, A. M. Jayich, F. Marquardt, S. M. Girvin, and J. G. Harris, "Strong dispersive coupling of a high-finesse cavity to a micromechanical membrane," *Nature*, vol. 452, no. 7183, pp. 72–75, 2008.

[30] S. Gröblacher, K. Hammerer, M. R. Vanner, and M. Aspelmeyer, "Observation of strong coupling between a micromechanical resonator and an optical cavity field," *Nature*, vol. 460, no. 7256, pp. 724–727, aug 2009. [Online]. Available: http://www.nature.com/articles/nature08171

[31] E. Verhagen, S. Deléglise, S. Weis, A. Schliesser, and T. J. Kippenberg, "Quantum-coherent coupling of a mechanical oscillator to an optical cavity mode," *Nature*, vol. 482, no. 7383, pp. 63–67, 2012.

[32] J. D. Teufel, T. Donner, D. Li, J. W. Harlow, M. S. Allman, K. Cicak, A. J. Sirois, J. D. Whittaker, K. W. Lehnert, and R. W. Simmonds, "Sideband cooling of micromechanical motion to the quantum ground state," *Nature*, vol. 475, pp. 359 EP –, jul 2011. [Online]. Available: https://doi.org/10.1038/nature10261

[33] M. Rossi, D. Mason, J. Chen, Y. Tsaturyan, and A. Schliesser, "Measurement-based quantum control of mechanical motion," *Nature*, vol. 563, no. 7729, pp. 53–58, nov 2018. [Online]. Available: https://doi.org/10.1038/s41586-018-0643-8http://www.nature.com/articles/s41586-018-0643-8

[34] F. Tebbenjohanns, M. L. Mattana, M. Rossi, M. Frimmer, and L. Novotny, "Quantum control of a nanoparticle optically levitated in cryogenic free space," *Nature*, vol. 595, 2021. [Online]. Available: https://doi.org/10.1038/s41586-021-03617-w

[35] U. Delić, M. Reisenbauer, D. Grass, N. Kiesel, V. Vuletić, and M. Aspelmeyer, "Cavity Cooling of a Levitated Nanosphere by Coherent Scattering," *Physical Review Letters*, vol. 122, no. 12, pp. 1–6, 2019.

[36] D. Windey, C. Gonzalez-Ballestero, P. Maurer, L. Novotny, O. Romero-Isart, and R. Reimann, "Cavity-Based 3D Cooling of a Levitated Nanoparticle via Coherent Scattering," *Physical Review Letters*, vol. 122, no. 12, pp. 1–5, 2019.

[37] U. Delić, M. Reisenbauer, K. Dare, D. Grass, V. Vuletić, N. Kiesel, and M. Aspelmeyer, "Cooling of a levitated nanoparticle to the motional quantum ground state," *Science*, vol. 367, no. 6480, pp. 892–895, 2020.

[38] J. Guo, R. Norte, and S. Gröblacher, "Feedback Cooling of a Room Temperature Mechanical Oscillator close to its Motional Ground State," *Physical Review Letters*, vol. 123, p. 223602, 2019.

[39] C. Whittle, E. D. Hall, S. Dwyer, N. Mavalvala, V. Sudhir, R. Abbott, A. Ananyeva, C. Austin, L. Barsotti, J. Betzwieser, C. D. Blair, A. F. Brooks, D. D. Brown, A. Buikema, C. Cahillane, J. C. Driggers, A. Effler, A. Fernandez-Galiana, P. Fritschel, V. V. Frolov, T. Hardwick, M. Kasprzack, K. Kawabe, N. Kijbunchoo, J. S. Kissel, G. L. Mansell, F. Matichard, L. McCuller, T. McRae, A. Mullavey, A. Pele, R. M. Schofield, D. Sigg, M. Tse, G. Vajente, D. C. Vander-Hyde, H. Yu, H. Yu, C. Adams, R. X. Adhikari, S. Appert, K. Arai, J. S. Areeda, Y. Asali, S. M. Aston, A. M. Baer, M. Ball, S. W. Ballmer, S. Banagiri, D. Barker, J. Bartlett, B. K. Berger, D. Bhattacharjee, G. Billingsley, S. Biscans, R. M. Blair, N. Bode, P. Booker, R. Bork, A. Bramley, K. C. Cannon, X. Chen, A. A. Ciobanu, F. Clara, C. M. Compton, S. J. Cooper, K. R. Corley, S. T. Countryman, P. B. Covas, D. C. Coyne, L. E. Datrier, D. Davis, C. Di Fronzo, K. L. Dooley, P. Dupej, T. Etzel, M. Evans, T. M. Evans, J. Feicht, P. Fulda, M. Fyffe, J. A. Giaime, K. D. Giardina, P. Godwin, E. Goetz, S. Gras, C. Gray, R. Gray, A. C. Green, E. K. Gustafson, R. Gustafson, J. Hanks, J. Hanson, R. K. Hasskew, M. C. Heintze, A. F. Helmling-Cornell, N. A. Holland, J. D. Jones, S. Kandhasamy, S. Karki, P. J. King, R. Kumar, M. Landry, B. B. Lane, B. Lantz, M. Laxen, Y. K. Lecoeuche, J. Leviton, J. Liu, M. Lormand, A. P. Lundgren, R. Macas, M. MacInnis, D. M. Macleod, S. Márka, Z. Márka, D. V. Martynov, K. Mason, T. J. Massinger, R. McCarthy, D. E. McClelland, S. McCormick, J. McIver, G. Mendell, K. Merfeld, E. L. Merilh, F. Meylahn, T. Mistry, R. Mittleman, G. Moreno,

C. M. Mow-Lowry, S. Mozzon, T. J. Nelson, P. Nguyen, L. K. Nuttall, J. Oberling, R. J. Oram, C. Osthelder, D. J. Ottaway, H. Overmier, J. R. Palamos, W. Parker, E. Payne, R. Penhorwood, C. J. Perez, M. Pirello, H. Radkins, K. E. Ramirez, J. W. Richardson, K. Riles, N. A. Robertson, J. G. Rollins, C. L. Romel, J. H. Romie, M. P. Ross, K. Ryan, T. Sadecki, E. J. Sanchez, L. E. Sanchez, T. R. Saravanan, R. L. Savage, D. Schaetz, R. Schnabel, E. Schwartz, D. Sellers, T. Shaffer, B. J. Slagmolen, J. R. Smith, S. Soni, B. Sorazu, A. P. Spencer, K. A. Strain, L. Sun, M. J. Szczepa czyk, M. Thomas, P. Thomas, K. A. Thorne, K. Toland, C. I. Torrie, G. Traylor, A. L. Urban, G. Valdes, P. J. Veitch, K. Venkateswara, G. Venugopalan, A. D. Viets, T. Vo, C. Vorvick, M. Wade, R. L. Ward, J. Warner, B. Weaver, R. Weiss, B. Willke, C. C. Wipf, L. Xiao, H. Yamamoto, L. Zhang, M. E. Zucker, and J. Zweizig, "Approaching the motional ground state of a 10-kg object," *Science*, vol. 372, no. 6548, pp. 1333–1336, 2021.

[40] S. A. Saarinen, N. Kralj, E. C. Langman, Y. Tsaturyan, and A. Schliesser, "Laser cooling a membrane-in-the-middle system close to the quantum ground state from room temperature," *Optica*, vol. 10, no. 3, p. 364, mar 2023. [Online]. Available: https://opg.optica.org/viewmedia.cfm?uri=optica-10-3-364&seq=0&html=truehttps://opg.optica.org/abstract.cfm?uri=optica-10-3-364https://opg.optica.org/optica/abstract.cfm?uri=optica-10-3-364

[41] R. Riedinger, S. Hong, R. A. Norte, J. A. Slater, J. Shang, A. G. Krause, V. Anant, M. Aspelmeyer, and S. Gröblacher, "Non-classical correlations between single photons and phonons from a mechanical oscillator," *Nature*, vol. 530, no. 7590, pp. 313–316, feb 2016. [Online]. Available: http://www.nature.com/articles/nature16536

[42] D. J. Wilson, V. Sudhir, N. Piro, R. Schilling, A. Ghadimi, and T. J. Kippenberg, "Measurement-based control of a mechanical oscillator at its thermal decoherence rate," *Nature*, vol. 524, no. 7565, pp. 325–329, 2015.

[43] D. Mason, J. Chen, M. Rossi, Y. Tsaturyan, and A. Schliesser, "Continuous force and displacement measurement below the standard quantum limit," *Nature Physics*, vol. 15, no. 8, pp. 745–749, 2019. [Online]. Available: https://arxiv.org/abs/1809.10629

[44] J. Chen, M. Rossi, D. Mason, and A. Schliesser, "Entanglement of propagating optical modes via a mechanical interface," *Nature Communications*, vol. 11, no. 1, 2020. [Online]. Available: https://doi.org/10.1038/s41467-020-14768-1

[45] R. Riedinger, A. Wallucks, I. Marinković, C. Löschnauer, M. Aspelmeyer, S. Hong, and S. Gröblacher, "Remote quantum entanglement between

two micromechanical oscillators," in *Nature*, vol. 556, no. 7702, 2018, pp. 473–477. [Online]. Available: https://doi.org/10.1038/s41586-018-0036-z

[46] J. F. Clauser, M. A. Horne, A. Shimony, and R. A. Holt, "Proposed experiment to test local hidden-variable theories," *Phys. Rev. Lett.*, vol. 23, pp. 880–884, Oct 1969. [Online]. Available: https://link.aps.org/doi/10.1103/PhysRevLett.23.880

[47] I. Marinković, A. Wallucks, R. Riedinger, S. Hong, M. Aspelmeyer, and S. Gröblacher, "Optomechanical bell test," *Phys. Rev. Lett.*, vol. 121, p. 220404, Nov 2018. [Online]. Available: https://link.aps.org/doi/10.1103/PhysRevLett.121.220404

[48] Y. Chu and S. Gröblacher, "A perspective on hybrid quantum opto- And electromechanical systems," *Applied Physics Letters*, vol. 117, no. 15, 2020.

[49] S. Barzanjeh, A. Xuereb, S. Gröblacher, M. Paternostro, C. A. Regal, and E. M. Weig, "Optomechanics for quantum technologies," *Nature Physics*, vol. 18, no. 1, pp. 15–24, 2022.

[50] G. Kurizki, P. Bertet, Y. Kubo, K. Mølmer, D. Petrosyan, P. Rabl, and J. Schmiedmayer, "Quantum technologies with hybrid systems," *Proceedings of the National Academy of Sciences of the United States of America*, 2015. [Online]. Available: www.pnas.org/cgi/doi/10.1073/pnas.1419326112

[51] V. Giovannetti, S. Lloyd, and L. MacCone, "Advances in quantum metrology," *Nature Photonics*, vol. 5, no. 4, pp. 222–229, 2011.

[52] C. L. Degen, F. Reinhard, and P. Cappellaro, "Quantum sensing," *Rev. Mod. Phys.*, vol. 89, p. 035002, Jul 2017. [Online]. Available: https://link.aps.org/doi/10.1103/RevModPhys.89.035002

[53] T. D. Ladd, F. Jelezko, R. Laflamme, Y. Nakamura, C. Monroe, and J. L. O'Brien, "Quantum computers," *Nature*, vol. 464, no. 7285, pp. 45–53, 2010.

[54] D. Wang, J. Wu, and X. Yi, "Optical quantum computing," *Proceedings - International Conference on Natural Computation*, vol. 2016-January, no. December, pp. 390–397, 2016.

[55] P. Krantz, M. Kjaergaard, F. Yan, T. P. Orlando, S. Gustavsson, and W. D. Oliver, "A quantum engineer's guide to superconducting qubits," *Applied Physics Reviews*, vol. 6, no. 2, 2019.

[56] N. Lauk, N. Sinclair, S. Barzanjeh, J. P. Covey, M. Saffman, M. Spiropulu, and C. Simon, "Perspectives on quantum transduction," *Quantum Science and Technology*, vol. 5, no. 2, 2020.

[57] N. Gisin and R. Thew, "Quantum communication," *Nature Photonics*, vol. 1, pp. 165–171, 2007.

[58] N. Gisin, G. Ribordy, W. Tittel, and H. Zbinden, "Quantum cryptography," *Reviews of Modern Physics*, vol. 74, no. 1, pp. 145–195, mar 2002. [Online]. Available: https://link.aps.org/doi/10.1103/RevModPhys.74.145

[59] J. I. Cirac, P. Zoller, H. J. Kimble, and H. Mabuchi, "Quantum State Transfer and Entanglement Distribution among Distant Nodes in a Quantum Network," *Physical Review Letters*, vol. 78, no. 16, pp. 3221–3224, 1997.

[60] H. J. Kimble, "The quantum internet," *Nature*, vol. 453, no. 7198, pp. 1023–1030, jun 2008. [Online]. Available: https://doi.org/10.1038/nature07127

[61] H. J. Briegel, W. Dür, J. I. Cirac, and P. Zoller, "Quantum repeaters: The role of imperfect local operations in quantum communication," *Physical Review Letters*, vol. 81, no. 26, pp. 5932–5935, dec 1998. [Online]. Available: https://link.aps.org/doi/10.1103/PhysRevLett.81.5932

[62] A. I. Lvovsky, B. C. Sanders, and W. Tittel, "Optical quantum memory," *Nature Photonics*, vol. 3, no. 12, pp. 706–714, dec 2009. [Online]. Available: https://www.nature.com/articles/nphoton.2009.231

[63] U. Gaubatz, P. Rudecki, S. Schiemann, and K. Bergmann, "Population transfer between molecular vibrational levels by stimulated Raman scattering with partially overlapping laser fields. A new concept and experimental results," *Journal of Chemical Physics*, vol. 92, no. 9, pp. 5363–5376, May 1990.

[64] M. Fleischhauer and M. D. Lukin, "Dark-state polaritons in electromagnetically induced transparency," *Phys. Rev. Lett.*, vol. 84, pp. 5094–5097, May 2000. [Online]. Available: https://link.aps.org/doi/10.1103/PhysRevLett.84.5094

[65] C. Liu, Z. Dutton, C. H. Behroozi, and L. V. Hau, "Observation of coherent optical information storage in an atomic medium using halted light pulses," *Nature*, vol. 409, no. 6819, pp. 490–493, Jan 2001. [Online]. Available: https://doi.org/10.1038/35054017

[66] L.-M. Duan, M. D. Lukin, J. I. Cirac, and P. Zoller, "Long-distance quantum communication with atomic ensembles and linear optics," *Nature*, vol. 414, no. 6862, pp. 413–418, Nov 2001. [Online]. Available: https://doi.org/10.1038/35106500

[67] B. Julsgaard, J. Sherson, J. I. Cirac, J. Fiurášek, and E. S. Polzik, "Experimental demonstration of quantum memory for light," *Nature*, vol. 432, no. 7016, pp. 482–486, Nov 2004. [Online]. Available: https://doi.org/10.1038/nature03064

[68] A. V. Gorshkov, A. André, M. Fleischhauer, A. S. Sørensen, and M. D. Lukin, "Universal approach to optimal photon storage in atomic media," *Phys. Rev. Lett.*, vol. 98, p. 123601, Mar 2007. [Online]. Available: https://link.aps.org/doi/10.1103/PhysRevLett.98.123601

[69] M. Fleischhauer, A. Imamoglu, and J. P. Marangos, "Electromagnetically induced transparency: Optics in coherent media," Tech. Rep. 2, 2005.

[70] A. Schliesser, "Cavity Optomechanics and Optical Frequency Comb Generation with Silica Whispering-Gallery-Mode Microresonators," Ph.D. dissertation, Ludwig–Maximilians–Universität, oct 2009. [Online]. Available: papers3://publication/uuid/B5659D20-E155-4B17-99D4-52679EB8C884

[71] S. Weis, R. Rivière, S. Deléglise, E. Gavartin, O. Arcizet, A. Schliesser, and T. J. Kippenberg, "Optomechanically Induced Transparency," *Science*, vol. 330, no. 6010, pp. 1520–1523, 2010. [Online]. Available: http://science.sciencemag.org/content/330/6010/1520

[72] A. H. Safavi-Naeini, T. P. Alegre, J. Chan, M. Eichenfield, M. Winger, Q. Lin, J. T. Hill, D. E. Chang, and O. Painter, "Electromagnetically induced transparency and slow light with optomechanics," *Nature*, vol. 472, no. 7341, pp. 69–73, 2011. [Online]. Available: https://www.nature.com/articles/nature09933.pdf

[73] S. Zaske, A. Lenhard, C. A. Keßler, J. Kettler, C. Hepp, C. Arend, R. Albrecht, W. M. Schulz, M. Jetter, P. Michler, and C. Becher, "Visible-to-telecom quantum frequency conversion of light from a single quantum emitter," *Physical Review Letters*, vol. 109, no. 14, pp. 1–5, 2012.

[74] Y. Tsaturyan, A. Barg, E. S. Polzik, and A. Schliesser, "Ultracoherent nanomechanical resonators via soft clamping and dissipation dilution," *Nature Nanotechnology*, vol. 12, no. 8, pp. 776–783, Aug 2017. [Online]. Available: https://doi.org/10.1038/nnano.2017.101

[75] G. S. MacCabe, H. Ren, J. Luo, J. D. Cohen, H. Zhou, A. Sipahigil, M. Mirhosseini, and O. Painter, "Nano-acoustic resonator with ultralong phonon lifetime," *Science*, vol. 370, no. 6518, pp. 840–843, 2020. [Online]. Available: http://science.sciencemag.org/

[76] A. Beccari, D. A. Visani, S. A. Fedorov, M. J. Bereyhi, V. Boureau, N. J. Engelsen, and T. J. Kippenberg, "Strained crystalline nanomechanical resonators with quality factors above 10 billion," *Nature Physics*, vol. 18, no. 4, pp. 436–441, 2022. [Online]. Available: http://arxiv.org/abs/2107.02124

[77] M. J. Bereyhi, A. Beccari, R. Groth, S. A. Fedorov, A. Arabmoheghi, T. J. Kippenberg, and N. J. Engelsen, "Hierarchical tensile structures with ultralow mechanical dissipation," *Nature Communications*, vol. 13, no. 1, 2022. [Online]. Available: http://arxiv.org/abs/2103.09785

[78] Y. Seis, T. Capelle, E. Langman, S. Saarinen, E. Planz, and A. Schliesser, "Ground state cooling of an ultracoherent electromechanical system," *Nature Communications*, vol. 13, no. 1, 2022.

[79] V. Fiore, Y. Yang, M. C. Kuzyk, R. Barbour, L. Tian, and H. Wang, "Storing optical information as a mechanical excitation in a silica optomechanical resonator," *Phys. Rev. Lett.*, vol. 107, p. 133601, Sep 2011. [Online]. Available: https://link.aps.org/doi/10.1103/PhysRevLett.107.133601

[80] D. P. Lake, M. Mitchell, D. D. Sukachev, and P. E. Barclay, "Processing light with an optically tunable mechanical memory," *Nature Communications*, vol. 12, no. 1, p. 663, Jan. 2021, number: 1 Publisher: Nature Publishing Group. [Online]. Available: https://www.nature.com/articles/s41467-021-20899-w

[81] B. Stiller, M. Merklein, C. Wolff, K. Vu, P. Ma, S. J. Madden, and B. J. Eggleton, "Coherently refreshing hypersonic phonons for light storage," *Optica*, vol. 7, no. 5, pp. 492–497, May 2020. [Online]. Available: https://opg.optica.org/optica/abstract.cfm?URI=optica-7-5-492

[82] T. A. Palomaki, J. W. Harlow, J. D. Teufel, R. W. Simmonds, and K. W. Lehnert, "Coherent state transfer between itinerant microwave fields and a mechanical oscillator," *Nature*, vol. 495, no. 7440, pp. 210–214, Mar 2013. [Online]. Available: https://doi.org/10.1038/nature11915

[83] P. Magnard, S. Storz, P. Kurpiers, J. Schär, F. Marxer, J. Lütolf, T. Walter, J.-C. Besse, M. Gabureac, K. Reuer, A. Akin, B. Royer, A. Blais, and A. Wallraff, "Microwave quantum link between superconducting circuits housed in spatially separated cryogenic systems," *Phys. Rev. Lett.*, vol. 125, p. 260502, Dec 2020. [Online]. Available: https://link.aps.org/doi/10.1103/PhysRevLett.125.260502

[84] A. Wallucks, I. Marinković, B. Hensen, R. Stockill, and S. Gröblacher, "A quantum memory at telecom wavelengths," *Nature Physics*, vol. 16, no. 7, pp. 772–777, Jul 2020. [Online]. Available: https://doi.org/10.1038/s41567-020-0891-z

[85] A. M. Jayich, J. C. Sankey, B. M. Zwickl, C. Yang, J. D. Thompson, S. M. Girvin, A. A. Clerk, F. Marquardt, and J. G. Harris, "Dispersive optomechanics: A membrane inside a cavity," *New Journal of Physics*, vol. 10, 2008.

[86] P. W. Milonni and J. H. Eberly, *Laser Physics*. John Wiley & Sons, Inc., 2010.

[87] P. Meystre and M. S. III, *Elements of Quantum Optics*. Springer verlag Berlin Heidelberg, 2010.

[88] S. Schmid, L. G. Villanueva, and M. L. Roukes, *Fundamentals of Nanomechanical Resonators*. Springer, 2016.

[89] L. Catalini, M. Rossi, E. C. Langman, and A. Schliesser, "Modeling and Observation of Nonlinear Damping in Dissipation-Diluted Nanomechanical Resonators," *Physical Review Letters*, vol. 126, no. 17, 2021.

[90] L. Catalini, "Nonlinear phenomena in dissipation diluted nanomechanical resonators," Ph.D. dissertation, PhD School of Science at the University of Copenhagen, 2022.

[91] M. Rossi, "Quantum measurement and control of a mechanical resonator," Ph.D. dissertation, PhD School of Science at the University of Copenhagen, 2020.

[92] L. Landau and E. M. Lifshitz, *Theory of Elasticity*. Butterworth Heinemann, 1986.

[93] B. Lautrup, *Physics of Continuous Matter*. cRC Press, 2011.

[94] P. G. Ciarlet, "A justification of the von kármán equations," *Archive for Rational Mechanics and Analysis*, vol. 73, no. 4, pp. 349–389, Dec 1980. [Online]. Available: https://doi.org/10.1007/BF00247674

[95] P. L. Yu, T. P. Purdy, and C. A. Regal, "Control of material damping in High-Q membrane microresonators," *Physical Review Letters*, vol. 108, no. 8, pp. 1–5, 2012.

[96] C. Zener, *Elasticity and anelasticity of metals*. University of Chicago Press, 1948.

[97] E. H. Kennard, *Kinetic Theory of Gasses*, 1st ed. McGraw-Hill Book Company Inc., 1938.

[98] H. Y. M. Bao H. Yang and Y. Sun, "Energy Transfer Model for Squeeze-Film Air Damping in Low Vacuum," *Journal of Micromechanics and Microengineering*, no. 12, pp. 341–346, 2002.

[99] I. Wilson-Rae, "Intrinsic dissipation in nanomechanical resonators due to phonon tunneling," *Physical Review B - Condensed Matter and Materials Physics*, vol. 77, no. 24, pp. 1–31, 2008.

[100] G. D. Cole, I. Wilson-Rae, K. Werbach, M. R. Vanner, and M. Aspelmeyer, "Phonon-tunnelling dissipation in mechanical resonators," *Nature Communications*, vol. 2, no. 1, pp. 231–238, 2011. [Online]. Available: http://dx.doi.org/10.1038/ncomms1212

[101] I. Wilson-Rae, R. A. Barton, S. S. Verbridge, D. R. Southworth, B. Ilic, H. G. Craighead, and J. M. Parpia, "High-Q nanomechanics via destructive interference of elastic waves," *Physical Review Letters*, vol. 106, no. 4, pp. 1–4, 2011.

[102] A. Jöckel, M. T. Rakher, M. Korppi, S. Camerer, D. Hunger, M. Mader, and P. Treutlein, "Spectroscopy of mechanical dissipation in micromechanical membranes," *Applied Physics Letters*, vol. 99, no. 14, 2011.

[103] M. H. J. de Jong, M. A. ten Wolde, A. Cupertino, S. Gröblacher, P. G. Steeneken, and R. A. Norte, "Mechanical dissipation by substrate–mode coupling in SiN resonators," *Applied Physics Letters*, vol. 121, no. 3, p. 032201, 07 2022. [Online]. Available: https://doi.org/10.1063/5.0092894

[104] R. Lifshitz and M. Roukes, "Thermoelastic damping in micro- and nanomechanical systems," *Physical Review B - Condensed Matter and Materials Physics*, vol. 61, no. 8, pp. 5600–5609, 2000.

[105] L. G. Villanueva and S. Schmid, "Evidence of surface loss as ubiquitous limiting damping mechanism in SiN micro- and nanomechanical resonators," *Physical Review Letters*, vol. 113, no. 22, 2014.

[106] A. H. Ghadimi, S. A. Fedorov, N. J. Engelsen, M. J. Bereyhi, R. Schilling, D. J. Wilson, and T. J. Kippenberg, "Elastic strain engineering for ultralow mechanical dissipation," *Science*, vol. 360, no. 6390, pp. 764–768, 2018. [Online]. Available: https://www.science.org/doi/abs/10.1126/science.aar6939

[107] M. Xu, D. Shin, P. M. Sberna, R. van der Kolk, A. Cupertino, M. A. Bessa, and R. A. Norte, "High-Strength Amorphous Silicon Carbide for Nanomechanics," pp. 1–26, 2023. [Online]. Available: http://arxiv.org/abs/2307.01271

[108] G. D. Cole, P. L. Yu, K. Siquans, R. Moghadas Nia, J. Schmöle, J. Hoelscher-Obermaier, T. P. Purdy, W. Wieczorek, C. A. Regal,

and M. Aspelmeyer, "Tensile-strained InxGa1-xP membranes for cavity optomechanics," *Applied Physics Letters*, vol. 104, no. 20, 2014. [Online]. Available: http://dx.doi.org/10.1063/1.4879755

[109] M. Bückle, V. C. Hauber, G. D. Cole, C. Gärtner, U. Zeimer, J. Grenzer, and E. M. Weig, "Stress control of tensile-strained In1-xGaxP nanomechanical string resonators," *Applied Physics Letters*, vol. 113, no. 20, 2018. [Online]. Available: http://dx.doi.org/10.1063/1.5054076

[110] S. K. Manjeshwar, A. Ciers, F. Hellman, J. Bläsing, A. Strittmatter, and W. Wieczorek, "High-Q Trampoline Resonators from Strained Crystalline InGaP for Integrated Free-Space Optomechanics," *Nano Letters*, 2023.

[111] M. J. Bereyhi, A. Arabmoheghi, A. Beccari, S. A. Fedorov, G. Huang, T. J. Kippenberg, and N. J. Engelsen, "Perimeter Modes of Nanomechanical Resonators Exhibit Quality Factors Exceeding 109 at Room Temperature," *Physical Review X*, vol. 12, no. 2, 2022. [Online]. Available: http://arxiv.org/abs/2108.03615%0Ahttp://dx.doi.org/10.1103/PhysRevX.12.021036

[112] D. Shin, A. Cupertino, M. H. J. de Jong, P. G. Steeneken, M. A. Bessa, and R. A. Norte, "Spiderweb nanomechanical resonators via bayesian optimization: Inspired by nature and guided by machine learning," *Advanced Materials*, vol. 34, no. 3, p. 2106248, 2022. [Online]. Available: https://onlinelibrary.wiley.com/doi/abs/10.1002/adma.202106248

[113] D. Høj, F. Wang, W. Gao, U. B. Hoff, O. Sigmund, and U. L. Andersen, "Ultra-coherent nanomechanical resonators based on inverse design," *Nature Communications*, vol. 12, no. 1, pp. 1–8, 2021. [Online]. Available: http://dx.doi.org/10.1038/s41467-021-26102-4

[114] E. Yablonovitch, "Inhibited spontaneous emission in solid-state physics and electronics," *Phys. Rev. Lett.*, vol. 58, pp. 2059–2062, May 1987. [Online]. Available: https://link.aps.org/doi/10.1103/PhysRevLett.58.2059

[115] Y. Tsaturyan, A. Barg, A. Simonsen, L. G. Villanueva, S. Schmid, A. Schliesser, and E. S. Polzik, "Demonstration of suppressed phonon tunneling losses in phononic bandgap shielded membrane resonators for high-Q optomechanics," *Opt. Express*, vol. 22, no. 6, pp. 6810–6821, mar 2014. [Online]. Available: http://www.opticsexpress.org/abstract.cfm?URI=oe-22-6-6810

[116] C. B. Møller, R. A. Thomas, G. Vasilakis, E. Zeuthen, Y. Tsaturyan, M. Balabas, K. Jensen, A. Schliesser, K. Hammerer, and E. S. Polzik, "Quantum back-Action-evading measurement of motion in a negative mass reference frame," *Nature*, vol. 547, no. 7662, pp. 191–195, 2017.

[117] R. A. Thomas, M. Parniak, C. Østfeldt, C. B. Møller, C. Bærentsen, Y. Tsaturyan, A. Schliesser, J. Appel, E. Zeuthen, and E. S. Polzik, "Entanglement between distant macroscopic mechanical and spin systems," *Nature Physics*, vol. 17, no. 2, pp. 228–233, 2021.

[118] Y. Akahane, T. Asano, B.-S. Song, and S. Noda, "Fine-tuned high-q photonic-crystal nanocavity," *Opt. Express*, vol. 13, no. 4, pp. 1202–1214, Feb 2005. [Online]. Available: https://opg.optica.org/oe/abstract.cfm?URI=oe-13-4-1202

[119] Y. Tsaturyan, "Ultracoherent soft-clamped mechanical resonators for quantum cavity optomechanics," Ph.D. dissertation, PhD School of Science at the University of Copenhagen, 2019.

[120] M. Rossi, D. Mason, J. Chen, and A. Schliesser, "Observing and Verifying the Quantum Trajectory of a Mechanical Resonator," *Physical Review Letters*, vol. 123, no. 16, p. 163601, oct 2019. [Online]. Available: https://journals.aps.org/prl/abstract/10.1103/PhysRevLett.123.163601

[121] A. Kaushik, H. Kahn, and A. H. Heuer, "Wafer-level mechanical characterization of silicon nitride MEMS," *Journal of Microelectromechanical Systems*, vol. 14, no. 2, pp. 359–367, 2005.

[122] J. Kepler, *De cometis libelli tres*, 1619.

[123] E. F. Nichols and G. F. Hull, "A Preliminary Communication on the Pressure of Heat and Light Radiation," *Phys. Rev. (Series I)*, vol. 13, no. 5, pp. 307–320, nov 1901. [Online]. Available: https://link.aps.org/doi/10.1103/PhysRevSeriesI.13.307

[124] P. Lebedew, "Untersuchungen über die druckkräfte des lichtes," *Annalen der Physik*, vol. 311, no. 11, pp. 433–458, 1901. [Online]. Available: https://onlinelibrary.wiley.com/doi/abs/10.1002/andp.19013111102

[125] E. F. Nichols and G. F. Hull, "The pressure due to radiation. (second paper.)," *Physical Review (Series I)*, vol. 17, no. 2, pp. 91–104, 1903.

[126] V. Giovannetti and D. Vitali, "Phase-noise measurement in a cavity with a movable mirror undergoing quantum Brownian motion," *Phys. Rev. A*, vol. 63, no. 2, p. 23812, jan 2001. [Online]. Available: https://link.aps.org/doi/10.1103/PhysRevA.63.023812

[127] V. Dumont, S. Bernard, C. Reinhardt, A. Kato, M. Ruf, and J. C. Sankey, "Flexure-tuned membrane-at-the-edge optomechanical system," *Opt. Express*, vol. 27, no. 18, pp. 25 731–25 748, Sep 2019. [Online]. Available: https://opg.optica.org/oe/abstract.cfm?URI=oe-27-18-25731

[128] A. Barg, Y. Tsaturyan, E. Belhage, W. H. Nielsen, C. B. Møller, and A. Schliesser, "Measuring and imaging nanomechanical motion with laser light," *Applied Physics B: Lasers and Optics*, vol. 123, no. 1, pp. 1–8, 2017.

[129] A. Barg, "Optomechanics with soft-clamped silicon nitride membranes and carrier-mediated forces in coupled quantum wells," Ph.D. dissertation, PhD School of Science at the University of Copenhagen, 2018.

[130] M. B. Kristensen, "A laser interferometer for characterization of micromechanical resonators," 2019.

[131] J. Bechhoefer, "Feedback for physicists: A tutorial essay on contro," *Reviews of Modern Physics*, vol. 77, no. 3, pp. 783–836, 2005.

[132] M. Prevedelli, T. Freegarde, and T. W. Haensch, "Phase locking of grating-tuned diode lasers," p. 4, 1995. [Online]. Available: http://link.springer.com/10.12942/lrr-2005-4

[133] U. Schünemann, H. Engler, R. Grimm, M. Weidemüller, and M. Zielonkowski, "Simple scheme for tunable frequency offset locking of two lasers," *Review of Scientific Instruments*, vol. 70, p. 242, 1999. [Online]. Available: https://doi.org/10.1063/1.1149573

[134] D. Mason, "Dynamical behavior near exceptional points in an optomechanical system," Ph.D. dissertation, Faculty of the Graduate School of Yale University, 2018.

[135] J. Poirson, F. Bretenaker, M. Vallet, and A. L. Floch, "Analytical and experimental study of ringing effects in a fabry–perot cavity. application to the measurement of high finesses," *J. Opt. Soc. Am. B*, vol. 14, no. 11, pp. 2811–2817, Nov 1997. [Online]. Available: https://opg.optica.org/josab/abstract.cfm?URI=josab-14-11-2811

[136] M. J. Lawrence, B. Willke, M. E. Husman, E. K. Gustafson, and R. L. Byer, "Dynamic response of a fabry–perot interferometer," *J. Opt. Soc. Am. B*, vol. 16, no. 4, pp. 523–532, Apr 1999. [Online]. Available: https://opg.optica.org/josab/abstract.cfm?URI=josab-16-4-523

[137] S. K. Steensen, "Two-dimensional phononic bandgap devices for ultracoherent mechanical modes," 2017.

[138] C. Østfeldt, "Quantum optomechanics for hybrid spin-membrane entanglement," Ph.D. dissertation, PhD School of Science at the University of Copenhagen, 2022.

[139] B. Lounis and M. Orrit, "Single-photon sources," *Reports on Progress in Physics*, vol. 68, no. 5, pp. 1129–1179, 2005.

[140] P. Lodahl, S. Mahmoodian, and S. Stobbe, "Interfacing single photons and single quantum dots with photonic nanostructures," *Reviews of Modern Physics*, vol. 87, no. 2, pp. 347–400, 2015.

[141] R. Uppu, F. T. Pedersen, Y. Wang, C. T. Olesen, C. Papon, X. Zhou, L. Midolo, S. Scholz, A. D. Wieck, A. Ludwig, and P. Lodahl, "Scalable integrated single-photon source," *Science Advances*, vol. 6, no. 50, dec 2020. [Online]. Available: https://www.science.orghttps://www.science.org/doi/10.1126/sciadv.abc8268

[142] N. Tomm, A. Javadi, N. O. Antoniadis, D. Najer, M. C. Löbl, A. R. Korsch, R. Schott, S. R. Valentin, A. D. Wieck, A. Ludwig, and R. J. Warburton, "A bright and fast source of coherent single photons," *Nature Nanotechnology*, pp. 1–5, jan 2021. [Online]. Available: http://www.nature.com/articles/s41565-020-00831-x

[143] L. Béguin, J. P. Jahn, J. Wolters, M. Reindl, Y. Huo, R. Trotta, A. Rastelli, F. Ding, O. G. Schmidt, P. Treutlein, and R. J. Warburton, "On-demand semiconductor source of 780-nm single photons with controlled temporal wave packets," *Physical Review B*, vol. 97, no. 20, pp. 1–8, 2018.

[144] L. Zaporski, N. Shofer, J. H. Bodey, S. Manna, G. Gillard, M. H. Appel, C. Schimpf, S. F. Covre da Silva, J. Jarman, G. Delamare, G. Park, U. Haeusler, E. A. Chekhovich, A. Rastelli, D. A. Gangloff, M. Atatüre, and C. Le Gall, "Ideal refocusing of an optically active spin qubit under strong hyperfine interactions," *Nature Nanotechnology*, vol. 18, no. 3, pp. 257–263, 2023.

[145] J. Lavoie, J. M. Donohue, L. G. Wright, A. Fedrizzi, and K. J. Resch, "Spectral compression of single photons," *Nature Photonics*, vol. 7, no. 5, pp. 363–366, 2013. [Online]. Available: www.nature.com/naturephotonics

[146] M. Karpinski, M. Jachura, L. J. Wright, and B. J. Smith, "Bandwidth manipulation of quantum light by an electro-optic time lens," *Nature Photonics*, vol. 11, no. 1, pp. 53–57, 2017. [Online]. Available: www.nature.com/naturephotonics

[147] M. Allgaier, V. Ansari, L. Sansoni, C. Eigner, V. Quiring, R. Ricken, G. Harder, B. Brecht, and C. Silberhorn, "Highly efficient frequency conversion with bandwidth compression of quantum light," *Nature Communications*, vol. 8, pp. 1–6, 2017. [Online]. Available: http://dx.doi.org/10.1038/ncomms14288

[148] F. Sośnicki, M. Mikołajczyk, A. Golestani, and M. Karpiński, "Aperiodic electro-optic time lens for spectral manipulation of single-photon pulses,"

Applied Physics Letters, vol. 116, no. 23, p. 234003, jun 2020. [Online]. Available: https://aip.scitation.org/doi/abs/10.1063/5.0011077

[149] M. A. Seidler, X. J. Yeo, A. Cerè, and C. Kurtsiefer, "Spectral Compression of Narrowband Single Photons with a Resonant Cavity," *Physical Review Letters*, vol. 125, no. 18, 2020.

[150] J. Gil-Lopez, M. Santandrea, G. Roeland, B. Brecht, C. Eigner, R. Ricken, V. Quiring, and C. Silberhorn, "Improved non-linear devices for quantum applications," *New Journal of Physics*, vol. 23, no. 6, 2021.

[151] F. Sośnicki, M. Mikołajczyk, A. Golestani, and M. Karpiński, "Interface between picosecond and nanosecond quantum light pulses," *Nature Photonics*, pp. 1–7, 2023. [Online]. Available: http://arxiv.org/abs/2211.05112

[152] B. Da Lio, C. Faurby, X. Zhou, M. L. Chan, R. Uppu, H. Thyrrestrup, S. Scholz, A. D. Wieck, A. Ludwig, P. Lodahl, and L. Midolo, "A Pure and Indistinguishable Single-Photon Source at Telecommunication Wavelength," *Advanced Quantum Technologies*, vol. 5, no. 5, 2022.

[153] E. M. G. Ruiz, "Single-photon sources as a key resource for developing a global quantum network," Ph.D. dissertation, PhD School of Science at the University of Copenhagen, 2023.

[154] R. Valivarthi, M. G. Puigibert, Q. Zhou, G. H. Aguilar, V. B. Verma, F. Marsili, M. D. Shaw, S. W. Nam, D. Oblak, and W. Tittel, "Quantum teleportation across a metropolitan fibre network," *Nature Photonics*, vol. 10, no. 10, pp. 676–680, 2016.

[155] R. Stockill, M. Forsch, G. Beaudoin, K. Pantzas, I. Sagnes, R. Braive, and S. Gröblacher, "Gallium Phosphide as a Piezoelectric Platform for Quantum Optomechanics," *Physical Review Letters*, vol. 123, no. 16, p. 163602, oct 2019. [Online]. Available: https://link.aps.org/doi/10.1103/PhysRevLett.123.163602http://arxiv.org/abs/1909.07850http://dx.doi.org/10.1103/PhysRevLett.123.163602

[156] K. Schneider, Y. Baumgartner, S. Hönl, P. Welter, H. Hahn, D. J. Wilson, L. Czornomaz, and P. Seidler, "Optomechanics with one-dimensional gallium phosphide photonic crystal cavities," *Optica*, vol. 6, no. 5, p. 577, may 2019. [Online]. Available: https://doi.org/10.1364/OPTICA.6.000577https://www.osapublishing.org/abstract.cfm?URI=optica-6-5-577

[157] H. Ren, M. H. Matheny, G. S. MacCabe, J. Luo, H. Pfeifer, M. Mirhosseini, and O. Painter, "Two-dimensional optomechanical crystal cavity with high quantum cooperativity," *Nature*

Communications, vol. 11, no. 1, 2020. [Online]. Available: http://dx.doi.org/10.1038/s41467-020-17182-9

[158] C. J. Hood, H. J. Kimble, and J. Ye, "Characterization of high-finesse mirrors: Loss, phase shifts, and mode structure in an optical cavity," *Physical Review A - Atomic, Molecular, and Optical Physics*, vol. 64, no. 3, p. 7, 2001.

Appendices

A Cavity Finesse Characterization

The most important characterization of an assembled cavity is to quantify the optical losses, determining the cavity finesse. In the ideal case this is given by the mirror transmissivities, though in practice excess loss is always present. To measure the finese one needs to know both the cavity free spectral range and linewidth, see eq. (2.5), so here we describe our methods for determining both.

A.1 FSR Measurement

To measure the free spectral range, we utilize our ability to lock our two lasers at a controlled frequency offset. By then scanning over the cavity resonance and monitoring their joint reflection, we know the two lasers are detuned by the FSR, when the two reflection dips coincide, see figure A.1.

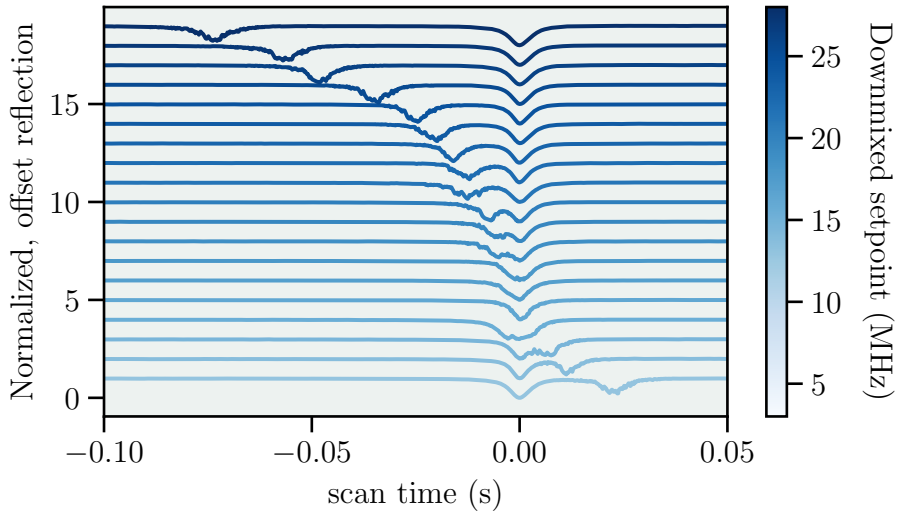

Figure A.1: Determination of the cavity free spectral range. We vary the setpoint of the downmixed beatnote of the two offset-locked lasers, while monitoring the cavity reflection. When the reflection dips coincide, the lasers are detuned by the free spectral range.

From the frequency of the downmixing synthesizer and the setpoint, we can then extract the cavity FSR. An alternative, but similar approach that one needs a single laser is to sweep the frequency of a phase modulation of said laser. If one scans more than one FSR over the cavity, the half-FSR can be identified when the upper and lower sidebands from each longitudinal mode overlap spectrally.

A.2 Linewidth Measurement

Our favourite approach to measure the cavity linewidth again involves a phase-modulated laser. In a scan over the resonance, one can use the fact that the two sidebands have a very well-defined frequency spacing from the carrier (or each other) to calibrate the abcissa from time to frequency. Alternatively, one can measure a cavity ringdown by recording the transmitted light as the cavity is tuned close to resonance and the input light is abruptly switched off, eg. with an intensity modulator.

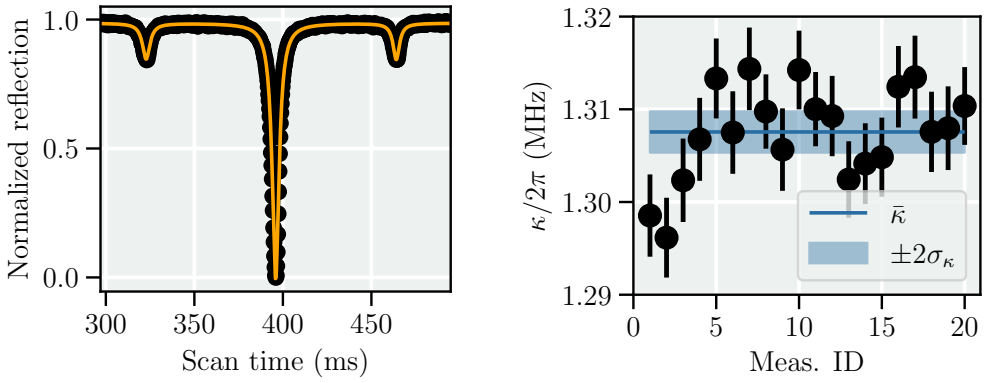

Figure A.2: Cavity linewidth from phase-modulated scans. Left: an expemplary trace of the normalized reflection in black with a fit to a model of three Lorentzian reflection dips in orange. Right: By repeating such measurements (black points, errorbars indicates ± twice the fit uncertainty) we can extract a mean value and standard error on the mean, indicated by the blue line and shaded area respectively.

The sideband calibration has the advantage of being simpler to repeat quickly, as is desirable in a characterization technique, since one scans over the resonance, rather than having to carefully approach it.

From a fit to three Lorentzian dips, we can extract the linewidth κ^{time} and spacing of the sidebands $\Delta_{\text{SB}}^{\text{time}}$ in time units. Knowing the modulation frequency Ω_{mod}, we can find the cavity linewidth κ in frequency units as

$$\kappa = 2\Omega_{\text{mod}} \frac{\kappa^{\text{time}}}{\Delta_{\text{SB}}^{\text{time}}}, \tag{A.1}$$

where $\Delta_{\text{SB}}^{\text{time}}$ defines the distance between the sidebands. In figure A.2 we illustrate this method, showing a reflection measurement and the extracted average linewidth from series of such measurements. In addition to this approach, used during cavity assembly, we also extract in-situ cavity linewidths from OMIT spectroscopy (as described in section 5.1.2).

A.3 Extracting the Excess Loss

With measurements of the FSR and linewidth, and knowledge of mirror transmissivities, we can now extract the excess loss of the cavity. This is an important number, since it tells us how well-aligned a membrane is, and misalignment typically manifests as additional loss. Additionally this excess loss leads to a reduced overcoupling, which translates to a reduced measurement efficiency. Figure A.3 illustates this approach. We plot the finesse as a function of excess loss, and extract the excess loss for our particular measurement from the measured finesse, as shown in figure A.3. With the excess loss determined, we can infer the overcoupling corresponding to the measured excess loss. In practice we never find excess-loss below $\approx 10 \times 10^{-6}$ and more typically around $\approx 20 \times 10^{-6}$, even for an empty cavity. This is roughly consistent with the specifications from the manufacturer of 5×10^{-6} per mirror, with measurements erring slightly on the higher side, which most likely is due to imperfect, though still good, cleanliness of the mirror faces.

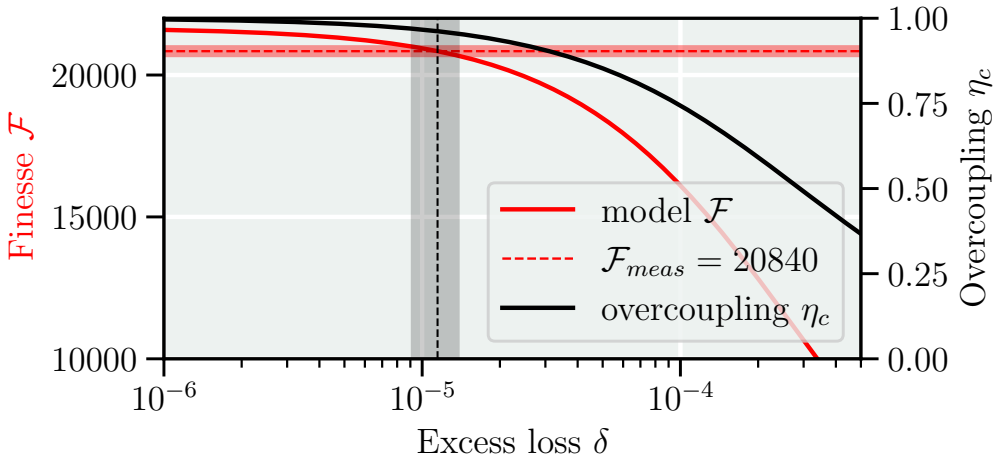

Figure A.3: Extraction of excess loss from finesse meaurements. In red we plot the finesse (solid red) for increasing excess loss and fixed mirror transmissivities ($|t_1|^2 = 280 \times 10^{-6}$, $|t_2|^2 = 10 \times 10^{-6}$) and identify the intersection of our measurement (dashed red). Simultaneously, we plot the overcoupling η_c in a similar manner, and infer the corresponding value, given the excess loss.

B TMM With a Misaligned Membrane

In this appendix we describe the principles of the membrane tilt simulations. The treatment will not be thorough, with the eager reader referred to the thesis of Christoffer Østfeldt [138].

The core idea is to extend the transfer-matrix method calculation of section 5.2 to encompass multiple optical modes. Additionally the multiple optical modes (that are eigenmodes for the cavity field and hence orthogonal) are coupled by scattering off the membrane. This scattering can either come about from tilt of the membrane, such that its normal is no longer parallel with the optical axis of the cavity, or from transverse misalignment of a phononic-crystal membrane, where light can diffract of phononic crystal holes, cf. figure B.1.

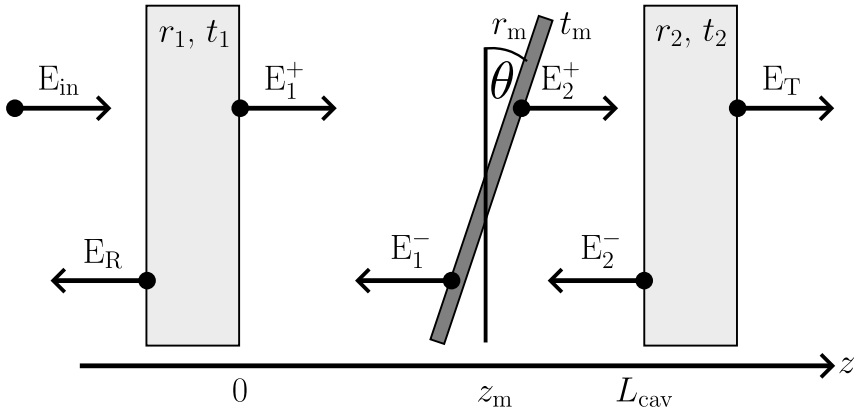

Figure B.1: TMM with a misaligned membrane. In contrast to the ideal case studied in 5.2, we now implement two tilt-angles θ_X and θ_Y of the membrane with respect to the cavity axis.

At a glance, the mathematical approach for treating these effects (again: details in [138]) is to first expand the propagating intra-cavity fields on a truncated eigenbasis. Then various coupling mechanisms can be included. For the present case we only consider the consequences of a tilted membrane, to benchmark which tilt angles can be tolerated. We present simulation results from the numerical model, for different angles of tilt. From the simulations (figures B.2-B.9), we identify $\theta = 1\,\mathrm{mrad}$ as the transition point for whether or not tilt couples the fundamental cavity mode to a higher order transverse mode from the lower longitudinal family in our cavity. The transverse mode order is encoded from (dark) blue over green through yellow to red representing increasingly higher order modes.

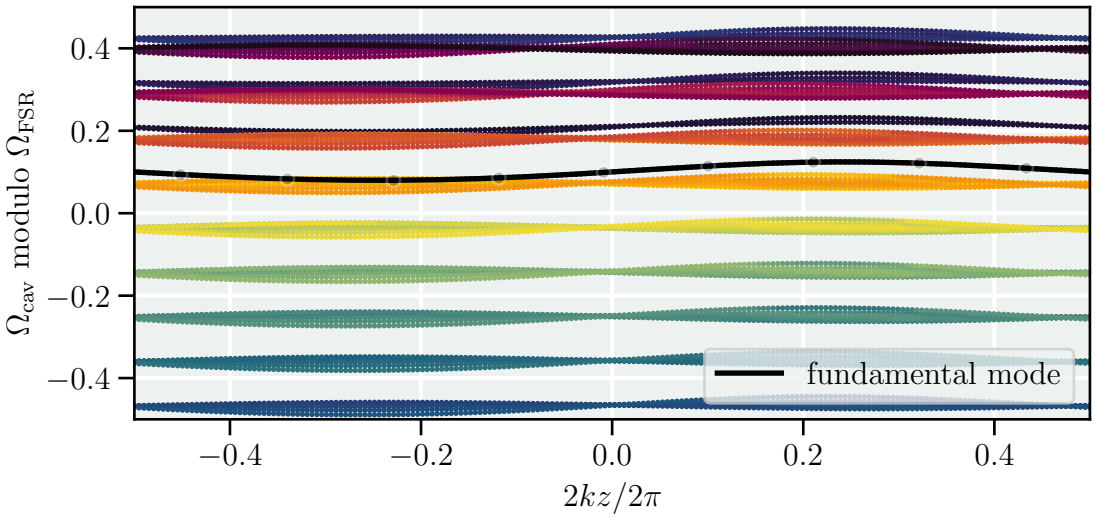

Figure B.2: Tilt-induced modecoupling for $\theta = 2\,\mathrm{mrad}$.

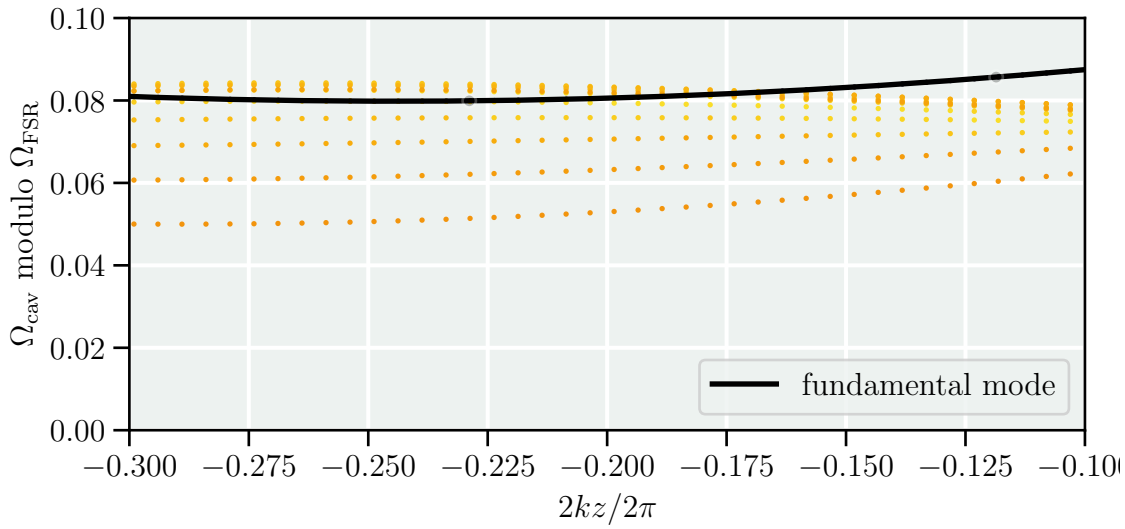

Figure B.3: Tilt-induced modecoupling for $\theta = 2\,\mathrm{mrad}$ zoomed on critical region.

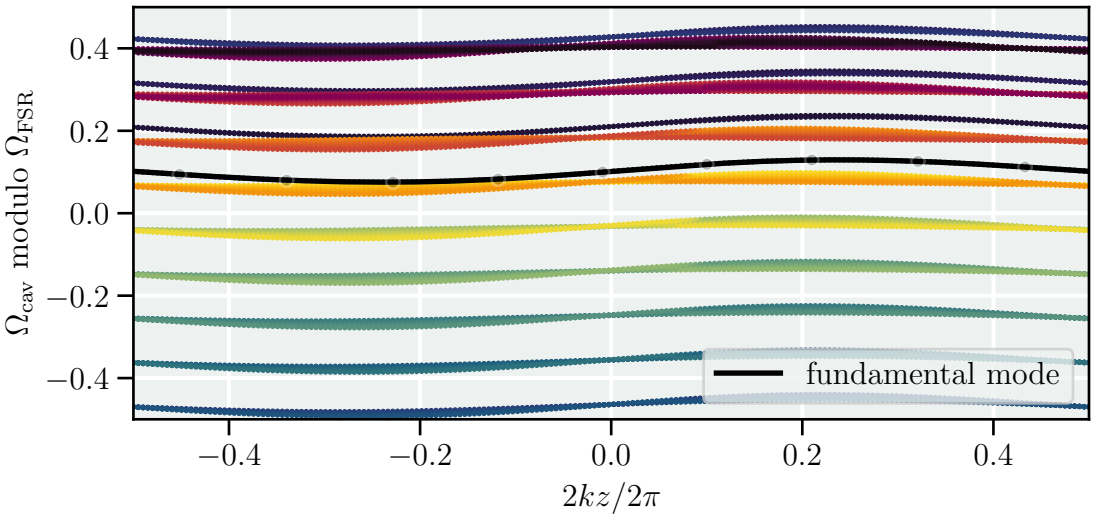

Figure B.4: Tilt-induced modecoupling for $\theta = 1\,\mathrm{mrad}$.

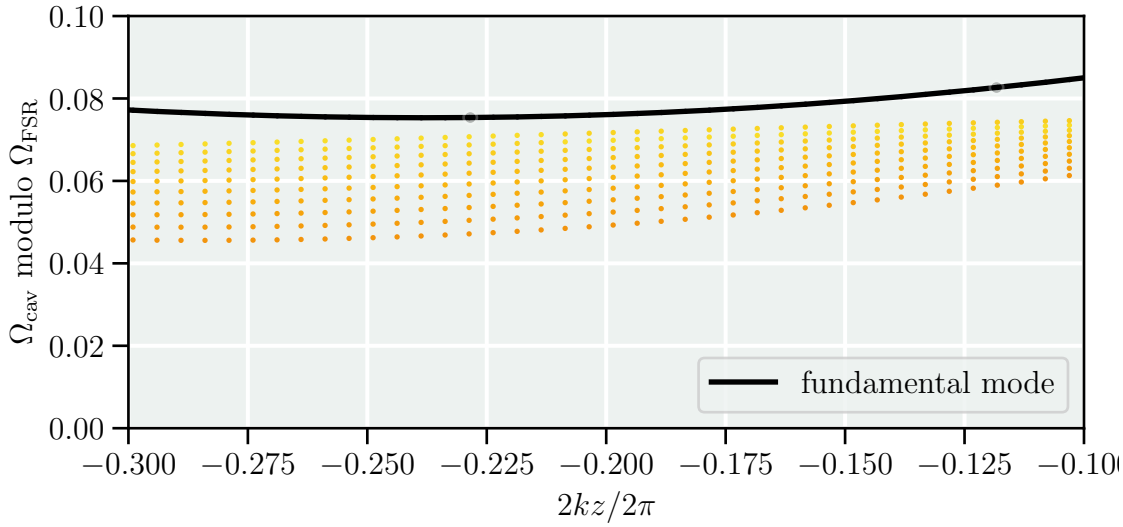

Figure B.5: Tilt-induced modecoupling for $\theta = 1\,\mathrm{mrad}$ zoomed on critical region.

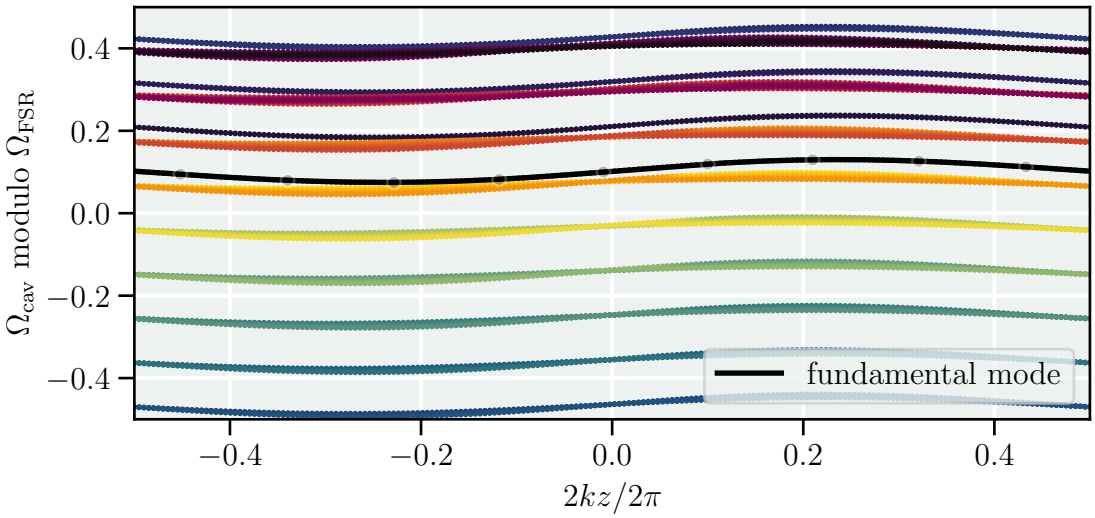

Figure B.6: Tilt-induced modecoupling for $\theta = 0.8\,\mathrm{mrad}$.

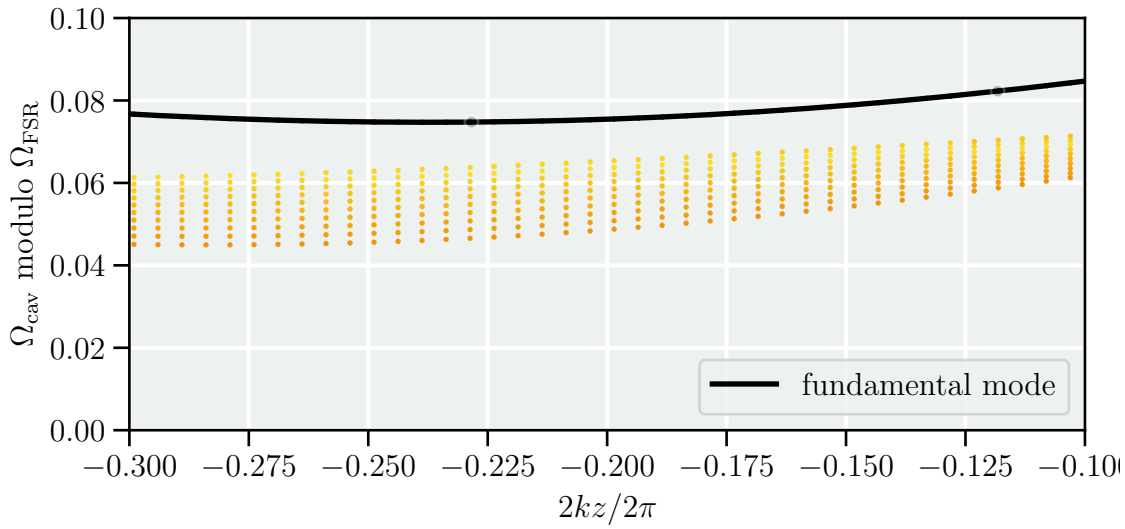

Figure B.7: Tilt-induced modecoupling for $\theta = 0.8\,\mathrm{mrad}$ zoomed on critical region.

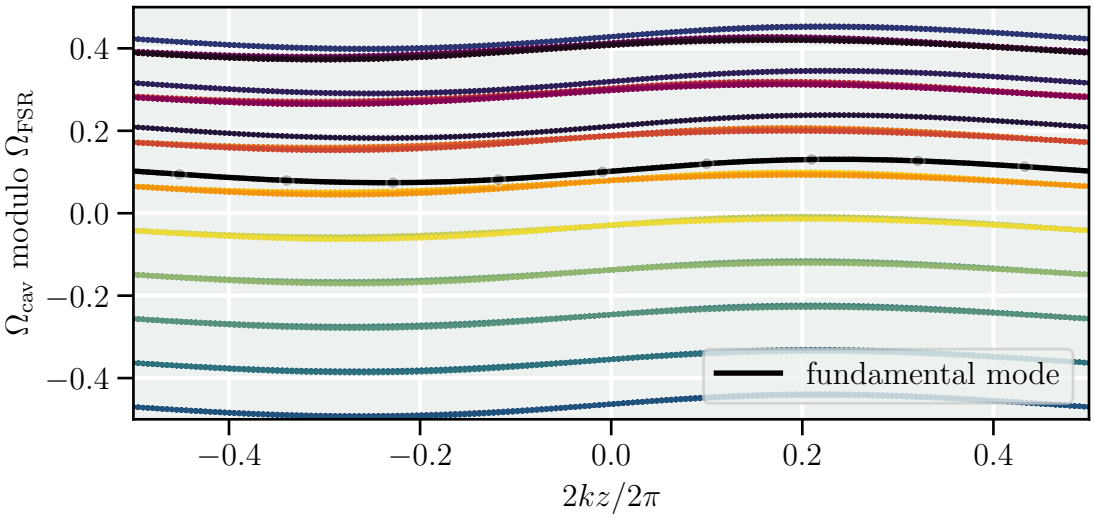

Figure B.8: Tilt-induced modecoupling for $\theta = 0.5\,\mathrm{mrad}$.

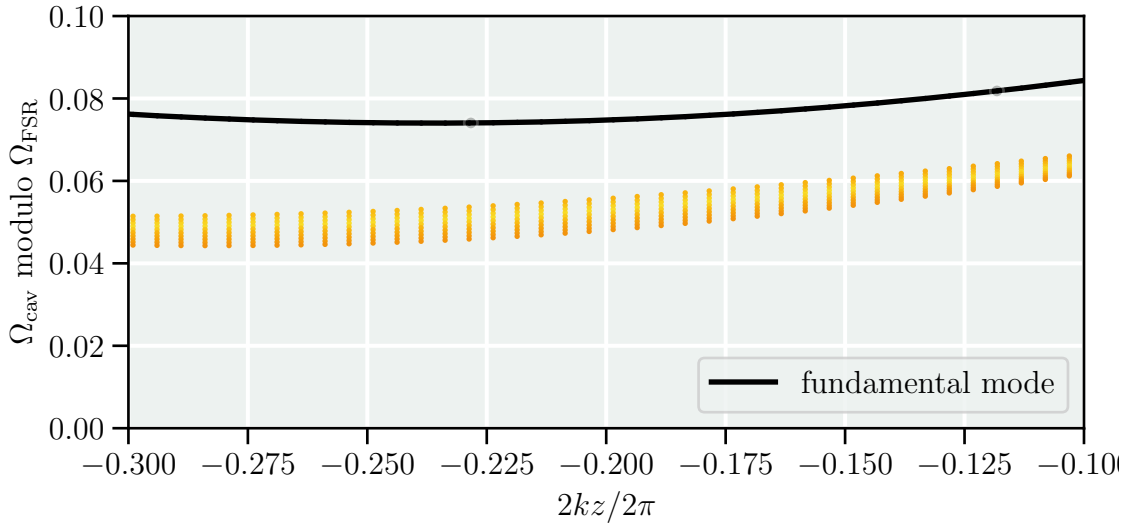

Figure B.9: Tilt-induced modecoupling for $\theta = 0.5\,\mathrm{mrad}$ zoomed on critical region.

C Cavity Mirrors

Here we describe the mirrors comprising the optomechanical cavity introduced in section 8.

Our mirrors are dielectric coatings of quarter-wave bi-layer stacks with alternating low- and high index materials [158], on fused Silica substrates. The substrates are from LayerTec and the coatings are done by Five Nine Optics.

We have a set of highly-reflective, plano-plano mirrors, with a specified power transmission $T_P = 10 \times 10^{-6}$ and slightly transmissive plano-concave with a radius of curvature ROC = 50 mm with transmission $T_C = 280 \times 10^{-6}$. The backside of each mirror is anti-reflection coated (specified $R < 0.01\%$). The specified transmission coefficients are for a wavelength $\lambda = 1550$ nm. The mirror transmissions for a range of wavelengths is shown in figure C.1, as measured by Five Nine Optics.

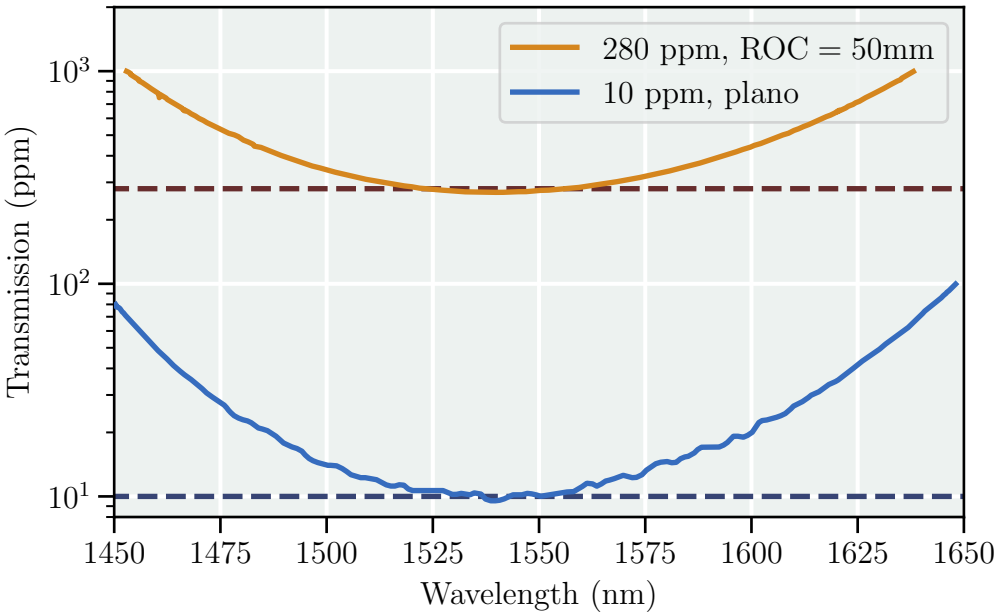

Figure C.1: Cavity mirror transmission curves. Data from Five Nine Optics. The plano-plano high-reflector coating curve is shown in blue, with $T_P = 10 \times 10^{-6}$ indicated by the dark blue dashed line. The data for the slightly transmissive curved mirror is plotted in orange with $T_C = 280 \times 10^{-6}$ indicated by the dark red dashed line.

D Single-Photon Experiment SNR Estimate

In this appendix we detail a calculation of the expected signal-to-noise ratio (SNR) in a single-photon input optomechanical quantum memory experiment.

D.1 Density matrix

We model loss and inefficiency as a beamsplitter and write the single photon state $|\psi\rangle$ to be detected after storage as

$$|\psi\rangle \coloneqq a^\dagger |0\rangle \to \sqrt{\eta} a_\parallel^\dagger |0\rangle + \sqrt{1-\eta} a_\perp^\dagger |0\rangle , \tag{D.1}$$

i.e. we detect the mode $a_\parallel^\dagger$ with probability η and loose a fraction $1-\eta$ to the mode $a_\perp^\dagger$ that we don't detect. We describe this through a reduced density matrix where we trace over the $\perp$ subspace. To do so, we first calculate the full density matrix

$$\begin{aligned}\rho = |\psi\rangle\langle\psi| = &\left(\sqrt{\eta} a_\parallel^\dagger |0\rangle + \sqrt{1-\eta} a_\perp^\dagger |0\rangle\right)\left(\langle 0| a_\parallel \sqrt{\eta} + \langle 0| a_\perp \sqrt{1-\eta}\right) \\ =&\eta |1_\parallel 0_\perp\rangle\langle 1_\parallel 0_\perp| + (1-\eta)|0_\parallel 1_\perp\rangle\langle 0_\parallel 1_\perp| + \\ &\sqrt{\eta(1-\eta)}\left(|1_\parallel 0_\perp\rangle\langle 0_\parallel 1_\perp| + |0_\parallel 1_\perp\rangle\langle 1_\parallel 0_\perp|\right).\end{aligned} \tag{D.2}$$

Then we trace over the $\perp$ subsystem,

$$\begin{aligned}\rho_\parallel =&\mathrm{Tr}_\perp[\rho] = \langle 0_\perp|\rho|0_\perp\rangle + \langle 1_\perp|\rho|1_\perp\rangle \\ =&\eta |1_\parallel\rangle\langle 1_\parallel| + (1-\eta)|0_\parallel\rangle\langle 0_\parallel|\end{aligned} \tag{D.3}$$

Since we only consider the $\parallel$ subsystem from now on, we will omit the subscripts.

D.2 Variance of quadratures

We will measure the variance some phase-space quadrature of the field described be the above density matrix. First we brush up a few basic equations. We define a general phase-space quadrature $X(\theta)$ as

$$X(\theta) = \sigma_0\left(a^\dagger e^{i\theta} + a e^{-i\theta}\right). \tag{D.4}$$

Here σ_0^2 is the variance of the ground state. We recall the variance of an operator A

$$\mathrm{var}(A) = \left\langle A^2 \right\rangle - \langle A \rangle^2 , \tag{D.5}$$

and expectation values

$$\langle A \rangle = \mathrm{Tr}\left[\rho A\right]. \tag{D.6}$$

We can now calculate $\mathrm{var}(X(\theta))$ using eq.D.5. We first find

$$\begin{aligned}
\langle X(\theta) \rangle &= \mathrm{Tr}\left[\rho X(\theta)\right] \\
&= \sigma_0 \langle 0| \left(\eta |1\rangle \langle 1| + (1-\eta) |0\rangle \langle 0|\right) \left(a^\dagger e^{i\theta} + a e^{-i\theta}\right) |0\rangle + \\
&\sigma_0 \langle 1| \left(\eta |1\rangle \langle 1| + (1-\eta) |0\rangle \langle 0|\right) \left(a^\dagger e^{i\theta} + a e^{-i\theta}\right) |1\rangle \\
&= 0.
\end{aligned} \tag{D.7}$$

The second moment,

$$\begin{aligned}
\left\langle (X(\theta))^2 \right\rangle = \sigma_0^2 \Big(& \langle 0| \left(a^\dagger a^\dagger e^{2i\theta} + aa e^{-2i\theta} + 2n + 1\right) \left(\eta |1\rangle \langle 1| + (1-\eta) |0\rangle \langle 0|\right) |0\rangle + \\
& \langle 1| \left(a^\dagger a^\dagger e^{2i\theta} + aa e^{-2i\theta} + 2n + 1\right) \left(\eta |1\rangle \langle 1| + (1-\eta) |0\rangle \langle 0|\right) |1\rangle \Big) \\
&= \sigma_0^2 \left((1-\eta) + \eta(1+2)\right) \\
&= \sigma_0^2 \left(1 + 2\eta\right).
\end{aligned} \tag{D.8}$$

From eq.D.5 we now find

$$\mathrm{var}(X(\theta)) = \sigma_0^2 (1 + 2\eta) \tag{D.9}$$

The two terms in this result can be interpreted as vacuum noise plus the signature of the single single photon.

D.3 Variance of the variance

As eq.D.9 shows, the actual quantity we want to measure is itself a variance. In order to estimate the uncertainty on our measurement we thus need a meaningful way of talking about variance as a fluctuating quantity, and in particular "the variance of the variance".

One approach is to consider the *sample variance* s^2. Consider N samples from a distribution with central moments μ_k. Then the sample variance is

$$s^2 = \frac{1}{N}\sum_{i=1}^{N}(X_i - \bar{X})^2, \tag{D.10}$$

where $\bar{X}$ is the sample mean. Using eq. D.5 we can write the variance of s^2 as

$$\mathrm{var}(s^2) = \left\langle s^4 \right\rangle - \left\langle s^2 \right\rangle^2. \tag{D.11}$$

We thus have to calculate $\langle s^2 \rangle$ and $\langle s^4 \rangle$. Starting with $\langle s^2 \rangle$:

$$\begin{aligned}
\left\langle s^2 \right\rangle &= \left\langle \frac{1}{N}\sum_{i=1}(X_i - \bar{X})^2 \right\rangle \\
&= \frac{1}{N}\left\langle \sum_{i=1}\left(X_i - \frac{1}{N}\sum_{j=1}X_j\right)^2 \right\rangle \\
&= \frac{1}{N}\left\langle \sum_{i=1}\left(X_i^2 - \frac{2}{N}X_i\sum_{j=1}X_j + \frac{1}{N^2}\sum_{j=1}X_j\sum_{k=1}X_k\right)\right\rangle \\
&= \frac{1}{N}\sum_{i=1}\left(\left\langle X_i^2\right\rangle(1-\frac{2}{N}) - \frac{2}{N}\left\langle X_i\sum_{j\neq i}X_j\right\rangle + \frac{1}{N^2}\sum_{j=1}\left\langle X_j^2\right\rangle + \frac{1}{N^2}\sum_{j\neq k}\langle X_jX_k\rangle\right)
\end{aligned} \tag{D.12}$$

where we have used the linearity of the expectation value and written out the square of a sum in two terms, one containing matching indices $i = j$ and one containing different indices $i \neq j$. Evaluating the sums gives:

$$\begin{aligned}
\left\langle s^2 \right\rangle &= \left\langle X^2 \right\rangle \frac{N-2+1}{N} + \langle X\rangle^2 \frac{2(N-1)}{N}(1-2) \\
&= \frac{N-1}{N}\left(\left\langle X^2\right\rangle - \langle X\rangle^2\right) \\
&= \frac{N-1}{N}\mu_2.
\end{aligned} \tag{D.13}$$

Which gives us the second term in eq.D.11. Writing out $\langle s^4 \rangle$

$$\begin{aligned}
\left\langle s^4 \right\rangle = \left\langle \left(s^2\right)^2 \right\rangle &= \left\langle \left[\frac{1}{N} \sum_i \left(X_i - \frac{1}{N} \sum_j X_j \right)^2 \right]^2 \right\rangle \\
&= \left\langle \frac{1}{N^2} \left[\sum_i X_i^2 - \frac{2}{N} \sum_i X_i \sum_j X_j + \frac{1}{N^2} \sum_i \left(\sum_j x_j \right)^2 \right]^2 \right\rangle \\
&= \left\langle \left[\frac{1}{N} \sum_i X_i^2 - \left(\frac{1}{N} \sum_i X_i \right)^2 \right]^2 \right\rangle \\
&= \frac{1}{N^2} \left\langle \left(\sum_i X_i^2 \right)^2 \right\rangle - \frac{2}{N^3} \left\langle \sum_i X_i^2 \left(\sum_j X_j \right)^2 \right\rangle + \frac{1}{N^4} \left\langle \left(\sum_j x_j \right)^4 \right\rangle .
\end{aligned} \tag{D.14}$$

It is now convenient to transform to a central variable $X_i \to X_i - \langle X \rangle$. This will allow us to drop any terms $\propto \langle X \rangle$ and does not affect the variance:

$$\begin{aligned}
\mathrm{var}(y - \langle y \rangle) &= \left\langle (y - \langle y \rangle)^2 \right\rangle - \langle y - \langle y \rangle \rangle^2 \\
&= \left\langle y^2 + \langle y \rangle^2 - 2y \langle y \rangle \right\rangle - (\langle y \rangle - \langle y \rangle)^2 \\
&= \left\langle y^2 \right\rangle - \langle y \rangle^2 = \mathrm{var}(y)
\end{aligned} \tag{D.15}$$

We attack one term at a time. The first term:

$$\begin{aligned}
\left\langle \left(\sum_i X_i^2 \right)^2 \right\rangle &= \left\langle \sum_i X_i^4 \right\rangle + \left\langle \sum_i \sum_{j \neq j} X_i^2 X_j^2 \right\rangle \\
&= N \left\langle X^4 \right\rangle + N(N-1) \left\langle X^2 \right\rangle^2 .
\end{aligned} \tag{D.16}$$

The second term:

$$\begin{aligned}
\left\langle \sum_i X_i^2 \left(\sum_j X_j \right)^2 \right\rangle &= \left\langle \sum_i X_i^2 \left(X_i + \sum_{j\neq i} X_j \right) \left(X_i + \sum_{k\neq i} X_k \right) \right\rangle \\
&= \left\langle \sum_i X_i^4 + \sum_i X_i^3 \sum_{k\neq i} X_k + \sum_i X_i^3 \sum_{j\neq i} X_j + \sum_i X_i^2 \left(\sum_{j\neq i} X_j \right)^2 \right\rangle \\
&= \left\langle \sum_i X_i^4 \right\rangle + 2 \left\langle \sum_i X_i^3 \right\rangle \left\langle \sum_{j\neq i} X_j \right\rangle + \\
&\left\langle \sum_i X_i^2 \left(\sum_{j\neq i} X_j^2 + \sum_{k\neq j\neq i} X_j X_k \right) \right\rangle \\
&= N \left\langle X^4 \right\rangle + N(N-1) \left\langle X^2 \right\rangle^2
\end{aligned} \tag{D.17}$$

where we have dropped any terms $\propto \langle X \rangle$, like discussed.

The third term:

$$\begin{aligned}
\left\langle \left(\sum_i X_i \right)^4 \right\rangle &= \left\langle \sum_i X_i \left(X_i + \sum_{j\neq i} X_j \right) \left(X_i + \sum_{k\neq i} X_k \right) \left(X_i + \sum_{l\neq i} X_l \right) \right\rangle \\
&= \left\langle \sum_i X_i^4 \right\rangle + 3 \left\langle \sum_i X_i^3 \sum_{j\neq i} X_j \right\rangle + \\
&3 \left\langle \sum_i X_i^2 \left(\sum_{j\neq i} X_j \right)^2 \right\rangle + \left\langle \sum_i X_i \left(\sum_{j\neq i} X_j \right)^3 \right\rangle \\
&= N \left\langle X^4 \right\rangle + 3 \left\langle \sum_i X_i^2 \left(\sum_{j\neq i} X_j^2 + \sum_{k\neq j\neq i} X_j X_k \right) \right\rangle \\
&= N \left\langle X^4 \right\rangle + 3 \left\langle \sum_i X_i^2 \sum_{j\neq i} X_j^2 \right\rangle \\
&= N \left\langle X^4 \right\rangle + 3N(N-1) \left\langle X^2 \right\rangle^2 .
\end{aligned} \tag{D.18}$$

Inserting the final line of eqs.D.16,D.17,D.18 into eq.D.12:

$$
\begin{aligned}
\left\langle s^4 \right\rangle &= \frac{1}{N^2}\left(N\left\langle X^4\right\rangle + N(N-1)\left\langle X^2\right\rangle^2\right) \\
&- \frac{2}{N^3}\left(N\left\langle X^4\right\rangle + N(N-1)\left\langle X^2\right\rangle^2\right) \\
&+ \frac{1}{N^4}\left(N\left\langle X^4\right\rangle + 3N(N-1)\left\langle X^2\right\rangle^2\right) \\
&= \left\langle X^4\right\rangle\left(\frac{1}{N} - \frac{2}{N^2} + \frac{1}{N^3}\right) + \left\langle X^2\right\rangle^2\left(\frac{N-1}{N} - \frac{2(N-1)}{N^2} + \frac{3(N-1)}{N^3}\right) \\
&= \left\langle X^4\right\rangle\frac{N^2-2N+1}{N^3} + \left\langle X^2\right\rangle^2\frac{N^2(N-1)-2N(N-1)+3(N-1)}{N^3} \\
&= \frac{N-1}{N^3}\left(\left\langle X^4\right\rangle(N-1) + \left\langle X^2\right\rangle^2(N^2-2N+3)\right) \\
&= \frac{N-1}{N^3}\left(\mu_4(N-1) + \mu_2^2((N-1)^2+2)\right)
\end{aligned}
\tag{D.19}
$$

where we have substituted the central moments μ_n for the raw moment $\langle X^n\rangle$ of the central variable. All together now thee variance from eq.D.11 becomes:

$$
\begin{aligned}
\mathrm{var}(s^2) &= \left\langle s^4\right\rangle - \left\langle s^2\right\rangle^2 \\
&= \frac{N-1}{N^3}\left(\mu_4(N-1) + \mu_2^2((N-1)^2+2)\right) - \left(\frac{N-1}{N}\mu_2\right)^2 \\
&= \mu_4\left(\frac{(N-1)^2}{N^3}\right) + \mu_2^2\left(\frac{(N-1)\left((N-1)^2+2\right)}{N^3} - \frac{(N-1)^2}{N^2}\right) \\
&= \mu_4\left(\frac{(N-1)^2}{N^3}\right) + \mu_2^2\left(\frac{(N-1)^3+2(N-1)-N(N-1)^2}{N^3}\right) \\
&= \frac{N-1}{N^3}\left(\mu_4(N-1) + \mu_2^2\left((N-1)^2+2-N(N-1)\right)\right) \\
&= \frac{N-1}{N^3}\left(\mu_4(N-1) + \mu_2^2\left(N^2+1-2N+2-N^2+N\right)\right) \\
&= \frac{N-1}{N^3}\left(\mu_4(N-1) - \mu_2^2(N-3)\right).
\end{aligned}
\tag{D.20}
$$

If we assume $N \gg 1$ such that $N \approx N-1 \approx N-3$, we note that eq.D.20 reduces to a $1/N$ scaling:

$$
\mathrm{var}(s^2) \approx \frac{N}{N^3}(\mu_4 N - \mu_2^2 N) = \frac{1}{N}(\mu_4 - \mu_2^2) \tag{D.21}
$$

If we make the further simplification of assuming Gaussian statistics with well-known moments $\mu_4 = 3\sigma^4$ and $\mu_2 = \sigma^2$, where σ^2 is the population variance (and in this case the quantity we actually want to measure, $\sigma^2 = \sigma_0^2(1+2\eta)$) we find:

$$\mathrm{var}(s^2) \approx= \frac{1}{N}(3\sigma^4 - \sigma^4) = \frac{1}{N}2\sigma_0^4(1+2\eta)^2. \tag{D.22}$$

We are now in a position to estimate a signal-to-noise ratio as,

$$\begin{aligned} SNR &:= \frac{\text{signal - background}}{\text{noise}} = \frac{\sigma_0^2(1+2\eta-1)}{\sqrt{\mathrm{var}(s^2)}} \\ &= \frac{\sigma_0^2 2\eta}{\sqrt{2/N}\sigma_0^2(1+2\eta)} \\ &= \sqrt{2N}\frac{\eta}{1+2\eta} \end{aligned} \tag{D.23}$$

D.4 Moments for the probability distribution describing our state

Following Yurke and Stoler PRA 1987, we can calculate the moments of the probability distribution describing a mixture of a single photon and vacuum. In their language they introduce a variable

$$q = x + \left(\frac{1-\eta}{\eta}\right)^{1/2} y, \tag{D.24}$$

where x is a quadrature of the "signal" mode, i.e. the single photon, and y is the same quadrature, but of the "noise" mode, i.e. vacuum. They note that q is "proportional to" the measurement outcome, so if we take their result for the moments of q, and rescale q to fit our convention, i.e. introduce

$$q' := \eta^{1/2} q = \eta^{1/2} x + (1-\eta)^{1/2} y, \tag{D.25}$$

which resembles our density matrix to a great deal. Now since the expectation value operator is linear, we can simply rescale the result of their calculation, i.e.

$$\langle (q')^n \rangle = \left\langle (\eta^{1/2} q)^n \right\rangle = \eta^{n/2} \langle q^n \rangle \tag{D.26}$$

where $\langle q^n \rangle$ denotes the n'th moment of q. They find an expression for $\langle q^n \rangle$

as

$$\langle q^n \rangle = \int_{-\infty}^{\infty} dq \frac{1}{\pi^{1/2}} q^n (1 - \eta + 2\eta^2 q^2) e^{-\eta q^2} \tag{D.27}$$

We can now calculate the moments required for finding the *actual* scaling of the SNR with η:

$$\mu_2 = \frac{1}{2}(1 + 2\eta) \tag{D.28}$$

$$\mu_4 = \frac{3}{4}(1 + 4\eta)\,. \tag{D.29}$$

Here the shot noise level is implicitly chosen to be $\sigma_0^2 = 1/2$, and we see that we recover our previous calculation of the variance (μ_2) from eq. D.9.

The SNR calculation becomes:

$$SNR = \frac{\text{signal - bkg.}}{\text{noise}} \tag{D.30}$$

$$= \frac{\eta}{\sqrt{\frac{N-1}{N^3}\left(\left(\frac{3}{4}(1+4\eta)\right)(N-1) - \left(\frac{1}{2}(1+2\eta)\right)^2 (N-3)\right)}} \tag{D.31}$$

In figure D.1 I show the results of the full calculation, eq. D.31 as well as the approximation of eq. D.23, which for high N shows good agreement for a low value of η, like we will have in first experiments.

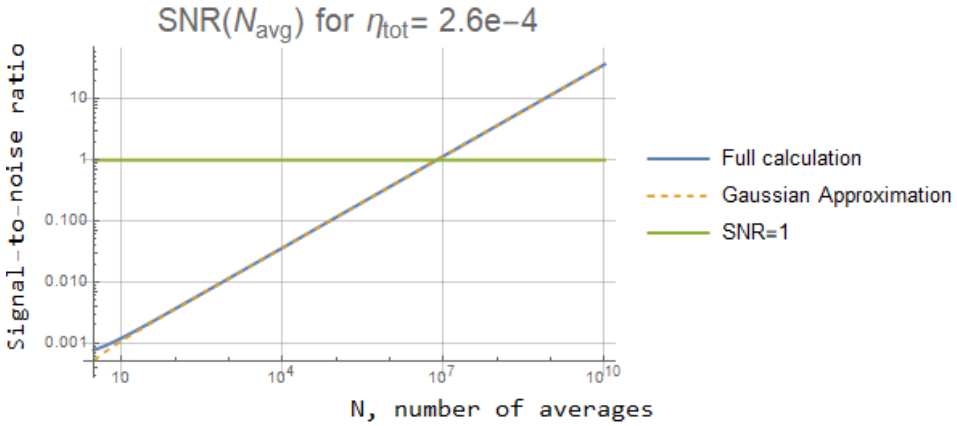

Figure D.1: Plot of SNR predictions of eq. D.23(D.31) in dashed orange (full blue) as well as a green line highlighting SNR = 1. For $N > 100$, the full calculation is well-reproduced by the Gaussian approximation.

E Optomechanical Cavity Schematics

In this appendix we show technical drawings of the pieces comprising the optomechanical cavity.

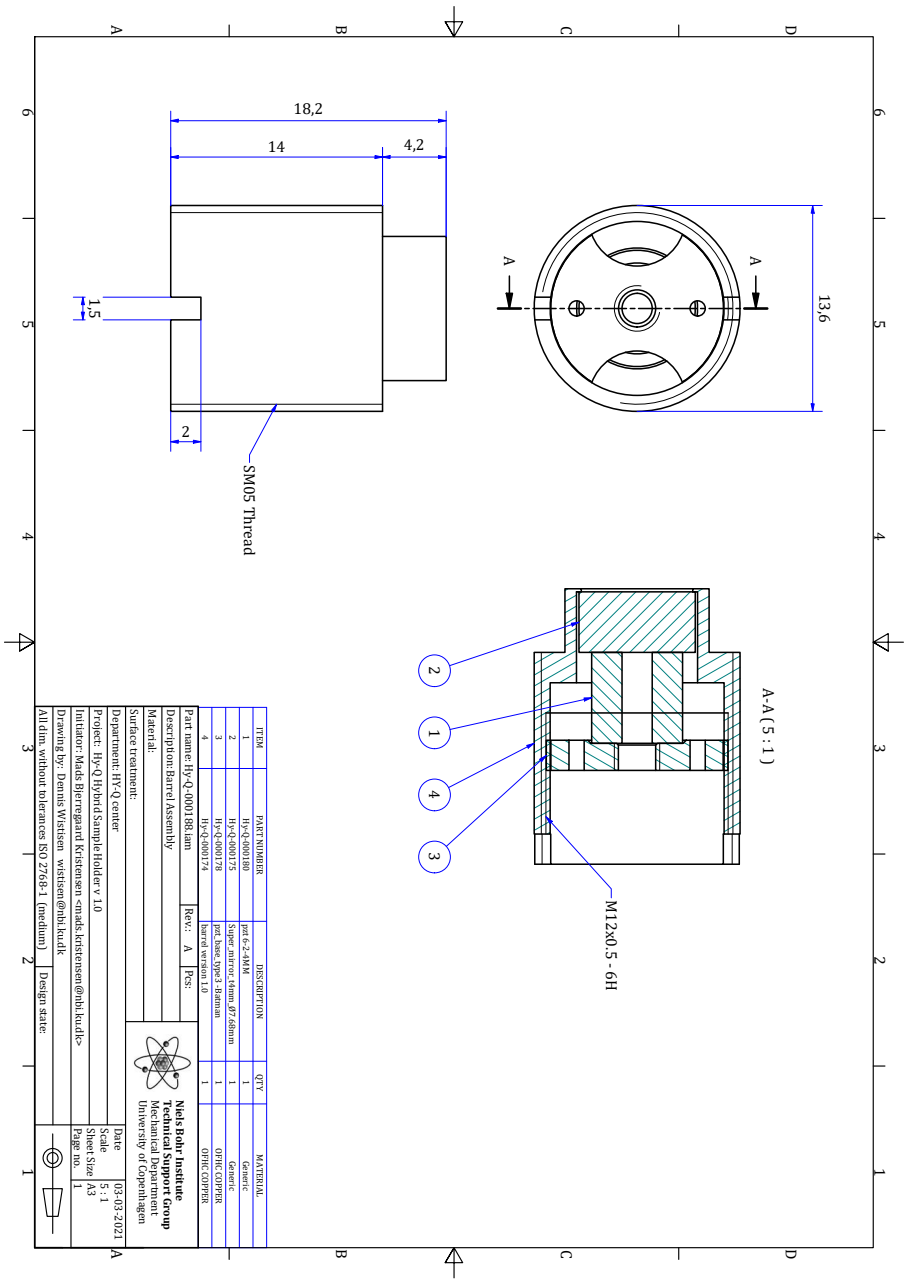

Figure E.1: Mirror holder barrel schematic. The ”barrel” (4) holds the mirror (2), which together with a piezo (1) is clamped with a custom screw (3).

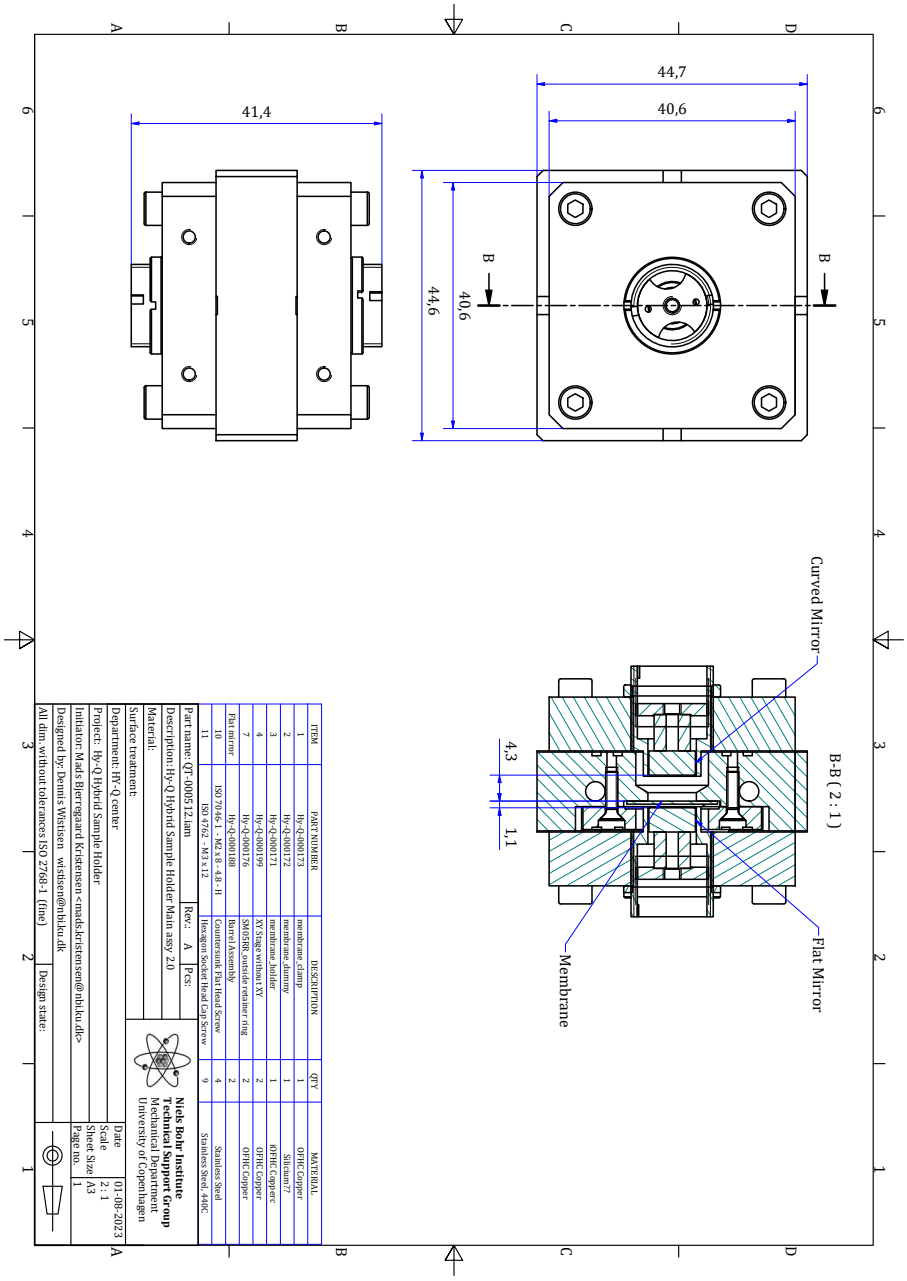

Figure E.2: Cavity assembly schematic. The assembly is comprised of three main parts: two mirror holders and one membrane holder. The membrane holder has through-holes for clamping to the cryostat coldfinger and a recess to accomodate the membrane. The membrane is clamped with a ”coin” lid. The mirror holders each host a mirror in a barrel-assembly (fig. E.1) and a screwed to the membrane holder.

F Tables of Symbols

Symbol	Definition	Description
r_i	-	Field reflection coefficient of i'th optic
t_i	-	Field transmission coefficient of i'th optic
L_{cav}	-	Cavity length
c	$299\,792\,458\,\mathrm{m\,s^{-1}}$	Speed of light in vacuum
τ_{rt}	$2L_{\mathrm{cav}}/c$	Cavity roundtrip time
κ_i	eq. (2.2)	Cavity energy decay rate through port i
κ	eq. (2.3)	Total cavity energy decay rate
η_{c}	eq. (2.4)	Cavity overcoupling
$\mathcal{F}$	eq. (2.5)	Cavity finesse
δ_{exc}	-	Excess cavity loss
ν_{FSR}	eq. (2.9)	Cavity free spectral range
$\Omega_{\mathrm{cav},n}$	$n\Omega_{\mathrm{FSR}}$	Resonant frequency of n'th longitudinal cavity mode
Ω_{L}	-	Laser frequency
Δ	$\Omega_{\mathrm{L}} - \Omega_{\mathrm{cav}}$	Detuning from a cavity mode
g_i	eq. (2.13)	Cavity g-parameter
R_i	-	Radius of curvature of i'th optic
$w(z)$	table 1	cavity beam radius
w_0	table 1	cavity waist
z_{R}	table 1	Rayleigh range
$R(z)$	table 1	cavity beamfront radius of curvature
a, $a^\dagger$	-	Annihilation, creation operator for a cavity mode
$s_{\mathrm{in/out}}$	-	Input/output photon flux from a cavity
$\chi_{\mathrm{cav}}(\Omega)$	eq. (2.29)	Susceptibility of a cavity

Table 6: Summary of used notation for the selected physical quantities describing optical cavities (section 2).

Symbol	Definition	Description
u_i	eq. (3.1)	Displacement vector
ε_{ij}	eq. (3.2)	Elastic strain tensor
σ_{ij}	eq. (3.3)	Elastic stress tensor
E	-	Young's modulus
ν	-	Poisson's ratio
w	u_z	Out-of-plane displacement
h	-	Membrane thickness
$\varepsilon_{\alpha\beta}$	eq. (3.6)	In-plane elastic strain tensor
$\sigma_{\alpha\beta}$	eq. (3.6)	In-plane elastic stress tensor
ρ	-	Mass density
D	$h^3E/(12(1-\nu^2))$	Flexural rigidity
λ	eq. (3.15)	Dimensionless stress parameter
Q	eq. (3.19)	Quality factor
Q	eq. (3.21)	Intrinsic quality factor
φ	eq. (3.21)	Loss angle
E_{eff}	eq. (3.23)	Effective (complex) Young's modulus
$\bar{\tau}$	eq. (3.24)	Zener model relaxation time
Δ_E	eq. (3.24)	Zener model relaxation strength
σ_{ij}^{con}	eq. (3.25)	Conservative component of elastic stress tensor
σ_{ij}^{dis}	eq. (3.25)	Dissipative component of elastic stress tensor
m_{eff}	table 2	Effective mass
Ω_{m}	table 2	Mechanical frequency
Γ_{m}	table 2	Mechanical energy decay rate
$\chi_q(\Omega)$	eq. (3.28)	Dimensioned mechanical susceptibility
q	-	Dimensioned mechanical position coordinate
p	-	Dimensioned mechanical momentum coordinate
a	-	Phononic crystal lattice constant
$b, b^\dagger$	-	Annihilation, creation operators for a mechanical mode

Table 7: Summary of used notation for the selected physical quantities describing mechanical resonators and phononic engineering (sections 3, 4).

Symbol	Definition	Description
G	$-\partial\Omega_{\mathrm{cav}}/\partial q$	Frequency pull parameter
g_0	Gx_{zpf}	Vacuum optomechanical coupling rate
α	-	Strong coherent field amplitude
$X_{\mathrm{L}}, Y_{\mathrm{L}}$	eq. (5.15)	Dimonsionless optical quadrature operators
$X_{\mathrm{m}}, Y_{\mathrm{m}}$	eq. (5.15)	Dimonsionless mechanical quadrature operators
$\chi_{\mathrm{eff}}(\Omega)$	eq. (5.19)	Effective mechanical susceptibility
$\Delta\Omega_{\mathrm{m}}$	eq. (5.20)	Optical spring shift
Γ_{opt}	eq. (5.20)	Optomechanical damping
Γ_{eff}	$\Gamma_{\mathrm{m}} + \Gamma_{\mathrm{opt}}$	Effective mechanical bandwidth
$\mathcal{C}$	eq. (5.22)	Classical coorperativity
$\bar{n}_{\mathrm{final}}$	eq. (5.27)	Final sideband cooled phonon occupation
$\mathcal{C}_{\mathrm{q}}$	eq. (5.28)	Quantum coorperativity
$2kz$	-	Membrane position relative to cavity standing wave
η_{MO}	eq. (5.47)	Mechanical-optical mode overlap

Table 8: Summary of used notation for the selected physical quantities describing cavity optomechanics (section 5).